Titre: Title:	Effect of Growth Conditions and Surface Treatment on the Performance of Protective Coatings on Aircraft Engine Components
Auteur: Author:	Erika Judith Herrera Jimenez
Date:	2021
Type:	Mémoire ou thèse / Dissertation or Thesis
Référence: Citation:	Herrera Jimenez, E. J. (2021). Effect of Growth Conditions and Surface Treatment on the Performance of Protective Coatings on Aircraft Engine Components [Ph.D. thesis, Polytechnique Montréal]. PolyPublie. https://publications.polymtl.ca/5609/

URL de PolyPublie: PolyPublie URL:	https://publications.polymtl.ca/5609/
Directeurs de recherche: Advisors:	Ludvik Martinu, & Jolanta-Ewa Sapieha
Programme: Program:	Génie des matériaux

POLYTECHNIQUE MONTRÉAL

affiliée à l’Université de Montréal

Effect of growth conditions and surface treatment on the performance of protective coatings on aircraft engine components

ERIKA JUDITH HERRERA JIMENEZ

Département de génie physique

Thèse présentée en vue de l’obtention du diplôme de *Philosophiæ Doctor*

Génie des matériaux

Février 2021

POLYTECHNIQUE MONTRÉAL

affiliée à l'Université de Montréal

Cette thèse intitulée :

Effect of growth conditions and surface treatment on the performance of protective coatings on aircraft engine components

présentée par **Erika Judith HERRERA JIMENEZ**

en vue de l'obtention du diplôme de *Philosophiæ Doctor*

a été dûment acceptée par le jury d'examen constitué de :

Clara SANTATO, présidente

Jolanta-Ewa SAPIEHA, membre et directrice de recherche

Ludvik MARTINU, membre et codirecteur de recherche

François SCHIETTEKATTE, membre

Stephen MUHL, membre externe

DEDICATION

To my Mom and Dad.

ACKNOWLEDGEMENTS

Foremost, I would like to express my gratitude to my directors Prof. Jolanta Ewa Sapieha and Prof. Ludvik Martinu for providing me with the opportunity to complete my Ph.D. thesis. I would like to thank them for their valuable guidance, scholarly inputs, and consistent encouragement throughout the research work. I consider it a great honour to have the opportunity to do my doctoral studies under their guidance and to learn from their research experience.

I would also like to thank Prof. Avi Raveh for his advice, discussions, and suggestions. I consider it a great honour to have the opportunity to learn from his vast experience.

The thesis would not have been successfully completed without the help I received from Dr. Etienne Bousser and Dr. Thomas Schmitt. I would like to express my special appreciation and gratitude to them for discussions, assistance in carrying out experimental tests, ideas, encouragement, and valuable advice.

Thanks to Pratt and Whitney Canada, especially Elvi Dalgaard and Joel Larose, for the support provided during the advancement and completion of this Ph.D. thesis.

I gratefully acknowledge the participation of members of the jury in my Ph.D. defense, Profs. Clara Santato, Stephen Muhl, Francois Schiettekatte, Marek Balazinski and Rene Mayer as représentant du doyen.

I am most grateful to Dr. Nicolas Vanderesse, Prof. Philippe Bocher, Dr. Damian Batory and Dr. Oleg Zabeida for their invaluable time and guidance to complete the experimental part of this work.

I would also like to thank Francis Turcot, Sébastien Chénard, Samuel Cardinal, Francis Boutet and Jean-Philippe Massé for their expert technical assistance.

All my gratitude to Alana Doyle and Dr. Mike Boldrick for their invaluable support, time, and help to gain confidence in my language skills to communicate ideas, results, and conclusions.

Thanks to all my colleagues from the LaRFIS group, especially Jacques Lengaigne, Antonin Riera, Thaddaea Rath, Phillip Rumsby, Yuxiao Wu, Josefina Crespo, Thomas Poirie, Fabrice Pougoum, Jingcheng Qian, Francis Blanchard, Stephen Brown, Bill Baloukas, Marwan Azzi, Louis Dubé, Rodrigue Beaini, Sasha Woodward, Simon Loquai, Michael Laberge, Soroush Hafezian, Amaury Kilicaslan, William Trottier-Lapointe, Martin Caron, Julien Gagnon, Julien Schmitt, Aleksandar

Miletic, Artem Shelemin, Veronika Simova, Medard Koshigan, Erwens Broustet and Adela Jagerova for the discussions and time shared in the office, labs or sometimes outside of Poly.

My special gratitude to my invaluable Russian team (Andrey Potiforov and Mary Zhuldybina) and my dear friends (Adriana Gallegos Melgar, Jorge Linares, David Guzman, Silvia Rivqa Soto, Yalina Garcia, Wilber Antunez, Karla Garcia, Berenice Herrera, Erika Montes, Juan Ruacho, Immanne Chatri, Alma Mora, and Elnaz Alebrahim) for their support and encouragement.

Last but not least, I would like to thank my beloved family, my Mom (Gricelda Ivonne Jimenez), my Dad (J. Antonio Herrera R.), my siblings (Yessica, Carolina, Ana, and Tony R.), and my nieces and nephew (Tessa, Dany, Erika and Ezio). All of them have been a key part of every step through my research carrier.

RÉSUMÉ

Dans l'industrie aérospatiale, de nombreuses formes de défaillance des matériaux, dues à des dommages causés par des sollicitations externes et à la fatigue des structures, peuvent entraîner des événements catastrophiques s'ils ne sont pas détectés à temps. Les composantes se déplaçant à grande vitesse sont particulièrement sujettes à la fissuration car elles sont exposées à des environnements difficiles et à des contraintes élevées. Tout au long de la durée de vie d'un avion, la probabilité de formation et de propagation de fissures causées par des dommages matériels augmente, ce qui représente des défis importants pour le développement et la performance en service des moteurs.

Le sujet de cette thèse de doctorat a été proposé en réponse aux besoins de l'industrie aérospatiale pour mieux comprendre l'initiation et la propagation des fissures ainsi que les mécanismes de dégradation, notamment l'érosion, l'usure et la fatigue, pour retarder la défaillance fatale des composants situés à l'intérieur d'un moteur à réaction. Ce travail se concentre sur l'étude du matériau Ti-6Al-4V revêtu en raison de son utilisation répandue dans certaines des composantes de moteur les plus critiques, généralement dans les pièces de stator et de rotor.

Les procédés d'ingénierie de surface devraient envisager des revêtements de protection avec des propriétés tribo-mécaniques "idéales" et des procédés pour contrôler les contraintes résiduelles (RS). À cet égard, la finition de surface des revêtements et des substrats est essentielle, car la défaillance des fissures débute généralement à la surface des composantes. Les revêtements en céramique sont devenus la solution la plus fréquemment recherchée pour la protection du moteur à réaction. L'architecture du revêtement et la ténacité qui en découle ont été reconnues comme des facteurs clés, notamment pour la résistance à l'érosion par particules solides et à l'usure. Les revêtements de protection ont été abordés dans la littérature disponible, comme en témoignent les nombreuses contributions de notre propre laboratoire. Il a été clairement conclu que la manière la plus importante de faire progresser ce domaine est de mieux comprendre et d'adapter les RS qui, si elles sont bien contrôlées, peuvent atténuer la détérioration des surfaces et la sollicitation extérieure.

En réponse, cette thèse se concentre sur l'étude des revêtements de protection sous forme de couches simples et de multicouches, avec différentes valeurs de RS et différents profils en profondeur de RS par rapport à la performance mécanique. Dans la première partie de ce travail, nous avons étudié les revêtements TiN monocouche, pulvérisés de manière réactive sur des substrats de Ti-6Al-4V, tout en évaluant l'effet de trois approches d'ingénierie des interfaces: a) le traitement par plasma d'argon, b) la nitruration de surface par plasma, et c) l'implantation de titane. Chaque interface a affecté la microstructure et la texture du revêtement et du substrat. Par conséquent, les propriétés mécaniques et tribo-mécaniques présentent des variations significatives. La dureté du Ti-6Al-4V a été augmentée de ~5 GPa à 15 GPa par le prétraitement de surface, et la dureté du TiN a augmenté de 21 GPa lorsqu'il a été déposé sur du Ti-6Al-4V non prétraité à 29 GPa après le prétraitement de surface à l'azote. Le revêtement de TiN et les couches interfaciales ont présenté un RS élevé en compression entre -4,0 GPa et -2,4 GPa dans le revêtement, et dans le substrat de Ti-6Al-4V un RS entre -800 MPa et -200 MPa a été observé à des profondeurs de plusieurs centaines de nanomètres jusqu'à environ 4 µm.

Dans la deuxième partie de la thèse, nous avons étudié les mécanismes de fracture du Ti-6Al-4V revêtu de TiN avec différents prétraitements de surface en utilisant des tests de micro-tension. Le traitement de l'interface semble affecter particulièrement le mécanisme de fracture en termes de résistance à la traction et de limite d'élasticité du Ti-6Al-4V. Cependant, le revêtement de TiN avec un RS à forte compression au niveau de la couche d'interface et à l'intérieur du revêtement lui-même peut atténuer l'effet néfaste des traitements d'interface. Les résultats montrent que le comportement mécanique du revêtement est régi de manière significative par la réponse collective du système revêtement/substrat pour retarder la nucléation et la propagation des fissures à travers le substrat, et donc retarder la fracture de la composante. Les propriétés élasto-plastiques telles que le taux de libération d'énergie critique, la résistance à la rupture et la résistance au cisaillement interfacial montrent que l'amélioration des propriétés mécaniques des revêtements et des interfaces en TiN influence la réponse à la rupture du système revêtu. Les revêtements de TiN présentant une ingénierie de surface différente présentent une nucléation de fissures pour une déformation comprise entre 0,9 % et 1,1 %, tandis que le taux de libération d'énergie critique (15 J/m^2 et 19,7 J/m^2) et la résistance au cisaillement interfacial (550-760 MPa) sont principalement influencés par la résistance à la compression du revêtement.

Dans la dernière partie de ce travail, le prétraitement de nitruration est retenu comme le traitement d'interface principal pour l'évaluation des différentes architectures de revêtements. Plus

précisément, elle est consacrée à une étude détaillée de la résistance à l'usure et de la fracturation des systèmes monocouches TiN et ZrN et des systèmes multicouches ZrN/TiN avec différentes périodes de modulation allant de 1 à 100 nm. La dureté et la résistance à l'usure des films ont été améliorées en diminuant la périodicité dans l'architecture multicouche grâce à la formation d'une solution solide et donc au renforcement des interfaces entre les couches. De plus, nous avons proposé que l'énergie mécanique stockée dans les films en termes de RS est libérée pour favoriser la formation d'une solution solide.

Les procédés d'ingénierie de surface proposés dans ce travail, et en particulier l’amélioration de la compréhension de leur effet sur les niveaux de RS et sa distribution en profondeur, se sont avérés être des solutions prometteuses pour retarder la dégradation et atténuer les mécanismes de fracture sur les composants métalliques pour les applications aéronautiques.

ABSTRACT

In the aerospace industry, many forms of material failure due to foreign object damage and fatigue of structures may lead to catastrophic events if they are not detected in time. Components moving at high speeds are particularly subject to cracking since they are exposed to harsh environments and to high stress levels. Through aircraft's lifetime, there is an increased likelihood of crack formation and propagation caused by material's damage, which represent significant challenges for engine development and in-service performance.

The subject of this Ph.D. thesis has been proposed as a response to the needs of the aerospace industry to gain a better understanding of crack initiation, crack propagation and of the degradation mechanisms, especially erosion, wear and fatigue, to retard fatal failure on components located within a jet engine. This work focuses on a study of coated Ti-6Al-4V material due to its wide use on some of the most critical engine components, typically in stator and rotor parts.

Surface engineering processes should consider protective coatings with 'ideal' tribo-mechanical properties and processes to tailor residual stress (RS). In this respect, surface finishing of coatings and substrates is vital since crack failure normally originates at the component's surface. Ceramic coatings have become the most frequently sought solution for the protection of the jet engine. Coating architecture and the related toughness have been recognized as key factors, particularly for the solid particle erosion and wear resistance. Protective coatings have been covered in the available literature as documented by numerous contributions from our own laboratory. It has been clearly concluded that the most important way to advance this field is to better understand and tailor RS that, if well controlled, can mitigate surface deterioration and external solicitation.

In response, this thesis focuses on the investigation of protective coatings in the form of single layers and multilayers, with different RS values and RS depth profiles in relation to the mechanical performance. In the first part of this work, we studied single layer TiN coatings, reactively sputtered onto Ti-6Al-4V substrates, while assessing the effect of three interface engineering approaches: a) Argon plasma treatment, b) plasma surface nitriding, and c) Titanium sub-plantation. Each interface modified the microstructure and texture of both, coating and substrate. Consequently, the mechanical and tribo-mechanical properties show significant variation. The hardness of Ti-6Al-4V was enhanced from ~5 GPa to 15 GPa by the surface pre-treatment, and the hardness of TiN increased form 21 GPa when deposited onto non-pre-treated Ti-6Al-4V to 29 GPa following nitrogen surface pre-treatment. TiN coating and interfacial layers presented a high compressive RS between -4 GPa to -2.4 GPa within the coating, and between -800 MPa to -200 MPa into a depth of several hundreds of nanometers to about 4 μm within the Ti-6Al-4V substrate.

In the second part of the thesis, we studied the fracture mechanisms of TiN-coated Ti-6Al-4V with different surface pre-treatments using micro-tensile testing. The interface treatment appears to particularly affect the fracture mechanism in terms of ultimate tensile strength and yield strength of Ti-6Al-4V. However, TiN coating with a high compressive RS at the interface layer and within the coating itself can mitigate the detrimental effect of interface treatments. The results show that the coating's mechanical behavior is significantly governed by the coating-substrate system's collective response to delay crack nucleation and propagation through the substrate, and therefore delay the component fracture. The elasto-plastic properties such as critical energy release rate, fracture toughness and interfacial shear strength show that the enhancement of the mechanical properties of TiN coatings and interfaces influences the fracture response of the coated system. TiN with different surface engineering present a crack nucleation between 0.9% to 1.1%, while the critical energy release rate (15 J/m^2 and 19.7 J/m^2) and interfacial shear strength (550-760 MPa) are mainly influenced by the compressive RS in the coating.

In the final part of this work, nitriding pre-treatment is the selected interface for the evaluation of different coating architectures. Specifically, is devoted to a detailed study of the wear resistance and fracturability of TiN and ZrN single layer and ZrN/TiN multilayer systems with various modulation periods ranging from 1 to 100 nm. The hardness and the wear resistance of the films were enhanced by decreasing the periodicity in the multilayer architecture due to the formation of a solid solution and hence strengthening of the interfaces between layers. In addition, we proposed that the mechanical energy stored in the films in terms of the RS is released to favor solid solution formation.

The surface engineering processes proposed in this work, and particularly the better understanding of their effect on the RS levels and its depth distribution, have been shown to be a promising solution to delay degradation and mitigate fracture mechanisms on metallic components for aeronautical applications.

TABLE OF CONTENTS

DEDICATION iii

ACKNOWLEDGEMENTS iv

RÉSUMÉ vi

ABSTRACT ix

TABLE OF CONTENTS xi

LIST OF TABLES xv

LIST OF FIGURES xvi

LIST OF SYMBOLS AND ABBREVIATIONS xxii

CHAPTER 1 INTRODUCTION 1

1.1 Problem identification 5

1.2 Objectives 6

1.3 Organization of the thesis 6

1.4 Research contributions 7

CHAPTER 2 LITERATURE REVIEW 10

2.1 Substrate selection 10

2.1.1 Ti-6Al-4V properties 10

2.1.2 Ti-6Al-4V substrate after PVD processes 13

2.2 Surface engineering 13

2.2.1 Protective coatings and interfacial layers 14

2.2.2 PVD processes 14

2.2.3 Surface treatments 20

2.3 Mechanical properties of coated systems 23

2.3.1 Origin of the stress 26

2.3.2 Residual stress analysis 34

2.3.3 Tribology of coated systems 35

2.3.4 Nitride coatings 36

CHAPTER 3 EXPERIMENTAL METHODOLOGY 45

3.1 Substrate preparation 45

3.2 PVD techniques – Surface engineering processes 46

3.2.1 Magnetron sputtering 46

3.2.2 Deposition system 46

3.3 Crystallographic, microstructural and morphological characterization 50

3.3.1 Microscopy 50

3.3.2 XRD Diffraction 52

3.4 Mechanical characterization 54

3.4.1 Residual stress 54

3.4.2 Curvature technique 59

3.4.3 Nanoindentation 60

3.4.4 Tensile test 61

3.4.5 Scratch test 63

3.5 Wear test 65

CHAPTER 4 ARTICLE 1: EFFECT OF PLASMA INTERFACE TREATMENT ON THE MICROSTRUCTURE, RESIDUAL STRESS PROFILE, AND MECHANICAL PROPERTIES OF PVD TIN COATINGS ON TI-6AL-4V SUBSTRATES 67

4.1 Abstract 67

4.2 Introduction 68

4.3 Experimental methods 71

4.3.1 Sample preparation....71
4.3.2 Characterization methods....74
4.3.3 Mechanical characteristics....75
4.3.4 Microstructural characteristics....77
4.4 Results and Discussion....78
4.4.1 Effect of sample mounting on the residual stress....78
4.4.2 Residual stress depth profiles and mechanical properties....81
4.4.3 Microstructural characteristics of the films, surfaces and interfaces....83
4.5 Summary and conclusions....93
4.6 Acknowledgment....95
CHAPTER 5 ARTICLE 2: FRACTURE MECHANISM OF TIN COATINGS ON TI-6AL-4V SUBSTRATES: ROLE OF INTERFACES AND OF THE RESIDUAL STRESS DEPTH PROFILE 96
5.1 Abstract....96
5.2 Introduction....97
5.3 Experimental methods....100
5.3.1 Sample preparation....100
5.3.2 Microstructural characteristics....102
5.3.3 Mechanical characteristics....103
5.4 Results....104
5.4.1 Microstructural characteristics....104
5.4.2 Hardness, Young’s modulus, residual stress and scratch resistance....106
5.4.3 Tensile test characterization....110
5.5 Discussion....117

5.6 Conclusion.......121
5.7 Acknowledgments.......122
CHAPTER 6 ARTICLE 3: SOLID SOLUTION HARDENING IN NANOLAMINATE ZRN-TIN COATINGS WITH ENHANCED WEAR RESISTANCE.......123
6.1 Abstract.......123
6.2 Introduction.......124
6.3 Experimental methods.......125
6.4 Results and discussions.......127
6.4.1 Effect of periodicity on the structure and mechanical properties.......127
6.4.2 Phenomenological model of solid solution phase formation.......133
6.5 Summary and conclusions.......136
6.6 Acknowledgments.......137
CHAPTER 7 FRACTURABILITY STUDY ON MULTILAYER COATINGS.......138
7.1 Context.......138
7.2 Experimental methodology.......139
7.3 Results and discussions.......139
7.4 Discussion.......145
7.5 Conclusion.......147
CHAPTER 8 GENERAL DISCUSSION.......148
CHAPTER 9 CONCLUSIONS AND RECOMMENDATIONS.......154
9.1 Conclusions.......154
9.2 Recommendations.......157
REFERENCES.......159

LIST OF TABLES

Table 1.1 Publications in the form of articles in peer-reviewed journals. 8

Table 1.2 Oral and poster presentations at international conferences and symposia. 8

Table 1.3 Collaboration with other universities and scholarships. 9

Table 2.1 Physical properties of Titanium 11

Table 2.2 Composition of Ti-6Al-4V (wt.%). 12

Table 2.3 Specific properties of Ti-6Al-4V alloy in its two main heat-treated conditions. 12

Table 2.4 Zone structures in sputtered coatings, modified from. 19

Table 2.5. Summary of the main characteristics of different models and the origin of intrinsic stress in PVD coatings. 32

Table 2.6 Relationship between process parameters and preferred orientation (PO) in TiN coatings Table taken from. 38

Table 2.7 Mechanical properties of TiN/TiC multilayer coatings. 44

Table 3.1 PVD optimized conditions for the plasma interfaces, ZrN/TiN multilayer, ZrN and TiN coatings used at the DC magnetron sputtering during this study. 48

Table 4.1 Mechanical properties of the interface layers and of the coated samples determined by nanoindentation, GIXRD, and scratch testing (the latter one performed at 0° and 90° orientations). 83

Table 5.1 Crystallite size (CS) and preferential orientation (PO) of TiN coatings on Ti64 with different interface treatments. 106

Table 5.2 Mechanical properties of all samples extracted from nanoindentation and micro-tensile tests. 112

Table 7.1 Fracture properties of the single layer and multilayer structures. Hardness and Young's modulus obtained by nanoindentation are given in the parenthesis. 145

Table 8.1 Activities and characterization techniques required for the realization of this thesis. .148

LIST OF FIGURES

Figure 1.1 Schematic representation for turbo-jet engine from Rolls Royce. Cold and hot sections are indicated by blue and red color, respectively. 3

Figure 2.1 Schematic representation of Ti unit cells. 11

Figure 2.2 Schematic representation of the influence of alloying elements on α- and β- fields. ...12

Figure 2.3 Structure zone models for coating growth: a) Model proposed by Movchan and Demchishin; b) Model proposed by Thornton for sputtered metal coatings; and c) the latest model proposed by A. Anders. 18

Figure 2.4 Schematic representation of a coated substrate showing coating, interface, and substrate with the main properties to be considered in this work. 20

Figure 2.5 Idealized intrinsic stress vs. normalized momentum, P_n, which is related to the kinetic energy of particles impacting the coating surface per atom condensed and integrated into the coating. 28

Figure 2.6 Schematic representation of the energetic particles originating at the sputtering target that may strike the coating and produce structural modification and gas incorporation. Particles from the plasma are superimposed on those originating at the target. 29

Figure 2.7 Intrinsic stress as a function of a) Ar pressure , and b) applied substrate bias. 31

Figure 2.8 Macromechanical contact conditions for different mechanisms that influence friction when a hard spherical slider moves on a coated flat surface. 36

Figure 2.9 Unit cell of the FCC structure. 37

Figure 2.10 Phase diagram of a) TiN, and b) ZrN. 37

Figure 2.11 Hardness as a function of effective Young's modulus for nitride coatings. 39

Figure 2.12 Measured coating residual stress on silicon (red bars) and steel substrates (orange bars); fracture toughness (purple bars) was calculated from FEM stress simulations and scratch test cracking behaviour; cracking resistance (green points) was measured by the bend test for

DLC, MoS_2 and TiN-coated steel surfaces with elastic moduli in the range of E = 39–475 GPa. 41

Figure 2.13 Abrasive wear on tools coated with TiN-based coatings: a) Life enhancement and b) flank wear on coated tool *vs* length of feed....................41

Figure 2.14 Toughening mechanism in ceramic multilayer materials. 43

Figure 2.15 Crack propagation as a function of crack length and friction coefficient as a function of distance for single-layer and multi-layer coatings. 44

Figure 3.1 Magnetron sputter-deposition system. 47

Figure 3.2 X-ray diffraction. 53

Figure 3.3 Schematic representation of X-ray diffractometer with a grazing incidence configuration. 54

Figure 3.4 Penetration depth vs. $sin^2\psi$ calculated for different α angles using equation with a schematic of a coated sample showing the penetrating (primary) and exit beams and their respective angles. 57

Figure 3.5 Deconvolution of diffracted peaks extracted from a measurement done at α=8° on TiN on Ti-6Al-4V substrate....................58

Figure 3.6 Typical nanoindentation curve from loading and unloading vs. penetration depth on the coated sample. 61

Figure 3.7 The two in situ tensile test configurations: a) continuous, b) interrupted tests, and c) dog-bone sample coated sample being tested and after failure with a close up to surface cracks. 63

Figure 3.8 Overview of a scratch testing on coated sample. 64

Figure 3.9 Optical images present L_{C1} and L_{C2} of TiN coating. 65

Figure 3.10 Top view of linear reciprocating ball-on-flat wear configuration. 66

Figure 4.1 Schematic representation of a) stainless steel sample holder, front and cross-section views, with clamped (CL) and freely attached (NC) samples, and b) sample orientation as defined by the green arrow. 74

Figure 4.2 Residual stress measured by XRD in different sample orientations: a) Effect of orientation on clamped samples with TiN films deposited after the three different pre-treatments; b) RS at 0^o and 90^o for disc and rectangular substrates clamped and not-clamped to the substrate holder following different plasma treatments and TiN deposition without pre-treatment. 80

Figure 4.3 Residual stress profiles of TiN coatings deposited on clamped rectangular Ti64 with different interface treatments measured by XRD at a) 0° and b) 90° sample orientations. ...82

Figure 4.4 Diffractograms of a) the Ti64 substrate after different surface pre-treatments at 0° sample orientation, and b) of the TiN films deposited on Ti64 with different interfaces at 0° and 90° sample orientations. 86

Figure 4.5 Texture coefficient of (111), (200) and (220) planes of the TiN coating on Ti64 with the three different interfaces at a) 0° and b) 90° sample orientations. 87

Figure 4.6 TKD phase maps (top-a) and inverse pole figure (IPFX) maps (bottom-b) of the cross-sections of the TiN coatings on the three different interfaces. The colours in (a) represent TiN and Ti phases in the EBSD phase map as marked, and the coloured grains in (b) mean various orientations identified by the index of the IPFX. 90

Figure 4.7 Bright field TEM images (top-a) and TKD local misorientation maps (bottom-b) of coated samples with different interface treatments. Green and red doted rectangles indicate the interface zone. 91

Figure 4.8 Dark field (DF) TEM image of the representative TiN-Ar cross-section (center). The encircled numbers 1, 2 and 3 in various regions of the DF image represent areas where SAED patterns were measured on other samples with different interfaces: SAED patterns in region 1 correspond to the TiN coating (white circles), region 3 is the Ti (Blue circles) from substrate in TiN-Ar, and the regions 2 (right side of the central Figure) are the SAED patterns of the interface zone in TiN-Ar, TiN-Nit and TiN-Ti samples, respectively. 93

Figure 5.1 Schematic representation of flat rectangular thin sample and dog-bone tensile sample with their corresponding dimensions. 102

Figure 5.2 Cross-section SEM images of a) TiN-Nit, b) TiN-Ti and c) TiN-Ar specimens after micro-tensile testing; the scale bar in (c) corresponds to all three SEM images (5 kV, secondary electron detector). The loading direction goes approximately from the left to the right. 105

Figure 5.3 Diffractograms of the TiN films deposited on Ti64 with different interfaces. 106

Figure 5.4 Hardness and reduced Young's modulus of a) Ti64 with surface treatments, and b) TiN-coated specimens with different interfaces. 107

Figure 5.5 a) RS in the near surface region in the Ti64 alloy following different plasma treatments; b) RS depth profiles of TiN coatings on Ti64 with different interfaces, from the coating surface to the substrate. The blue doted arrows (horizontal and vertical) schematically indicate the penetration depth of the X-ray beam on the coated system during the measurement; all measurements were performed by GIXRD. 109

Figure 5.6 Micro-scratch tracks for TiN coatings with three different interface treatments where the L_{C1} and L_{C2} areas are illustrated. 110

Figure 5.7 Stress-strain (*S*-*S*) curves for the a) surface-treated Ti64, and b) coated specimens with different interfaces....................111

Figure 5.8- Average crack density as a function of the engineering strain of TiN coatings on Ti64 with different interfaces: (a) crack onset, (b) multiplication, (c) saturation, and (d) specimen fracture. 113

Figure 5.9 Representative confocal optical images of TiN-Nit surfaces as a function of the engineering strain: (a) crack onset, (b) multiplication, (c) saturation, and (d) secondary crack stages. The red arrows in images (a) identify initial cracks, and in (d) secondary cracks. ..114

Figure 5.10 SEM images of treated surfaces of Ti64 at 1mm (top) and 5mm (bottom) distances from the fracture zone after the tensile test. 115

Figure 5.11 SEM images of the TiN-Ti specimen show a) panorama of the fracture zone, and b) a cross section view, after the tensile test. 116

Figure 5.12 SEM images of coated specimens with different interface treatments. Images were taken at 0, 1, 3 and 5 mm distances from the fracture zone after the tensile test.................117

Figure 5.13 COS, coating residual stress (RS) and interfacial shear strength (τ) as a function of critical energy release rate (G_C) for TiN coatings with different interfaces.........................120

Figure 6.1 Schematic presentation of the thickness distribution when tailoring the single layer, multi-layer and nanolaminate systems studied in this work. 126

Figure 6.2 SEM cross section micrographs of the ZrN-TiN systems at low (Top) and high magnifications (Bottom) obtained using an electron beam acceleration voltage of 15 kV: (a) L = 1 nm, (b) L = 10 nm, and (c) L = 100 nm periods. 129

Figure 6.3 X-ray patterns of the ZrN-TiN systems: a) different modulations represented by the values of L, and b) a partial pattern of a coating with L = 10 nm. 130

Figure 6.4 Lattice parameters a (a) and crystallite size D (b) of monolithic ZrN and TiN coatings and of various ZrN/TiN multilayer coatings as a function of the nanolaminate layer modulation, L. 131

Figure 6.5 Wear coefficient K as a function of the H/E_r (a) and of H^3/E_r^2 (b) ratios for the ZrN-TiN nanolaminate structures...132

Figure 6.6 Mechanical properties (H, H/E_r and H^3/E_r^2 values) of the nanolaminate ZrN-TiN films as a function of the crystallite size. 133

Figure 6.7 Effect of modulation on the total residual stress in the single layer, multilayer and nanolaminate coatings..136

Figure 7.1 Schematic representation of toughening and strengthening mechanisms in ceramic multilayer coatings [201] 139

Figure 7.2 Residual stress of single layer and multilayer systems on nitrided Ti-6Al-4V obtained by Stoney equation. 140

Figure 7.3 S-S curves of TiN-Nit and ZrN/TiN during continuous tensile tests. 141

Figure 7.4 Crack density curves of TiN-Nit and ZrN/TiN systems. 142

Figure 7.5 SEM images of parallel and secondary surface cracks on TiN-Nit and ZrN/TiN systems taken at 0, 1, 3, and 5 mm distance from the fracture zone after the tensile load was removed. 143

Figure 7.6 SEM images of the fracture in the multilayer system cross-section after tensile test: a) surface secondary crack propagation through coating, and b) two areas as close-up of a lateral crack between layers (green square) and a zig-zag crack though layers (blue square). 144

Figure 8.1 Different materials in a jet engine. 149

LIST OF SYMBOLS AND ABBREVIATIONS

a: lattice parameter

a_o: strain-free lattice constant

AC: alternate current

A_0: original cross-sectional area

Al: Aluminum

AlN: Aluminium nitride

Ar: Argon

a_a: relaxed lattice parameters of the substrate

a_c: relaxed lattice parameters of coating

Bcc: body-centered cubic

BB: Bragg-Brentano

CL: clamped substrate

C: carbon

CS: crystallite size

CTE: coefficient of thermal expansion

COS: crack onset strain

C_{CRACK}: length of the crack

CrN: chrome nitride

CVD: chemical vapor deposition

D: crystallite size average

DC: direct current

DIC: digital image correlation

DF: dark field

E: Young’s modulus

E_C: Young’s modulus of coating

EDS: energy dispersive X-ray spectrometry

E^*: normalized delivered energy flux

E_r: reduced Young’s modulus

eV: electron-volts

F: force

Fe: Iron

FCC: face centered cubic structure

FIB: Focussed Ion beam

$f(\psi)$: function of the single-crystal elastic constants

$F_{ij}(hkl, \varphi,\psi)$: function corresponding to X-ray stress factor.

GIXRD: grazing incidence X-ray diffraction

G_C: critical energy release rate

$g(\alpha_D \beta_D)$: dimensionless coefficient given by Dunduru’s parameters

H: hardness

HV: Vickers hardness

hcp: hexagonal close packed structure

hkl: Miller index

HfN: Hafnium Nitride

H_2O_2: hydrogen peroxide

h: penetration depth

h_s: thickness of substrate

h_c: thickness of coating

I_x: intensity of the incident beam

IBAD: ion beam assisted deposition

IPFX: inverse pole figure map

J_i/J_{Ti}: Ion/metal flux ratio

K: wear coefficient

K: toughness

K_{1c}: fracture toughness

keV: kiloelectron volt

k_y: constant

L: modulation periods

LSCM: laser scanning confocal microscope

L_C: critical normal load

L_{C1}: critical load 1

L_{C2}: critical load 2

nc: nanocomposite

N_2: gas nitrogen

NC: Non clampled substrates

NbN: Niobium nitride

H_2: gas hydrogen

NH_3: ammonia

NaCl: sodium chloride

O: oxygen

P_n: normalized momentum

PECVD: plasma enhanced chemical vapour deposition

PIII: Plasma Immersion Ion Implantation, Plasma Based Ion Implantation

PSII: Plasma Source Ion Implantation

P: normal applied load

P_{max}: maximum load

PO: preferred orientation

PVD: physical vapour deposition

HiPIMS: high power impulse magnetron sputtering

r_D: deposition rate

R: curvature radius

R_0*: initial* curvature radius

RF: radio frequency

RS: Residual stress (Pa)

s: sliding distance

S: stiffness

S_1, S_2: X-ray elastic constants

Si_3N_4: Silicon nitride

SAED: Selected area electron diffraction

SEM: Scanning electron microscope

SZM: structure zone model

Ti64: alloy Ti-6Al-4V; titanium-6aluminum-4vanadium alloy

TiN: Titanium nitride

Ti-Zr-N: Titanium-zirconium-nitride alloy

$T_{c\ (hkl)}$: texture coefficient

t-EBSD: Transmission electron backscatter diffraction

TEM: Transmission electron microscopy

TKD: transmission Kikuchi diffraction

Ts, T:* substrate temperature

T_m: melting temperature

Ti: Titanium

t: coating’s thickness

UTS: ultimate tensile strength

V: worn value

V_b: Negative bias voltage

W: wear rate

W: power (watts)

wt%: weight percent

XRD: x-ray diffraction

XEC: X-ray elastic constants

YS: yield stress

z: surface

ZrN: Zirconium nitride alloy

Zr: zirconium

Greek letters and symbols

α: alpha, incidence angle,

α_s: thermal expansion coefficient of substrate

α_c: thermal expansion coefficient of coating

$\beta = \theta - \psi$: exit angles of the incoming and diffracted X-ray

ε: épsilon: strain

$\theta_{(hkl)}$: tetha; diffraction angle

λ: lambda, wavelength

μ:mu, linear coefficient of absorption

μ: friction coefficient

σ: sigma: stress

σ_Y: yield stress

σ_C: critical stress given

σ_{th}: thermal stress

σ_i: intrinsic stress

σ_e: extrinsic stress

$\tau_{x\text{-}ray}$: penetration depth value

υ: upsilon, Poisson ratio

υ_c: Poisson ratio of coating

τ: tau, interfacial shear strength

ϕ: phi, azimuth angle

$\psi_{(hkl)}$: psi, angle between the scattering vector and normal to the surface

°	Degrees
°C	degrees Celsius
µm	microns
%	percentage

CHAPTER 1 INTRODUCTION

The aerospace industry has a significant economic impact around the world. Since 1981, annual sales and production of commercial aircraft materials and components have increased 228%. In the next 10 years, commercial aircraft production levels are expected to increase at least 27% due to the ongoing growth in global gross domestic production, the defense industry and passenger travel [1]. According to the pre-Covid-19 estimates, the aerospace and defense industry is expected to grow between 3 and 4% in 2020, reaching an estimated US$1.9 trillion to US$2.1 trillion by 2023, as governments worldwide, especially the USA, China, Russia and India, continue to renovate and recapitalize their militaries. Moreover, it is estimated that nearly 40,000 new airplanes will be produced by 2040 [2]. The projected growth of the aerospace industry will result in high demand for fuel efficient, as well as durable, safe, environmentally friendly, and cost-effective aircraft components, while also requiring rapid production and superior quality control. These requirements represent numerous economic and scientific challenges.

During operation, an aircraft can be exposed to harsh environments and often extreme weather conditions like storms or icings. Even under ideal conditions, the component materials would suffer certain degradation, such as erosion, wear or fatigue, resulting from elevated temperatures and fluctuating stress, particle impact [3]–[5]. Historically, material damage has been one of the major causes of aircraft accidents. This damage may appear in the form of permanent structural deformation (plastic strains), cracks, deterioration of the structure, or lack of functionality [6]. In the aerospace industry, many forms of material failure due to fatigue of structures may lead to catastrophic effects if they are not detected in time. As the aircraft ages, there is an increased likelihood of crack formation and propagation caused by material damage, which requires closer attention and higher maintenance costs [7], [8].

Historic examples of accidents caused by material failure include the De Havilland Comet plane crashes in 1954 and 1955, where metal fatigue was caused by design defects. Calculations revealed that up to 70% of the aircraft's ultimate stress under pressure was concentrated on the corners of the aircraft's square windows (i.e., avoidable stress concentrations led to fatigue cracks). In addition, some improper riveting led to fatigue cracks after repeated pressurization cycles. In 1989, an undetected fatigue crack in an engine fan blade on a McDonell Douglas DC-10 led to the catastrophic and deadly in-flight failure of the engine. In 1996, another undetected fatigue crack led to catastrophic engine failure during take-off of a McDonnell Douglas MD-88 [9]. Findings from these accidents were part of the basis for revisions of aviation requirements for cabin strength, reduction of stress concentrations, and improved crack detection.

The potential for fatigue of aircraft components and structural failure is something that anyone in the aeronautic industry is familiar with. Structural, often catastrophic, failure occurs when cracks of an aircraft component are not detected early enough. The cracks are initially very small and not easily detected. Such microscopic cracks can lead to large-scale damage when they are exposed to the flight environment. Large components moving at high speeds, such as engines, are particularly subject to cracking, especially because they are exposed to high stress levels and to harsh environments [10]. Components are rigorously inspected and tested before they are certified for any application, in order to guarantee their operational performance under every possible environment. Safety in every aspect of airplane design, construction, and operation is now fundamental, therefore material fatigue and/or failure must be considered during aircraft's design and maintenance.

One of the most promising methods used for the protection of aircraft components from problems caused by aggressive environments and high operating temperatures is the application of protective coatings. The improvement of erosion-, corrosion- and wear-resistance by applying protective coatings on these materials can provide interesting solutions, but their application should ensure the ideal coating-substrate properties to retard or stop failure mechanisms (e.g., cracks and fatigue).

During the last few years, engineers and scientists have made important progress in coatings that improve the safety and performance of aircraft components, such as wings, fuselage, landing gear, turbine blades and other jet-engine parts. Most modern commercial and military airplanes are powered by jet engines, which also are known as gas turbine engines. Their shapes and sizes can vary, but they all have certain parts in common (Figure 1.1). There is an inlet (air intake) at the front of the engine, followed by a compressor. The compressed air passes into the combustion section (burner), where the air is mixed with fuel and burned. The hot exhaust gas then passes through the turbine and out the nozzle, which is shaped to accelerate the exhaust gas and produce thrust. The compressor and turbine are composed of many rows of small airfoil-shaped blades.

Some rows are connected to the inner shaft which rotates at high speed. These turbine blades are also called rotors. Other rows of blades are stationary and are called stators.

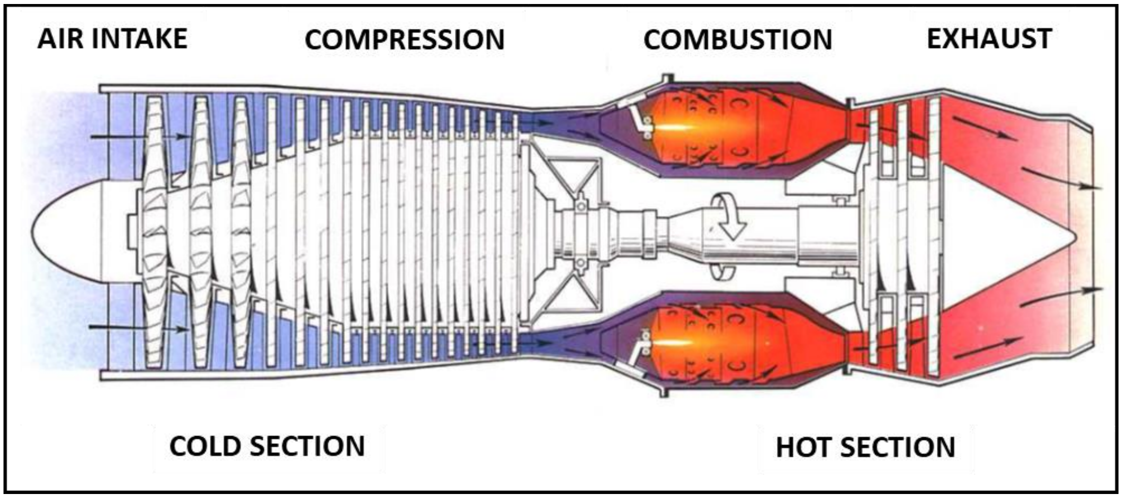

Figure 1.1 Schematic representation for turbo-jet engine from Rolls Royce. Cold and hot sections are indicated by blue and red color, respectively [11].

Titanium and stainless steel alloys have been widely used for compressor component applications because of their high strength-to-weight ratio and high corrosion resistance. However, due to the extreme conditions they are exposed to, compressor components also require an extensive variety of protective coatings, including wear-, erosion-, and corrosion-resistant, ice-phobic, anti-fretting, and thermal-barrier coatings [5]. The coatings used on Ti-6Al-4V (Ti64) compressor parts must provide high hardness, as well as wear-, corrosion- and erosion-resistance [12], [13]. TiN coatings are widely used to protect compressor parts, specifically because, among the nitride-based coatings, it is the most thermodynamically stable one, and it has been widely used due to its combination of covalent and metal-like characteristics. It possesses a unique combination of physical and mechanical properties, such as good electrical and thermal conductivity, and high hardness (H ~20–22 GPa), and chemical inertness and high melting temperature (T_m=3222 K).

The application of certain coating structures (e.g., single layer, bilayer, multilayer, and nanostructured coatings) can help to optimize the tribological and mechanical properties of systems. Ti/TiN multilayer films generally present better erosion- and wear-resistance than a single layer TiN film, because of an increase in the hardness and toughness of the material created by multilayer structures. It has been reported that Ti/TiN multilayer coating designs enhance erosion resistance due to a multi-step process cracking [14], [15].

TiN coatings can be fabricated by plasma enhanced chemical vapour deposition (PECVD) and physical vapour deposition (PVD) techniques [16]. PVD processes such as electron beam deposition, cathodic arc evaporation, magnetron sputtering, and its most advanced variant, high power impulse magnetron sputtering (HiPIMS) are widely used in the industry [17], [18].

Microstructural, mechanical and tribological coating properties vary significantly with deposition methods and processing conditions. Residual stress (RS) typically develops during coating deposition. The mechanisms which create such RS include grain growth, gas entrapment, and/or phase transition. It is essential to control the RS to ensure that the coatings do not crack, buckle, or delaminate [19].

There is a strong relationship between RS and the coating microstructure. Control of RS in thin films during sputter depositions is maintained by controlling sputtering conditions such as pressure, substrate bias, and the energy and flux of the particles striking the substrate and the growing film surface.

Thornton’s structure zone model (SZM) [20] is generally applied for gaining insight into the effect of growth conditions on the microstructure of the sputtered thin films. The SZM is a qualitative illustration of the physical film properties resulting from the growth processes. This model shows the film structure as a function of two important parameters: the homologous temperature, T/T_m (T – substrate temperature, T_m – coating material melting temperature), and the pressure (Ar pressure).

Surface treatments and coatings designed to enhance the tribological performance among other things, must retard or stop mechanisms that could reduce the fatigue strength of a metallic substrate by delaying crack appearance and propagation. The evaluation of surface treatments and coating effects on the fracture mechanisms of coated Ti-alloys represents an important need in the aerospace industry. The understanding of deformation distribution in the individual layers is critical to determine the overall mechanical response of the coating-substrate system. Industrial components are designed to prevent loading within the plastic domain under normal service conditions, because they can only tolerate a limited amount of plastic deformation under these unique working conditions [9]. The aerospace industry routinely uses shot peening to increase surface compressive stresses and reduce fracture in bulk materials [21]. Authors have reported that the introduction of compressive residual stresses often produces beneficial effects on the resistance to certain failure mechanisms [5], [21]–[23].

This thesis is devoted to a systematic study of the microstructure and RS effects on failure mechanisms of coated Ti-6Al-4V. Mechanical and tribological properties of TiN and ZrN as monolayers (single-layers), and ZrN/TiN multilayers on Ti-6Al-4V with three different plasma pre-treatments were evaluated. X-ray diffraction (XRD) and a multi mechanical technique approach were used to determine residual stress gradients on coated specimens and to assess the effect of predetermined RS profiles on the fracture mechanism of the systems, while studying the strain concentration, crack initiation and crack propagation.

1.1 Problem identification

During an aircraft’s operation, the engines are exposed to harsh environmental factors, which deteriorate the materials. Jet engines are also subjected to speed and temperature variations, which cause high stresses in some of the components. The number of times that the jet engine speeds up and temperatures are varied is directly correlated with component durability. Operation at constant high speed and high temperature for long periods of time also shorten the engine’s lifespan [9].

Normally, the materials used in the aerospace industry undergo surface mechanical and/or heat treatment(s), such as shot peening, deep rolling, or hot/cold working. These treatments provide high strength, increase near-surface dislocation density, and induce RS into the surface of the material (to a depth of a hundred microns). A controlled RS can inhibit crack initiation and drastically delay crack propagation. Additionally, the compressor blade materials normally are protected against erosion and wear. For this, protective coatings have a strong impact, because they prevent compressor blades from premature loss of material. The coatings must have good mechanical and tribological properties, excellent adhesion, and they must be smooth, without vulnerable stress points. Therefore, even if mechanical pre-treatments have shown excellent results for bulk material, they are not an ideal solution to be performed into alloys that will be protected by a coating, especially due to the RS relaxation and surface roughness created after the treatment. Thus, surface pre-treatments applied by plasma techniques to enhance the adhesion of protective coatings, such as nitriding, ion bombardment and ion implantation are considered preferable.

Surface treatments, coatings and metallic substrates have been investigated separately; however, conclusive results on the durability of coated metallic components have not been made, especially in relation to RS and the stress depth profile. The impact of coatings and plasma pre-treatments on Ti-alloy surface and their potential for retarding crack propagation has not yet been explored as a viable means of creating safer aircraft components with a longer life span.

1.2 Objectives

In response to the needs of the aerospace industry and in order to gain a better understanding of failure mechanisms of coated aerospace components, the main objective of this thesis was to understand the level of residual stress (including the stress depth profile) in the protective coating systems, and how this stress affects the durability (crack or defect formation and propagation, scratch- and wear resistance) of aerospace metallic substrates.

The specific objectives of this thesis can be summarized as follows:

1. To establish a stress assessment methodology (including depth profile and anisotropy) and investigate how the stress depth profile depends on the film growth when considering different interfaces.

2. To assess crack initiation and propagation in relation to the residual stress depth profile, understanding the effect on crack onset strain, COS, critical energy release rate, Gc, and interfacial shear strength, τ, to determine fracture mechanism of coated systems.
3. To investigate the effect of multilayer and nanolaminate architecture on the residual stress, and tribomechanical properties and crack propagation.

1.3 Organization of the thesis

This thesis is composed of seven chapters, starting with an introduction to the topic of the research in Chapter 1. Chapter 2 summarizes the existing literature and provides background on the development of interface layers and protective coatings, especially nitride coatings, as well as the techniques used to fabricate them. The coating methodologies and characterization techniques used are described in Chapter 3. The principal results with respect to the tribo-mechanical properties of two coating architectures (single layer and multilayer) with interface layers on Ti-6Al-4V substrates are presented in the form of three peer-reviewed articles in Chapters 4, 5, and 6. In the first article, Chapter 4, a TiN single layer coating (model material) was used to evaluate the effect of three interface layers (Ar etched, nitrided and Ti implanted) produced by PVD techniques on the microstructural and tribo-mechanical properties of the coated systems. This chapter presents a systematic study of RS and RS depth profiles through the coating-interface-substrate system. The second article, Chapter 5, reports on the evaluation of crack evolution and fracture mechanisms of TiN coatings on Ti-6Al-4V with different interface layers, studied by scratch and tensile testing techniques. The fracture mechanisms are evaluated as a function of the RS and its depth profile in the coatings. In the third article, Chapter 6, the fabrication, and the tribo-mechanical analysis of TiN, ZrN single layer and ZrN/TiN nanolaminate films are presented. Chapter 7 describes highly complementary results obtained throughout the thesis work that were not included in the published articles. This includes crack evaluation, tensile strength, and adhesion properties of ZrN/TiN multilayer systems. Chapter 8 presents a general discussion of the main results compared to the literature. Finally, Chapter 9 highlights the main conclusions of the work, as well as a proposition of future work.

1.4 Research contributions

This thesis work gave rise to three publications in the form of papers in peer-reviewed journals which represent the body of this thesis (Table 1.1), while each article addressed a specific objective described in the previous section. The oral and poster presentations at three international conferences and symposia were given (Table 1.2), and the work led to collaboration with international universities and scholarships (Table 1.3).

Table 1.1 Publications in the form of articles in peer-reviewed journals.

Herrera-Jimenez, E. J., Bousser, E., Schmitt, T., Klemberg-Sapieha, J. E., & Martinu, L. (2021). "Effect of plasma interface treatment on the microstructure, residual stress profile, and mechanical properties of PVD TiN coatings on Ti-6Al-4V substrates". Accepted in *Surface and Coatings Technology, SCT.*
Herrera-Jimenez, E. J., Vanderesse, N., Bousser, E., Schmitt, T., Bocher, P., Klemberg-Sapieha, J. E., & Martinu, L. (2021). "Fracture mechanism of TiN coatings on Ti-6Al-4V substrates: Role of interfaces and of the residual stress depth profile". Submitted to *Surface and Coatings Technology, SCT.*
Herrera-Jimenez, E. J., Raveh, A., Schmitt, T., Bousser, E., Klemberg-Sapieha, J. E., & Martinu, L. (2019). "Solid solution hardening in nanolaminate ZrN/TiN coatings with enhanced wear resistance". *Thin Solid Films, 688*, 137431.

Table 1.2 Oral and poster presentations at international conferences and symposia.

E. J. Herrera Jimenez, N. Vanderesse, T. Schmitt, E. Bousser, P. Bocher, L. Martinu and J.E. Klemberg-Sapieha. "*In situ* micro-tensile testing of TiN coatings: deformation and fracture in relation to residual stress" ICTMCF, San Diego, CA, USA. (May 2019).
E. J. Herrera, A. Raveh, Z. Rozek, T. Poire, T. Schmitt, L. Martinu and J.E. Klemberg-Sapieha. "Solid solution hardening in nanolaminate ZrN/TiN multilayer coatings" RQMP, Montreal, Canada. (2017).
E. J. Herrera Jimenez, M. Laberge, T. Schmitt, E. Bousser, G. Kamath, L. Martinu and J.E. Klemberg-Sapieha. "Interface control for enhanced performance of hard protective coatings". Sponsored Student. SVC 59th Annual Technical Conference, Society of Vacuum Coaters, Indianapolis, USA. (May 2016).

Table 1.3 Collaboration with other universities and scholarships.

Professor Phillipe Bocher. “In situ fracturability test development”. École de technologie supérieure (ÉTS), Université du Québec, Montréal, QC, Canada. (20017-2019).
Professor Damian Batory. “Residual stress profile measurements by XRD technique”. Lodz University of Technology, Poland. (Oct. 2017).
Jane and Frank Warchol Scholarship by SVC-Foundation - Scholarship awarded for the research project, “Protective nanocomposite coatings – HiPIMS for aerospace applications”. (2016-2017 academic year).

CHAPTER 2 LITERATURE REVIEW

This chapter reviews the background knowledge of this thesis work, based on theory and on literature reviews. Many substrates and coating methods were evaluated as part of this thesis. The evaluation process and details of the chosen substrate and coating methods are discussed. The surface engineering performed by PVD techniques are introduced, along with the basics of microstructural and tribo-mechanical properties of the coatings and interface layers. Fracture mechanisms and their characterization are then discussed, with particular emphasis on the significance and origin of RS in the coating-substrate systems.

2.1 Substrate selection

There are numerous metallic substrates that are used in the various components of an aircraft jet engine. These include steels, aluminium-, nickel-, cobalt- and titanium-based alloys. Of these alloys, only a select few are capable of handling the high temperatures and harsh environments that turbine blades and compressor components are exposed to. Based on years of operational experience coupled with improvements in alloy composition, the list of alloys used for compressor components has been refined. One of the most popular ones today is Ti-6Al-4V. As this alloy has also been found to accept coatings well, it was chosen as the substrate for this research.

2.1.1 Ti-6Al-4V properties

At low temperature, titanium (Ti) has a hexagonal close packed structure (hcp), which is called α titanium. However, at high temperature the stable structure is body-centered cubic (bcc), known as β titanium. Their atomic unit cells are presented in Figure 2.1. The β-transition temperature for pure titanium is about 820°C and is dependent on the amount of incorporated impurities leading to a large variation in the properties of titanium alloys [24], [25]. Selected physical properties of Ti are presented in Table 2.1.

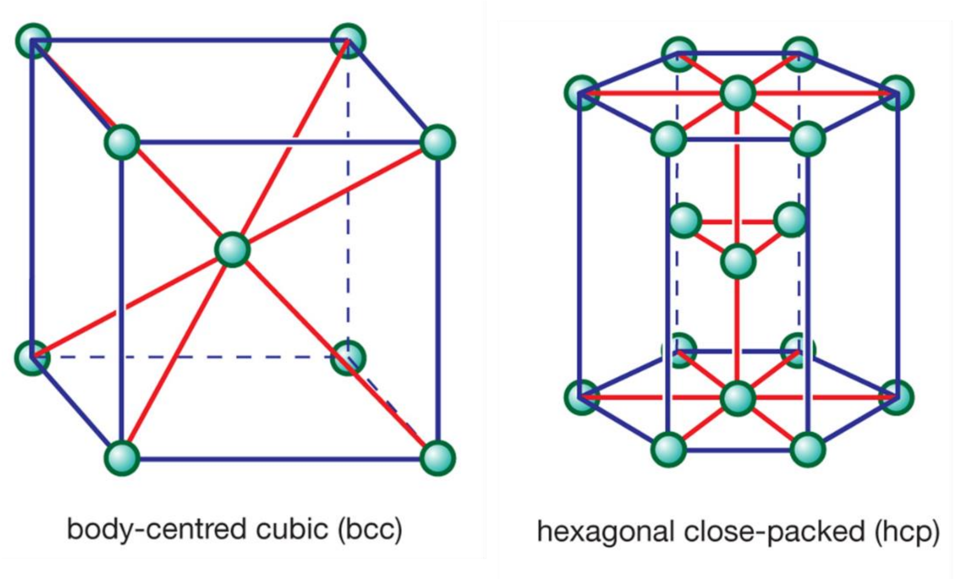

Figure 2.1 Schematic representation of Ti unit cells [26].

Table 2.1 Physical properties of Titanium

Property	Density (g/cm^3)	Melting point (°C)	Thermal conductivity (W/mK)	Elastic modulus (GPa)	Reactivity with oxygen	Corrosion resistance	Metal price
Ti	4.5	1670	15-22	115	High	High	High

Titanium alloys are divided into three main phase distributions, as presented in Figure 2.2: i) alpha (α), ii) alpha-beta ($\alpha+\beta$), and iii) beta (β). Ti-6Al-4V has the ($\alpha+\beta$) distribution, the Al and V alloying elements serving as α- and β-stabilizers, respectively. Table 2.2 shows the elemental composition of Ti-6A-4V. The microstructural and mechanical properties of Ti-6Al-4V are influenced by the individual properties of α- and β-phases, their arrangement and volume fraction [27]. Fine grain sizes increase strength and ductility, retard crack nucleation, and normally present super-plastic deformation. On the other hand, coarse microstructures have higher resistance to creep and fatigue crack growth, while equiaxed microstructures present high ductility and fatigue strength, with high tolerance to super-plastic deformation. Lamellar structures show high fracture toughness and superior resistance to creep and crack growth. And finally, the microstructure, which combine the properties of lamellar and equiaxed structures, have a well-balanced properties profile. Ti-6Al-4V alloy can be annealed or solution-treated and aged bar [28]. Specific mechanical properties for these conditions are presented in Table 2.3. Some standard specifications for Ti-6Al-4V as annealed or solution and aged bars are AMS-4928, AMS-4967 and AMS-4965.

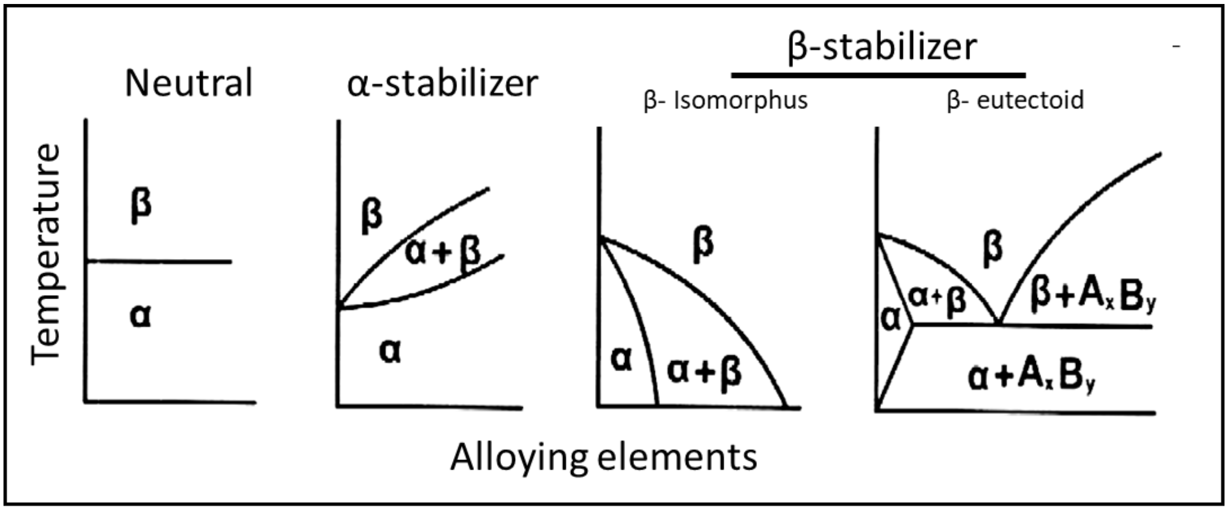

Figure 2.2 Schematic representation of the influence of alloying elements on α- and β- fields [25].

Table 2.2 Composition of Ti-6Al-4V (wt.%) (ATI Ti-6Al-4V, Grade 5, 2012).

	C	**Fe**	**N**	**Al**	**V**	**O**	**Ti**
wt%, min	-	-	-	5.50	3.50	-	
wt%, max	0.10	0.30	0.05	6.75	4.50	0.20	Balance

Table 2.3 Specific properties of Ti-6Al-4V alloy in its two main heat-treated conditions.

Material	**Tensile Strength (MPa)**	**Yield Strength (MPa)**	**Elastic modulus (GPa)**	**Hardness (HV)**	**Thermal conductivity (W/mK)**
Annealed bar	895	825	110	340	7.3
Solution + aged bar	1035	965	110	360	7.5

2.1.2 Ti-6Al-4V substrate after PVD processes

Ti64 has many mechanical properties that make it an excellent structural material for turbine-related applications, but it has poor tribological properties, which is problematic. The enhancement of tribological properties on Ti-alloys have been achieved by PVD treatments. The friction coefficient and volumetric wear rate have been shown to be lower for Ti-6Al-4V implanted with N_2 ions than for untreated Ti-6Al-4V [29], [30].

Elements, such as oxygen, calcium, phosphor, boron, carbon, helium, and nitrogen implanted on Ti, have been explored [31]–[34]. These elements produced an increase in the hardness of the alloy and reduced the coefficient of friction due to a homogenization of the α- and β-phases and formation of nitride, oxide, and carbide precipitates on the substrate surface [35], [36]. In the case of surface treatments, like nitriding, the use of high temperatures during implantation lead to grain growth and microstructural transformations. Therefore, low temperatures are recommended to improve the mechanical properties, such as hardness [36], [37], while not affecting the fatigue strength and ductility [38]–[41]. As a result, the depth of nitrogen diffusion will increase and the hardness and thus the load-bearing capacity and wear resistance of the surface can be improved [13], [42]–[47]. Studies of plasma nitriding treatments of Ti64 showed that the initial hardness of ~5 GPa could increase to ~13 GPa in the first 5 μm due to the nitrogen diffusion to a depth of 15 μm [48]–[50]. Indeed, the use of an interface layer between the coating and the Ti64 improve chemical and mechanical bonding between the substrate and the PVD coatings [51]. In the case of Ti alloys coated with protectives coatings, the use of Ar bombardment to create an interface layer leads to higher adhesion of coatings due to surface activation by the Ar atoms during physical etching that increase the surface energy at the substrate surface. M. Pizzorni showed that Ar vacuum processes on Ti-6Al-4V involve a reduction of surface micro-roughness in terms of Sq parameters and a redistribution of peaks and valleys, leading to optimal morphological properties when the adhesion is a desired property [52].

2.2 Surface engineering

Surface engineering is used in varied applications. The extent (depth) of the near-surface region depends on which industry one is referring to, varying from millimeters or centimeters for cement road surfaces to nanometers for graphene and some biological applications. Even for the specific case of aircraft jet engine turbine blades, there is mechanical surface engineering for the base alloy which may have effects that extend millimeters into the material, and there is surface engineering in the form of protective coatings and interface layers, that extend mere microns. In this thesis, the focus is on PVD coatings and pre-treatment processes in the surface of the base alloy (substrate) typically including thicknesses and depths up to several micrometers.

2.2.1 Protective coatings and interfacial layers

Coatings are widely used on metallic materials, such as Ti alloys, mainly because they can enhance the material's oxidation resistance, tribological properties and/or load-bearing capacity. A coating is a layer applied between the external environment, and the substrate material. Coatings or films may be used to protect or add functionality (e.g., wear-, erosion-, scratch-, and/or oxidation-resistance, high hardness, etc.). Sometimes, films are applied only to accomplish esthetic requirements. The coatings that have a mix of mechanical and tribological properties are known as protective coatings. Such coatings must be uniform, well adhered, pore-free, and perhaps even self-healing. The use of a topcoat or a multiple-layer system is common to achieve all requirements. Moreover, in certain industrial applications, the use of a substrate pre-treatment is also needed to enhance the component properties and reduce processing time. Surface treatment processes involve the modification of the top layer of the substrate through mechanical, heat, plasma, laser-assisted, diffusion treatments. Such surface treatments on a metallic substrate can improve the tribomechanical properties of coating-substrate systems by creating an intermediate layer. The properties and adherence of the interface layer can be of great importance in the interaction between coating and substrate.

2.2.2 PVD processes

Coating of Ti alloy components can be carried out by chemical vapor deposition (CVD), physical vapor deposition (PVD), or thermal or plasma spray. PECVD process has also been frequently used for hard coating deposition [30]. Coatings prepared by PVD methods usually include intermetallic or compound layers. The history of these PVD processes, especially sputtering and evaporation deposition techniques, goes back to the nineteenth century when Grove (1852) sputtered metal particles from the cathode in a glow discharge. At nearly the same time, Faraday (1857) produced evaporated thin films during the explosion of fuse-like metal wires in an inert atmosphere. Both deposition techniques have been widely investigated and are used to produce coatings of various materials, such as metals, alloys, ceramics, compounds, and organic materials. Nowadays, the most frequently used PVD processes are arc vapor deposition [53], magnetron sputtering [54], [55], and a combination of magnetron and arc processes [56], [57].

For the purpose of this work, the sputtering process was primarily considered. In reactive sputtering, the substrate is coated by films using metallic targets and a reactive gas, mixed with an inert working gas (e.g., Ar). The resulting coating can be a solid solution of the target metals doped with the reactive element, a compound, or a mixture of the two [58]. Sputtered coatings vary from nanometers to many microns in thickness and generally have a columnar structure and a smooth coating surface without the presence of macroparticles [59].

Reactive sputtering of thin films has been widely investigated for many decades. The reactive sputtering process can be divided into three modes: (i) metallic, (ii) transition and (iii) reactive. These three modes can be created according to the amount of reactive gas used during the film deposition. Magnetron sputtering in reactive mode is known to have a low deposition rate compared to the one produced by the metallic mode with pure metals as a target or an alloyed target [60].

The decrease in deposition rate is mainly due to a reaction of the reactive gas with the surface of the sputtered target, which can form a compound layer on the target surface. Normally, Ti targets are used to deposit TiN or TiO_2, when nitrogen or oxygen is used as reactive gas. This may result in target poisoning and, as a consequence, we observe a decrease of sputtering yield and magnetron discharge voltage, U_d. It also results in the rise of the hysteresis effect. The voltage polarity of magnetron cathodes periodically changes from negative to positive. When the cathode voltage U_d is negative, the target material is sputtered [60], however, when U_d is positive, the surface of the insulating layer on the uneroded areas is discharged due to the electron bombardment. Arc formation can be controlled if the positive charge accumulated on the uneroded areas is discharged before reaching a critical value at which the electric field across the insulating layer overpasses its dielectric strength. A radio frequency, rf (13.56 MHz), is an ideal sputtering method when using materials with an insulating nature or to avoid dielectric layer formed on the target surface. However, the deposition rates obtained using rf generator are usually low; only 50% of the power output from the generator is used in the sputtering process. Thus, the deposition rates obtained by rf sputtering are always around 50% of those obtained from a metal target by direct current (dc) sputtering [61]. An rf or midfrequency, MF, bipolar pulsed discharge can be used to create sufficient flux of bombarding gaseous species. The plasma density achieved with rf and bipolar pulsing is of the order of 10^9 cm^{-3}, and the ion flux to the substrates is in the range of 0.1–1 mA cm^{-2}. The higher flux allows faster and more efficient cleaning of the substrate and avoids oxide formation [62].

In conventional continuous dc magnetron sputtering the power dissipated in the plasma results in a plasma density (electron density) in the order of up to 10^{11} cm^{-3} in a close vicinity of the target with a typical average electron energy of a few electron volts (eV). This is a relatively low plasma density and results in ion to neutral ratios of sputtered material of around one percent. One way of increasing the number of ionizing electron collisions is to increase the electron density and the average electron energy [63][64]. The increase in plasma density can be achieved by increasing the power applied to the cathode. However, since most of the power applied to the cathode is transformed into heat, the technique is limited to a relatively small power density before the target cooling is insufficient.

High plasma density, without overheating the target, can be achieved by applying high power in pulses with a low duty cycle. The duty cycle is a measure of the pulse on time in comparison to the period time. In this way the peak power on the cathode surface can reach values of several kW cm^{-2}. The method, first reported by Kouznetsov et al. [65] is called high power pulsed magnetron sputtering (HPPMS or HiPIMS - High power impulse magnetron sputtering) HiPIMS can produce high ion fluxes with a high metal content similar to an arc discharge. HiPIMS is an impulse short pulse sputtering method where the peak power on the target reaches 3 kW cm^{-2} at a target current density of 2 A cm^{-2}. Pulses generated by HiPIMS comprise high fractions of metal ions often double ionized with gas ion to metal ion ratios of 1:1. HiPIMS is a powerful tool for substrate etching and interface engineering. The adhesion of HiPIMS-pretreated coatings is comparable to that of Ar glow and cathodic arc pretreated coatings.

The crystallinity of the substrate grains is preserved during cleaning. The substrate surface is highly reactive and allows nucleation in an oriented fashion over large areas. A high degree of local epitaxial growth is achieved using the HIPIMS technique for pretreatment and deposition that is comparable in nature to the interfaces obtained by cathodic arc, but without the droplet problem encountered in an unfiltered arc and the limited productivity and scalability of a filtered arc [66]–[68].

Specific microstructural characteristics can be obtained by using the structure zone model (SZM). This model describes the effect of the deposition parameters on the morphology and microstructure of the films. The first SZM was proposed by Movchan & Demchishin in 1969 [69]. Figure 2.3 shows SZM modifications [70] which describe more specifically the microstructure evolution between Zone 1 and Zone 2, called Zone T, and consider the sputtering gas [71]. The latest SZM, proposed by A. Anders [72], considers various technological advancements. In this model, the coating microstructure varies with substrate temperature, T^*, and normalized delivered energy flux, E^*, and coating thickness, t^* (Figure 2.3c). Structure zone models qualitatively predict mainly four types of microstructure (zones) as a function of T/T_m, where T is the substrate temperature and T_m is the coating material melting point.

In the three SZMs, in Zone 1 ($T/T_m<0.3$) thin crystals with rounded tops are separated by voided boundaries. This zone is characterized by low activation energy and low surface diffusion, resulting in metallic deposits with high hardness but low strength. The transition zone, Zone T, consists of a dense array of not well-defined fibrous grains without voided boundaries. In Zone 2 ($0.3<T/T_m<0.5$), a smooth coating is formed by columnar grains with well-defined and dense inter-crystalline boundaries. The grain size increases with temperature through the coating thickness. Finally, in Zone 3 ($0.05< T/T_m<1$), the film consists of equiaxed grains with a crystallized grain surface. The grain diameters increase with temperature and energy [73]. A comparison between zone structures and properties for sputtered coatings is presented in Table 2.4.

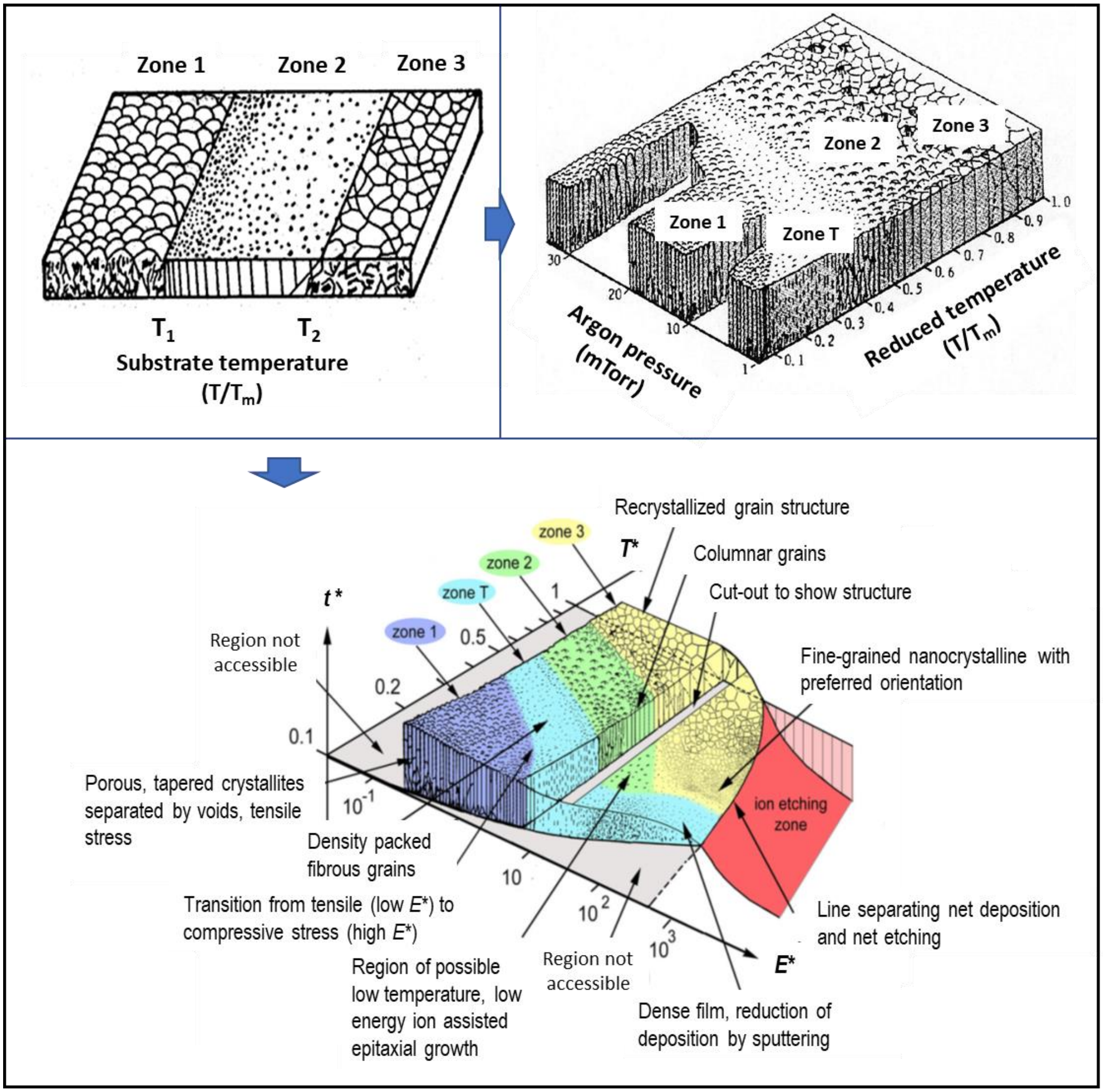

Figure 2.3 Structure zone models for coating growth: a) Model proposed by Movchan and Demchishin; b) Model proposed by Thornton for sputtered metal coatings [73]; and c) the latest model proposed by A. Anders [72].

Table 2.4 Zone structures in sputtered coatings, modified from [58].

Zone	**T_S/T_M**	**Structural characteristics**	**Film properties**
1	<0.1 at 0.15 Pa to <0.5 at 4 Pa	Voided boundaries, fibrous grains. Zone 1 is promoted by substrate roughness and oblique deposition	Hard
T	0.1 to 0.4 at 0.15 Pa, ~0.4 to 0.5 at 4 Pa	Fibrous grains, dense grain boundary arrays	High dislocation density, hard, high strength, low ductility
2	0.4 to 0.5	Columnar grains, dense grain boundaries	Hard, low ductility
3	0.6-1.0	Large equiaxed grains, crystallized grain structure	Low dislocation density, soft recrystallized grains

According to the SZM, the main parameters influencing the microstructure during coating deposition are substrate temperature and ion bombardment. In general, a specific microstructure requires high T/T_m values, in order to keep low deposition temperature, T. One can benefit from additional ion bombardment used to decrease T/T_m while controlling the microstructure. In magnetron sputter deposition, the energetic ion bombardment (Ar ions) can create defects and induce stress, which influences the mechanical properties of the coatings.

While the mechanical properties of coatings are usual focus of the studies, their adhesion strength is critical for their successful performance. The adhesion failure in coated systems is given by general failure modes defined as cracking events which can occur in the coating or in the substrate (cohesive failure), or at the interface (adhesive failure). In the coating failure mode median cracks or a periodic array of cracks in the coating propagate to the interface and deflect, while in the interface failure cracks start and propagate along with the interface, or extend to coating and substrate, normally leading to buckling or spalling. Finally, the substrate failure induces interfacial failure as cracks which propagate along interface. The adhesion failure can describe the interfacial toughness used to predict the failure onset and crack propagation of a system [74].

Good adhesion is characterized by strong chemical and mechanical bonding across the interfacial region, low stress gradients either from intrinsic or external loads, absence of an easy fracture mode, and no long-term degradation mechanisms. A low degree of chemical bonding and/or poor interfacial contact between the coatings and substrate lead to poorly adhering coatings [75]. Therefore, surface treatments of substrates are a key part of surface engineering for industrial applications. Appropriate optimization of the interface layer, which acts as a transition layer, improves both chemical and mechanical bonding between layers and enhances the adhesion [51], [75].

Surface modification by the pre-treatment of metallic substrates, such as Ti alloys, can be divided into different types: i) thermal treatment, ii) thermo-chemical treatment, iii) surface cleaning, iv) surface modification, v) shot peening, vi) ion bombardment, and vii) ion implantation [49], [76], [77]. Figure 2.4 shows the characteristic parts of a coated system, defining the interface region, and gives the main characteristics of each part.

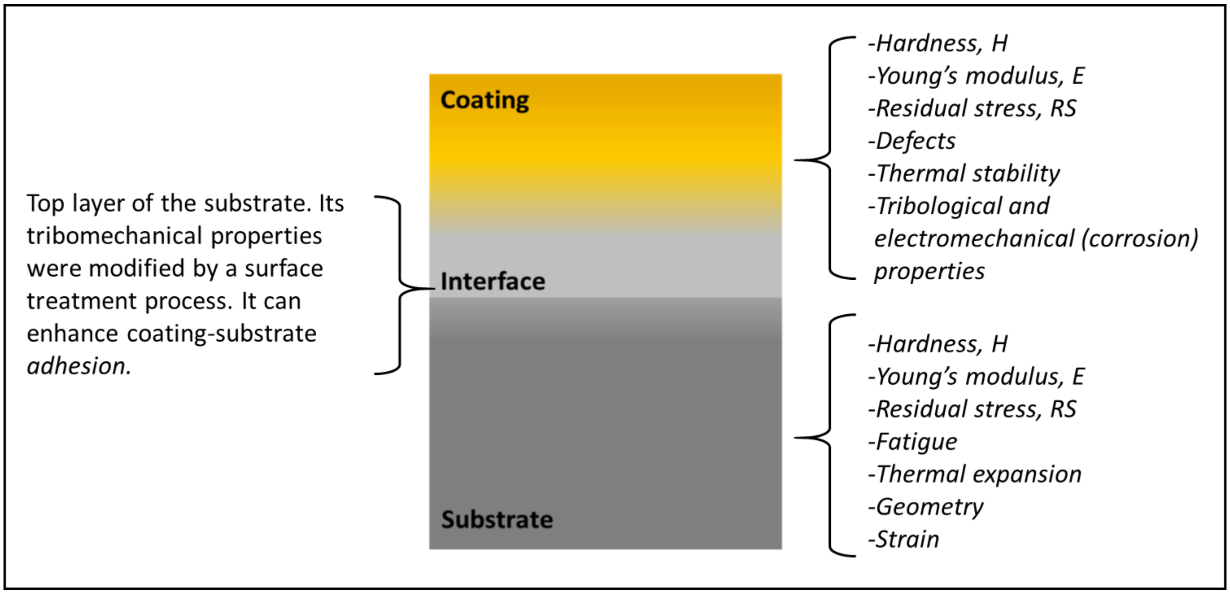

Figure 2.4 Schematic representation of a coated substrate showing coating, interface, and substrate with the main properties to be considered in this work.

2.2.3 Surface treatments

Among different surface treatments to enhance the surface tribo-mechanical properties and to improve the adhesion of the protective coatings, two are very popular: thermo-chemical treatments such as boriding, carburizing, and nitriding, or plasma-assisted surface treatments such as ion bombardment and ion implantation [32], [76].

2.2.3.1 Ion bombardment – sputter cleaning plasma treatment

Ion bombardment (e.g., Ar plasma) is considered a fundamental step to clean the surface before coating deposition. Sputter cleaning is a common technique performed to remove contaminants from the surface layers and to provide the appropriate activation energy of the substrate surface. Ion bombardment can move surface atoms from their lattice positions and incorporate molecular and atomic ions incident at hyperthermal kinetic energy ~1-10^3 eV, causing compositional and structural changes, while influencing the substrate properties and the microstructure of the subsequent growing coatings.

The incorporation mechanisms of neutrals, radicals, or ions in a coating growing at the rf-biased electrode is different according to the particles involved. The radicals and neutrals normally interact with atoms from the growth surface being physically or chemically adsorbed, while the ions can be implanted below the growth surface promoting competition effects by displacing vacancies in the substrate and creating disorder into the coating [78].

This process leads to the formation of an interface layer with a different stoichiometry than the substrate. Generally, the depth of interaction between Ar ions and the atoms of the substrate is dependent on the process energy [78]. Alloys exposed to ~1 keV ion bombardment at fluences of 10^{13}-10^{16} ions-cm^{-2} can suffer amorphization, crystallisation, and/or stoichiometric changes on the surface at around 10 nm depth. The final surface structure is related to the disordered regions created by the impacting ions [79]. The use of plasma for ion bombardment enhances the chemical reactions and diffusion of reactive species on the surface and can also be a heating source for the material being treated [80].

2.2.3.2 Ion implantation

Ion implantation is a doping process in which accelerated ions are directed to the surface of a material. This process uses high initial energy (typically tens to hundreds of keV) [81] to introduce ions in the near surface region of any material (around 10 nm for 1 keV and less than 20 nm with the cascade effect). Once the ions penetrate the surface layer, they lose energy in two types of interactions: i) elastic collisions with substrate nuclei, and ii) inelastic collisions with electrons.

The first one causes displacement of the surface atoms from their initial positions causing crystal damage. Heavy ions can displace thousands of atoms, and even if most of those defects may annihilate during the cooling phase of the displacement cascade, the process creates severe damage, and can lead to amorphization of the crystalline structure. Elastic collision can also be used to dope thin layers close to substrate surface. When the surface layer is bombarded with inert gas ions, the ions transfer all of their kinetic energy to the atoms adjacent to the surface, while penetrating the sub-layer of substrate. In this case, inelastic collisions with electrons ionize the atoms of the substrate and can cause transformation of the structure [82].

Ion implantation is a useful process to modify the tribo-mechanical properties, such as erosion-, wear- and oxidation- resistance of alloys such as titanium, steels and aluminium alloys [84], Ion implantation adds atoms to an already formed material, so it should lead to compressive stress in most situations and it can form new phases of higher density [87]–[89].

This treatment can also be performed using HiPIMS, which has the unique feature of short duration power impulses that can result in very high peak instantaneous power ($3x10^3$ Wcm^{-2}) and current densities (1-5 $A\text{-}cm^{-2}$), and hence high ionisation rates (30-100%) of the sputtered material, i.e., several orders of magnitude higher than the conventional magnetron sputtering processes (~0.01-0.1 $A\text{-}cm^{-2}$, 1 Wcm^{-2}, and 0.1%, respectively). HiPIMS plasma contains significant proportions of singly and doubly charged metal ions whose relative densities are determined by the peak power of the discharge [18]. Low stress and good adhesion are among the characteristics that can be achieved by ion implantation treatment using HiPIMS [62].

2.2.3.3 Nitriding

Nitriding is a surface-hardening process in which nitrogen atoms are used to modify the surface of a metallic substrate. This treatment has been performed on titanium alloys to obtain surface hardening by forming metal nitride and enhance the substrate wear resistance. Nitrogen has a high solubility in α-Ti, which results in a significant increase in the strength of the surface layer. The nitriding methods are: i) plasma, ii) ion-beam, iii) laser, and iv) gas nitriding.

Plasma nitriding treatment forms two thin layers on Ti alloys [41], a compound layer and a diffusion layer which both can enhance the tribo-mechanical properties of the substrate. The formation of these layers and their thickness depend of the temperature and time of nitriding treatment. Normally they are formed at high temperature (>500 °C) [86]. The compound layer consists of TiN, δ phase, with FCC crystal structure (Fm3m space group) and Ti_2N, ε phase, with tetragonal crystal structure (P42-mnm space group). TiN is stable over a wide range of N contents, ranging from 0.43 to 1.08 at%, and has a typical hardness of 2500 HV, while Ti_2N is stable over ~33.3 at.% of N and has a hardness of 1500 HV [87]–[91]. The compound layer has been reported to be a TiN layer on top of a mixture of randomly oriented polycrystalline TiN and highly oriented Ti_2N. Clusters of fine precipitates (50–100 Å), which consist of Al, V, Cr, and Fe elements, can be present as part of this layer [88]. The compound layer has a typical thickness of 1–4 µm [36], [88], [92], [93]. However, in applications where durability is a critical characteristic of the material, this is not a desirable layer since it is very brittle.

The second layer, underneath the compound layer, is known as the diffusion zone. It consists of a region of nitrogen-stabilized α-titanium, that is, α case, in a typical range of several microns (2 to 25 µm) deep [86], [94], with a typical hardness of 800–1000 HV. Nitrogen atoms harden the diffusion zone, especially at the near surface and it gradually decreases toward the bulk. The depth of nitrogen diffusion is dependent on the process parameters as well as the phase composition of titanium alloys, due to different solubility limits and diffusion rates of nitrogen in α- and β-titanium [95], [96]. Nitrogen atoms diffuse three times faster in β-Ti phase compared to α-Ti phase, but has limited solubility in the β-phase [97], [98].

The effect of nitriding on the microstructure is strongly associated with the composition of titanium substrate and the nitriding process parameters such temperature, pressure, composition and duration of the nitriding plasma [36], [99]–[101]. Plasma nitriding of titanium alloys is typically carried out using a nitrogen-rich plasma (N_2, N_2–Ar, N_2–H_2, or N_2–NH_3) for 2 to 80 hours [38], [86], [102]–[105]. This treatment normally requires a temperature between 400°C to 1100°C.

Plasma nitriding results in enhanced hardness [36], [37] and oxidation resistance of Ti alloys. However, it reduces fatigue strength when high temperatures are used during the treatment [37], [106].

2.3 Mechanical properties of coated systems

The importance of mechanical properties on coated systems for engineering applications is obvious; components are exposed to loads and external stresses that can cause deformation and fracture of the material. The ability of a material to resist deformation and fracture under certain operating conditions can be evaluated from the relationship between stress, σ, and strain, ε. This stress-strain relationship reflects the behaviour of a material under loading according to its elastic and plastic response. Elastic properties of a material are those which make it return to the original shape after being exposed to certain loads. In the elastic region, stress and strain are related to each other linearly, characterized by Young's modulus, E, described by the Hooke's law

$$\sigma = \varepsilon E \tag{2.1}$$

On the other hand, a material is considered to behave plastically when the stress is high enough that the material cannot completely return to its original shape, and the Hooke's law is not applicable anymore. Normally, there is a gradual transition between elastic to plastic behaviour. The beginning of plastic regime is observed just before the yield strength, σ_Y, is reached. This is one of the critical values for the durability of coated systems; however, the σ_Y from a coatingcannot be calculated from the stress-strain diagram because it represents the elastoplastic interaction of the whole system (coating and substrate). Therefore, the use of hardness, H, and E, extracted from indentation techniques is recommended, especially since these two fundamental mechanical properties of coated materials are often related to their wear- abrasion- and erosion- resistance. H is the resistance of the material to localized deformation. It is related to the contact pressure of a tip as it is pressed into the material surface. The measured E is related to the reduced Young's modulus, E_{r} given by $E_r = E/(1-\upsilon^2)$ where υ is the Poisson ratio.

For coatings, H and E are determined from the loading/unloading curves can be measured by nanoindentation techniques [107]. Their correct measurement is fundamental to evaluating material resistance to both elastic and plastic deformations. There are several approaches to describe and possibly predict the resistance of coatings; for this purpose the following parameters have been proposed: Elastic behaviour in terms of the H/E ratio [108], [109], the material's ability to resist permanent damage given by the H/E^2 ratio [110], and the material's ability to dissipate energy at plastic deformation during loading defined by the H^3/E^2 ratio [107].

Another important value, obtained from the stress-strain diagram, is the maximum stress that a material can tolerate under uniaxial loading, known as the tensile strength, or ultimate tensile strength (UTS). The UTS is given by the maximum load, P_{max}, applied to the specimen divided by its original cross-sectional area, A_0:

$$\sigma_{UTS} = \frac{P_{max}}{A_0} \qquad 2.2$$

The toughness is also an important mechanical property of coated structures. The toughness of a material, *K*, is its ability to absorb energy in the plastic range (the material's ability to tolerate deformation without cracking or fracture). The fracture toughness, K_{1c}, is defined as the resistance to crack propagation. For, K_{1c}, it is assumed that a crack exists, whereas such an assumption is not made for plain toughness. The subscript “1c” stands for mode 1 crack opening, where the crack opens under a normal tensile stress perpendicular to the plane of the crack. This can be determined by tensile or indentation testing, as given in Eq 2.3 [111] [112] and 2.4 [109], respectively:

$$K_{1c} = \sqrt{\frac{\sigma_C^2 tE}{2*E}\left[\pi g(\alpha_D \beta_D)\right]} \qquad 2.3$$

$$K_{1c} = \alpha_1 \left(\frac{H}{E_r}\right)^{1/2} \left(\frac{P_{max}}{C_{crack}^{3/2}}\right) \qquad 2.4$$

where σ_c is the critical stress given by $\sigma_c = E\varepsilon_{COS}$. . ε corresponds to the tensile strain of crack onset, and E_r is the reduced Young’s modulus of the coating, $g(\alpha_D\beta_D)$ is a dimensionless coefficient given by Dunduru’s parameters [113], and t is the coating’s thickness. C_{crack} is the radial crack length, σ is the stress at the crack tip, P_{max} is the maximum load, *H* corresponds to hardness, and α_1 is an empirical constant related to the indenter geometry.

The main mechanisms that affect hardness are: i) dislocation-induced plastic deformation, ii) nanostructure of materials, and iii) attractive forces between atoms [114]. Hardness enhancement of coatings is strongly dependent on the grain size, 10 nm typically being a critical size to obtain the highest hardness; if the grain size is reduced, the yield strength can remain constant or decrease. Therefore, hardening can be achieved by grain refinement, and is described by the Hall-Petch relationship [115]:

$$\sigma_y = \sigma_o + \frac{k_y}{\sqrt{d}} \qquad 2.5$$

where σ_y is the intrinsic yield stress, σ_o is a material constant that corresponds to the Peiperl’s frictional stress or resistance to dislocation motion in a single crystal, d is the crystallite size, and k_y is a constant.

RS influence the overall mechanical properties of a coating and consequently affect the performance of the coated component. Once cracking or spalling occurs, the substrate is left vulnerable to environmental attack. The definition of failure for a component depends on its use, but a general definition is a loss of structural integrity, either by cracking, void growth, or delamination. The relaxation of stresses can lead to failure; therefore, the understanding of the mechanisms of stress and relaxation processes is important to prevent fatal consequences [70], [116], [125], [126], [117]–[124].

The presence of compressive stress in the coating and in the interfacial layers is a beneficial property for engineering applications, and surface treatment should be applied to the surface of materials. The first layer of a coating deposited on a substrate will grow by arranging atoms with neighboring atoms from the surface of the substrate. Generally, in crystalline materials a mismatch exists between the lattice parameters of the coating and substrate, which displace atoms from their equilibrium position, creating a misfit strain. The strain field results in elastic forces that produce stress in the coating and in the substrate. In the case of coatings on very stiff substrates, the overall dimensions of the system are controlled by the substrate, and the strain is given by $\varepsilon_0 = (a_S - a_c)/a_c$ where a_S and a_c are the relaxed lattice parameters of the substrate and coating [127].

2.3.1 Origin of the stress

For the purpose of this research, we consider two aspects of RS: i) the characteristic length scale over which the stresses equilibrate [128], [129], and ii) their origin and evolution (Pauleau, 2001). The distribution and origin of the RS in a functional coating can affect the performance, reliability, and lifetime of material components. The RS can have an impact on the adhesion and the fracture toughness of coatings [130], [131], on the performance of aerospace components [16], on the physical properties such as conductivity [132] or piezoelectricity [133], and on the coatings nanostructures [134].

The sum of the RS through the body of a component must be zero. The length in any direction over which the stress equilibrates is defined as the characteristic length. Therefore, RS is categorized according to three characteristic length scales: Type I, known as macrostress, involves stress on the continuum level, which ignores the microstructure of different layers. This type of stress equilibrates over a length equal to the size of the component. A possible consequence of macrostress would be the plastic bending of the structure. On this scale, the stresses can be described by continuum mechanics. Type II, or microstress, equilibrates on a length of a few grain diameters, and may be referred to as intergranular stress. Such stress may originate from inhomogeneity on the scale of the grain size. Type III, also called microstress, occurs at a finer scale from heterogeneous behaviour at the atomic scale. This type of microstress is normally related to the grain boundaries.

The origin and evolution of RS in coatings and their interface with the substrate are dependent on the deposition technique and coating process parameters. PVD coatings may have tensile or compressive RS, depending on the deposition parameters. Total RS results from the contributions of thermal, σ_{th}, intrinsic, σ_i, and extrinsic stresses, σ_e [117]:

$$\sigma = \sigma_{th} + \sigma_i + \sigma_e \qquad 2.6$$

2.3.1.1 Thermal stress

Thermal stress, σ_{th}, occurs due to a difference in the thermal expansion coefficients of the coating and substrate if the deposition process is not performed at room temperature. During the deposition process, this difference produces a biaxial strain, ε, in the coating under a deposition temperature, T_d. The change of temperature in the coating-substrate system is related only to elastic strain, ε. Thermal stresses are given by [135]:

$$\sigma_{th} = \left(\frac{E_c}{1-\nu_c}\right)\varepsilon = \left(\frac{E_c}{1-\nu_c}\right)(\alpha_s - \alpha_c)(T_d - T) \qquad 2.7$$

Where E_c and ν_c are the Young's modulus and Poisson's ratio of the coating, respectively; α_s and α_c are the thermal expansion coefficients of substrate and coating, respectively; and T is the temperature during the stress measurement.

2.3.1.2 Intrinsic stress

Intrinsic stresses, σ_i, develop during processing, are often associated with the microstructure (morphology, texture, grain size) of the coating [136]. The intrinsic stress in coatings that are deposited at low temperatures varies with the normalized momentum (energy), P_n, of the particles impacting the coating surface. The ideal curve of intrinsic stress presented in Figure 2.5 shows three different zones according to the normalized momentum, which is the total kinetic energy of species colliding with the coating surface per atom condensed and integrated into the coating. Each zone of this curve corresponds to the stress observed with the microstructure described by the SZM. Changes in microstructure develop intrinsic stresses by influencing the density of the coating and the substrate bonding.

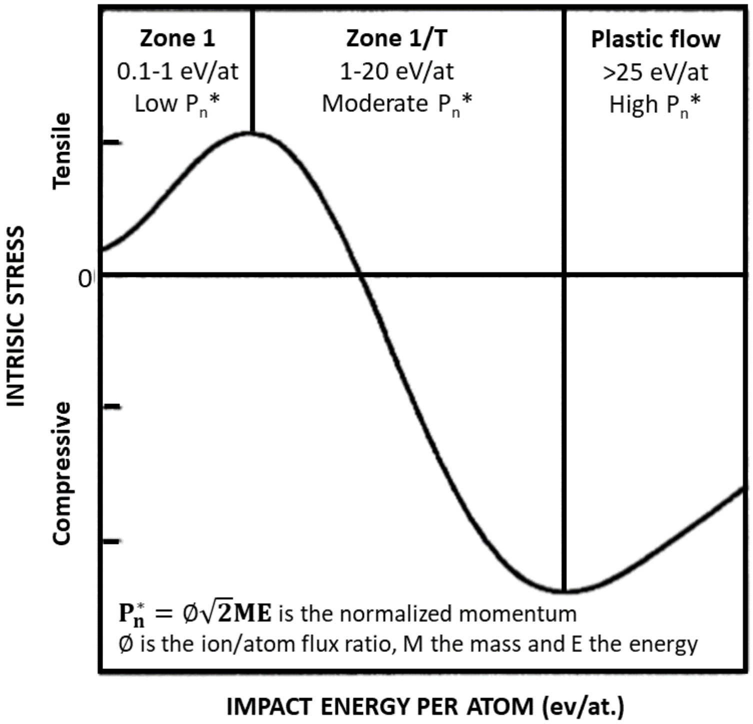

Figure 2.5 Idealized intrinsic stress vs. normalized momentum, P_n, which is related to the kinetic energy of particles impacting the coating surface per atom condensed and integrated into the coating [117].

The mechanisms created by energetic particle bombardment (such as ions or energetic neutrals) that influence the microstructure and therefore the stress are related to the nature, flux, angle of incidence and gas pressure of the particles during the PVD process. The understanding of these relations is complex for plasma-based processes, mainly because of the interdependency of deposition energy and flux.

During sputter deposition, the substrate is exposed to two kinds of species: i) sputtered atoms, and ii) back-reflected neutralized inert gas. The species can varied according to the electrical connection on the substrate, and the conductivity between substrate and film; there can also exist a direct bombardment of plasma ions on the substrate (see Figure 2.6). The energy and flux of energetic species are a function of the process parameters and the geometry of the system. Momentum and energy transfer from sputtered and back-reflected atoms and from energetic ions are the reason for many structural modifications and RS observed in sputtered coatings. Normally, the ion energy related to the difference between a plasma potential and a surface potential creates ion bombardment. The surface potential can be ground, floating, or negative bias with a DC-bias applied by a power supply or a self-induced negative potential of the substrate holder and substrate by RF-power.

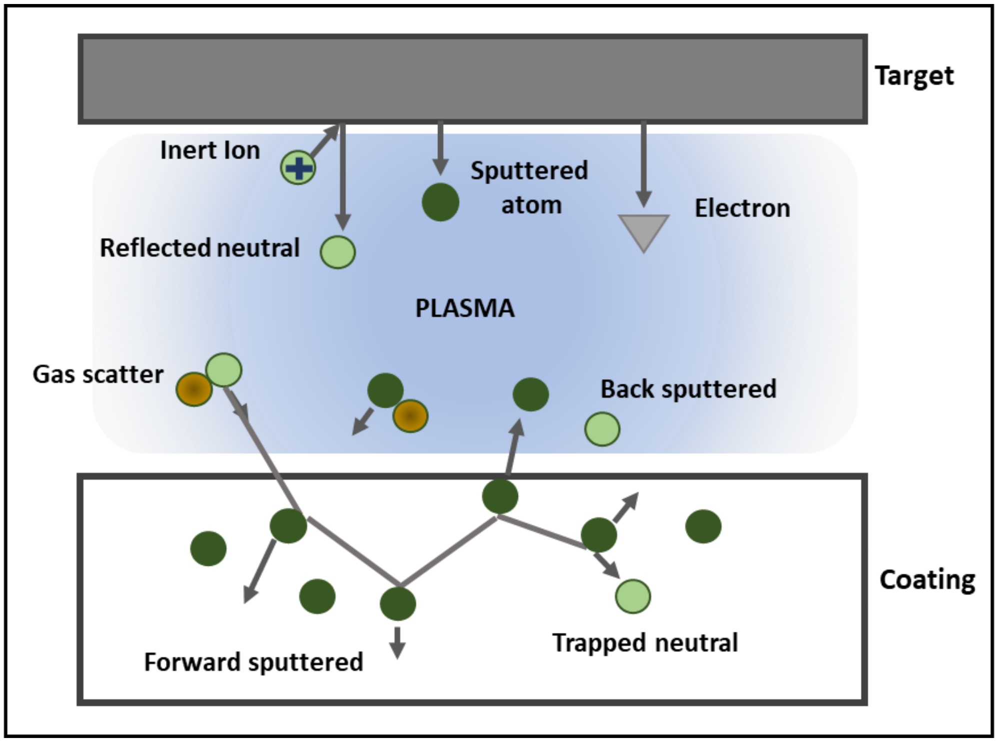

Figure 2.6 Schematic representation of the energetic particles originating at the sputtering target that may strike the coating and produce structural modification and gas incorporation. Particles from the plasma are superimposed on those originating at the target [119].

The inert ions that reach a target are neutralized before getting reflected. The particles with enough initial energy exceed the sputtered atom energy. The atomic peening mechanism varies as a function of the coefficient of energy and the particle reflection, which depends on the target-sputtering gas mass ratio (M_2/M_1) and on the incident energy [119]. The fraction of the incident energy transferred to the coating is an important quantity for stress data interpretation, particularly at low incident energies. With Ar, He, and Xe ions as inert gases, the fraction of kinetic energy transferred to the substrate surface in an energy range from 1 to 4000 eV is insensitive to the incident energy down to 50 - 100 eV, decreasing rapidly at lower energy [137]–[139].

2.3.1.3 Parameters influencing the stress

The main process parameters that influence intrinsic stress are gas pressure, substrate bias, the target-sputtering gas mass ratio, substrate orientation, cathode geometry and chemical reactions involved in the process. These factors have a relationship with one another during coating deposition, and all have an effect on the evolution of the microstructure while developing grain characteristics that determine the zone in the SZM [71], [134], [140]–[142].

The stress variation with increasing negative bias voltage is similar to the dependence observed as a function of gas pressure, as shown in Figure 2.7. This similarity is because a common stress-generation mechanism occurs, although the nature of the involved particles is not necessarily the same. There are three characteristic intrinsic stress regimes associated with sputtering pressure: i) compressive stress at low pressure, decreasing in magnitude as the pressure increases, until ii) a transition from compressive to tensile stress at an intermediate pressure, called the stress transition pressure, and iii) increasing tensile stress with increasing pressure up to a maximum, at which the magnitude of the tensile stress decreases with further increase in sputtering pressure.

At high negative bias voltage, ion bombardment with more energetic particles leaves a higher fraction of residual radiation-type damage in the form of clusters of point defects and/or trapping of atoms at grain boundary sites as a consequence high level of compressive stress is created [134]. At lower negative bias voltage, the stress decreased. For coatings produced under low bias voltage and high gas pressure where gas scattering led to attenuation of particle energy and flux, the grain-boundary-relaxation form tensile stress. The transition from tensile to compressive stresses that occurs with increasing negative bias and reducing pressure develops a similar microstructure of the coating [143]. Bias voltage on substrate imposes a high impact on the relationship between particle energy and coating stress. The energy of gas ions in bias sputtering exceeds the one obtained by modulating the deposition pressure. With bias sputtering, the possible particle energy is defined by the target and sputtering gas mass ratio (M_2/M_1). Thus, the stress remains constant at high energy due to plastic flow. The mechanism by which bombardment influences the coating growth and stress, requires knowledge of the nature of particles and their flux, which is experimentally problematic in plasma-based processes [134].

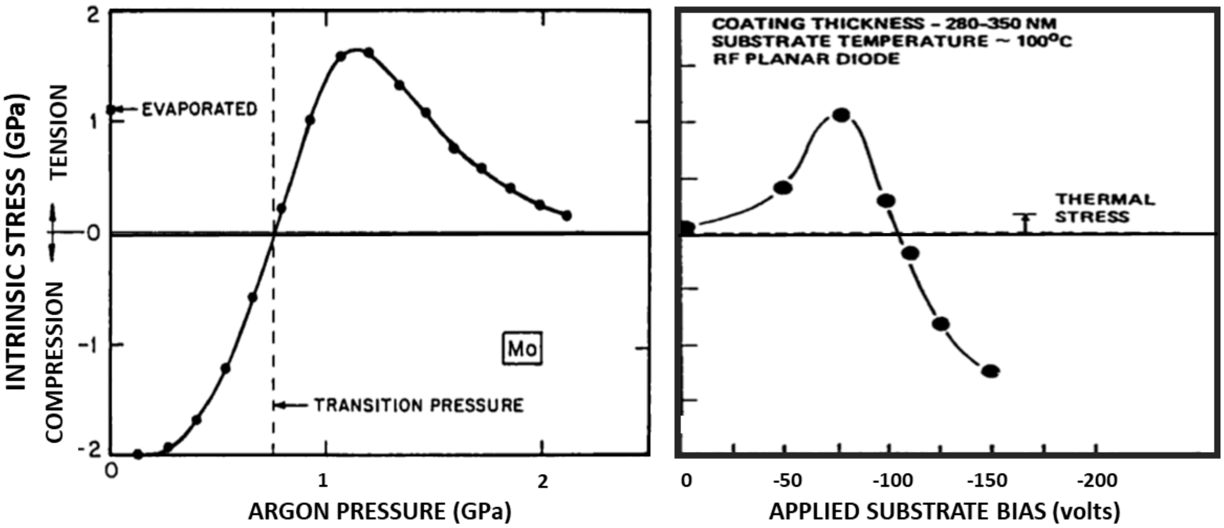

Figure 2.7 Intrinsic stress as a function of a) Ar pressure [144], and b) applied substrate bias [119], [145].

Some of the main models established to explain the origin and mechanisms of stresses have been separated in the tensile and compressive stresses of sputtered coatings [119], [134], [140]. These models explain the main causes of the formation of intrinsic stress during PVD processes. A list of such models with some of their characteristics and the stress type generated is presented in Table 2.5.

Table 2.5. Summary of the main characteristics of different models and the origin of intrinsic stress in PVD coatings.

Model	**Mechanism**	**Cause**	**Parameter**	**Stress type**	**Microstructure**
Tensile stress	Kinetic and thermal energy	Low mobility of atoms	Energetic particle bombardment $= 0 < T/Tm < 0.2$	Tensile	Porous, void rich
Surface tension		Attractive forces between atoms at interface		Tensile	Crystallites separated by small dimensions
Phase change		Phase transition and possible change of density	$T > T_{crystallization}$	Tensile	Crystallites with grain boundary
Buried layer	Constrained shrinkage and self-diffusion. Thermal process - Grain growth, defect annihilation, surface diffusion-induced mass transport	Annealing; Contraction of disordered liquid material; Elastic deformation (relaxation) of grains; Low adatom mobility	High deposition temperature; Annealing rate	↑ T ~ 0 to low tensile ↓ T = Tensile	
Grain boundary relaxation	Interatomic attractive forces acting across the gaps between grains		Deposition pressure	Tensile	Varied according to the pressure
Impurities	Lattice distortion	Incorporation of atoms with different sizes; Reaction at grain boundaries; Grain surface energy reduction		Ion bombardment = 0 → Compressive Ion bombardment $\neq 0$ → Low compressive to tensile	
Forward sputtering	Atomic peening	Energetic particles bombarding the film	Energetic particle bombardment $\neq 0 < T/Tm < 0.25$	Compressive	

2.3.1.4 Extrinsic stress

The extrinsic stresses, σ_e are also part of the RS in PVD coatings, but they can also be developed after processing. On the one hand, during plasma processes, different molecules can penetrate voids or defects of coatings causing interaction forces between adsorbed species, thus modifying the RS [146].

On the other hand, the thermal expansion mismatch is also a cause of extrinsic stress, one which is developed after the deposition process when the deposition temperature used was high enough to cause a mismatch between coating and substrate. For unbonded components, the incremental change in temperature ΔT leads to a displacement mismatch, $\varepsilon_0 = (\alpha_S - \alpha_c)\Delta T = \Delta\alpha\Delta T$, per unit length of the coating and substrate, with thermal-expansion coefficients α_c and α_S, respectively. However, a coherent bonding between coating and substrate requires atoms displacements through the interface, which move the atoms from their equilibrium positions. In the case of thick substrates or substrates with a high modulus compared to the coating, the substrate is much less compliant than the coating. Therefore, the system and its overall dimensions are dominated by the substrate forcing the coating to match it. When biaxial stress condition of a film which causes the elastic bending of a substrate applies, and assuming an ideal adhesion of coating-substrate system, the stress in the coating is given by $\sigma_0 = E_c\varepsilon_0(1 - \nu_c)$, where E_c and ν_c are Young's modulus and Poisson's ratio of the coating, respectively.

Another cause of extrinsic stresses resulting from the change in temperature is due to phase transformations. These have similar effects to those of thermal-expansion mismatches [127].

The main factors and parameters regarding the origin of residual stress concerning the PVD process have been described above. In addition to the parameters that influence the growth mechanisms of coatings or modify the substrate surface, resulting in residual stress on the coated component, there are three more factors that can influence the stress in coatings. They are: i) micro-bending during the deposition process, ii) the edge effect, and iii) the substrate geometry of substrates. All three can have a strong influence on the resulting stress in cases of anisotropic strains. Coated samples experience micro-bending due to external forces, such as the sample holder and clamping during the coating process [147].

2.3.2 Residual stress analysis

Surface engineering processes normally develop layers with complex gradients of phases, microstructure, and RS. Therefore, the microstructure and RS assessments are critical in coatings and near the substrate material's surface.

Considerable efforts have been made to develop different approaches to measure and analyze RS in coatings and multilayers systems [148]–[154]. Some of these approaches include variants of the curvature method [155], holographic transmission electron microscopy [156], micro-Raman spectroscopy [157], and electron backscattered diffraction [158], [159], combination of two techniques such as FIB with digital image correlation [160], [161], surface layer removal such as Ion beam layer removal method [162] and XRD approaches that include the use of different wavelengths by using regular XRD equipment up to synchrotron or neutron diffraction [163]. The XRD technique has been widely used for the RS analysis of surface and through depth profiles of polycrystalline materials [134], [164]–[166].

Conventional XRD methods are chosen mainly because of their accessibility, noncontact and non-destructive character. The traditional XRD method used to measure RS in thin films is known as the $sin^2\psi$ method, which measures the shift of a single *hkl* diffraction peak recorded for different ψ angles (rotation of the sample holder around the axis normal to the sample) to extract the residual strain. In this method, the RS is obtained by using the X-ray elastic constants (XEC) to convert the measured strain into the stress [154], [164]. A modified $sin^2\psi$ method [167] was proposed to measure highly textured coatings. In the modified $sin^2\psi$ method, the interplanar spacings of the different possible diffraction planes were determined using grazing-incidence XRD geometry with a fixed incidence beam angle. However, this approach was developed with the assumption of isotropic elastic behavior which leads to error when coatings present a high degree of anisotropy. Therefore, an additional approach based on the conventional and modified $sin^2\psi$ method but with a correction factor, $cos^2\alpha$, was developed [154].

The literature requires more information concerning measurements and analyses of RS depth profiles through polycrystalline thin films, multilayers, or graded coatings on a polycrystalline substrate in which all the layers have a similar composition. One of the main challenges during the analysis of polycrystalline coating-substrate systems was the interference between XRD patterns of each layer at diffracted peaks in 2θ positions during the single RS analysis of different crystalline layers.

2.3.3 Tribology of coated systems

Tribological properties, especially the wear rate or wear coefficient, *W*, are also essential factors for the evaluation of the performance of protective coatings. Wear can occur as an abrasive wear or adhesive wear. Both of them are critical for the selection of the material. The abrasive wear normally dominates the overall wear, however, adhesive wear exists also in the absence of abrasion. The coefficient of friction during wear mechanism indicates the ease of sliding causing a loss of energy and a possible increase of temperature in the material. The presence of a high coefficient of friction can increase adhesive and abrasive wear. The wear coefficient is proportional to the volume loss, *V*, and inversely proportional to the normal applied force, *P*, and the sliding distance, *S*:

$$W = \frac{V}{(P \cdot S)} \qquad 2.8$$

In coated systems, four main parameters have been established as the ones that control the tribological contact behaviour. These parameters are [168]: i) the coating-to-substrate hardness transition, ii) the coating thickness, iii) the surface roughness, and iv) the size and hardness of any debris. Figure 2.8 shows the twelve typical tribological contact conditions, with different mechanisms influencing friction when a hard, spherical slider moves on a coated flat surface. The mechanical mechanisms relate the tribological behaviour to the presence of one or multiple factors such as stress-strain distribution in the contact area, the elastic-plastic deformation, and the formation of debris and its dynamic evolution.

The relationship between the hardness of the coating and substrate is an important parameter. For materials such as nitrided coatings on a Ti alloy, which is considered a hard coating on a softer substrate, the friction and wear can be decreased by avoiding breaking both on a macro-scale and a micro-scale. Compressive RS in coatings can reduce the possibility of failure/fracture due to tensile forces. An additional decrease in friction and wear can be achieved by improving the load support, that is by increasing the hardness of the substrate while forming a stable solid solution to inhibit deflections and breaking due to counterpart load [168].

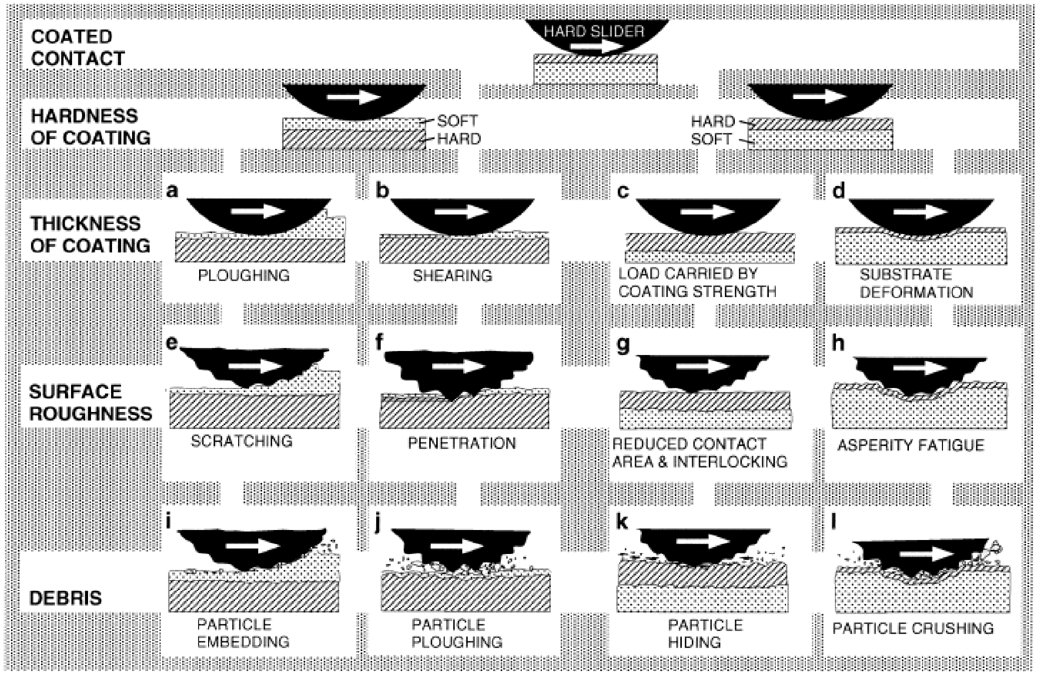

Figure 2.8 Macromechanical contact conditions for different mechanisms that influence friction when a hard spherical slider moves on a coated flat surface [168].

2.3.4 Nitride coatings

The deposition of protective coatings with a few microns thickness can improve the performance and enhance the lifespan of engineering components. Transition metal nitride coatings, such as TiN, ZrN, CrN, TaN, NbN, and HfN, are frequently used for aeronautical applications mainly because of their suitable mechanical properties and their wear-, erosion-, and corrosion resistance [15], [169]–[171]. These coatings normally consist of a mixture of covalent, metallic, and ionic bonds, resulting in high hardness, high melting temperatures; around 1500°C for CrN coatings and >2500°C for TiN, ZrN, TaN, NbN and HfN, excellent abrasion resistance, and chemical inertness, among other properties have been observed. TiN and ZrN have a face centered cubic (FCC) structure, where the N atoms are in the interstitial octahedral sites (Fm3m, space group 225), see

Figure 2.9. The phase diagrams for TiN an ZrN are shown in Figure 2.10. TiN exists as a solid solution containing nitrogen between 37.5 and 50% at.% N [172], whereas ZrN can accommodate non-metal vacancies and is generally written using the non-stoichiometric formula ZrN_{1-x}. The

presence of these defects and the variation in composition affect its mechanical properties [173], discussed in more detail below.

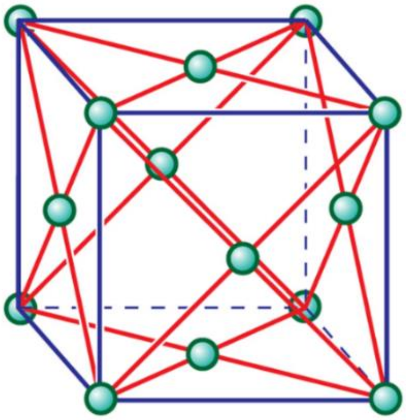

Figure 2.9 Unit cell of the FCC structure [26].

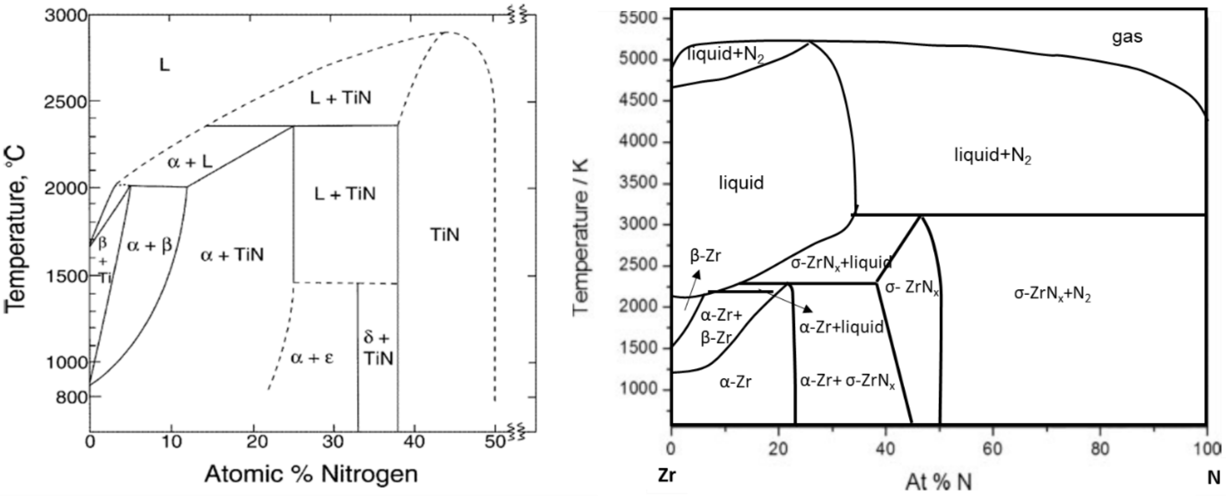

Figure 2.10 Phase diagram of a) TiN [172], [174], and b) ZrN [173].

2.3.4.1 TiN coatings

Titanium nitride is widely used for protective coatings due to its attractive tribo-mechanical properties, and due to its gold color, which makes its useful for esthetic purposes. The morphology of TiN coatings deposited by PVD is in the form of dense columns with elongated grains extending through the coating thickness. TiN growth with preferred orientation along the [111] and/or [100] crystallographic directions [175] can influence the mechanical properties (i.e., the elastic modulus of TiN along [111] is lower than along [100]) [176]. The (002) plane has the lowest surface energy for TiN, which is related to the packing density due to high number of nearest-neighbor atoms creating atomic bonds in that plane that are satisfied. The texture formation of polycrystalline TiN layers depends on the kinetics of growth, with consideration of the surface migration of adatoms [177], and on the thermodynamics and the competition between the surface free energy and the strain energy [178]. The preferential orientation in TiN evolves trough the thickness, as presented in Table 2.6. This is associated with the linear increase of surface energy in the coating during the growth [178].

Table 2.6 Relationship between process parameters and preferred orientation (PO) in TiN coatings Table taken from [179].

Parameter	**PO change with increasing parameter**	**Reference**
Ion/metal flux ratio, J_i/J_{Ti}	(111) → (002)	[177], [180], [181]
N_2/Ar ratio	(111) → (002)	[182]–[187]
Coating thickness	Random → (002)→(111) Random → (002)	[188], [189] [177], [180], [182], [190]
Negative bias voltage, V_b	(002) → (111) → (220) (002) → (111) → (002)	[186] [191]
Power, W	(002) → (111)	[188], [189]
Temperature, T	(111) → (002)	[184], [192]

The hardness of TiN coatings is normally around 20-22 GPa, while the Young's modulus is in the range of 350 GPa, however, the characteristic hardness and Young's modulus of thin coatings can be enhanced by applying interface pre-treatments on the substrate surface. Figure 2.11 shows the linear relationship between H and E_r, for various magnetron-sputtered protective coatings. When the H/E_r ratio is greater than 0.1, the coatings provide enhanced resistance to plastic deformation and distribute load applied to the coating over a wider area than do other protective coatings, which delays the appearance of cracks. These coatings are considered to be hard and tough [114].

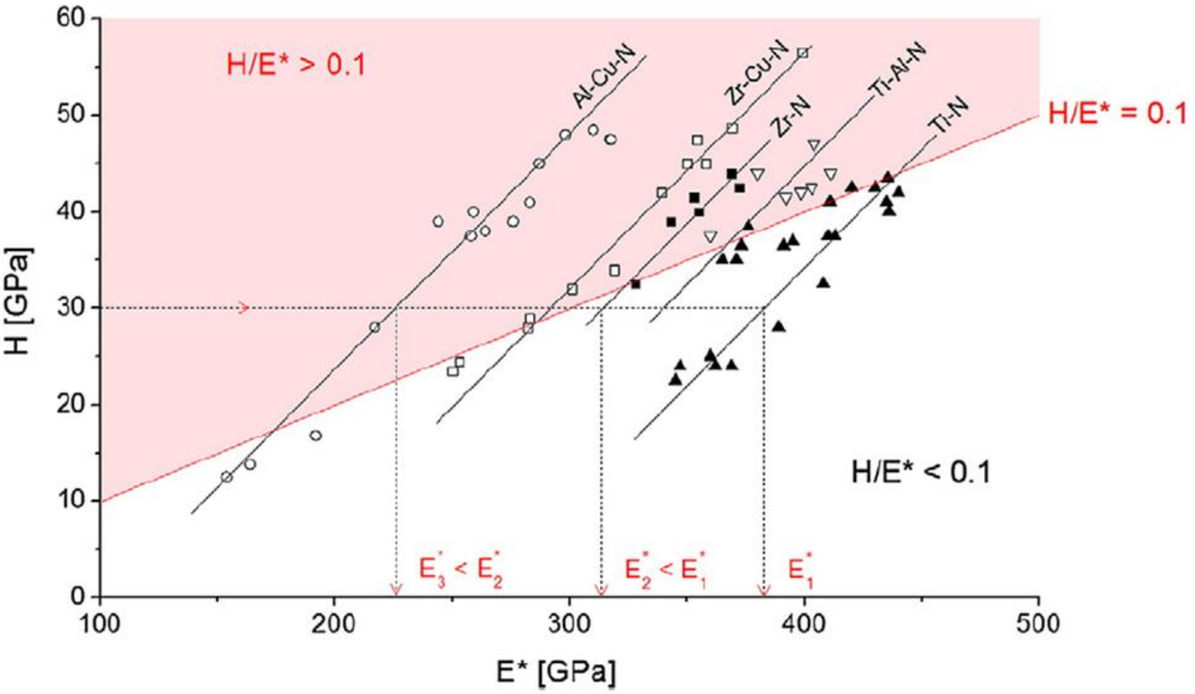

Figure 2.11 Hardness as a function of effective Young's modulus for nitride coatings [114].

In general, higher hardness is associated with higher RS in the coatings. Compressive RS are necessary to delay crack propagation and to improve the fracture toughness of the coating. Characteristic values of RS in TiN coatings range from ~1 GPa in tension to 10 GPa in compression, depending on the deposition parameters, substrate and final thickness. The fracture toughness, K_{1C}, of TiN on steel varied from 3.8 to 8.7 MPa·m$^{1/2}$ [193]. Figure 2.12 shows RS, K_{1C} and cracking resistance values reported for TiN coatings on three different substrates. The value of K_{1C} of TiN increases with increasing elastic modulus of the coating, and higher RS results in higher K_{1C} as can be observed on TiN coating with a Young's modulus of 475 GPa and a RS of -4 GPa, compared to TiN coatings with a Young's modulus of 305 GPa and a RS of -3 GPa, or to DLC and MoS_2 with elastic modulus in the range of 39 to 147 GPa and RS close to zero.

2.3.4.2 ZrN coatings

Zirconium nitride, ZrN, coatings and TiN present a high miscibility, while Zr can diffuse into TiN forming a solid solution. Magnetron-sputtered ZrN coatings have a preferential orientation in the (200) plane, and the formation of additional phases, such as Zr_2N and Zr_3N_4, is relatively easy. The over-stoichiometry of N reaches around 15 at.%, much more than in TiN coatings. This behaviour is because the tetrahedral sites in ZrN are larger than in TiN, and consequently, the formation of N_2 interstitials requires less energy [194].

Just as for TiN, and as also shown in Figure 2.12, when the H/Er ratio is greater than 0.1, ZrN coatings are considered to provide enhanced resistance to plastic deformation and to distribute the load applied to the coating over wider area than do other protectives coatings [114]. These characteristics make it an optimal material for applications where cracks should be avoided, and the films should be tough.

Nitride coatings, such as TiN and ZrN deposited by PVD, suffer from poor adhesion strength to alloy substrates. The reasons for this are high internal stress plus poor chemical bonding to the substrate. The use of an interface layer as a gradient layer with controlled mechanical and structural properties through layers has been shown to provide a beneficial influence on the adhesion strength for TiN and ZrN coatings deposited at RT, 300 and 400 °C, and to increase the hardness of ZrN coatings, especially at high temperature [51], [195].

The use of an alloying element, such as Zr, Al or C, for example, enhances the protective properties, making TiN even more attractive [196]. The enhancement of tool life with ternary-TiN coatings (Figure 2.13) is attributed to the solid-solution strengthening effect of the alloying element in the TiN lattice [197]. The formation of dense layers or ternary phases on the coating by using an alloying element is beneficial, as shown by low crater depth, and low flank wear created by caused in the cutting edge due to abrasive wear during surface machined (Figure 2.13b). TiZrN offers excellent protection against abrasive wear loads at high temperatures, which is attributed to the stabilization effect of zirconium in the fcc TiN unit cell, and to the possible formation of a thin ZrO_2 layer on the top of the coating, which reduces wear [172].

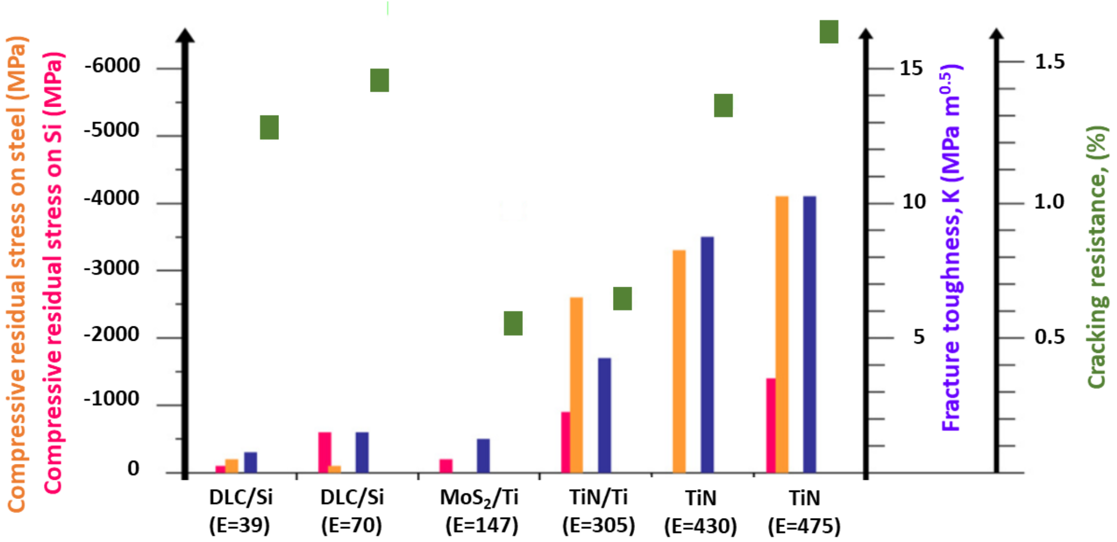

Figure 2.12 Measured coating residual stress on silicon (red bars) and steel substrates (orange bars); fracture toughness (purple bars) was calculated from FEM stress simulations and scratch test cracking behaviour; cracking resistance (green points) was measured by the bend test for DLC, MoS_2 and TiN-coated steel surfaces with elastic moduli in the range of E = 39–475 GPa. Adapted from [193].

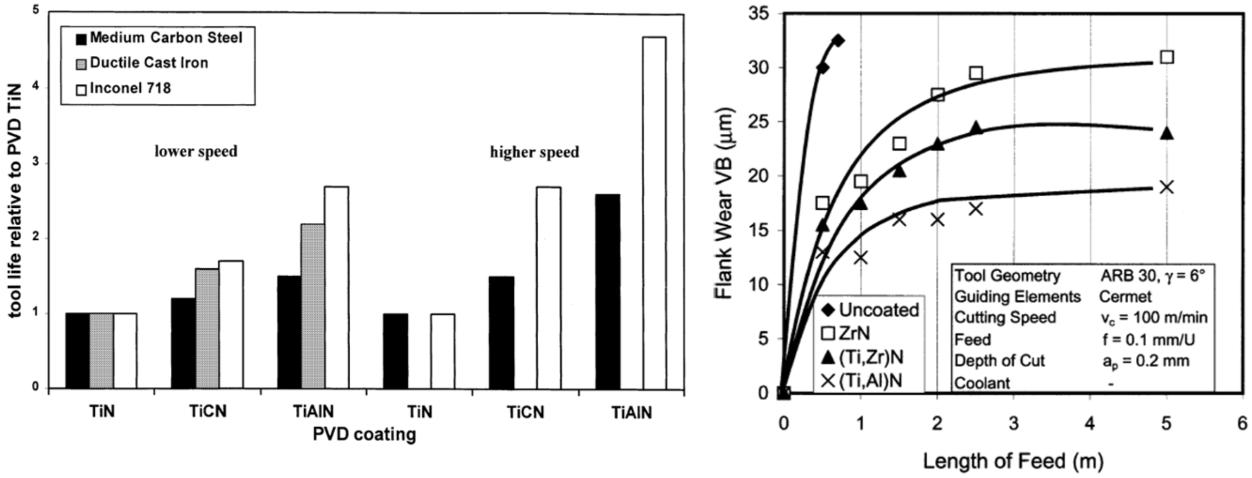

Figure 2.13 Abrasive wear on tools coated with TiN-based coatings: a) Life enhancement and b) flank wear on coated tool *vs* length of feed [172], [197]

2.3.4.3 Nitride multilayers

Coatings in the form of multilayers, such as ZrN/TiN, and graded layers where physical and/or structural properties are controlled along the coated system have mechanical properties superior to those of nitride monolayers.

Multilayer architecture considers the individual layers and the interface, in order to control the final properties and performance of the coated system. Three types of multilayer architectures can be fabricated: i) a limited number of single layers that interrupt the columnar grain growth and combine the properties of different materials; ii) multiple single layers, in which the interface volume acts as sites for energy dissipation, plus they have the advantage of architecture with a limited number of single layers; and iii) superlattice coatings, in which the layers with different composition are chosen to have similar chemical bonding, similar atomic radii, and lattice distances and layer thicknesses in the range of lattice dimensions. These architectures can produce materials with properties and characteristics not possible in single-layer coatings; similarly, nanocomposite coatings can be formed by nanometer size crystals, by nanograins surrounded by an amorphous phase (nanocomposites), or a mixture of nanograins with varied crystallographic orientations [114], [198], [199].

The optimization of nanoscale strain by multilayers with different modulation periods and ratios enhances the mechanical and tribological properties of the coating, making it superior to those of the TiN or ZrN alone [200]. The interface between single layers are sites of energy dissipation and crack deflection, leading to a toughening and strengthening of the complete system [201]. The different mechanisms of toughening coatings are represented schematically in Figure 2.14.

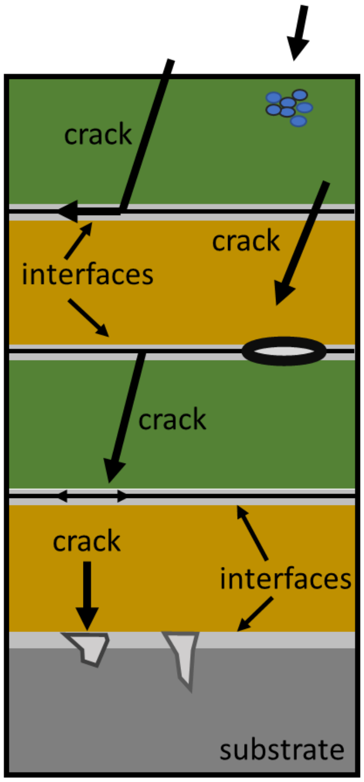

Energy dissipation in ceramic multilayer coatings (in-layer, interface, phase/grain boundaries and through coating effects)

Crack splitting, deflection and reduction of crack propagation at grain boundaries (**grain boundary toughening/hardening**)

Crack splitting, deflection and reduction of crack propagation at interfaces (**interface toughening/hardening**)

Local delamination at interfaces by opening nano-voids (crack energy dissipation, local stress relaxation, plasticity at nanoscale)

Figure 2.14 Toughening mechanism in ceramic multilayer materials [201].

In PVD multilayer coatings, for example, TiN/TiC, when the number of single layers is increased, the hardness, toughness and surface homogeneity of the system are enhanced, while the friction coefficient and wear rate are reduced (Figure 2.15). The counter-body used on the pin on disk wear tests was a pin of WC-6 wt.% Co (3 mm diameter). The WC-6 wt.% Co ball with an applied force of 10 N, was always subjected to TiC coating surfaces because TiN was decided to be deposited firstly to have a better adhesion to the substrate. A further comparison of the properties is presented in Figure 2.15. The enhancement in the hardness and toughness of multilayer coatings can be attributed to the many interfaces which block dislocation movement across the interface between the TiC and TiN layers of multilayer stack [202].

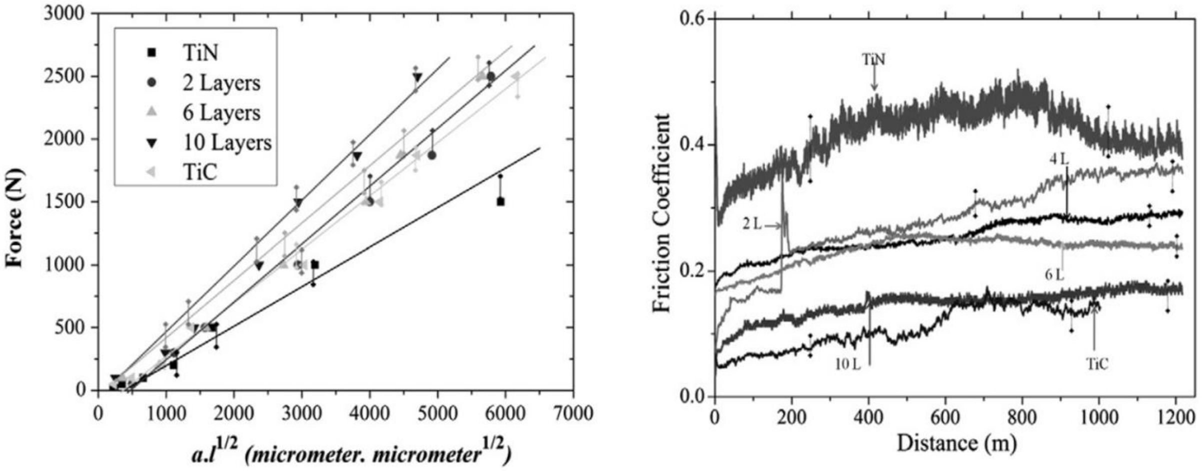

Figure 2.15 Crack propagation as a function of crack length and friction coefficient as a function of distance for single-layer and multi-layer coatings [202].

Table 2.7 Mechanical properties of TiN/TiC multilayer coatings [202].

Sample	**Layer thickness (μm)**	**Hardness (GPa)**	**Wear rate ($10^{-7}mm^3/N\ m$)**	**Friction coefficient**	**Toughness (MPa $m^{1/2}$)**
TiN	2.0-3.0	20.0±1	6.67 ± 0.5	0.40-0.50 ± 0.05	8.7
TiC	2.0-3.0	27.0±1	3.26 ± 0.5	0.10-0.12 ± 0.05	13.2
2 layers	1.0	27.4±1	4.60 ± 0.5	0.20-0.35 ± 0.07	14.1
4 layers	0.5-0.6	27.9±1	1.10 ± 0.5	0.20-0.30 ± 0.04	14.3
6 layers	0.3-0.5	28.5±1	0.11 ± 0.5	0.20-0.25 ± 0.03	14.5
10 layers	0.2-0.3	29±1	0.05 ± 0.5	0.10-0.20 ± 0.05	17.7

CHAPTER 3 EXPERIMENTAL METHODOLOGY

This chapter describes the experimental methodology applied in this work, including the sample preparation, PVD processes description, and characterization techniques. First, the sample preparation process before plasma treatment is described, followed by a brief introduction of the magnetron sputtering working principle, in particular the deposition system and parameters used in this work to develop interface layers and TiN and ZrN films and ZrN/TiN multilayer coatings. Finally, an overview of the fundamentals of the microstructural, mechanical, and tribological characterization techniques is presented. For each characterization technique such as microstructural evaluation, stress characterization, mechanical and tribological tests, we prepared at least four identical samples to ensure the repeatability of the results. Except for the case of TEM and EBSD techniques where the sample was evaluated only for selected samples due to limitation of equipment use.

3.1 Substrate preparation

The surface characteristics of base material have a strong impact on the microstructural, mechanical, and tribological properties of coatings. The quality of the sample preparation process is critical for the performance and durability of coated components.

In this work, two geometries of Ti-6Al-4V substrates were used to meet the different requirements of each characterization equipment employed during the study, specifically, thin flat substrate used for the microstructural and mechanical characterization techniques and dog-bone-shaped coupons required for the micro-tensile test analysis.

The Ti-6Al-4V substrate preparation was performed in three steps: First, a Ti-6Al-4V thin sheet was cut using a waterjet cutting machine to obtain the dog-bone shape. Then, an abrasive paper (SiC paper) was used to grind the thin flat and dog-bone samples in order to remove all visible marks on their surfaces. Finally, the polishing process was performed to remove all artefacts created by the grinding process. The samples were polished with free abrasive particles embedded in a lubricant solution on a cloth sliding across the sample surfaces. The pressure, time and subsequent abrasive particle sizes varied according to the abrasion resistance of the alloy and the final characteristics required on the specimen surfaces [203]. The Ti-6Al-4V substrates were polished using a Struers LaboPol-5 polishing machine with SiC paper from 400 to 1200 grit and water-sprayed continuously. This stage was done at a speed of ~250 rpm until all visible imperfections at the specimen surfaces were removed. Then, a Logitech PM2A precision polishing machine was used with SiC paper of 2000 and 4000 grit to remove all visible scratches created during the previous step. Finally, a mirror-like surface finish was obtained with a cloth and colloidal silica (particle size 5 nm) plus H_2O_2 and distilled water. The final polishing of the flat thin samples was done on a Struers machine (at ~250 rpm, in each case, for a maximum of 30 mins). The dog-bone samples received an extra step to ensure homogeneous thickness along the specimen required during the micro-tensile testing. Therefore, dog-bone samples were polished for 24 hrs using a VibroMet 2 vibratory polisher.

3.2 PVD techniques – Surface engineering processes

3.2.1 Magnetron sputtering

Sputtering is one of the main categories of PVD processes. Sputtering is a non-thermal vaporization process, where metal atoms are mechanically ejected and ionized from a target by momentum transfer during the impact of ions or energetic neutral atoms (bombarding particles), accelerated from a plasma by an electric field. The coatings result from the condensation of the sputtered particles on a substrate. Magnetron sputtering was the process selected to prepare the interface layers and coatings used in this study.

3.2.2 Deposition system

In this study, interface layers, ZrN/TiN multilayers, and TiN and ZrN coatings were performed using a magnetron sputtering system in RF mode schematically shown in Figure 3.1. The deposition chamber was equipped with two 50 mm-diameter planar magnetrons and a planar rotational substrate holder 60 mm away from the targets. For the plasma process to produce single-layer coatings, only Ti target was activated, while the other remained closed and not powered. For the multilayer coatings, both targets were activated; however, each target was covered by a shutter, which was alternatively opened and closed to protect the corresponding target according to the plasma composition required.

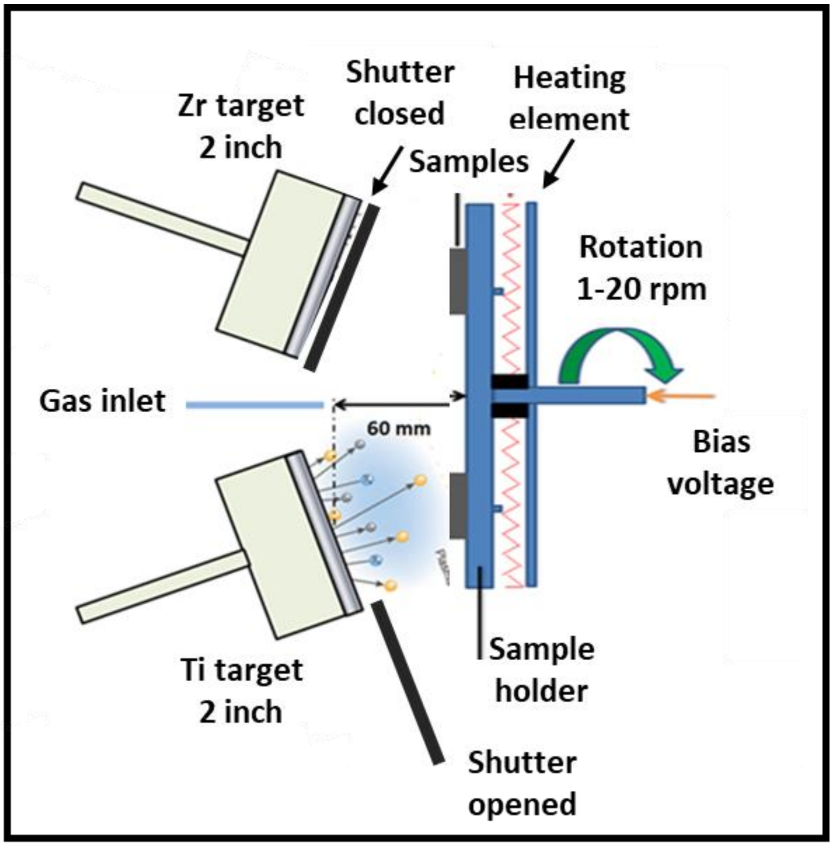

Figure 3.1 Magnetron sputter-deposition system.

Before deposition, all the substrates were ultrasonically cleaned using detergent with deionized water, acetone, and ethanol. A turbomolecular pump backed by a rotary pump was used to evacuate the vacuum chamber down to a base pressure lower than 1×10^{-6} Torr. The substrates mounted on a vertical rotational sample holder located in front of both magnetrons and separated by 60 mm were uniformly heated up to ~400°C by a heating element positioned behind the entire sample holder. The temperature was measured in the center and close to the edges of the substrate surface with a thermocouple before starting the plasma processes.

Two sets of samples were prepared, one including the multilayer architecture, and the second one including the single-layer one. Several parameters, especially pressure, bias voltage, gas flow and time were evaluated in order to create surface treatments and coatings with different architectures. All optimized deposition conditions and process characteristics to assess compressive RS with different levels while controlling coating-substrate adhesion are summarized in Table 3.1. The preparation of both sets was done following three main steps: i) Sputter cleaning using Ar atmosphere, ii) Surface pre-treatment to form an interface layer, and iii) Coating deposition.

Table 3.1 PVD optimized conditions for the plasma interfaces, ZrN/TiN multilayer, ZrN and TiN coatings used at the DC magnetron sputtering during this study.

Process	**Working parameters**	**Set 1 – Multilayer coatings**	**Set 2 – Single-layer coatings**
Sputter cleaning	RF bias voltage -substrate	-900 V	-600 V
	Ar pressure	5 mTorr	5 mTorr
	Ar flow rate	100 sccm	30 sccm
	Time	60 min	30 min
Ar plasma	Substrate RF bias voltage		-600 V
	Gas pressure		5 mTorr
	Ar flow rate		30 sccm
	Time		30 min
Nitriding	Substrate RF bias voltage	-400 V	-400 V
	Total gas pressure	390-400 mTorr	400 mTorr
Step 1	Gas flow rate	120 sccm ($Ar:H_2$) = 80:20	120 sccm ($Ar:H_2$) = 80:20
	Time	30 min	30 min
Step 2	Gas flow rate	120 sccm (N_2+ H_2) = 80:20	120 sccm (N_2+ H_2) = 80:20
	Time	60 min	120 min

Process	**Working parameters**	**Set 1 – Multilayer coatings**	**Set 2 – Single-layer coatings**
Ti implantation	HiPIMS bias voltage - substrate		-630 V
	HiPIMS-Target power		400 W
	Gas pressure		5 mTorr
	Pulse length		55 µs
	Frequency		300 Hz
	Gas flow rate		30 sccm
	Time		120 min
Coating deposition	RF bias voltage - substrate	-120 V	-120 V
	Target power	225 W Ti: 1 Ampere Zr: 1 Ampere	225 W Ti: 1 Ampere
	Pulsing	300 kHz	300 kHz
	Substrate materials	Ti64 50x25 mm^2 Silicon wafer (100)	Ti64 50x25 mm^2 Ti64 dog-bone
	Gas pressure	5 mTorr	5 mTorr
	Time	Calculated from the deposition rate of ZrN layer (45-60 min for 1 µm)	Calculated from the deposition rate of TiN layer (60 min for 1 µm)

Coating deposition processes varied between 45 to 60 min for 1 μm thickness, according to the erosion rate from the Ti target, which was calculated by measuring the sputtering racetrack of the target after deposition.

In the next section, the characterization techniques used during this study to evaluate microstructure, texture, residual stress, tribo-mechanical properties and fracture mechanisms will be described. RS measurements as well as the characterization of other mechanical properties such as H, Er, L_{C1} and L_{C2} present an experimental error normally between 5 to 10%.

3.3 Crystallographic, microstructural and morphological characterization

The crystallography, microstructure and morphology of substrates and coatings can be studied using microscopy, profilometers and diffraction techniques.

3.3.1 Microscopy

The *Scanning electron microscope (SEM)* uses secondary electrons which are re-emitted from the sample surface to form an image. The technique has a high lateral and vertical resolution, allowing one to observe ~10 nm size particles. In this work, a Field-Emission Scanning Electron Microscope (FE-SEM, JEOL JSM 7600F) was used to evaluate the surface and cross-section of samples to assess the coating thicknesses, coating morphology and microstructure of coated systems and for fracture zones observation after tensile testing. The FE-SEM is equipped with an *energy dispersive X-ray spectrometry (EDS),* which was employed to investigate the composition of coatings and interfaces.

Transmission electron microscopy (TEM) is a microscopy technique in which a beam of electrons is transmitted through an ultrathin sample (10-100 nm) to form an image from the electrons. This equipment can capture details as small as a single column of atoms. TEM microscopes frequently involve different operation modes, such as scanning TEM imaging (STEM), diffraction and spectroscopy. In TEM analysis the diffraction of electrons can help to determine the lattice structure and to identify crystallographic phases.

Transmission Electron Backscatter Diffraction (t-EBSD) analysis is a SEM-based electron diffraction technique, which provides considerable improvement of the spatial resolution over conventional EBSD, for crystallographic analyses. The diffraction signal is formed by collecting Kikuchi-scattered transmitted electrons in a SEM microscope. The specimen needs to be tilted, between 10° to 20° from normal, and this reduces the projected surface area. Similar to samples prepared for TEM analyses, ultrathin samples are required for t-EBSD, possibly < 100 nm, in order to reduce the maximum total scattering length before the electrons can be detected [204]. This technique allows one to evaluate the microstructure and crystallography of TiN coatings with different interfaces.

Cross-section of TiN on Ti64 with different interfaces for TEM and t-EBSD analyses were prepared by the *focused ion beam* (FIB) technique, using a Hitachi model FB-2000A microscope. Each sample was thinned down to a thickness of around 100 nm at 30 kV to obtain electron-transparent samples. The TEM technique was performed in a Jeol 2100F microscope equipped with a field-emission electron source. Selected area electron diffraction (SAED) bright, and dark field images were used to evaluate the influence of each interface treatment on the crystallographic properties of the coating, the interlayer and the substrate, separately.

The *transmission Kikuchi diffraction (TKD)* measurements were performed in a Hitachi Cold FE SU8230 SEM equipped with a Bruker eFlash HD detector and Bruker Quantax as an acquisition software. An acceleration voltage of 30 kV was used with a 0.5 nm resolution and step sizes ranging from 0.004 to 0.006. The EBSD data was analyzed using Oxford Instruments HKL Channel 5 software while indexing patterns with the following crystal structures: hcp-Ti with a space group of $P6_3/m2/m2/c$ and fcc-TiN with a space group of $F\ 4/m\bar{3}2/m$.

Optical microscopy is a technique widely used to study the surface morphology of the material. Optical microscopes use visible light and lenses (normally, 100x, 200x, 500x, and 1000x) to magnify images, and they form part of different characterization systems used during this study; for example, nanoindentation, scratch, wear, and tensile testing.

In this work, an LSCM Olympus LEXT OLS4100 apparatus was used to obtain a series of intensity images captured by a blue laser with a wavelength at 405 nm on a 2D scan of the surface at a focus step, equal to 60, then the height of the surface is calculated to build a 3D image by the Olympus laser scanning software. The images of the corresponding topographic map before and during *in situ* tensile testing were acquired using a 20x magnification under a 640x640 μm area.

On the other hand, the topography of scratch and wear tracks were evaluated using a Zeiss Axioscope A1 optical microscope and the Sloan Dektak III profilometer by moving a diamond-tipped stylus with 2 μm radius, respectively.

3.3.2 XRD Diffraction

X-ray diffraction (XRD) is a non-destructive technique used to evaluate the structure and crystallinity of materials at the atomic or molecular level. Only crystalline or polycrystalline materials can be measured using this approach. XRD occurs when X-rays are scattered by a periodic structure order. X-rays have wavelengths in the order of 0.01 to 10 nm. When these rays scatter from a material with a determined structure, interference occurs (either constructive or destructive), causing a pattern of higher and lower intensities. The incident X-ray beam is diffracted different planes of the material. The path length magnitude depends only on the distance between the crystal planes and the incident angle of the X-ray beam. This is given by the Bragg equation:

$$n\lambda = 2d\ sin\theta \qquad 3.1$$

Constructive interference occurs only if the path difference ($2d\ sin\theta$) is a multiple (n=1, 2, 3, …) of the wavelength used, λ, of the X-ray beam. The Bragg equation allows to calculate the distance, d, between the lattice planes of the material. 2θ is defined as the angle between the incident and the diffracted beam. The X-ray diffraction of different planes in a material is described in Figure 3.2. The diffractograms resulting from XRD measurements are presented in a plot of X-ray intensity *vs.* the angle 2θ, which is considered the fingerprint of a sample.

With the XRD technique, it is possible to identify the material and calculate the relative quantity of different components presented in it (phase composition). The preferred orientation, crystallographic texture, and information of the unit cell (lattice parameters, crystalline size, and strain) can be also evaluated.

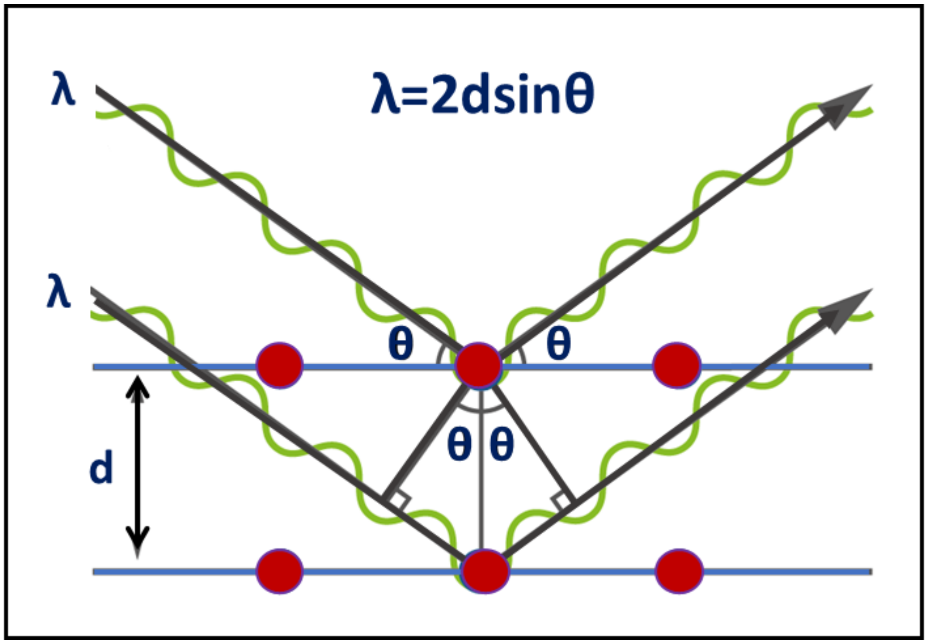

Figure 3.2 X-ray diffraction.

In this work, the crystallographic structure and the microstructural phase were analyzed by two XRD devices. The first set of samples were measured using a Bragg-Brentano (BB) geometry on the Philips X'PERT X-ray Diffractometer with a Cu target (Kα line, $\lambda = 0.154$ nm) operated at 30 kV and 40 mA. A complementary analysis of the first set of samples and a complete study of the second set were carried out under grazing incidence X-ray diffraction (GIXRD) configuration (see Figure 3.3) on the Bruker D8-Discover X-ray diffractometer with a Cu target (Kα radiation, wavelength $\lambda = 0.154$ nm) operated at 40 kV and 40 mA, a divergence slit of 0.2 mm, a parallel collimator and a Göbel mirror were used to obtain a parallel beam configuration. The crystallographic structure, the lattice parameter, the crystallite size, and the texture coefficient of TiN coatings and interface layers were determined using a grazing incidence geometry to extract information from the coating and interface, separately. The texture coefficient of the coated samples was evaluated by the intensity ratio of the three main *hkl* planes as $(I_{(hkl)}/I_{0(hkl)})/[(1/n)\Sigma(I_{(hkl)}/I_{0(hkl)})]$, where $I_{(hkl)}$ is the measured relative intensity of the (*hkl*) diffraction plane, and $I_{0(hkl)}$ is the relative intensity from all of the *(hkl)* planes in the coating extracted from the reference powder diffraction file corresponding to TiN phase [205]–[207]. The crystallite size was estimated by Williamson-Hall method. Additional software such as EVA and Jade was used during the XRD analysis to determine phase composition, *d*-spacing and peak intensity.

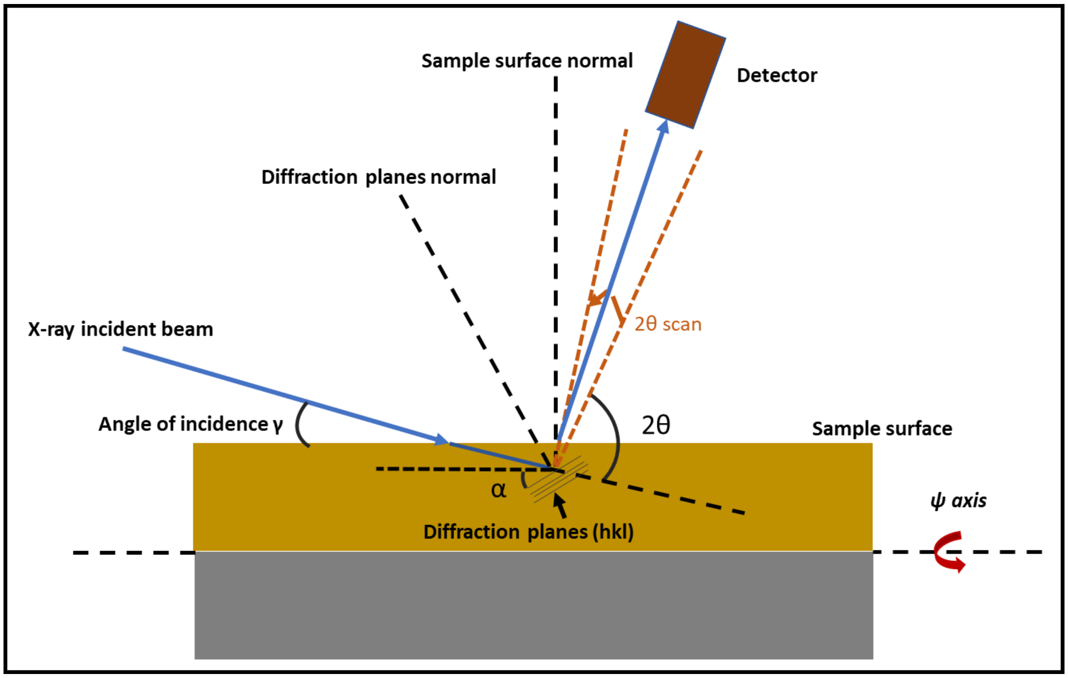

Figure 3.3 Schematic representation of X-ray diffractometer with a grazing incidence configuration.

3.4 Mechanical characterization

3.4.1 Residual stress

The determination of RS within coatings has been extensively investigated for thin and thick coatings. The study of RS in polycrystalline thin coatings is commonly addressed using X-ray diffraction techniques or the substrate curvature (Stoney) approach.

X-ray diffraction is a non-destructive technique for precisely determining the RS on the surface of bulks or through coated samples. In diffraction stress investigations, the interatomic lattice spacing, and thus the elastic strain, are measured directly [208].

Typically, the stress gradients are evaluated only through the coating thickness; however, external parameters to the coating fabrication can create a stress gradient through the coating's in-plane surface. Therefore, the understanding of anisotropic properties is critical. Some authors reported an anisotropic RS behaviour on TiN coatings [167], [209]. Perry et al. [167] reported 20% anisotropy effect on RS values using XRD measurement with fixed incidence multiple *hkl* planes. The anisotropy behavior has been related to the variation of the experimental values corresponding to X-ray elastic constants (XECs). XECs are different for each *hkl* plane on anisotropic crystals due to the feature of elastic constants, and they can be calculated by taking into account the plot (a *vs. f(ψ)*), where *f(ψ)* is a function of the single-crystal elastic constants ($S_1 = \frac{-\nu}{E}$ and $\frac{1}{2}S_2 = \frac{(1+\nu)}{E}$). [209]. Therefore, the application of the multi *hkl* method using a grazing incidence angle (GIXRD) geometry is recommended for this particular study.

The RS at the surface and at the interface, and the RS profiles through the coating-interface-substrate from the second set of samples were measured by GIXRD using the multireflection method [148], [150], [210] to analyze the effect of each plasma process on the stress level. The system used to perform these measurements was the Bruker D8-Discover X-ray diffractometer, with a Cu target (Kα radiation, wavelength $\lambda = 0.154$ nm) and a Göbel mirror, to obtain a parallel beam configuration.

The RS profile measurements through coated systems performed by GIXRD using the multireflection method evaluate only a specific volume of a sample determined by the incidence angle, which is limited by the radiation absorption. The intensity of the incident beam is strongly dependent on the linear coefficient of absorption μ of the material according to the exponential law given by:

$$I_x = I_0 exp(-\mu x) \qquad 3.2$$

where x is the length of the ray path in the material and I_0 is the intensity of the incident beam (see Figure 3.4).

The strain ε is measured through GIXRD RS measurements at different angles ψ under the constraint of a small and fixed penetration depth value, τ. The range of angles ψ that can be evaluated is limited by the specific diffraction geometry. In the multireflection method, which is itself based on the conventional $sin^2\psi$ method, the angle ψ for a set of $\{hkl\}$ planes is given by:

$$\psi_{(hkl)} = \theta_{(hkl)} - \alpha \qquad 3.3$$

where $\psi_{(hkl)}$ is the angle between the scattering vector and normal to the surface, $\theta_{(hkl)}$ is the diffraction angle, and α corresponds to the incidence angle.

In order to perform depth profiles, GIXRD can be used to determine stress profiles along a perpendicular direction to the sample surface, z. The stress tensor is dependent on the X-ray penetration depth. Therefore, the strain is evaluated at different ψ and φ as a function of the penetration depth, τ. The penetration depth for an infinitely thick and homogeneous sample corresponds to 63% of the diffracted signal from a volume restricted by depth below the sample surface [165]. The penetration depth is given by:

$$\tau = \frac{sin\alpha\ sin\beta}{\mu\ (sin\alpha + sin\beta)} \tag{3.4}$$

where α and $\beta = \theta - \psi$ are the incident and exit angles of the incoming and diffracted X-rays, respectively. This equation is valid for $\alpha \geq 1$ [211]. The information depth $\bar{z}$, calculated over reflecting grains of a specific material, must also be averaged with the weight of the beam intensity over depth *z* under the surface. The information depth, also known as the effective depth $\bar{z}$ can be understood as the mean value of the *z*-depth, reduced by an attenuation factor:

$$\bar{z} = \frac{\int_0^t z exp(-z/\tau)dz}{\int_0^t exp(-z/\tau)dz} = \tau - \frac{t exp(-t/\tau)}{1 - exp(-t/\tau)} \tag{3.5}$$

for limited *t* or τ for *t*→∞.

The RS profiles through the coating-interface-substrate layers were measured using angles α = 1°, 2°, 3°, 5° and 10°, which cover penetration depths of 0.3 µm, 0.9 µm, 1.5 µm, 3 µm, and 5 µm, respectively. The penetration depth vs. $sin^2\psi$ for a Cu wavelength is presented in Figure 3.4. It shows that the stresses can be measured for different layers under the sample surface by setting different values of the α angle [212]. The penetration depth with α = 1°, 2° was calculated with the μ from the TiN coating because it was the material under study at those incidence angles. Then, the penetration depth for α = 3° was calculated for the coating and substrate using the μ of both materials separately. Given the average value of both τ, it was assumed that the penetration depth reached the interface zone since the TiN coatings were approximately 1 µm thick. Finally, for α= 5° and 10°, the μ from the Ti substrate was used.

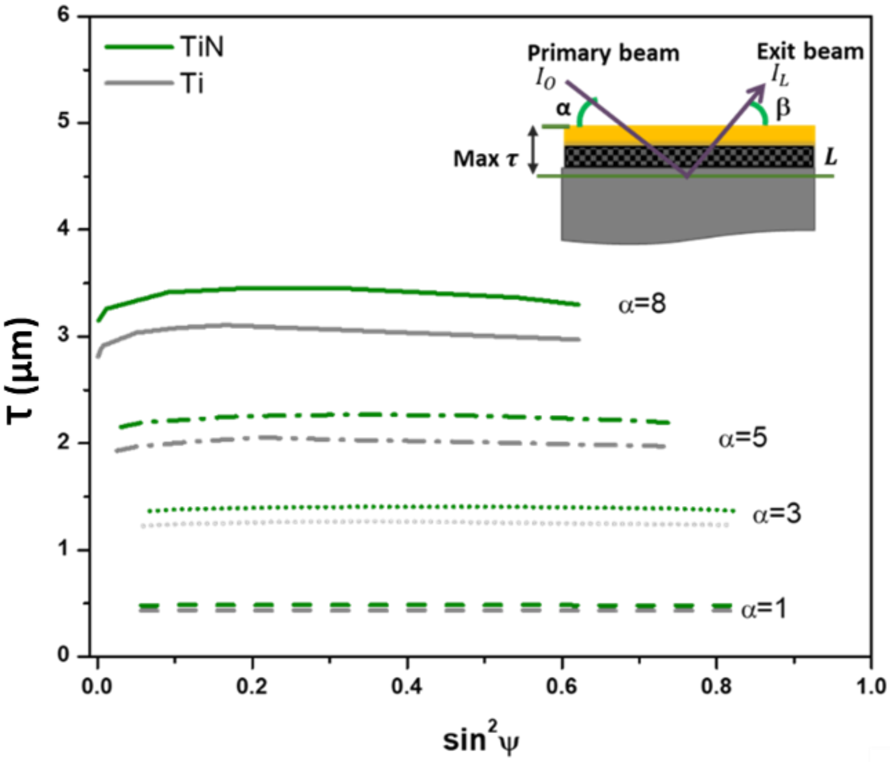

Figure 3.4 Penetration depth vs. $sin^2\psi$ calculated for different α angles using equation with a schematic of a coated sample showing the penetrating (primary) and exit beams and their respective angles.

For measurements done at the incidence angles α > 2°, all diffractograms correspond to the contribution of the coating, interface and substrate, see Figure 3.5. Therefore, there was an overlap of peak positions due to the presence of Ti in both materials and possible additional phases created by the interface plasma treatment. The RS was calculated by applying a deconvolution analysis with the Origin software to extract the 2θ coating and Ti64 peak positions independently. The exact position of the diffraction peaks must be determined with high accuracy, and so it was therefore critical to consider the peak profile and position, as well as the asymmetry of the background [213]. The first step of the peak fitting was to subtract the background of each diffractogram by applying a linear function to the bottom intensities on each side of all the peaks. Then, the center of gravity of each peak was determined by a theoretical function (i.e., Gauss, Person VII, Lorentz or Pseudo-Voigt) of fitting from the intensity profile. In this work the peak fitting was done using the Gauss and Person VII functions. The Gauss function is given by the full width at half maximum of the diffraction peak related to the ratio of the peak area to the peak maximum. The Person VII function is a flexible function for describing the peak profiles, intensities of the measured sample and it is defined by a shape parameter [213], [214]. The peak position used for the RS analyses was obtained after several peak corrections using first, the Gauss function, and then, the Person VII, to enhance the fitting of all peak profiles and intensities.

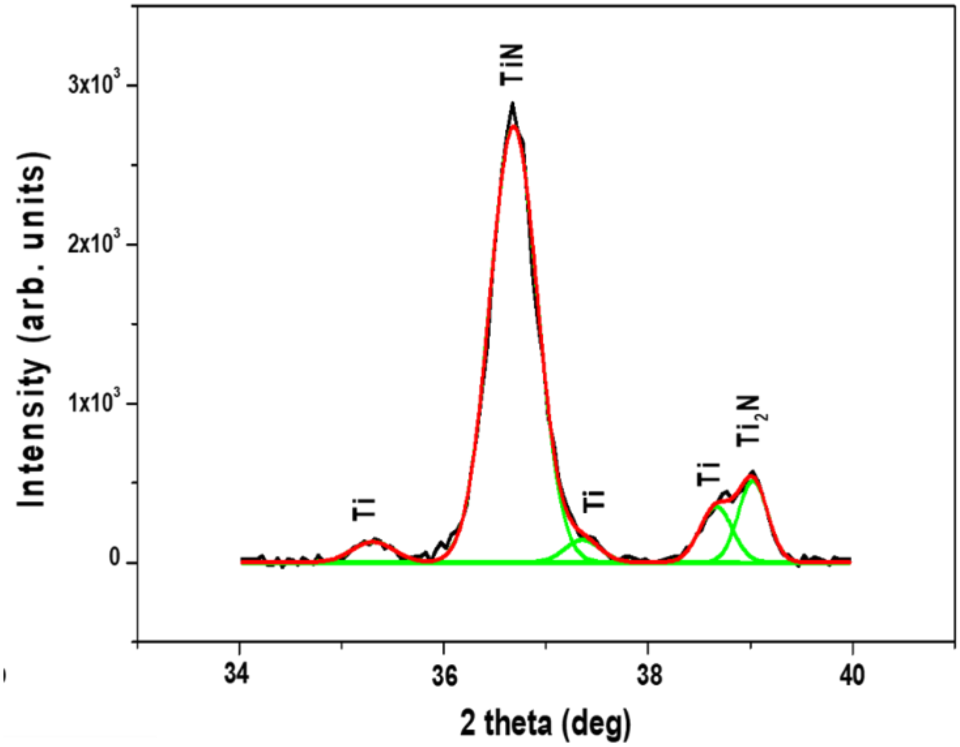

Figure 3.5 Deconvolution of diffracted peaks extracted from a measurement done at α=8° on TiN on Ti-6Al-4V substrate.

Then, for the stress determination, the so-called equivalent lattice parameter is used, $<a(\varphi,\psi)>_{(hkl)}$, and is determined as:

$$< a(\phi,\psi) >_{(hkl)} = \left[F_{ij}(hkl,\varphi,\psi)\sigma\right]a_o + a_o \qquad 3.6$$

where σ is the macro-stress, a_o is the strain-free lattice constant, and $F_{ij}(hkl, \varphi,\psi)$ corresponds to the X-ray stress factor. For cubic crystal structures such as TiN, the equivalent parameter is defined by:

$$< a(\phi,\psi >_{(hkl)} = < d(\phi,\psi >_{(hkl)} \sqrt{h^2+k^2+l^2} \qquad 3.7$$

For hexagonal structures such as Ti-6Al-4V, it is found by the equation:

$$< a(\phi,\psi) >_{(hkl)} = < d(\phi,\psi >_{(hkl)} \left\{ [\tfrac{4}{3}(h^2+hk+k^2)] + \frac{l^2}{(c/a)^2} \right\}^{1/2} \qquad 3.8$$

The σ and a_o fitting parameters can be obtained by adjusting the $<a(\varphi,\psi)>_{(hkl)}$ values of d, c and a used in equation 3.8. The azimuth angle, ϕ, is selected arbitrarily; the ψ angle depends on the diffraction angle for a given reflection *hkl*, and the values of the *c/a* parameter are known from the characteristic lattice parameters of a hexagonal structure. A data adjustment is done by linear regression to obtain a higher quality experimental fitting.

Then, considering the standard equations of X-ray elastic constants (XECs) S_1 and ½(S_2), which are defined as $S_1 = -\upsilon/E$ and $\frac{1}{2}S_2 = (1+\upsilon)/E$, where υ and E are the Poisson ratio and Young's modulus, respectively, and are specific for each family of planes *hkl*. We know that:

$$a_\varphi = \sigma a_0 \left(\frac{1}{2}S_2 sin^2\varphi + 2S_1\right) + a_0 \qquad 3.9$$

Plotting $<a(\varphi)>_{(hkl)}$ versus $F_{ij}\,(hkl,\ \varphi,\ \psi)$, where:

$$F_{ij}(hkl,\varphi,\psi) = \left(\frac{1}{2}S_2 sin^2\varphi + 2S_1\right)\ldots \qquad \ldots.3.10$$

is used to calculate a_o at $\sin^2\varphi$ equal to zero, and to extract the σa_o from the slope of the linear fit of $sin^2\psi$ plot that can be reduced to:[148], [152].

$$\frac{\sigma}{E} = \frac{a_o - a(0)}{2\nu a_o} \ldots\ldots\ldots\ldots\ldots\ldots\ldots\ldots\ldots\ldots\ldots\ldots..\ 3.11$$

3.4.2 Curvature technique

The overall residual stress value of coated substrates can be calculated by the Stoney equation, given as:

$$\sigma = \frac{E_S}{6(1-\upsilon_S)}\frac{h_S^2}{h_C}\left(\frac{1}{R} - \frac{1}{R_0}\right) \qquad 3.12$$

where E_S is the Young's modulus, υ_S is the Poisson's ratio, and h_S and h_C correspond to the thickness of the substrate and coating, respectively. R and R_0 are the curvature radii of the substrate after and before coating deposition. This analysis requires that the samples have certain characteristics, such as: the thickness of the substrate and coating should be smaller than the lateral dimensions; the deformation and rotations should be infinitesimal; the coating thickness should be substantially smaller than that from the substrate; both materials should be homogeneous and the stress and radius of the curvature should be constant on the whole surface of the plate [215].

In this work, a Tencor Flexus Model 2900 instrument, a laser deflection technique was used to measure the substrate curvature before and after coating deposition on a silicon wafer or thin Ti64 substrate by measuring the curvatures at room temperature in the air atmosphere along the substrate to determine the RS for the first set of samples.

3.4.3 Nanoindentation

The nanoindentation technique is used to measure the mechanical properties, such as the hardness, *H,* and the reduced Young's modulus, E_r, of surfaces on a microscopic scale. During testing, an indenter, which is a diamond tip shaped as a pyramid or as a sphere, is pushed with a small load onto the surface of the material. The final depth of the indentation is varied between hundred of nanometers to a maximum of 4 microns according to the material and the test parameters. The hardness of the sample is obtained by measuring the force, *F*, required to push the indenter tip into the material to the indentation depth. For their part, the elastic modulus or the stiffness, *S*, of the material are calculated by observing the degree to which the material returns to its previous shape (see Figure 3.6). Additionally, by observing the fracturing around the indentation, an indication of the fracture strength (fracture toughness) of the surface can also be made.

Hardness, *H*, and reduced Young's modulus, E_r, on interface layers and on coatings were determined by depth-sensing indentation (TI950 Triboindenter, Bruker) using a Berkovich pyramidal tip with an area function calibrated by a fused silica standard. Individual *H* and E_r values were obtained by applying the widely accepted Oliver and Pharr analysis method [216]. For each sample, the coating or interface layer properties were obtained using the ISO standard 14577 part 4 [217] methodology from the *H* and E_r depth profiles measured using three 10 x 10 indentation matrices on each sample with peak loads varying from 100 to 9000 μN.

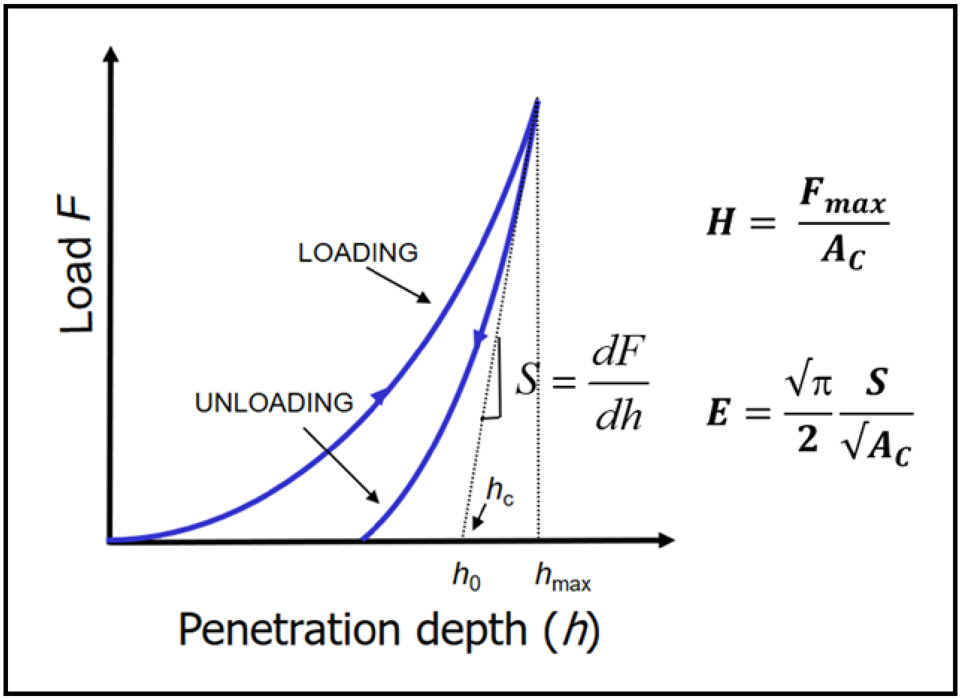

Figure 3.6 Typical nanoindentation curve from loading and unloading vs. penetration depth on the coated sample.

3.4.4 Tensile test

Tensile testing is a destructive test process that provides information about the tensile strength, yield strength (at yield and at breakpoints), ductility of the metallic material, tensile strength, tensile modulus, tensile strain, elongation, and percent elongation at yield and at breakpoints. Tensile test experiments measure the force required to break a sample and the elongation tolerated by the sample [218]. In coated materials, the evaluation of the surface provides great insight into the coating fracture properties, such as crack onset strains (COS) and crack evolution.

In this study, samples of TiN coatings on Ti-6Al-4V with different interfaces and ZrN/TiN multilayers on nitrided Ti64 were evaluated. Micro tensile tests were carried out in tension with a Kammrath & Weiss ± 5 kN micro tensile apparatus. The displacement rate applied was 2.5 µm/s and the macroscopic strain was measured with a Keyence LS-7030M optical extensometer (Keyence). The test was divided into two different test configurations: i) continuous test, and ii) interrupted test. The goal of the continuous configuration was to assess the stress-strain (S-S) diagrams and evaluate the macroscopic mechanical properties of treated and coated specimens, such as ultimate the tensile stress (UTS), Young's modulus (E), the yield stress (YS), and the strain to fracture. The samples tested were continuously recorded at 1 image per second by means of a custom LabVIEW (National Instruments, Austin, TX, US) program synchronized with the tensile machine. The strain fields provided information regarding the evolution of strain localization in the elastic and plastic domains of Ti-6Al-4V exposed to an axial force.

The goal of the interrupted configuration was to obtain high resolution images of the specimen’s surface at increasing displacements during the test to detect COS and to evaluate crack evolution and roughness. The specimens evaluated by the interrupted configuration (Figure 3.7b) were tested under a Laser Scanning Confocal Microscope (LSCM) Olympus LEXT OLS4100 apparatus to obtain a series of intensity laser images and the corresponding topographic map. The spatial resolution was set to 0.15 µm/pixel. The loading process was performed with a crosshead (cyclical) displacement rate of 2 µm/s. Images and height maps were acquired at increasing displacement and load values corresponding to higher (controlled) stress and strain applied to the specimen. During the test, each specimen was loaded in ranges of 25 N and by displacement steps of 50 µm past the elastic limit, YS, until complete failure to ensure the detection of crack appearance and observe any crack evolution. The crosshead displacement was maintained during image acquisition to keep the coating cracks open, making them as visible as possible. The crack density curves, which are expressed as a number of cracks/mm, were evaluated from each image by counting the intersections between six vertical lines, with a length of 640 µm and cracks. The crack density increases with the increased load until it reach a saturation crack number and spacing between two cracks in the surface of the material, then the failure occurs defined by the total strain in the S-S curve.

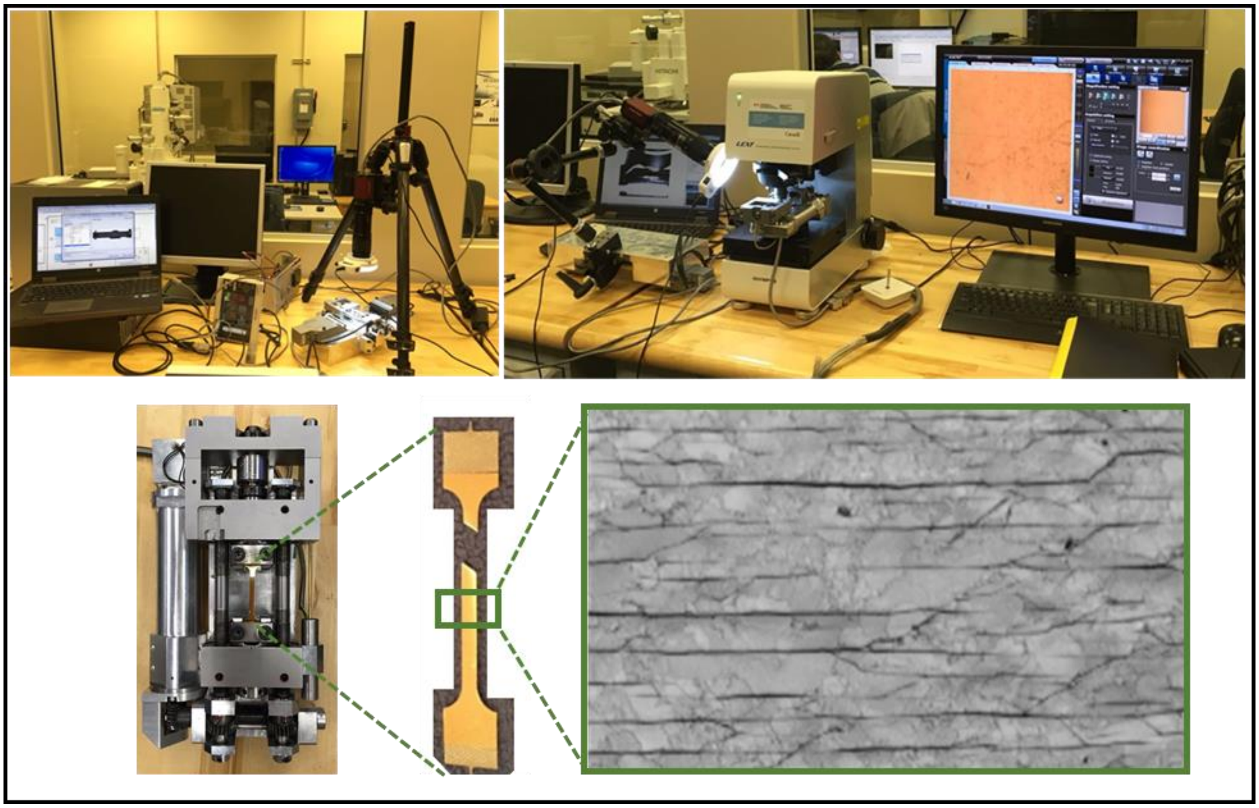

Figure 3.7 The two in situ tensile test configurations: a) continuous, b) interrupted tests, and c) dog-bone sample coated sample being tested and after failure with a close up to surface cracks.

3.4.5 Scratch test

Scratch testing is a technique used to evaluate the adhesive and cohesive strength of hard coatings. For this study, the scratch test was generally used to quantitatively evaluate the adhesion of coatings to substrates. It is important to mention that the scratch test was performed according to the ASTM C28 standard [219] and the Advanced Ceramics Committee [220]. The adhesion strength of a coating is the force needed to separate it from a substrate [221]. Optimization of the adhesion strength between the coating and substrate is a key factor in the functionality of a coated component because it is usually the primary failure mechanism in a coating-substrate system [220].

Coating adhesion is one of the most difficult properties to quantify in a coated system, mainly because its response to a scratch load is not a basic property, but a response of a system to an applied test condition [222]. The quantitative scratch adhesion system test used for this work is shown in Figure 3.8.

The scratch test is performed using a diamond indenter with a rounded diamond tip (Rockwell), which is applied across the sample surface under an increasing normal load with a constant speed. The load force management can use a constant or a progressive mode. A progressive mode load refers to a force that increases stepwise or linearly.

The European standard prEN 1071-3 [223], described as the measurement of "critical load" values associated with characteristic failure events occurring when a stylus is drawn across the coating with a normal load applied. According to [223], there exist three types of characteristic failure occurring in scratch testing: L_{C1} corresponds to the forward chevron cracks at the borders of the scratch track, it is form at the closest end of the event to the scratch track start. L_{C2} is the forward chevron cracks at the borders of the scratch track, with local interfacial spallation or with gross interfacial spallation; it corresponds to the failure event that occurs first, and at the closest end of the event to the scratch track start. Finally, L_{C3} is the gross interfacial shell-shaped spallation occurring at the first point where the substrate can be seen at the centre of the track in a crescent that goes completely through the track.

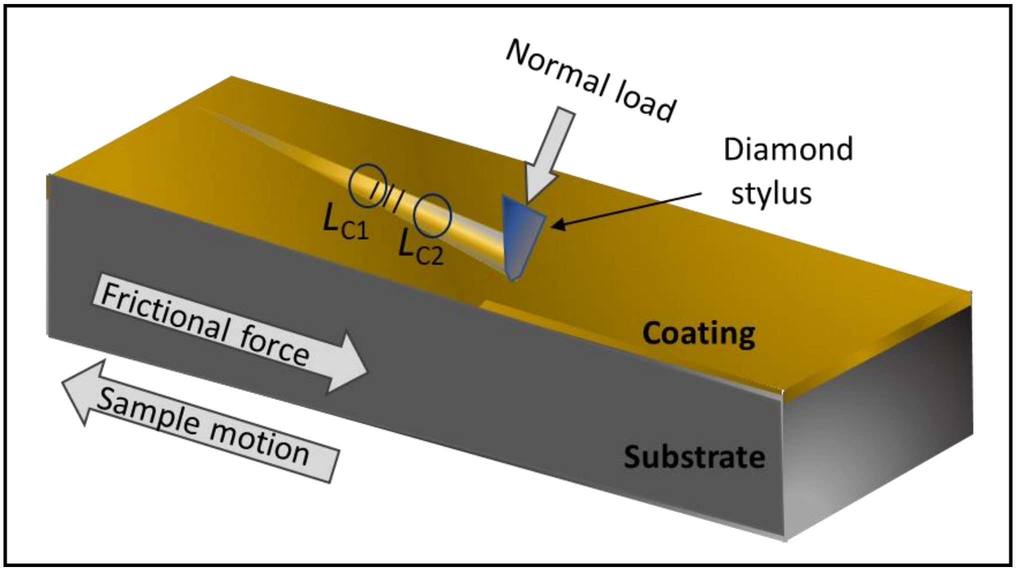

Figure 3.8 Overview of a scratch testing on coated sample.

In this work, the cohesive failure of the coating, known as the critical load 1 (L_{C1}), and the coating adhesion or critical load 2 (L_{C2}) were evaluated using a Micro-Combi Tester apparatus (Anton Paar). A Rockwell C indenter with a 200 µm tip radius was used under a progressively increasing load from 0.03 to 30 N, with a speed of 5 µm/s over a length of 9 mm. L_{C1} and L_{C2} are presented in

Figure 3.9. L_{C1} was determined as the normal force where the first crack across the scratch track was observed, while L_{C2} was considered as the point where delamination of the coating occurred.

For a hard coating on a softer substrate, the critical load is identified when cracks and deformed regions are observed, and then, when spallation and buckling failure modes result from interfacial detachment. Finally, for the case of hard coatings on hard substrates, the Lc considers the chipping observed in the scratch test as almost identical to the lateral fracture observed in the scratch testing of bulk ceramics. Technically, besides the adhesion between the substrate and coating, Lc, also depends on the tip radius, the loading rate, and the substrate and coating mechanical properties such as the hardness, the fracture strength, the modulus of elasticity, damage mechanisms, the microstructure, the RS in the coating, and the surface roughness. Therefore, the measured Lc allows one to compare different degrees of adhesion [224].

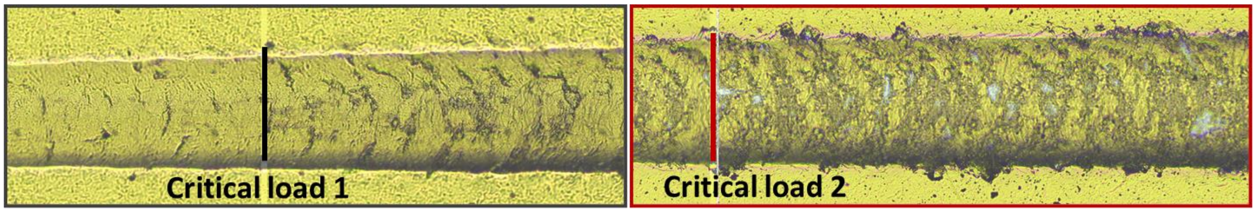

Figure 3.9 Optical images present L_{C1} and L_{C2} of TiN coating.

3.5 Wear test

Wear resistance is one of the most important tribo-mechanical properties of materials. Wear is defined as the surface damage or loss of material from one or both solid surfaces which are in a sliding, rolling, or impact motion relative to one another. Wear can occur in different mechanisms, such as adhesive-, abrasive-, fatigue-, impact by erosion and percussion-, chemical- or corrosive-, and electric-arc-induced- wear.

The sliding wear tests are done by putting a known material, normally in the form of ball, against a horizontally mounted sample, with both materials being in contact and in relative motion. This test was used during this thesis work to measure the wear coefficient, W, and the friction coefficient, μ, of the coating from set 1 including single-layers and multilayer systems.

The wear configuration used during this work was the ball-on-flat test [225]. It has a linear configuration with bidirectional motion contact. It consists of a reciprocating horizontally mounted flat specimen that slides against a stationary ball-shaped upper specimen.

Wear analyses use the Archard equation given by [226]:

$$W = \frac{s * P}{V} \tag{3.13}$$

where V corresponds to the worn value, s is the sliding distance, P is the applied load and W is the wear coefficient.

In this work, the W value was evaluated using a linear reciprocating ball-on-flat tribometer (see Figure 3.10). Tests were performed at a room temperature of 295 K and 40% R.H. A normal load, F, of 3 N applied to an alumina ball (6.35 mm dia.) used as a counterpart material at a frequency of 2.5 Hz resulted in a linear speed of 5 cm/s, for a total distance, s, of 200 m.

The wear rate of a material is dependent on the counter face or material pair, the surface preparation, and the operating conditions. The rate for a material pair is normally presented in terms of the nondimensional wear coefficient. Wear rate is also presented in terms of a wear factor defined as the wear volume per unit applied normal load and per unit sliding distance (mm^3/Nm).

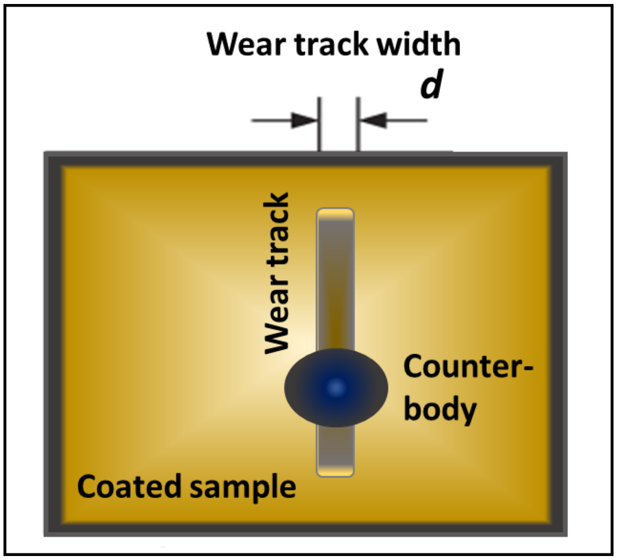

Figure 3.10 Top view of linear reciprocating ball-on-flat wear configuration [226].

CHAPTER 4 ARTICLE 1: EFFECT OF PLASMA INTERFACE TREATMENT ON THE MICROSTRUCTURE, RESIDUAL STRESS PROFILE, AND MECHANICAL PROPERTIES OF PVD TIN COATINGS ON TI-6AL-4V SUBSTRATES

E. J. Herrera-Jimenez, E. Bousser, T. Schmitt, J.E. Klemberg-Sapieha, L. Martinu

Department of Engineering Physics, Polytechnique Montréal, Box 6079, Station A, Montreal H3C 3A7, Quebec, Canada

The article was accepted in Surface and Coatings Technology (March 2021)

4.1 Abstract

Interface engineering is essential to enhance and to maintain the performance of protective coatings on metallic substrates. Plasma pre-treatments and coating deposition processes have shown to be an ideal solution to improve Ti-6Al-4V alloy mechanical and tribological properties, while enhancing components' durability. In the present work, we study model Titanium Nitride (TiN) coatings with three interface engineering surface treatment approaches using: a) Argon plasma, b) Titanium implantation, and c) plasma surface nitriding. In particular, we investigate the influence of the plasma pre-treatments on the microstructure, mechanical properties, especially residual stress (RS) and adhesion, of TiN coatings on Ti-6Al-4V substrates. X-Ray Diffraction, Transmission Electron Microscopy, and Transmission Kikuchi Diffraction were used as complementary techniques to evaluate the crystallographic and microstructural properties of the interfaces created by the three pre-treatment methods in order to elucidate their effect on the evolution of microstructure, hardness, RS and adhesion. The RS study involved surface and depth profiles through the coating-substrate system. Compressive RS values were found to vary between -1 GPa and -4 GPa throughout the TiN coatings, and from -0.2 to -0.8 GPa across the different interfaces. In addition, a strong RS anisotropy in dependence on the way how the substrate has been fixed to the holder (rigidly clamped or freely attached) shows a significant difference in the RS with a deviation of more than 100% in dependence on the orientation of coated samples during the XRD measurements. Experimental results show that Ar plasma and Ti implantation form interfaces with (200) and (111) preferential orientations within the TiN layers that exhibited a hardness of up to ~29 GPa and a Young's modulus of ~350 GPa.

4.2 Introduction

Titanium (Ti) alloys are widely used for automotive, aerospace, and biomedical applications due to their high strength-to-weight ratio, good fatigue life, and high biocompatibility. However, Ti alloys exhibit relatively poor tribological properties such as low wear-resistance and unstable coefficient of friction. Therefore, surface engineering on Ti alloys using different approaches has been proposed to enhance their mechanical and tribological characteristics by controlling the composition, microstructure, and stress [49], [80].

The use of an optimal surface pre-treatment before hard coating deposition onto Ti alloys, for example Ti-6Al-4V, is critical in order to delay or to avoid coating fracture, delamination, and excessive wear [38], [80], [227]–[229]. Therefore, modifying the physical and chemical properties of the interface between coating and substrate, creating an interfacial layer (interface) can enhance adhesion strength, increase hardness, promote crystalline texture, and induce RS gradients into the substrates [62], [230]. The most frequent surface physical vapor deposition (PVD) pre-treatments include ion bombardment, nitriding, and ion implantation processes.

Ion bombardment using a noble gas (e.g., Ar) leads to sputtering, heating and structural rearrangement of the surface atoms, while influencing the properties of the substrate and of the subsequently deposited film [51]. Pizzorni *et al.* showed that Ar^+ bombardment of Ti-6Al-4V gives rise to a reduction of surface micro-roughness, providing enhanced adhesion [52]. B. Jones *et al.*, presented a study of Ar plasma pre-treatment on stainless steel evaluating the microstructure and delamination resistance of DLC films. It was shown that bias voltage in a range between -300 V and -450 V leads to a removal of contaminants of the substrate surface, while a bias voltage of about -600 V induces formation of a nanostructured substrate surface with clear differences in packing arrangement between different areas. In addition, it was shown that the use of Ar plasma pre-treatment significantly influences the coating structure [231].

In the nitriding process, the processing time and temperature have significant effects on the composition and properties of the nitrided Ti-6Al-4V [232], [233]. Typically, nitriding at high temperature forms a nitrogen diffusion zone Ti(N) up to several microns (depending on the process time and treatment conditions), which consists of an interstitial solution of nitrogen in the hcp α-Ti phase [86], [94]. Even though the diffusion zone on Ti alloys has shown a minimal microstructure and phase composition modification [233], it enhances the hardness through a depth profile, which subsequently provides an optimal support for the TiN coatings.

Finally, during the ion implantation applied in conjunction with the High-power Impulse Magnetron Sputtering (HiPIMS) process [17], [56], the substrate is bombarded with accelerated metal ions that penetrate under the substrate surface (generally < 100 nm) [80], [234]. Metal ions, for example Ti ions, have a high bonding affinity and can be incorporated at lattice sites of the substrate as replacements or forming additional phases [62]. The ion implantation can modify a region of several micrometres into the substrate surface due to atomic peening and surface-region amorphization [80]. In numerous works, varied species, such as O, Ca, P, B, C, He and N implanted in Ti have been explored [31]–[34]. Implementation of these species has been shown to lead to an increase in hardness of the alloy and to a reduction of the coefficient of friction due to a homogenization of the α- and β-phases and formation of nitride, oxide, or carbide precipitates on the surface [35], [36].

Sputter-deposition of nitride coatings, particularly TiN, onto Ti-6Al-4V substrates is used in various industrial applications due to their attractive tribo-mechanical properties [12], [169]–[171]. The coating's microstructure is essential for the final performance of the coated component. Specific microstructural characteristics can be controlled during deposition by temperature, gas pressure, and the delivered energy flux through ion bombardment [235] according to the Structure Zone Model [71], [72]. Surface morphology of TiN coatings deposited by PVD frequently exhibits dense columnar grains. In the literature, TiN growth and texture mechanisms in terms of the growth kinetics, with consideration of the surface migration of adatoms [177], or of the thermodynamics and the competition between the surface free energy and the strain energy [178] have been described. The texture of TiN can be transformed from randomly oriented to (110) preferentially oriented, and then to a pronounced (111) orientation with increasing the coating thickness or increasing ion bombardment [236]. It has been reported that TiN coatings with preferred orientation along the [111] or [100] crystallographic directions can influence the mechanical properties (i.e., the elastic modulus along [111] is lower than along [100]) [175], [176]. However, the effect of possible implantation of energetic species below the coating surface and the out-diffusion of species from the bulk or interfacial layer to the TiN coating, should also be considered.

Besides the optimization of microstructure, the presence of compressive RS in the interfacial layers and coatings has a strong impact on the performance and durability of the coated component. In the last 30 years, the coating's RS measurements have been performed by X-Ray Diffraction (XRD) techniques [134], [164]–[166]. Considerable efforts have been made to develop different approaches to measure and analyze RS on coatings and multilayer systems [148]–[154]. Recently, Abadias et al. [134] presented a review on the main RS evaluation methods, describing the RS evolution in varied coating systems, including the problems and the solutions of coatings for aeronautical applications.

Components for industrial applications have different geometries, which, in addition to the parameters used during deposition processes, may also influence the coated part mechanical behaviour, for example, the RS state. Typically, the stress gradients are evaluated only through the coating thickness; however, external parameters to the coating fabrication can create a RS gradient through the coating's in-plane surface. Therefore, the understanding of anisotropic properties is critical. Perry et al. [167] described an anisotropy effect on RS values using XRD measurements with fixed incidence multiple *hkl* planes. The authors have shown a 20% difference in RS values based on the analysis of experimentally determined X-ray elastic constants (XECs) calculated considering the plots ($a(\psi)$ *vs.* $f(\psi)$), where $a(\psi)$ is the lattice parameter in direction (ψ) and $f(\psi)$ is a function of the single-crystal elastic constants (S1 and $\frac{1}{2}$S2). References [36] and [48] reported the XEC analyses on anisotropic materials such as TiN, HfN, ZrN and NbN coatings using Voight, Reuss, Kroner or modified Serruys approaches. The background of the X-ray RS measurements and the XECs calculations for coatings has been described in references [128], [164], [167], [209], [237]. Characteristic values of RS in TiN films were reported to range from ~1 GPa in tension to 10 GPa in compression, depending on the deposition parameters, substrate, and final coating thickness. TiN on Ti-6Al-4V typically exhibits RS of ~2 GPa to ~6 GPa in compression.

Numerous examples cited above illustrate the overall attempts to relate the film growth conditions with the tribo-mechanical properties and performance of the protective coatings in terms of the microstructure, while the average RS has been generally considered an important parameter to optimize the coating adhesion. However, because of the difficulty to compare the data from one study to the other due to a large number of intervening effects, there is a lack of clear understanding of the influence of the interface layers on the detailed microstructural characteristics and properties of the resulting films, in particular the RS and the related stress depth profiles.

In response, and motivated by the needs and requirements on the protective erosion-resistant coatings for aircraft engine components [12][16], the present study focuses on an in-depth correlation between surface treatments (creation of interface layers) and the growth and characteristics of hard polycrystalline protective films, while using TiN on Ti-6Al-4V substrates as a model system. Specifically, we compare three different pre-treatments, namely Ar plasma, plasma nitriding and Ti implantation, with respect to the TiN film characteristics assessed by a multi-technique approach combining XRD, Transmission Kikuchi Diffraction (TKD), Transmission Electron Microscopy (TEM), nanoindentation, and scratch-testing. We particularly investigate the influence of sample geometry and sample fixation on the substrate holder since this can generally lead to a known but not sufficiently quantified non-uniform distribution and anisotropy of RS through the coated system – This is accomplished by using different sample orientations during the XRD measurements, while this knowledge is very important in order to ensure the durability and mechanical performance of coated components exposed to different external loads. Finally, we study the effect of interface on the RS depth profile with a perspective to judiciously control the stress gradients to better mitigate external mechanical solicitation in future protective coating systems.

4.3 Experimental methods

This section describes the sample preparation and characterization techniques used to evaluate the interface layers and TiN coatings on Ti-6Al-4V substrates; this first includes the determination of the RS profiles in relation to XRD measurements, nanoindentation and scratch testing, followed by the microstructural assessment by XRD, TEM, and TKD.

4.3.1 Sample preparation

Ti-6Al-4V alloy (abbreviated Ti64 in the rest of the article) with two sample geometries was used as substrates for specific coatings analyses, namely flat rectangular coupons (50x25 mm^2) and disc-shaped specimens (25 mm diameter), all ~1 mm thick. Rectangular coupons were employed for the microstructural characterization, nanoindentation, RS profiles, and scratch testing, while the discs were used only for the RS measurements.

1) Before deposition, the substrates were polished and cleaned in several steps: a) grinding using SiC paper with 400 to 2000 grit and continuous water-spraying in a Struers LaboPol-5 polishing machine (stage rotation speed ~250 rpm), b) surface mirror-like finishing using colloidal silica (particle size 0.04 μm), H_2O_2 and distilled water, and c) ultrasonic pre-cleaning in acetone and isopropyl alcohol for 30 min.

2) Plasma-based pre-treatments and depositions were performed in a magnetron sputtering system (30 liters volume) turbomolecularly pumped to a base pressure of about 10^{-5} Torr. The system was equipped with a Pinnacle Plus (Advanced Energy) power supply connected to a magnetron head holding a 50 mm diameter Ti target (99.995% purity). An RF (Seren) or HiPIMS (Melec GmbH) power supplies was connected to the sample holder (150 mm diameter) to control the bias voltage, while the substrate temperature, T_s, was kept at 390±10°C and the rotation speed was ~20 rpm. For each deposition four substrates were mounted on the sample holder as shown in Figure 4.1: The substrates were either solidly clamped (CL) to the holder to restrict their thermal expansion, or they were freely held by a clip only on one side (not clamped – NC) allowing for thermal expansion.

The surface engineering process consisted of three main subsequent steps:

a) All samples were first Ar sputter-cleaned for 30 min at a negative bias of -600 V and a pressure of 5 mTorr. The sputter-cleaning was used to remove the substrate's surface native oxide layer while promoting surface activation (temporary increase of surface chemical reactivity).

b) During the second step, three different sets of samples were prepared using the following pre-treatments providing specific interface layers, namely:

Pre-treatment 1: Ar plasma treatment was applied for 30 min (in addition to the previous 30 min of Ar sputter cleaning) in an Ar atmosphere at a negative bias of -600 V at a pressure of 5 mTorr.

Pre-treatment 2: Plasma nitriding was applied in two stages, first with an additional surface activation for 30 min using an Ar/H_2 mixture ($Ar:H_2$ =4:1) at a negative bias of -400 V and a pressure of 400 mTorr, followed by a second nitriding step performed in an N_2/H_2 mixture ($N_2:H_2$ = 4:1) for 120 min at a negative bias of -400 V and a pressure of 400 mTorr.

Pre-treatment 3: Ti implantation was performed during 120 min using a HiPIMS power supply with two channels: one connected to the substrate holder and kept at a negative bias voltage of -600 V, and the other one connected to the Ti target while using a negative cathode voltage of -

630 V. The applied average power in each channel was 400 W with a pulse length of 55 μs and a frequency of 300 Hz.

c) Finally, during the third step, the TiN coating was deposited onto the pre-treated substrates from the procedures in (b) in an Ar/N_2 atmosphere at a pressure of 5 mTorr and a flow rate ratio of Ar:N_2 = 5:1, while the Ti target was sputtered using a P-DC discharge at a frequency of 300 kHz, a reverse time of 0.4 μs, and an average target power of 225 Watt (1.0 A). A constant RF-induced negative bias of -120 V (~300 W) was applied to the sample holder.

The different samples in this study are named according to the interface layers after pre-treatment. They are referred to as *Ar-plasma*, *Ti-impl* (for Titanium implantation), and *Nit* (for nitrided). Consequently, the coated specimens with the three different interfaces are defined as *TiN-Ar*, *TiN-Ti*, and *TiN-Nit*.

The coating thickness (typically about 1 μm) was determined by a Sloan Dektak III profilometer.

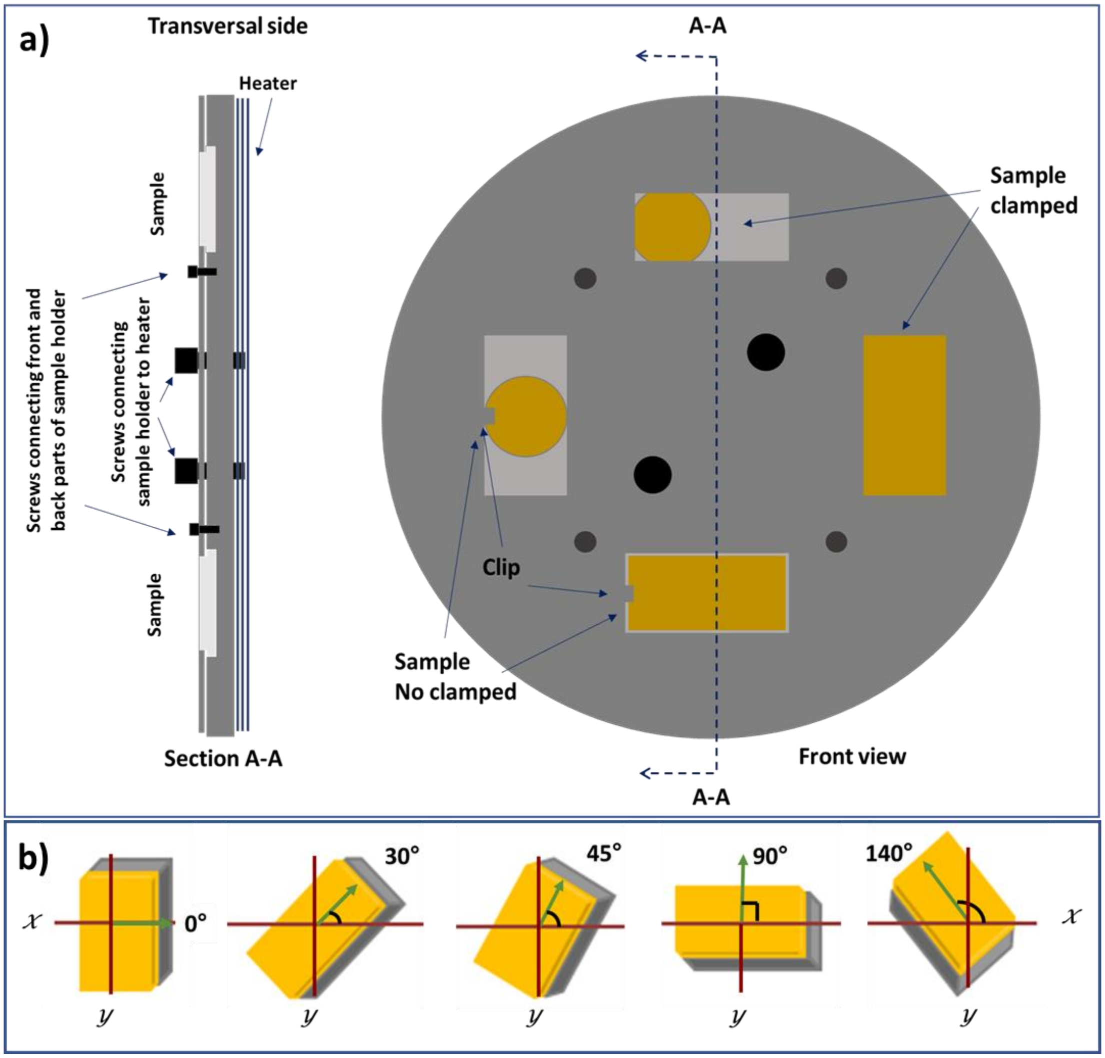

Figure 4.1 Schematic representation of a) stainless steel sample holder, front and cross-section views, with clamped (CL) and freely attached (NC) samples, and b) sample orientation as defined by the green arrow.

4.3.2 Characterization methods

Throughout this study, we have particularly paid attention to the effect of sample orientation when performing the XRD (and hence stress) as well as the scratch test measurements. Specifically, the measurements were performed at five sample orientations of 0°, 30°, 45°, 90°, and 140° as indicated by the green arrow in Figure 4.1b. Sample orientations of 0° and 90° were specifically used for scratch testing. In this case, the direction from the X-ray beam during XRD measurements and from the tip during scratching is described by the X-axis in Figure 4.1b.

4.3.3 Mechanical characteristics

Hardness, H, and reduced Young's modulus, E_r, on interface layers and on coatings were determined by depth-sensing indentation (TI950 Triboindenter, Bruker) using a Berkovich pyramidal tip with an area function calibrated by a fused silica standard. Individual H and E_r values were obtained by applying the widely accepted Oliver and Pharr analysis method [216]. For each sample, the coating or interface layer properties were obtained using the ISO standard 14577 part 4 [217] methodology from the H and E_r depth profiles measured using three 10 x 10 indentation matrices on each sample with peak loads varying from 100 to 9000 μN.

The micro-scratch testing was applied for the evaluation of adhesion and of the cohesive failures at different sample orientations. The cohesive failure of the coating, known as critical load 1 (L_{C1}) where the first crack occurred, and the coating adhesion or critical load 2 (L_{C2}), were evaluated for 0° and 90° sample orientations by micro-scratch testing using a Micro-Combi Tester apparatus (Anton Paar). A Rockwell C indenter with a tip radius of 200 µm was used under a progressively increasing load according to Reference [220], based on the ASTM C1624 – 05 norm, from 0.03 to 30 N with a speed of 10mm/min along a length of 9 mm.

The residual stress (RS) assessment by XRD measurements was carried out using the Bruker D8-Discover X-ray diffractometer with a Cu target (Kα radiation, wavelength $\lambda = 0.154$ nm) and a Göbel mirror to obtain a parallel beam configuration. All measurements were performed using a grazing incidence X-ray diffraction (GIXRD) configuration.

Coatings RS is composed of intrinsic and thermal stresses [238]. While intrinsic stresses originate in the coating deposition process itself, the thermal stresses are generated by a mismatch in Coefficients of Thermal Expansion (CTE) during the cooling of the coated samples post-deposition. Since the CTE for Ti64 and TiN coatings are $\sim 9.0\times10^{-6}$ °C^{-1} and $\sim 9.35\times10^{-6}$ °C^{-1}, respectively, the possible thermal stress generated when depositing at 390°C and cooling to room temperature is below 0.5 GPa. Therefore, since this thermal stress amplitude can be considered constant between the different coated systems in this study, the stress differences that will be observed can be considered to be intrinsic in nature without much contribution from thermal stresses.

In order to accurately determine the RS in the coatings, we first assessed the level of influence of the substrate clamping that may impose additional strain on the substrate-coating system.

Therefore, in our methodology to calculate RS we consider an anisotropic behaviour through the coated system [167]. Specifically, we applied GIXRD using the Multireflection method (MGIXRD) [148], [152] which is based on the conventional $sin^2\psi$ approach. The RS is thus an average of the contributions of several *hkl* planes of the grains on which the X-ray radiation is diffracted. To assure high precision of the RS determination, we performed the three following experiments:

(i) In the first experiment, rectangular substrates were **clamped** (CL) in the sample holder before subjecting them to the three different plasma pre-treatments followed by TiN coating deposition. RS on all such samples was measured for the five selected sample orientations at an X-ray penetration depth of ~0.3 μm using an incidence angle α=1°.

(ii) In the second experiment, the RS was measured on the sets of disc and rectangular substrates that were only plasma pre-treated (not coated) and only TiN coated (without pre-treatment). One set of both substrates was in the CL configuration (as in experiment (i)), while the second set was NC to eliminate any prior load. RS was measured for two sample orientations, 0 ° and 90 °, at a penetration depth of ~0.3 μm using an incidence angle α=1°.

(iii) In the third experiment, the RS profiles through the coating-interface-substrate regions were measured using different incidence angles, α = 1°, 2°, 3°, 5°, and 10°, that cover penetration depths of 0.3 μm, 0.9 μm, 1.5 μm, 3 μm, and 5 μm, respectively. The penetration depth for each incidence angle was estimated by considering the mass absorption coefficients, μ, from the TiN coating and the Ti64 substrate, that influence the X-ray beam when a higher α value is used. At incidence angles α= 3°, 5°, and 8°, the diffractograms reveal the contribution of coating, interface, and substrate. Therefore, an overlap of peak positions occurs due to the α–Ti phase in both materials and possible additional phases created by the interface pre-treatment. The RS was calculated by applying a deconvolution analysis by fitting with Gaussian functions and using Origin software to extract the 2θ positions of the coating and the Ti64 peaks independently. Then, the multireflection method was applied to obtain each RS profile.

RS measurements as well as the characterization of other mechanical properties such as *H*, *Er*, L_{C1} and L_{C2} present an experimental error normally between 5 to 10%.

4.3.4 Microstructural characteristics

XRD measurements of the interface layers and TiN coatings were done using the Bruker D8-Discover X-ray diffractometer with a Cu target (described in Section 4.3.3) to evaluate the crystallographic structure, the crystallite size (CS), and the texture coefficient ($T_{c\,(hkl)}$) [205]–[207]. The GIXRD measurements of the interface layers and coatings were done using incidence angles α=1° and α=3°, respectively, to assess the information from the surface of the substrate, and the penetration depth containing the maximum possible information on the coating. The texture coefficient of the coated samples was evaluated by the intensity ratio of the three main *hkl* planes as $(I_{(hkl)}/I_{0(hkl)})/[(1/n)\Sigma(I_{(hkl)}/I_{0(hkl)})]$, where $I_{(hkl)}$ is the measured relative intensity of the (*hkl*) diffraction plane, and $I_{0(hkl)}$ is the relative intensity from all of the *(hkl)* planes in the coating [205]–[207]. This allowed us to study the variation of texture orientation in relation to the different interface pre-treatments. The average crystallite size of the TiN coatings was estimated by the Williamson-Hall analysis [239].

Focused ion beam (FIB) milling using a Hitachi model FB-2000A microscope was used to prepare sample cross-sections for TKD (or sometimes called transmission-EBSD) analyses and TEM. Each sample was thinned down for electron-transparency to a thickness of around 100 nm using Ga^+ ions at 30 kV. The TKD measurements [240] were performed in a Hitachi Cold FE SU8230 SEM equipped with a Bruker e-Flash HD detector and Bruker Quantax acquisition software. An acceleration voltage of 30 kV was used with a 0.5 nm resolution and step sizes ranging from 4 to 6 nm. The EBSD data was analyzed using Oxford Instruments HKL Channel 5 software while considering the following crystal structures: hcp-Ti with a space group of $P6_3/m2/m2/c$, and fcc-TiN with a space group of $F\,4/m\bar{3}2/m$.

Finally, for the microstructural characterization, the TEM measurements were performed in a Jeol 2100F microscope equipped with a 200 kV field-emission electron source. Selected area electron diffraction (SAED) and the corresponding bright and dark field images were used to evaluate the influence of each pre-treatment on the crystallographic properties of the coating, the interfacial layer, and the substrate.

4.4 Results and Discussion

In the following section, we first present the description of the mechanical performance of the different parts of the coating/substrate system to assess the effect of sample mounting in order to assure the reliability and reproducibility of the results (Section 4.4.1). Subsequently, we study in detail the effect of surface pre-treatment on the evolution of the RS depth distribution (Section 4.4.2), followed by the results pertaining to the microstructure of the interfaces and of the deposited TiN films (Section 4.4.3).

4.4.1 Effect of sample mounting on the residual stress

In the first series of experiments, RS measurements have been performed on the rectangular specimens along the different orientations as described in section 4.3.2, and the results are presented in Figure 4.2. The Ti64 substrate before plasma treatment was evaluated as a reference, and it showed a constant RS of around -100±10 MPa, regardless of the sample orientation (Figure 4.2a), induced by the polishing process. Following plasma pre-treatment and TiN deposition on clamped substrates, however, the RS has been found to strongly depend on the sample orientation. While the values are relatively close to each other for 90° (-1,400 MPa for TiN-Ar and TiN-Ti, -1,800 MPa for TiN-Nit), the values significantly differ for other orientations (the largest differences are observed at 0° indicating RS of around -2,100±60 MPa, -3,100±90 MPa, and -3,700±100 MPa for the TiN-Ti, TiN-Ar, and TiN-Nit samples, respectively).

For comparison, we performed further RS analyses at 0° and 90° while using both the rectangular and disc specimens, CL and NC, before and after surface pre-treatment, and after applying TiN coatings on Ti64 without an interfacial layer (see Figure 4.2b). No significant effect of orientation is observed for the Ti64 alone, and for the interfacial layers (including Ar-plasma, Nitriding and Ti-implantation) the RS values show only a small difference of less than 10%, i.e., within the experimental error. On the other hand, a stronger influence of the sample fixation (CL vs NC) is seen for TiN-coated Ti64: Clamping imposes a difference of about 11% on disc-shaped samples, while it reaches up to 35% for the rectangular samples.

These results are particularly important with respect to the design and configuration of the substrate holder and substrate mounting during coating deposition. Even though the sample holders, such as the one illustrated in Figure 4.1a, are designed to impose minimum interaction with the substrate, certain contact between the holder and the substrate can impose a mechanical strain due to the CTE difference between materials involved in the system. The rectangular specimens' attachment to the sample holder by the edges limits their expansion/contraction during the coating process affecting the final stress in both orientations. In our particular case, the sample holder as well as the screws are made of stainless steel 304 with a CTE of 17.3 x 10^{-6} $°C^{-1}$, while the CTE of Ti64 is ~9.0 ×10^{-6} $°C^{-1}$. If clamped, this can lead to a compressive deformation in the central part of the sample which is indeed what may have affected the RS anisotropy. Specifically, at a substrate temperature of 390°C, the substrate bends along its short axis thus creating an additional strain in the middle. When cooled, the pre-strained substrate relaxes, thus imposing additional compressive stress in the film. As a consequence, a minimal effect on the stress is seen for the sample orientation at 90° (XRD measurements made with the X-ray beam parallel with the X-axis), while maximum effect is noticed at 0° (see Figure 4.1b and 2).

The results pertaining to the RS anisotropy in relation to the configuration of the substrate holder and substrate mounting, and the associated geometry during stress assessment are very revealing from the point of view of the reliability of data published in the literature [147]. Even if it is generally known that pre-strained substrates can affect stress assessment, it has not been obvious that the impact on stress can lead to differences of more than one hundred percent. On the one hand, it is for this reason that the published values for different coating materials and processes are rather inconsistent. The deformation and stresses thus formed can in general be described by the deflection of plates explained by plate theory [241] that is, however, outside of the scope of the present work. On the other hand, in many applications, for example the deposition of protective coatings on cutting tools, compressor blades and other components, the 3D substrates are generally not-clamped, so the effect of pre-straining is minimized. Finally, for the subsequent mechanical testing, to avoid any uncertainties, we studied the behavior for the clamped samples while reporting results for the two main orientations, namely 0° and 90°.

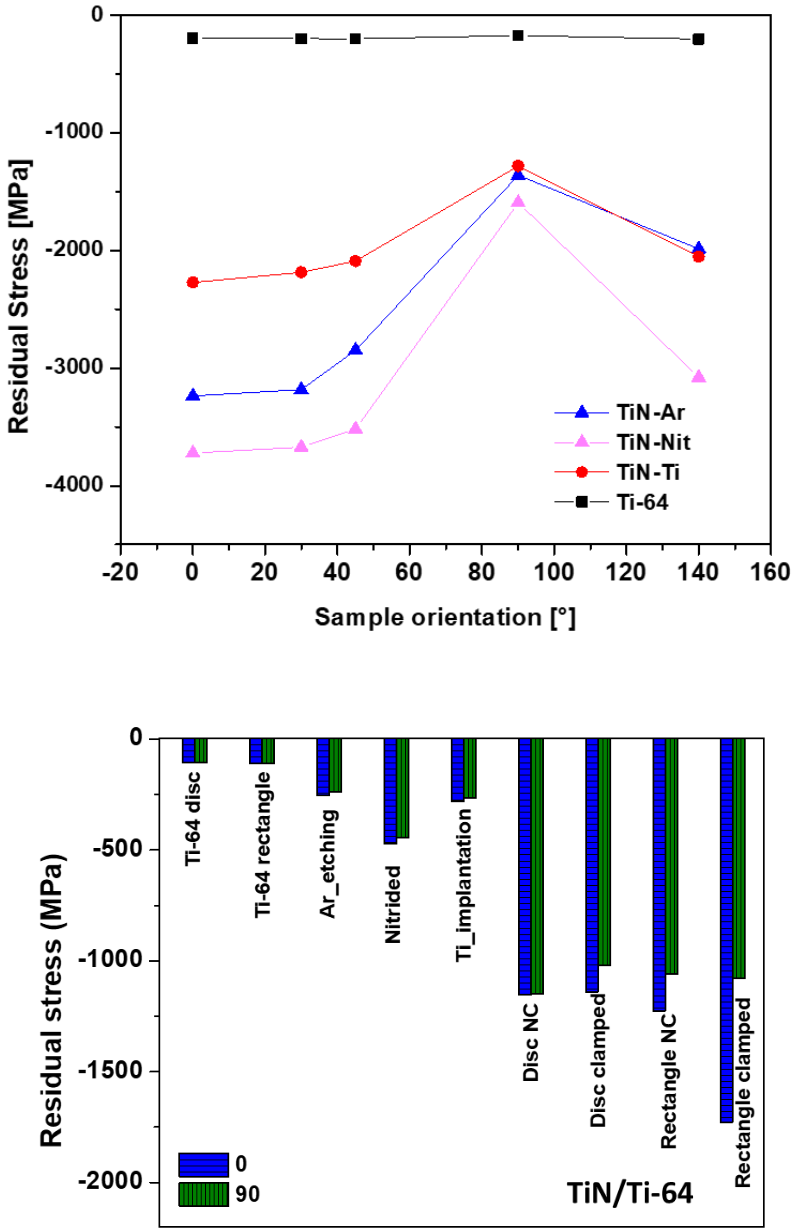

Figure 4.2 Residual stress measured by XRD in different sample orientations: a) Effect of orientation on clamped samples with TiN films deposited after the three different pre-treatments; b) RS at 0^o and 90^o for disc and rectangular substrates clamped and not-clamped to the substrate holder following different plasma treatments and TiN deposition without pre-treatment.

4.4.2 Residual stress depth profiles and mechanical properties

In the second series of experiments, we studied the RS depth profiles across the TiN coatings with different interfacial layers (see Figure 4.3). As expected from the analyses presented above, the most significant observation is the large difference (~1,500 MPa at the surface) between the compressive RS values for the 0° and 90° orientations. The RS in the interfacial layers before coating deposition are in a range between 250 to 500 MPa (see Figure 4.2b), and after coating deposition, they reach about 1,100 MPa and 700 MPa for the 0° and 90° orientations, respectively (see Figure 4.3a and b) At the same time, the RS within the Ti64 substrate increased by 300-500 MPa for both orientations, underlining the influence of interface treatment up to a 4 μm depth into the Ti64.

It is worth noting that the differences between the RS observed for the interface samples in Figure 4.2b and within the RS depth profiles, especially in the interface zone, in Figure 4.3 can be attributed to the XRD measurement methodology. In the first case, the RS corresponded to the near surface which in this case was the interface region. In the case of depth profiles, the RS represents the contribution of the coating region up to the selected penetration depth, where only information from the TiN peaks was used for RS analysis. Similarly, for the sub-layers corresponding to interface and substrate, the RS analyses are performed using the information from the peaks due to Ti64, while the presence of a top layer composed of TiN with high compressive stress level can influence the RS profiles within the sub-layers. As a consequence, the RS is systematically higher for the TiN-Nit system compared to the TiN-Ti and TiN-Ar samples.

The stress developed in the coating can be associated with the internal atomic rearrangement. Compressive RS in coatings is very often related to “atomic shot peening” during the sputtering process due to the collisions of the gas with the growing coating [242] and atom incorporation leading to micro-plastic deformation [243]. Considering that the coating is attached to the substrate, any microstructural changes, for example an excess of imbedded atoms in the interface, expands the material near the surface giving rise to compressive RS due to the constraint within the underlying layers [243], [244]. These compressive RS in the upper layers must be balanced by tensile stress in the substrate. These, however, were not observed in this study because of the limits of the XRD equipment used (i.e., limited incidence angle and fixed x-ray wavelength) which only allowed for values from the near-surface region to be measured.

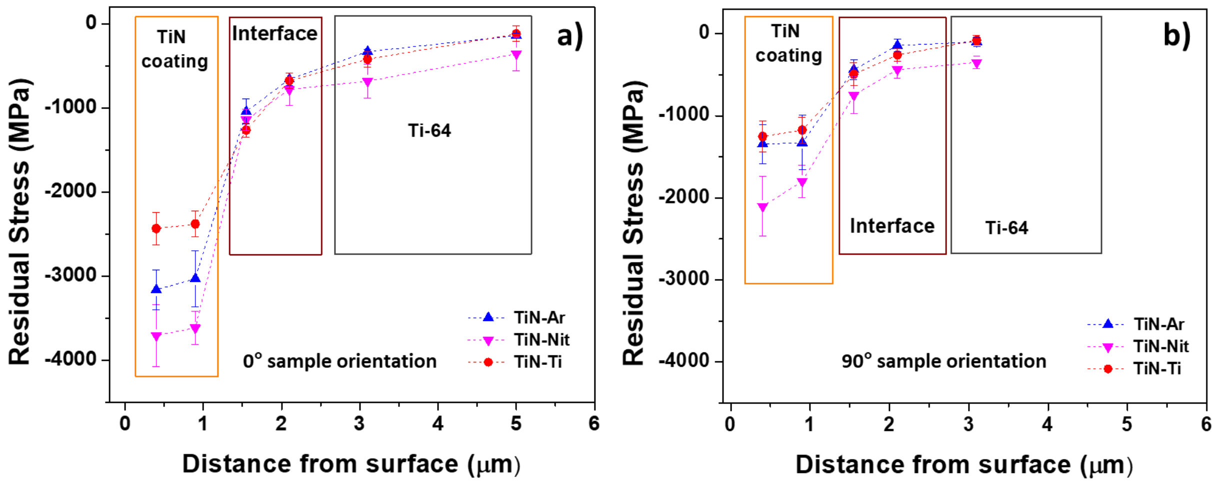

Figure 4.3 Residual stress profiles of TiN coatings deposited on clamped rectangular Ti64 with different interface treatments measured by XRD at a) 0° and b) 90° sample orientations.

The mechanical properties of the uncoated and coated samples are summarized in Table 4.1. Specifically, they include the *H* and *E*r values obtained by nanoindentation, and the onset of cohesive (L_{C1}) and adhesion (L_{C2}) failures by micro-scratch tests performed on the surfaces of each interfacial layer after the pre-treatment, and on the TiN coatings deposited on top of the different interfaces. On the one hand, the indentation hardness of the interface layers varied in the range from 10.2 to 15.5 GPa while surface hardening of Ti64 occurs due to plasma treatments that affect the substrate to a depth of few microns. On the other hand, all coatings in this work presented *H* values of around 29 GPa and *E*r values around 350 GPa. The *H* and *E*r results are in agreement with values for PVD TiN coatings reported by other authors [15], [245].

It is important to mention that the nanoindentation values in Table 4.1 are an average of 100 measurements performed at three randomly selected areas of the sample's surface (i.e. 300 indentations total per sample). For comparison, the overall stress of TiN coatings measured by the curvature method in our previous work on similar samples [5] showed about 1.7 GPa; this coincides rather well with the values obtained in the present work (about 1.5 GPa on TiN rectangle CL).

L_{C1} and L_{C2} values on the different samples presented in Table 4.1 follow the coatings' compressive RS level. However, there is also a relatively small but clear variation of the L_{C1} values depending on the sample orientation at 0° and 90°, that can be associated with the gradient of stress within the coating. The TiN-Ar and TiN-Ti samples show similar L_{C1} and L_{C2} values, while the TiN-Nit samples possess systematically higher L_{C1} and L_{C2} values for 0° and 90°. Table 4.1 Mechanical properties of the interface layers and of the coated samples determined by nanoindentation, GIXRD, and scratch testing (the latter one performed at 0° and 90° orientations). Table 4.1 indicates higher L_{C1} and L_{C2} for a higher RS for which we have also identified higher values of hardness.

Table 4.1 Mechanical properties of the interface layers and of the coated samples determined by nanoindentation, GIXRD, and scratch testing (the latter one performed at 0° and 90° orientations).

	H **(GPa)**	***E*r** **(GPa)**	***RS*** **- 0° (MPa)**	***RS*** **- 90° (MPa)**	**L_{C1} – 0° (N)**	**L_{C1}– 90° (N)**	**L_{C2} – 0° (N)**	**L_{C2} –90° (N)**
Ti64	5.2	140	110	105	-	-	-	-
Ar-plasma	11.0	168	-250	-235	-	-	-	-
Nitrided	15.5	195	-470	-440	-	-	-	-
Ti-impl	10.2	155	-280	-265	-	-	-	-
TiN-Ar	27.7	355	-3,150	-1,400	11.5	8.0	19.0	18.5
TiN-Nit	29.3	377	-3,700	-2,100	13.5	13.0	24	23.0
TiN-Ti	27.8	352	-2,400	-1,250	11.0	8.5	18	19.0

4.4.3 Microstructural characteristics of the films, surfaces and interfaces

This section presents the results of microstructural analysis of the interfaces and of the subsequently deposited TiN films in order to better understand the effect of the plasma pre-treatments and their impact on the RS and other mechanical performance.

Diffraction patterns in the 2θ range from 30° to 80° of the Ti64 substrate before and after different interface treatments are shown in Figure 4.4. Ti64 is composed of two phases of Ti, namely, α-Ti with hexagonal close-packed (HCP) structure and β-Ti with a body-centered cubic (BCC) structure. The XRD patterns of untreated and treated Ti64 reveal a strong signal of α-Ti phase. Therefore, we assigned the α-Ti phase (PDF 44-1294) with HCP structure to the corresponding indexation of Ti64. The three pre-treated Ti64 substrates gave rise to predominant α-Ti phase, especially following Ar plasma. However, nitriding and Ti implantation led to additional phases resulting in new features between 36° and 43°. The nitrided sample presents δ-TiN (PDF 38-1420) and Ti_2N (PDF 76-0198) phases with cubic structures. The presence of the additional phase is typical for nitrided Ti64 at high temperatures [246]. The Ti-impl sample shows an additional peak at ~42.3° corresponding to the (021) plane of α"- martensite Ti phase. This phase can be formed during the implantation process due to the high metal content (Ti ions implanted) compared to the low content of β stabilizer elements. Indeed, α' and α" Ti martensite phases are formed only in an α + β titanium alloy during the heat-treatment process, especially quenching. This occurs when Ti atoms dissolve into the alloy, forming a supersaturated α phase, while β stabilizer elements (i.e., V) from the alloy form a high solute region for the Ti phases resulting in the α"-Ti phase [247], [248].

Diffractogram patterns corresponding to TiN coatings with different interfaces were measured at 0° and 90° sample orientations (see Figure 4.4b). Each pattern presents δ-TiN coating with a NaCl structure (PDF 38-1420) where the diffracted peaks at 2θ angles of 36.5°, 42.6° and 61.7°, 73.9° and 77.5° belong to the (111), (200), (220), (311) and (222) diffraction planes, respectively. Besides the δ-TiN phase peaks, the presence of the α-Ti phase arises from the Ti64 substrate. Diffractograms of the two sample orientations (0° and 90°) show two main differences: First, a slight shift in peaks towards lower 2θ angle positions with an increment in the lattice parameter, at patterns obtained at the 90° orientation, and second, a difference in the resulting texture coefficients presented in Figure 4.5**.**

According to reference [206], if the $T_{c\ (hkl)}$ value is higher than one, a large number of crystallites are oriented in the direction of the specific crystalline *(hkl)* plane indicating a preferential orientation. Therefore, TiN-Ar and TiN-Ti samples exhibit a preferential (200) orientation with a smaller contribution of a mixture of (111) and (220) planes. In contrast, the TiN-Nit sample is characterized by a preferential (111) orientation coexisting with a mixture between (200) and (220) planes in similar amounts according to the sample orientation. However, it appears that the texture coefficient related to the (220) plane varies between both sample orientations. Comparing the (220) peaks, we observe that the intensity ratio for the 90° sample orientation is considerably higher than for the 0° orientation. We can conclude that these differences influence the RS of TiN coatings for different sample orientations as described in Section 4.4.2.

The texture of TiN coatings and formation of preferred orientations on the (111), (200), and (220) planes have been widely reported in relation to the deposition conditions, such as pressure, bias voltage, and temperature. In fact, the crystallographic texture develops during coating growth to minimize the total energy of the system [191]. It has been found that the presence of a strong (111) preferred orientation can be related to high stress conditions during the deposition process, such as in the case of the TiN-Nit sample. The (111) plane in the TiN crystal corresponds to the lowest strain energy due to anisotropy in the Young's modulus [191] and its alignment normal to the growth direction minimizes the total energy under the strain energy-dominated growth. On the other hand, the (200) plane was reported to present the lowest surface energy [178]. It is expected to be the preferred orientation when surface energy is the dominant contribution to the total energy.

However, it should be noted that other authors [249] have proposed that the nature or preparation of the substrate has an influence on the preferred orientation, for example, on ground and polished Ti showing (111) or (220) preferred orientations, respectively. Grant *et al.* [249] reported that the presence of a (002) orientation on Ti substrates with hcp structure contributes to the formation of (111) preferred orientation in TiN since both are close packed and possess very similar inter-atomic spacings of 0.2998 nm and 0.2950 nm, respectively. The 1.6% atomic mismatch between these two planes gives rise to a low interfacial strain, and therefore TiN (111) direction is favoured. In our case, the nitrided sample has a stronger (002) orientation than the Ar plasma and Ti impl surfaces; in addition, these interface pre-treatments developed additional phases (mainly δ-TiN phase). In fact, a combination of these factors can influence preferred orientation of the subsequent TiN coating by reducing the atomic mismatch and consequently affect the RS observed in Figure 4.3. TiN coatings with different interface pre-treatments present a lattice parameter between 4.24 and 4.25 Å, while the crystallite size is 11.5±0.3 nm for the TiN-Ar and TiN-Ti samples, and 15.2±0.2 nm for TiN-Nit, regardless of the sample orientation.

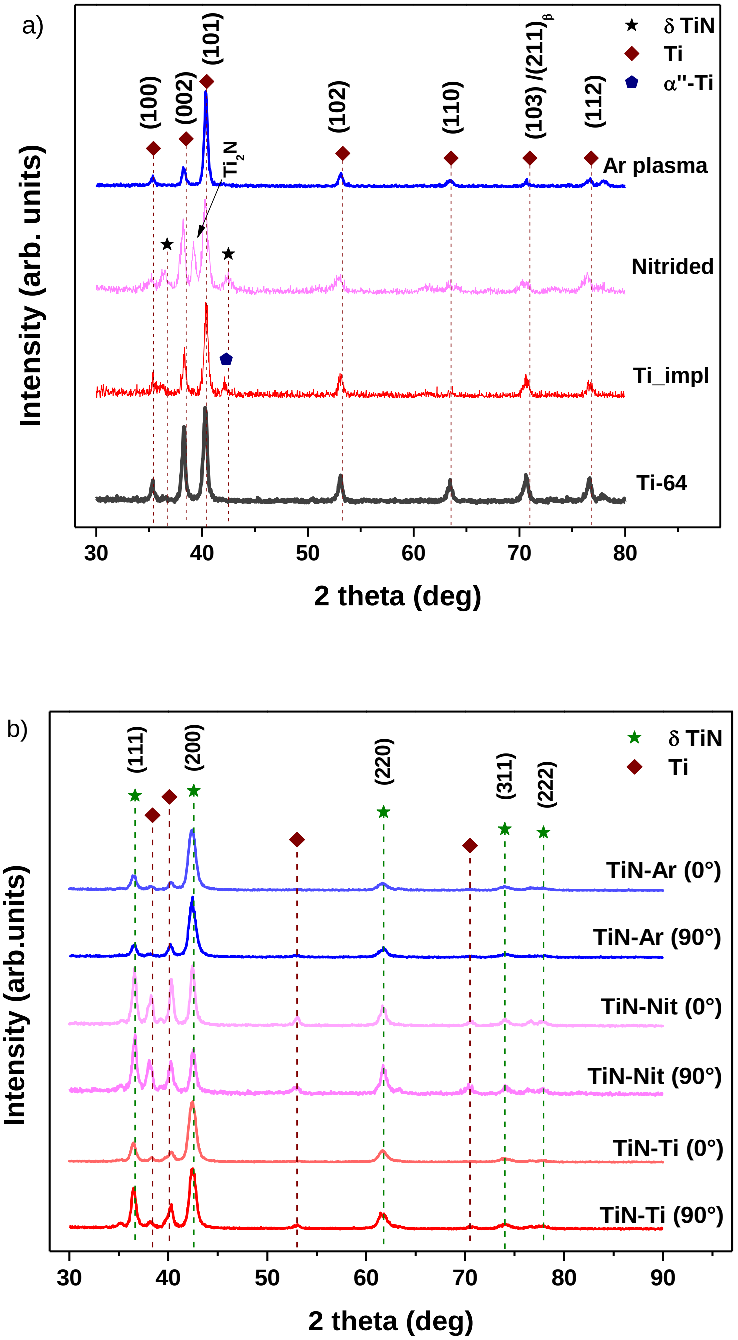

Figure 4.4 Diffractograms of a) the Ti64 substrate after different surface pre-treatments at 0° sample orientation, and b) of the TiN films deposited on Ti64 with different interfaces at 0° and 90° sample orientations.

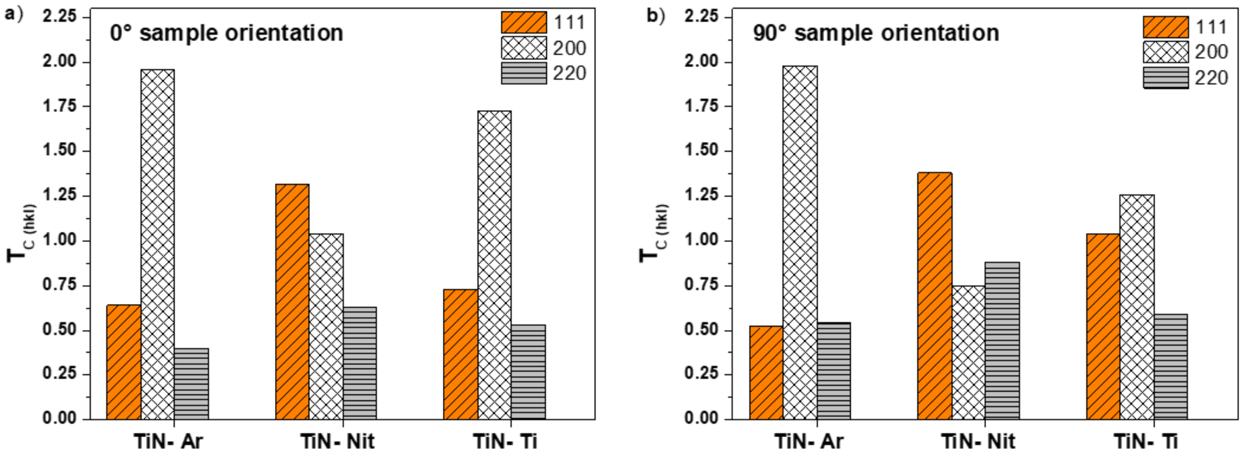

Figure 4.5 Texture coefficient of (111), (200) and (220) planes of the TiN coating on Ti64 with the three different interfaces at a) 0° and b) 90° sample orientations.

Further insights into the interface and coating texture have been gained by the TKD analyses of the FIB prepared cross-sections as illustrated in Figure 4.6**.** Overall phase and texture maps of the TiN/Ti64 coating system with different interfaces (Figure 4.6a) are presented, as well as the inverse pole figure maps (IPFX) parallel to the growth direction (labelled the x direction) of the coating (Figure 4.6b). The FCC-TiN phase with a F4/m$\bar{3}$2/m space group and the HCP-Ti phase with a space group P6$_3$/m2/m2/c were used to map the TiN coating and Ti substrate, respectively. In our case, the TKD phase maps confirmed the structure and phase distributions in the TiN coating and in the Ti64 substrate first indicated by the XRD analysis (see Figure 4.4). This includes the presence of structural differences within the interfacial layers indicated in the XRD patterns of Ti64 after the three pre-treatments (see Figure 4.4a). In the case of the Nit sample, the interface XRD pattern was identified as α-Ti phase with a 9% δ-TiN phase, calculated using Materials Data Inc Jade software base on the whole-pattern fitting method [250]. However, in the TiN-Nit phase map in Figure 4.6a we identified a minimum presence of TiN phase in the interface-substrate zone surrounded by a few grains that were not resolved by the TKD analysis, possibly there are other grains closer to the coating that were indexed as part of the TiN coating. For the Ti-impl sample, the interface layer was indexed in the XRD patterns as α-Ti phase with 2% of α’’ Ti phase according to the whole-pattern fitting method, however, these two Ti phases exhibit an HCP structure and similar lattice parameters (a ~2.9 Å and c ~4.6 Å), making it impossible to accurately distinguishing between them during pattern indexing.

The TiN-Ar coating exhibits small grains and a high concentration of defects (discontinuous grains). While this leads to poor pattern indexing, the grain morphology can nevertheless be distinguished in the Band Contrast signal in Figure 4.6a. In comparison, the TiN-Nit and TiN-Ti coatings show large, elongated grains in the film bulk (Figure 4.6b). The coating microstructure depends on the initial stage of growth during which the grain formation is influenced by the microstructure of the interfacial layer, leading to the formation of grains with different preferred orientations. Based on the TKD - IPF measurements (see Figure 4.6b), one can confirm that the grains within the TiN coatings present a texture with a preferred orientation resulting in 001 planes for the TiN-Ar and TiN-Ti systems, while the TiN-Nit coatings present a texture with a mix of three main orientations, which supports the XRD findings in terms of the texture coefficient (see Figure 4.5). In addition, one can notice a clear transition in the grain orientation within the TiN-Nit coating (Figure 4.6b) starting from near the interface towards the bulk of the coating. On the contrary, this is not observed in the TiN-Ti system in which the grains are preferentially oriented in the 001 direction both close to the interface and the film surface. It is hard to draw conclusions for the TiN-Ar coating due to the low indexing but the orientation seems uniform like the TiN-Ti coating.

The substrate grains are large and, due to small sampling size, no conclusion can be made regarding their overall texture. However, the grains close to the TiN coating, corresponding to the interface layer, are observed to show differences between the samples. On the sample TiN-Ar sample a finer interfacial Ti grain structure can be observed. In addition, the preferred orientations within the interfacial layers of the TiN-Ar and TiN-Nit systems correspond to the $\bar{1}2\bar{1}0$ and 0001 planes, respectively. On the other hand, TiN-Ti shows a gradient between 0001 and $01\bar{1}0$. Indeed, the high level of RS can be associated with structural phase transformations within the interface and the coating regions, that are directly affected by the ion bombardment during the plasma pre-treatment and deposition. Similarly, the surface compressive RS measured in interfacial layers was attributed to permanent lattice strain that resulted from the grain recrystallization, nitrogen diffusion, or Ti rearrangement within the crystalline structure [251].

The zones with low quality indexing seen in Figure 4.6, especially for the interfacial layers and for the coatings, can be related to the FIB preparation, very small grain size (i.e. high grain boundary density) and/or the presence of significant stress. While the 30 kV Ga^+ ion beam used during the FIB sample preparation could have deteriorated the overall diffraction signal by inducing damage at the surface of the FIB lamellas, it is not believed that this is the main cause of the low-quality indexing observed but only a contributing factor. First, it seems likely that the coating on the TiN-Ar sample and the interfacial regions of all three samples, were the worse affected because of their very small grain sizes as observed in the band contrast signals of Figure 4.6a. On the other hand, the remaining poorly indexed zones in the substrate in TiN-Ar and the complete TiN-Nit and TiN-Ti systems, are most probably attributed to the existence of high stress in the sample. This is confirmed by the EBSD misorientation maps (Figure 4.7b), which show higher local misorientation near the interface and in the coatings but affect only a few grain boundaries at the substrate.

Bright-field TEM images and misorientation maps of cross-sections of the interfacial layers and of the coating are shown in Figure 4.7. The coatings in all samples present a typical TiN microstructure with columnar, large, elongated grains, especially well developed in the TiN-Nit and TiN-Ti samples. Comparing the bright field images and misorientation maps, one can confirm a difference in grains at the interface layer identified with green or red dotted rectangles. The effect of Ar plasma Figure 4.7a and Ti implantation Figure 4.7c is visible only at a shallow depth of less than 150 nm from the substrate surface, exhibiting recrystallized grains and thin-uniform grains of the Ti64 material. The nitriding treatment presents large grains up to a depth of around 400 nm.

The misorientation maps shown in Figure 4.7b correspond to the local average misorientation. This is based on the kernel method that allows one to calculate the misorientation between all neighbour points within the TKD image acquired at high resolution. A kernel is known as a set of points with a determined size surrounding a specific scan point. Misorientation maps qualitatively show the dislocation density differences between non-deformed and deformed lattices. The green-scale colour shows a high misorientation and the blue-scale color shows a low misorientation.

The highest misorientation occurs at the grain boundaries of Ti64 of the three samples. Specifically, the TiN-Ar sample presents higher misorientation density within the area identified as interface zone, while in the TiN-Nit sample dislocation densities are spread homogeneously in the coating and in the interface. The TiN-Ti sample presents higher misorientation density in the coating, however, the area defined as the interface presents low-quality indexing and it was not possible to identify any gradient of misorientation in that specific area of the sample.

Figure 4.7b indicates homogeneous low angle misorientation density in the coatings. In fact, it has been shown that the increase in integrated low-angle misorientation density linearly varies with the residual stress [252], [253]. Specifically, as indicated Figure 4.7b, the high-density misorientation is primarily concentrated at the grain boundaries between the neighbouring coating and interface regions. Each sample exhibits a high density of dislocations that varies from the coating zone, across the interface toward the substrate as a consequence of different pre-treatments. In this respect, the TiN-Nit system shows a larger interface region that also possesses a homogeneous zone of high-density misorientations throughout a depth of at least 500 nm - this effect can be attributed to the long-range diffusion of nitrogen into the substrate from the nitriding process.

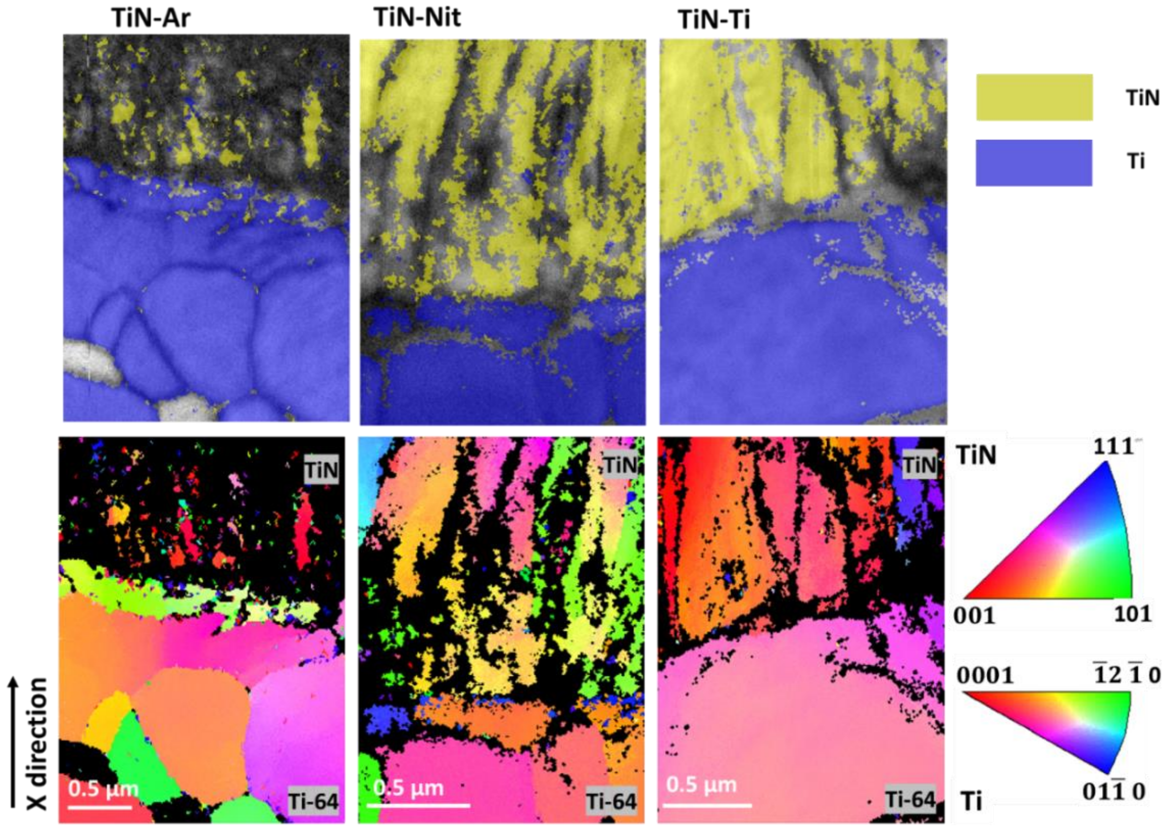

Figure 4.6 TKD phase maps (top-a) and inverse pole figure (IPFX) maps (bottom-b) of the cross-sections of the TiN coatings on the three different interfaces. The colours in (a) represent TiN and Ti phases in the EBSD phase map as marked, and the coloured grains in (b) mean various orientations identified by the index of the IPFX.

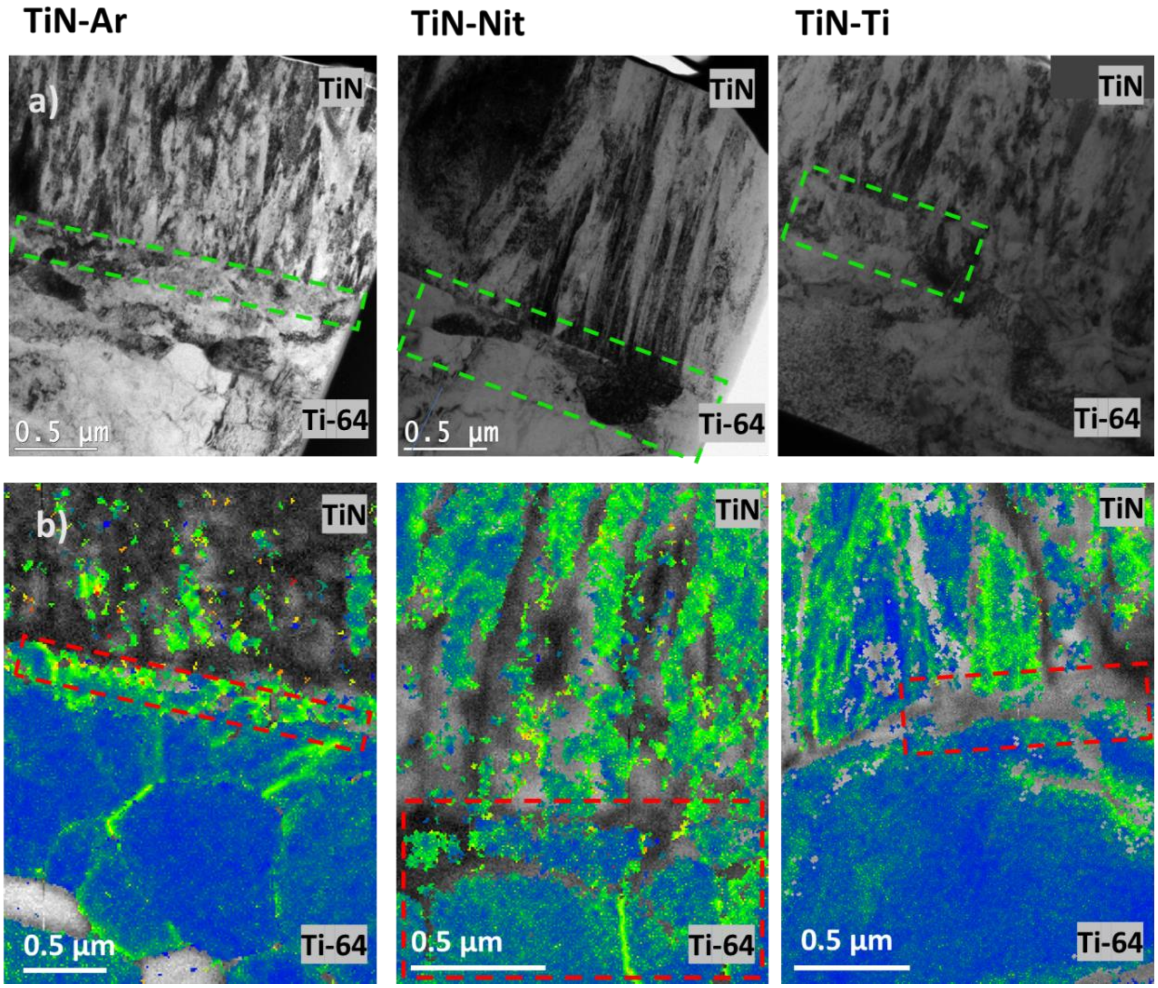

Figure 4.7 Bright field TEM images (top-a) and TKD local misorientation maps (bottom-b) of coated samples with different interface treatments. Green and red doted rectangles indicate the interface zone.

The associated dark field (DF) TEM micrographs of the cross-sections demonstrated a columnar grain structure grown perpendicularly to the substrate surface and they incorporate many polycrystalline domains. The TiN-Ar micrograph in Figure 4.8 is an example to show the identification of three different regions (coating as number 1, interface as number 2, and substrate as number 3) in the cross-sections where SAED measurements were performed. The SAED patterns on the polycrystalline domain of region 1 (white dotted circle) showed a cubic structure formed by (200), (220) and (222) lattice planes. The SAED patterns in region 3 (blue circle) showed an HCP structure formed by (101) and (102) lattice planes. Finally, the SAED results in region 2 (right side of the Figure) indicate the presence of TiN- and Ti-phases. Some diffraction rings of the Ti-phase are deformed compared to those in region 3, indicating a possible lattice plane strain related to RS.

The orientation of the grains within the interfacial layers depends on the ion energy and ion flux during pre-treatment and the diffusion of dissolved atoms (Ar, Ti, N). In Ar plasma and during Ti implantation, the arriving Ar^+ or Ti^+ ions are incorporated into the substrate to a depth of tens of nanometers as interstitials in the Ti64 lattice, and they interact with vacancies generated by the high energy bombardment [62]. In addition, the energy involved during the pre-treatments and coating deposition processes strongly influences the crystallographic properties. This effect has specifically been observed in the DF and SAED -TEM analyses in the interface zone (see the right side of Figure 4.8), as documented by the differences in lattice displacements that can be attributed to micro-strain due to the ion bombardment. The crystalline lattice constant of Ti64 (blue circles) is increased at the interface when the N and Ti atoms during plasma treatment interact with the Ti64 surface. Therefore, these atoms dissolved in the Ti-phase introduce stresses and cause elastic deformation of the crystalline structure.

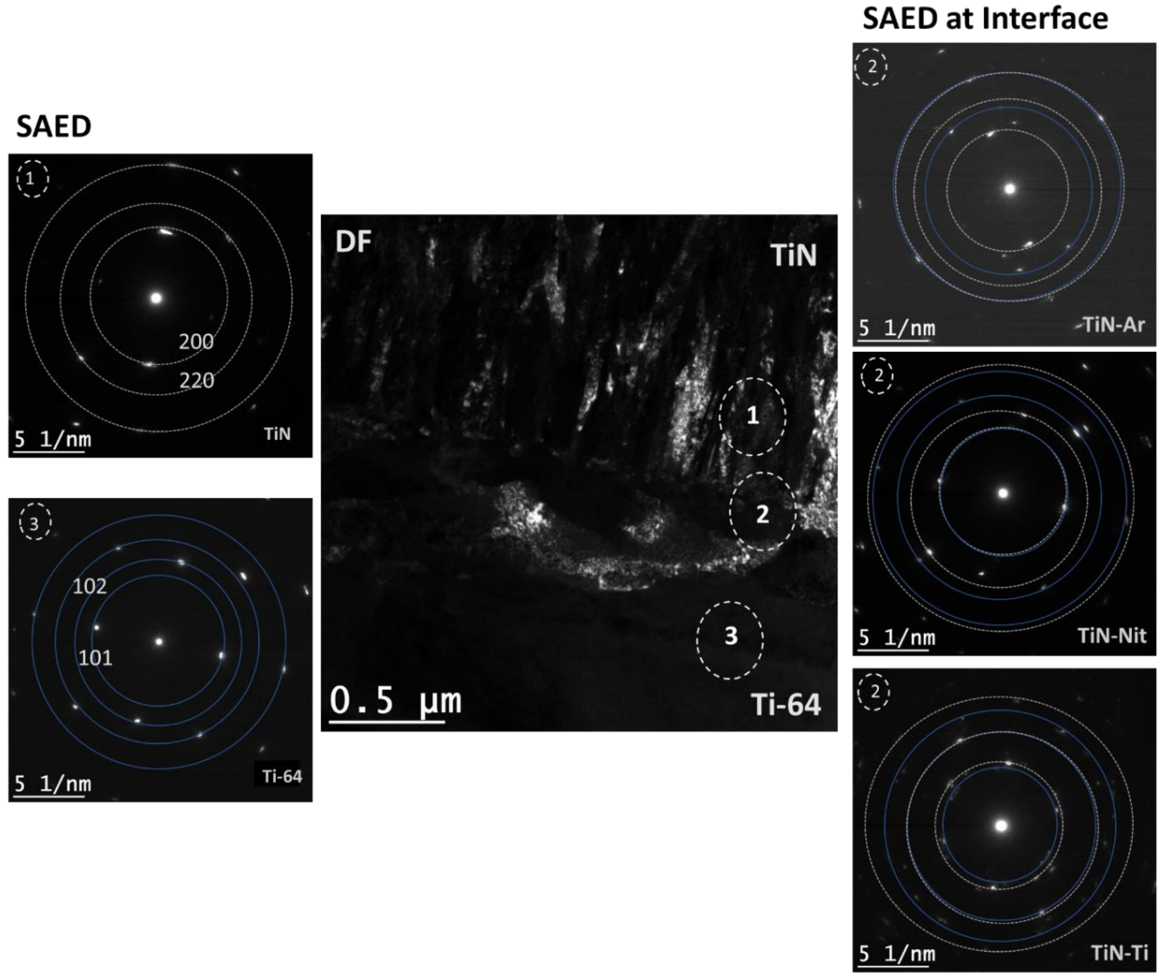

Figure 4.8 Dark field (DF) TEM image of the representative TiN-Ar cross-section (center). The encircled numbers 1, 2 and 3 in various regions of the DF image represent areas where SAED patterns were measured on other samples with different interfaces: SAED patterns in region 1 correspond to the TiN coating (white circles), region 3 is the Ti (Blue circles) from substrate in TiN-Ar, and the regions 2 (right side of the central Figure) are the SAED patterns of the interface zone in TiN-Ar, TiN-Nit and TiN-Ti samples, respectively.

4.5 Summary and conclusions

Model TiN coatings were deposited by reactive magnetron sputtering onto Ti64 substrates following different interface treatments using Ar plasma, Ti implantation and surface nitriding. Specific differences in the compressive RS have been discerned by the GIXRD measurements.

In the first part of the study, we have described and quantified a strong effect of the deposition methodology on RS, namely its anisotropy in dependence on the way how the substrate had been attached to the holder. In particular, we have found a significant difference in the RS values (more than 100%) for different orientations of the coated samples during the XRD measurements for situations when the substrates were rigidly clamped to the substrate holder. These differences were much smaller (comparable to the experimental error) when the substrates were non-clamped.

In the second part of the study, we compared analyses performed using XRD, TKD with Kikuchi diffraction, and TEM to demonstrate the effect of each interfacial layer on the microstructure and the texture of Ti64 surface and TiN coatings. We conclude that Ar plasma, Nitriding, and Ti implantation influence the near surface region of the Ti64 substrate due to Ar$^+$, N_2^+ or Ti$^+$ ion bombardment that causes local changes in strain, giving rise to surface/interface hardening, while some of the ions (Ti$^+$, N_2^+) have a high bonding affinity and can be incorporated at the substrate's lattice sites. Therefore, the created interface layers affected the growth of the TiN films and the coating microstructure including the crystallite size (11 to 16 nm) and the texture coefficient. The near surface of the Ti64 treated with Ar plasma, Nitriding and Ti implantation developed $\bar{1}2\bar{1}0$, 0001 and $01\bar{1}0$ preferred orientations, respectively. On the other hand, TKD analyses (especially the IPFX maps) support the findings based on XRD in terms of the TiN texture, coated systems resulted in 001 preferred orientation for TiN-Ar and TiN-Ti, and a transition in the grain orientation within TiN-Nit consisting of a mix where 001 and 111 planes predominate.

The difference in microstructure and texture imposed different levels of sub-surface compressive RS spanning to a depth of several micrometers under the Ti64 surface. We observed a large variation between related RS depth profiles for TiN (1 μm) coatings with RS values between -1 GPa and -4 GPa. The RS **gradient** spans over a depth of about 5 μm across which it varies from several MPa within the substrate to several GPa at the coating surface. The TiN-Nit sample presented the highest compressive RS level, while TiN-Ti exhibited the lowest compressive RS through the coated system.

The misorientations maps confirmed a high grain misorientation density due to the imposed RS in the coatings and within the interface layers within at least 500 nm for TiN-Nit, but below 100 nm for TiN-Ar and TiN-Ti. These observations were also confirmed by comparing the SAED patterns at different depths. The diffraction rings near the substrate’s surface (interface) presented lattice plane strain related to RS compared to those in the untreated Ti64. Similarly, to the misorientation maps, TEM measurements also confirmed consistent lattice strain through the TiN-Nit coating system.

The resulting differences in microstructure and the texture coefficient are related to the mechanical properties; specifically, H~29 GPa for TiN on pre-treated surfaces is significantly higher than H~21 GPa for the coating-substrate system without a pre-treatment. The micro-scratch analysis revealed that the compressive RS in the coating is the main parameter responsible for the cohesive failure behavior; this has been documented by a higher value of the L_{C1} critical load parameter at high compressive RS. Similarly, surface/interface nitriding has been found to enhance adhesion more than the Ar plasma exposure and Ti implantation as indicated by higher values of L_{C2}.

4.6 Acknowledgment

The authors wish to thank Dr. Damian Batory (Technical University of Lodz, Poland) for fruitful discussions. We thank Mr. Nicolas Brodusch (McGill Materials Characterization) for assistance in carrying out the TKD experimental tests, Mr. Francis Turcot and Mr. Sébastien Chénard for expert technical assistance. This project has been supported by the Natural Sciences and Engineering Research Council of Canada (NSERC) and Pratt & Whitney Canada through the NSERC Multisectoral Industrial Research Chair in Coatings and Surface Engineering grant (IRCPJ 433808-11), and through the NSERC Discovery Grants of JEKS RGPIN-2016-06409.

CHAPTER 5 ARTICLE 2: FRACTURE MECHANISM OF TIN COATINGS ON TI-6AL-4V SUBSTRATES: ROLE OF INTERFACES AND OF THE RESIDUAL STRESS DEPTH PROFILE

E. J. Herrera-Jimenez[1], N. Vanderesse[2], E. Bousser[1], T. Schmitt[1], P. Bocher[2], L. Martinu[1], J.E. Klemberg-Sapieha[1]

[1]*Department of Engineering Physics, Polytechnique Montreal, Box 6079, Station A, Montreal H3C 3A7, Quebec, Canada*

[2]*Département de génie mécanique, École de technologie supérieure, Montréal H3C 1K3, Québec, Canada*

The article was submitted to Surface and Coatings Technology (February 2021)

5.1 Abstract

The performance and integrity of coated engineering components rely on the time required for the appearance of defects and cracks and their propagation leading to delamination of the coating and degradation of the substrate. Optimization of the coating's mechanical properties such as hardness, residual stress (RS), and adhesion is essential to delay crack onset and propagation. In the present work, we investigate the mechanical properties and the failure mechanisms of model TiN coatings reactively sputtered onto Ti-6Al-4V substrates, while comparing three interface engineering approaches: a) Argon plasma treatment, b) plasma surface nitriding, and c) Titanium implantation. The TiN coatings possessed a hardness of ~29 GPa and a Young´s modulus of ~350 GPa. Multi-reflection grazing incidence X-ray diffraction was used to assess the compressive RS depth profile. Each interface engineering process was found to induce RS variation in the coating as well as in the adjacent interfacial area and in the substrate's near-surface layer ranging from -1 GPa to -2.2 GPa with different gradients. Cohesive failure, crack evolution and fracture toughness were studied using micro-scratch and micro-tensile tests. SEM analyses were performed on fracture samples identifying different surface grain deformation behaviour and surface cracks on Ti-6Al-4V with various interface treatments and TiN coatings. We found a close correlation between the RS of the coatings or the interface layers and the fracture mechanism. Specifically, higher compressive RS led to enhanced interfacial shear strength and critical energy release rate around 550 to 790 MPa, and ~18 J/m^2, respectively.

5.2 Introduction

Interface engineering is essential to maintain the performance of metallic components or products throughout their entire life in numerous areas of application including aerospace, energy, manufacturing and others. Microstructural, mechanical, and tribological characteristics are of prime importance to control and minimize component fracture, and to maintain and enhance its durability.

Titanium alloys such as Ti-6Al-4V are widely used due to their attractive properties such as low density, high strength to weight ratio, and high corrosion resistance [27]. The tensile strength of Ti-6Al-4V has been evaluated by different techniques, such as tensile testing and indentation. Carroll et al. presented a detailed summary of the mechanical properties obtained from tensile testing of Ti-6Al-4V manufactured by direct energy deposition, powder bed fusion, and electron beam melting [254]. The reported yield strength (YS) is in the range from 780 to 1260 MPa, while the ultimate tensile strength (UTS) varies between 775 and 1110 MPa, and the elongation from 1 to 16 % [28].

Since the plastic flow in metallic components often starts at the surface and then extends to deeper layers, the application of protective coatings, surface treatments, and interface engineering can effectively enhance the fatigue performance and durability of Ti-6Al-4V [49], [255]. However, these coated structures are usually exposed to external loads and extreme environmental conditions, that can trigger various degradation mechanisms in the coating-substrate system such as surface embrittlement, buckling, coating delamination and cracking [256], as well as corrosion and tribo-corrosion [257], [258]. Microstructure, surface roughness, stress concentration, non-uniform distribution of the mechanical properties, and the post thermo-mechanical treatments applied, dictate the fracture properties of hard coatings on Ti-6Al-4V [259].

It has been observed that the crack onset in the coating and its propagation towards the substrate lead to failure. To mitigate the deterioration processes, interface engineering of the Ti-6Al-4V/coating systems can improve chemical and mechanical bonding between the substrate and the Physical Vapor Deposited (PVD) coatings, enhance their adhesion, and delay crack nucleation or propagation through the substrate [51]. Surface treatment processes include modification of the top layer of the substrate through mechanical-, thermal-, plasma-, and/or diffusion-related phenomena. Specifically, surface treatments of the metallic substrate generally improve the tribo-mechanical properties of the coating-substrate systems by creating an intermediate layer also described as an interface or interfacial region (interphase) [230], [260].

Indeed, the adhesion between the coating and the substrate is one of the most important properties for enhancing coating-substrate system performance during their lifetime. Therefore, different pre-treatments applying plasma, heating, ion implantation, carburizing, and nitriding processes have been explored to create an intermediate layer. In addition, interface treatments can induce residual stress (RS) that can span to a depth of a few microns into the substrate. In addition to being particularly important for the control of adhesion [76], several studies have shown that coatings with an adequate level of compressive RS [157], [261], high hardness, and good adhesion can restrict plastic deformation, and thus enhance tensile strength and fracture resistance of the component [262]–[265]. Understanding the micro-mechanisms of deformation and fracture, and the influence of RS is necessary for further improvement of the coatings for fracture-critical applications [266].

In systems with appropriate optimization of compressive RS through coating-interface zones, cracks starting at the surface or within the coating can stop at the interface, thus delaying failure of the component [157]. However, coatings with high levels of compressive stress can present spallation immediately after coating deposition [261]. Bull has shown that an Ar plasma treatment significantly improves adhesion between the coating and the substrate and promotes a ductile interfacial failure in which no interfacial cracking is observed [267]. Nitriding and ion implantation treatments can also induce a large compressive RS at the surface, thus delaying the formation and propagation of microcracks [268], [269].

Transition metal nitride coatings, such as TiN, ZrN, CrN, TaN, NbN, and HfN are frequently used for aeronautical applications mainly because of their suitable mechanical properties and their wear-, erosion-, and corrosion resistance [12], [169]–[171], [229]. The microstructure of such coatings consists of a mixture of covalent, metallic, and ionic bonds, resulting in high hardness, high melting temperatures (for example, around 1500°C for CrN, and >2500°C for TiN, ZrN, TaN, NbN, and HfN), very good abrasion resistance and chemical inertness, among other properties.

TiN coatings have been shown to possess excellent mechanical characteristics [270], [271]; this includes a high energy release rate varying between 14 and 16 J/m^2, fracture toughness in a range from 1.6 to 2.7 MPa m$^{0.5}$, and an interfacial shear strength ranging from 32 MPa for coatings deposited on Silicon substrates [272], and up to 6.9 GPa for coated stainless steel substrates [273], [274].

Fracture toughness has been used as a critical characteristic in preventing catastrophic failure for structural materials. However, toughness evaluation for coatings is difficult due to the sample dimensions and varied test procedures; in the literature, the tests are divided into energy-based and stress-based methods. Tensile testing is an energy-based method with the advantage of a uniform strain field. It considers the energy release rate uniquely attributed to surface failure, specifically taking into account the local distribution of RS, which can control fracture initiation.

In a previous article [275], we presented a systematic study of the effect of three interface pre-treatments, namely Ar plasma, nitriding and Ti ion implantation, on the microstructure and RS depth profiles in TiN films on Ti-6Al-4V. We demonstrated that the interface pre-treatments can induce compressive RS (-200 MPa to -500 MPa) to a depth of a few microns into the Ti-6Al-4V substrate. In addition, the RS throughout the coatings varies from around -1 GPa to -2.2 GPa, depending on the surface treatment.

As a continuation, in the present work we investigate the fracture mechanisms of an application-relevant system consisting of model PVD-deposited TiN coatings on Ti-6Al-4V substrates with three different interfacial layers in relation to the RS depth profile. In particular, we investigate the contribution of each constituent (substrate, interface, and coating) to the mechanical behavior of the whole system. The interface layers studied here were prepared by Argon plasma treatment, plasma nitriding, and Titanium (Ti) implantation. Two main mechanical characterization techniques were used to evaluate TiN coating failure as a function of the RS; specifically, a) Micro-scratch testing was carried out on coated samples in order to evaluate cohesive failure and possible delamination of TiN from the Ti-6Al-4V substrate; and b) The micro-tensile tests were performed in two different modes (continuous and interrupted), and they were assisted by confocal laser scanning and optical microscopy that provided a detailed insight into the crack nucleation and propagation on the coated specimens.

5.3 Experimental methods

5.3.1 Sample preparation

1) Sample cutting and polishing: Flat rectangular samples and dog-bone-shaped coupons of Ti-6Al-4V alloy were used as substrates for interface treatments and coating deposition (see Figure 5.1). The flat rectangular samples (50x25 mm^2) were used for microstructural, nanoindentation, micro-scratch and RS characterization, while the dog-bone shaped coupons were used for micro-tensile testing. First, a Ti-6Al-4V sheet (380 μm thick) was cut in several dog-bone specimens using a water jet cutting machine. The surface was ground using a Struers LaboPol-5 polishing machine at a stage rotation speed of 250 rpm, using SiC paper with 400 to 1200 grit and continuous water-spraying. Subsequently, a Logitech PM2A precision polishing machine was used with SiC paper (2000 and 4000 grit) to remove all visible scratches. Finally, the surfaces of both substrate shapes were mirror-like finished with silica suspension (particle size 0.04 μm) including H_2O_2 and distilled water rinse. This final polishing step was carried out with a Struers machine at 300 rpm for 30 min on the rectangular samples and on both sides of the dog-bone samples. Then, only one side of the dog-bone samples was polished with a VibroMet 2 vibratory polisher for 24 h - This step was done to guarantee superior polishing results on the side of the sample to be plasma treated or coated, with homogeneous flatness and no deformation on the complete coupon that are critical characteristics during the micro tensile testing.

2) Plasma deposition system: All surface engineering processes (pre-treatments and depositions) were performed in a magnetron sputtering system (30 L volume, base pressure 10^{-5} Torr - turbomoleculary pumped) equipped with a Pinnacle Plus (Advanced Energy) power supply connected to a 50 mm diameter Ti target (99.995% purity). An RF power supply (Seren) or a High-Power Impulse Magnetron Sputtering (HiPIMS) generator (Melec GmbH) was connected to the sample holder to bias the substrate. A constant substrate temperature of T_s = 673 ± 10 K was used for all pre-treatment and coating deposition steps.

3) Surface engineering process consisted of three subsequent main steps:

A: Sample cleaning: Before any pre-treatment, all substrates were ultrasonically pre-cleaned in acetone and isopropyl alcohol for 30 min before being mounted in the vacuum chamber. One rectangular flat Ti-6Al-4V substrate and two dog bone specimens were fixed to the substrate holder. Ar sputter cleaning was applied for 30 min at a pressure of 5 mTorr and a negative bias of -600 V applied to the substrate. This operation aimed at removing the surface native oxide layer while promoting surface activation [80].

B: Surface pre-treatment processes: The substrates were exposed to one of the three treatments to provide specific interface layers.

i) *Plasma nitriding* was performed in two stages, first with an additional surface activation for 30 min in an Ar and H_2 atmosphere (Ar:H_2 =4:1) at a negative bias of -400 V. Second, the nitriding step was accomplished in an N_2 and H_2 atmosphere (N_2:H_2 = 4:1) for 120 min at a pressure of 400 mTorr and a negative bias of -400 V.

ii) *Ti implantation* was performed for 120 min using a HiPIMS power supply with two channels: one channel connected to the substrate holder and kept at a negative bias voltage of -600 V, and the other channel connected to the Ti target while using a negative cathode voltage of -630 V. The applied average power in each channel was 400 W with a pulse length of 55 μs and a frequency of 300 Hz.

iii) *Ar plasma* was applied for 30 min in Ar atmosphere at a negative bias of -600 V, and a pressure of 5 mTorr.

C: Coating deposition: Following surface pre-treatment, a TiN coating was deposited by pulsed-DC sputtering of the Ti target using a frequency of 300 kHz with a reverse time of 0.4 μs and a power of 225 Watt (1.0 A), and an Ar/N_2 mixture using a flow rate ratio Ar:N_2 =5:1 at a pressure of 5 mTorr. A constant negative bias of -120 V (~225 W) was applied to the substrate using RF power. Based on the previous study, these conditions lead to the formation of good quality hard TiN films with the microstructure and mechanical properties described in more detail in refs [229], [275].

After deposition, the coating thickness was determined using a Sloan Dektak III profilometer, and it was then confirmed by SEM cross-section analysis. The thickness of all TiN coatings was about 1 μm.

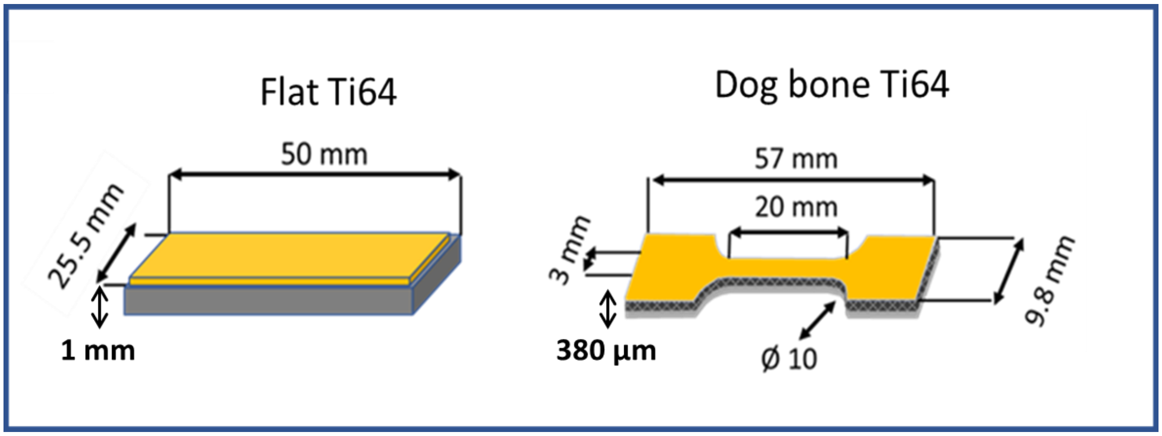

Figure 5.1 Schematic representation of flat rectangular thin sample and dog-bone tensile sample with their corresponding dimensions.

For the sake of brevity, the specimens will be named according to the main chemical element involved in their production. Therefore, the Ti-6Al-4V substrate specimens will be referred to as Ti64, the substrate with interface layers will be assigned as Ar plasma, Ti impl (for Titanium implantation), and Nit (for nitrided), while the coated specimens with its interface will be referred to as TiN-Ar, TiN-Ti, and TiN-Nit.

5.3.2 Microstructural characteristics

A laser scanning confocal microscope (LSCM) Olympus LEXT OLS4100 was used to evaluate the surface roughness on samples before and after pre-treatments and coating deposition processes. The surface roughness was measured using topographic (height) maps on Ti64 and on the coated samples. The average roughness observed was ~0.020±0.005 µm for the polished Ti64 and 0.30±0.05 µm and for the coated samples.

Images of the treated and coated samples after micro-tensile testing were examined using Field-Emission Scanning Electron Microscopy (FE-SEM, JEOL JSM 7600F) with an acceleration voltage of 5 kV. The observations of surfaces and cross-sections were performed directly on the fractured area without specific sample preparation.

The crystallographic structure, preferential orientation, and the crystallite size (CS) of the TiN coatings and of the interface layers were determined by XRD using a grazing incidence geometry. The XRD measurements were carried out with a Bruker D8-Discover X-ray diffractometer equipped with a Cu target (Kα radiation, wavelength λ = 0.154 nm) and a Göbel mirror to obtain a parallel beam configuration. The XRD patterns were measured using incidence angles α = 3°. The effect of crystallographic texture was taken into consideration by correcting the measured intensity of the coated samples. The intensity ratio of the three main *hkl* planes were evaluated as $(I_{(hkl)}/I_{0(hkl)})/[(1/n)\Sigma(I_{(hkl)}/I_{0(hkl)})]$, where $I_{(hkl)}$ is the measured relative intensity of the (*hkl*) diffraction plane, and $I_{0(hkl)}$ is the relative intensity from all of the *(hkl)* planes in the coating [205]–[207]. The average CS of the TiN coatings was estimated by the Williamson-Hall analysis [239].

5.3.3 Mechanical characteristics

The hardness, H, and the reduced Young's modulus, E_r, were determined by depth-sensing indentation (TI950 Triboindenter, Bruker) using a Berkovich pyramidal tip with an area function calibrated using a fused silica standard. Three 10x10 indentation matrices with the peak loads of the 100 indents varying from 100 to 9000 μN were performed, and individual indentation H and E_r values were obtained using the widely accepted Oliver and Pharr analysis method [216]. For each sample, the coating or surface properties were obtained using a methodology described in the ISO standard 14577 part 4 [217].

The RS of the interface layers and across the coating–interface-substrate structures were measured by grazing incidence X-ray diffraction (GIXRD) using the Multireflection method (MGIXRD) [148], [150], [276]. The RS obtained for the interface layers before coating deposition were measured using an incidence angle of α= 3°. In addition, the RS depth profiles measurements on coated samples were evaluated using incidence angles α = 1°, 2°, 3°, 5° and 10° to cover penetration depths from approximately 0.3 μm to 3 μm. Each angle was chosen to obtain information corresponding to coating, the interfacial layer and the substrate [275].

The micro-scratch testing was used to evaluate the adhesion and cohesive failure of the hard coatings. The tensile cohesive failure of the coating, known as critical load 1 (L_{C1}), and the coating adhesion or critical load 2 (L_{C2}), were evaluated using a Micro-Combi Tester apparatus (Anton Paar) with a Rockwell C indenter with a tip radius of 200 µm, under a progressively increasing load from 0.03 to 30 N at a speed of 10 mm/min along a length of 9 mm. L_{C1} was determined as the normal force where the first crack occurred, while L_{C2} was associated with the load at which delamination of the coating was first observed. Both of these were evaluated using post-mortem visual observation of the scratch tracks.

The micro-tensile tests were carried out in two different configurations: i) continuous, and ii) interrupted testing. Both types of tests were performed with a Kammrath & Weiss 5 kN micro-tensile apparatus using an applied displacement rate of 2.5 µm/s. The goal of the continuous tests was to assess the stress-strain (*S-S*) dependence in order to evaluate the macroscopic mechanical properties of the specimens, such as yield stress (YS), ultimate tensile stress (UTS), and strain to fracture. The macroscopic strain was measured with a Keyence LS-7030M optical extensometer. The main goal of the interrupted tests was to record high-magnification images at increasing applied strain to evaluate the crack evolution, and especially the appearance of cracks, known as crack onset strain (COS), which allows one to estimate the coating toughness. The interruption duration of the tensile test to acquire the images was approximately 1 min each cycle.

The interrupted tensile tests were performed under the LSCM Olympus LEXT OLS4100 microscope to record the sample's surfaces during the whole test procedure. Optical laser images and topographic (height) maps were acquired covering a 640x640 µm field of view with a spatial resolution of 0.16 µm/pixel. This microscopy technique allows one to study the crack evolution on the sample surfaces. The applied load and strain ranges were selected in order to ensure the detection of crack onset and to observe the complete crack evolution. The specimen was increasingly loaded in the elastic regime by steps of 25 N and then by displacement steps of 50 µm past the elastic limit, until complete failure. The crosshead displacement was maintained during image acquisition to keep the cracks open, making them as visible as possible. The crack density, expressed as the number of cracks per mm, was measured on the optical images with a custom script written for the image analysis program Fiji [277].

5.4 Results

In this section, we first describe the microstructural characteristics of the coating systems with different interfaces, followed by a description of the main mechanical elasto-plastic properties and RS depth profiles and their effect on the crack formation and propagation as documented by the tensile test results.

5.4.1 Microstructural characteristics

The coating-substrate systems including 1 µm thick TiN films with different interfaces are illustrated by SEM cross-section micrographs in Figure 5.2**.** All images reveal a predominantly columnar structure of the films. At these magnifications, the morphology of each interface layer does not exhibit any visible effect of the plasma treatments applied to the substrate prior to coating deposition. The images were taken after micro-tensile testing, therefore coatings present surface cracks.

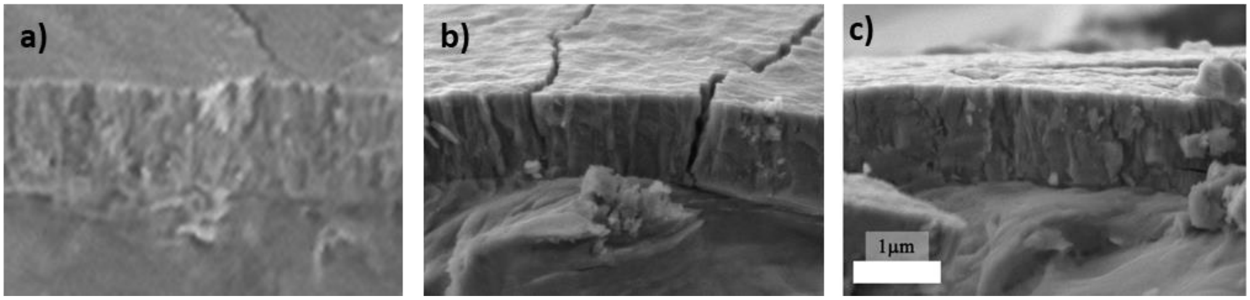

Figure 5.2 Cross-section SEM images of a) TiN-Nit, b) TiN-Ti and c) TiN-Ar specimens after micro-tensile testing; the scale bar in (c) corresponds to all three SEM images (5 kV, secondary electron detector). The loading direction goes approximately from the left to the right.

The crystallographic characteristics of the TiN/Interface/Ti64 systems are represented by the GIXRD diffraction patterns in Figure 5.3. Ti64 is composed of the two phases of Ti, namely, α-Ti with hexagonal close-packed (hcp) structure and β-Ti with a body-centered cubic (bcc) structure. The XRD patterns of untreated and uncoated Ti64 reveal a strong signal of the α-Ti phase. Therefore, we assigned the α-Ti phase (PDF 44-1294) with hcp structure to the corresponding indexation of Ti64. The patterns show that all coatings have a NaCl structure (δ-TiN, PDF 38-1420) with diffraction peaks at 2θ angles of 36.5°, 42.6° and 61.7°, 73.9° and 77.5° which are associated with the (111), (200), (220), (311) and (222) diffraction planes, respectively. Besides the δ-TiN phase peaks, the presence of α-Ti arises from the Ti64 substrate.

The crystallite sizes in the coatings gave smaller values of around 12 nm for the TiN-Ar and TiN-Ti samples, while for the TiN-Nit, we obtained ~16 nm. For TiN-Ar and TiN-Ti, we observed a higher (200) intensities, revealing a preferential orientation in the coatings, and a mix of (111) and (200) for TiN-Nit. For clarity, the XRD results are summarized in Table 5.1 The preferential orientation of these three coatings was previously studied in detail by transmission Kikuchi diffraction [275].

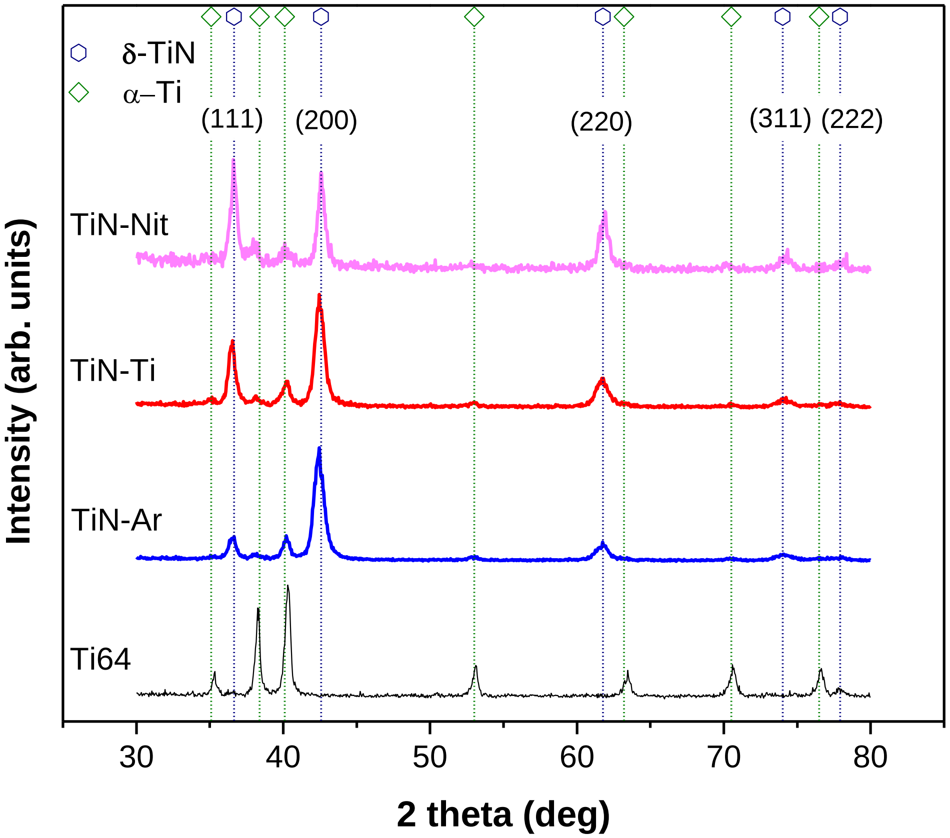

Figure 5.3 Diffractograms of the TiN films deposited on Ti64 with different interfaces.

Table 5.1 Crystallite size (CS) and preferential orientation (PO) of TiN coatings on Ti64 with different interface treatments.

TiN-Nit		***TiN-Ti***		***TiN-Ar***	
CS (nm)	**PO**	**CS (nm)**	**PO**	**CS (nm)**	**PO**
15.9	(111)-(200)	11.6	(200)	12.1	(200)

5.4.2 Hardness, Young’s modulus, residual stress and scratch resistance

Materials resistance to crack formation and propagation is closely related to the elasto-plastic properties. Figure 5.4 reports *H* and *Er* depth profiles for both the interfacial layers alone, and the complete coated samples with the three interface treatments. The dependence of *H* and *Er* on contact depth of treated Ti64 shows a sharp increase within the first 50 nm, especially for Nit, followed by a monotonic decrease further from the surface toward the substrate bulk properties. For comparison, *H* and *Er* of the Ti64 before plasma treatment are ~5 GPa and 140 GPa, respectively.

For the three TiN coated samples, *H* values are similar around 28±1 GPa, while *Er* decreases from 380 to 275 GPa as the contact depths go from 10 to 100 nm, in agreement with values reported for PVD TiN coatings [274], [278]. A summary of the mechanical properties is given in Table 5.2**.**

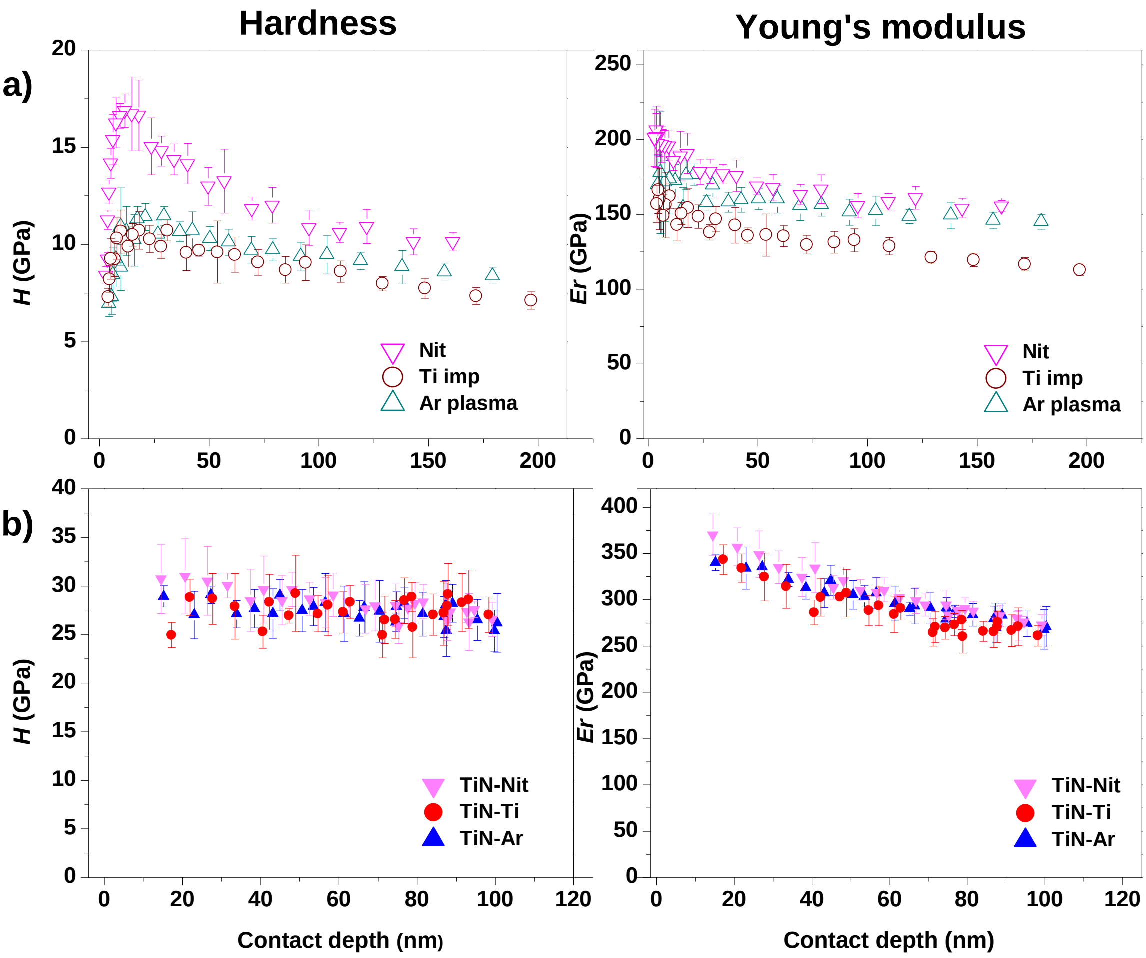

Figure 5.4 Hardness and reduced Young's modulus of a) Ti64 with surface treatments, and b) TiN-coated specimens with different interfaces.

RS values for the surface of the Ti64 substrate and of the interface layers are presented in Figure 5.5a. The substrate alone shows a low compressive RS around 110 MPa, probably imposed by surface preparation and cleaning. The Nit interface exhibits a higher RS compared to the Ar plasma and Ti impl samples.

The RS depth profiles for the TiN-coated samples are shown in Figure 5.5b. All systems exhibit compressive RS in all three regions of the depth-profile which include the coating, interface and near-surface substrate. Particularly notable is the difference in RS within the TiN coatings with different interface layers: The RS at the surface of the TiN-Nit sample is about 800 MPa greater than that of the TiN-Ti and TiN-Ar ones. A similar effect of RS is also seen within the interface layers themselves; however, the variation is significantly smaller: The compressive RS of the TiN-Nit system is systematically larger compared to its counterparts, but at a depth of 1.5 and 3.0 μm, it starts to be in the range of experimental error. This large difference between of the samples indicates that the choice of interface treatment has a strong effect on the RS levels in the TiN coating. Considering the stress balance, one can assume that the Ti64 substrates present tensile RS beyond 5 μm distance from the surface, as observed in the RS measurements reported previously [275].

The cohesive failure (L_{C1}) and adhesion (L_{C2}) of the TiN coatings with different interface treatments on Ti64 samples were evaluated by the micro-scratch technique (see Figure 5.6**)**. L_{C1} observed as tensile cracks, and L_{C2} identified in the form of buckling spallation along the scratch track, were formed by gradually increasing the load according to the ASTM C1624 – 05 standard [220]. The TiN-Nit sample exhibits the highest L_{C1} and L_{C2} values of ~13 N and ~23 N, respectively, compared to TiN-Ti and TiN-Ar that yield L_{C1} and L_{C2} values of about 8 N and 18 N, respectively. It should be noted that L_{C1} and L_{C2} increase with increasing RS, in conjunction with the type of the interface layer that plays a prominent role.

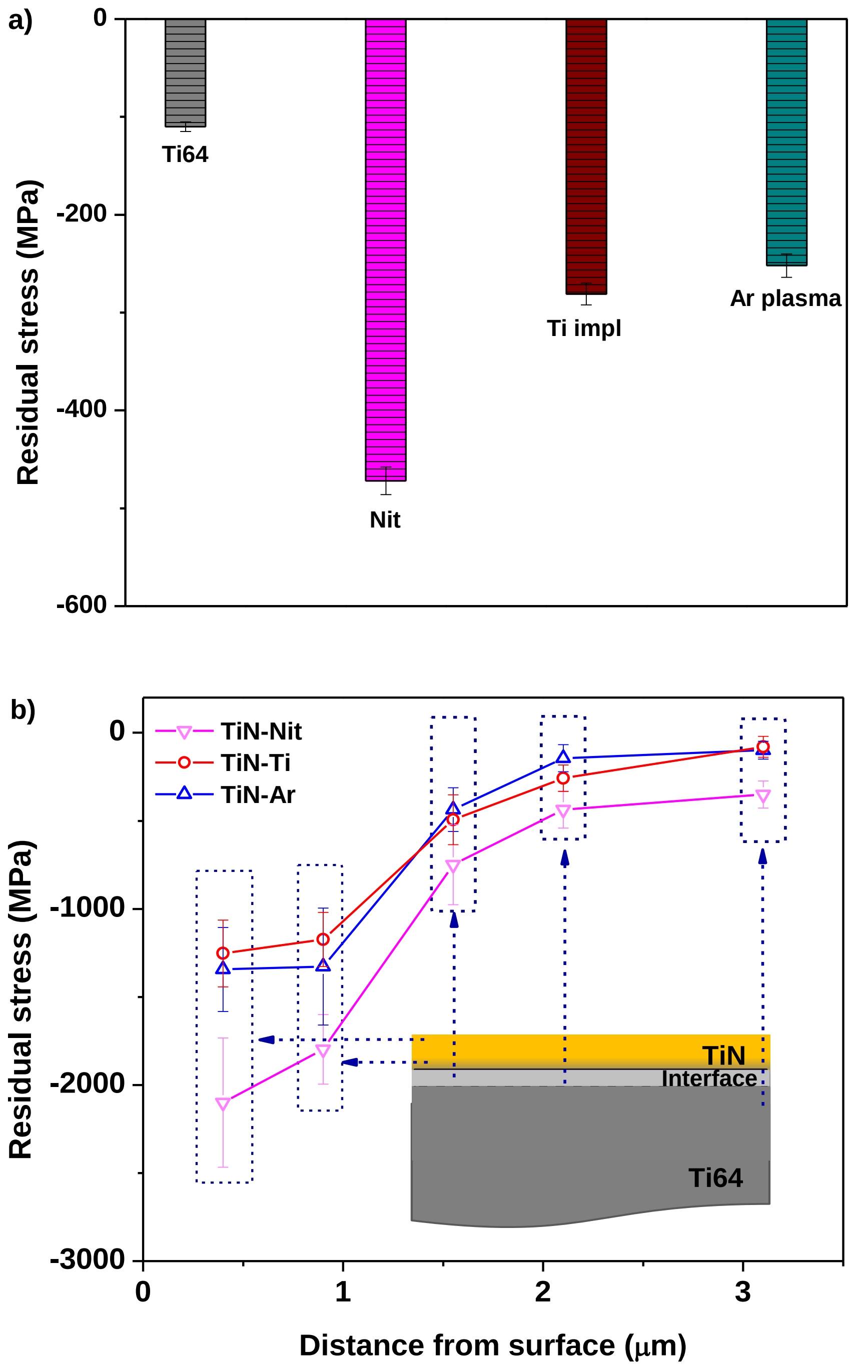

Figure 5.5 a) RS in the near surface region in the Ti64 alloy following different plasma treatments; b) RS depth profiles of TiN coatings on Ti64 with different interfaces, from the coating surface to the substrate. The blue doted arrows (horizontal and vertical) schematically indicate the penetration depth of the X-ray beam on the coated system during the measurement; all measurements were performed by GIXRD.

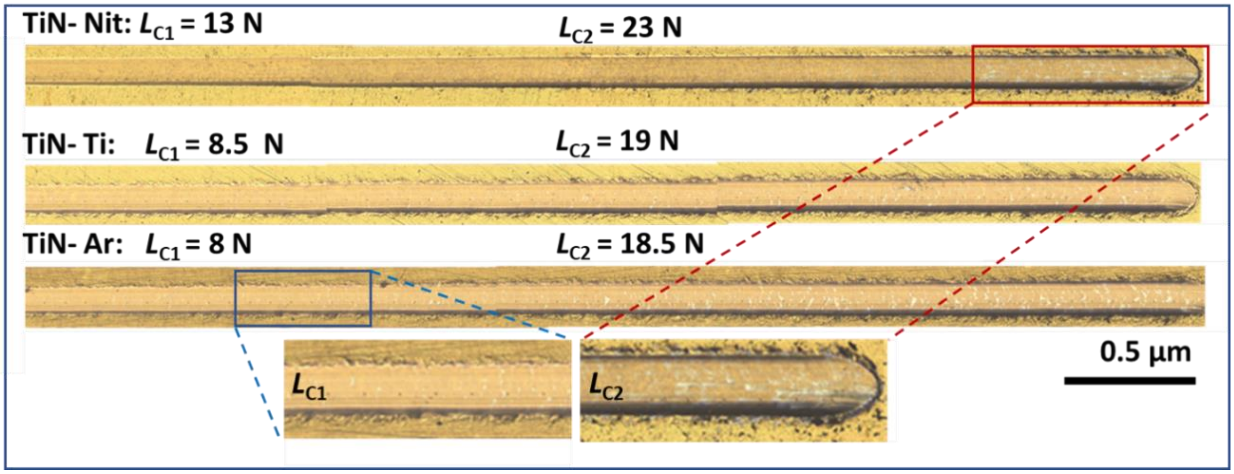

Figure 5.6 Micro-scratch tracks for TiN coatings with three different interface treatments where the L_{C1} and L_{C2} areas are illustrated.

5.4.3 Tensile test characterization

The Strain-Stress curves from continuous tensile tests for the surface treated and coated specimens are shown in Figure 5.7. they show a Young’s modulus similar to the substrate (approximately 100 GPa) in agreement with values reported in the literature for Ti64 [279]. The YS and UTS values for the treated and coated samples are slightly lower compared to the Ti64 alone, while the UTS values of the treated samples are comparable and within 10 to 15% variation. One can conclude that the strain to fracture is reduced by a factor of 1.5 to 2.2 for the Nit and Ti impl specimens, while for the Ar plasma treatment, it is similar to the initial material. Figure 5.7b shows that after the TiN coating deposition, the fracture strain becomes similar for all specimens, with a reduction factor of 1.6 to 1.8 compared to the uncoated material.

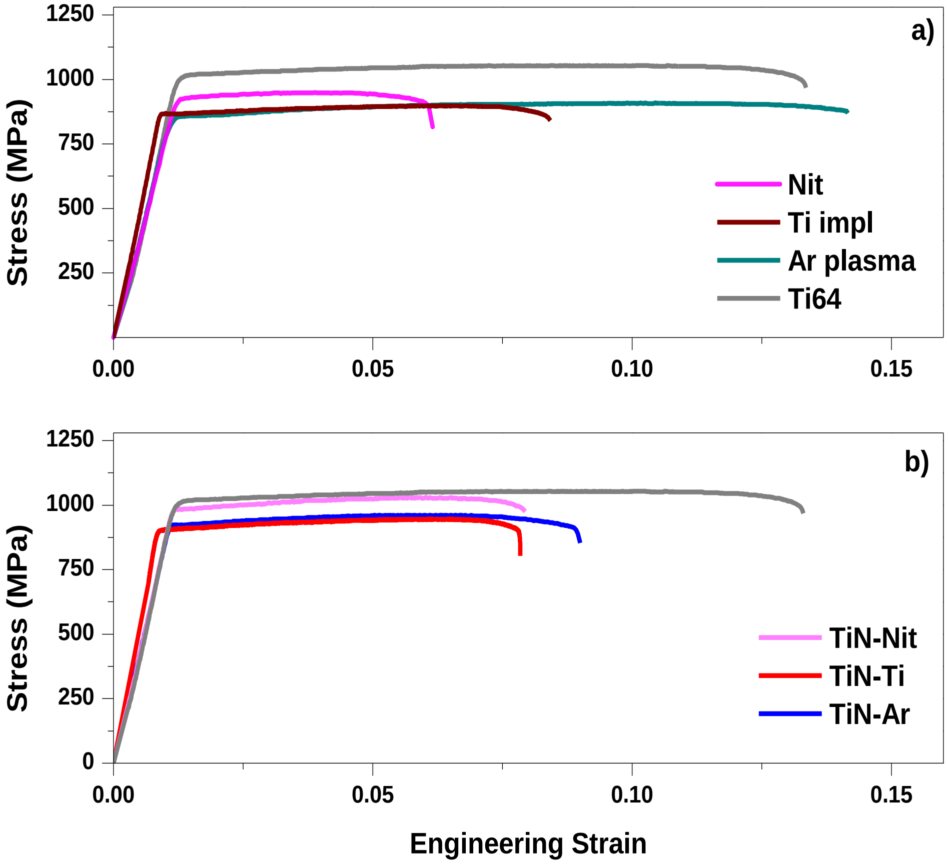

Figure 5.7 Stress-strain (*S*-*S*) curves for the a) surface-treated Ti64, and b) coated specimens with different interfaces.

The mechanical properties obtained from nanoindentation and micro-tensile testing are summarized in Table 5.2. The UTS and YS results of coated components are slightly higher for the TiN-Nit sample due to the elastic support created by the nitriding treatment on the substrate during tensile loading. Jaeger et al. [280] reported a UTS value of 491±82 MPa for a free-standing TiN coating, which was previously removed from the substrate, indicating that the UTS of TiN corresponds to almost half of the one from Ti64, which could influence the final UTS of a coated component. However, it is known that the UTS values for a coated specimen can in fact be influenced by the ratio between the coating and the substrate thickness. Specifically, studies on brittle thin coatings on metallic substrates have shown that when the thickness of the coating is minimum compared to the one of the substrate (for example, in our case the total thickness of the substrate is approximately 400 times thicker than that of the TiN coating), the Strain-Stress diagram for the complete substrate–coating system is governed by the substrate curve and the effect of the TiN coating on the resulting mechanical UTS can be neglected [281].

Table 5.2 Mechanical properties of all samples extracted from nanoindentation and micro-tensile tests.

Sample	**H (GPa)**	**Er (GPa)**	**YS (MPa)**	**UTS (MPa)**	**Strain to fracture**
Ti64	5.2	140	1022	1050	0.135
Nit	15.6	195	947	950	0.062
Ti impl	10.2	155	873	896	0.088
Ar plasma	11.0	168	867	912	0.140
TiN-Nit	29.3	377	1001	1018	0.078
TiN-Ti	27.7	352	909	937	0.074
TiN-Ar	27.8	355	920	938	0.082

The continuous tests described above were complemented by interrupted tests assisted by LSCM imaging in order to characterize the crack onset and evolution. The crack density curves against the applied strain for the coated specimens are plotted in Figure 5.8. All samples demonstrate the four typical stages of crack morphology, namely: i) crack onset, ii) multiplication, iii) saturation (presence of secondary cracks or cross-linking cracks), and iv) fracture [273]. The COS is defined by the first surface crack or a group of surface cracks detected on the observation area of the confocal microscope during the *in situ* micro tensile test. The COS values identified in Figure 5.8 are similar for the three interface treatments, ranging only from 0.9% and 1.0% for TiN-Ti and TiN-Ar samples, respectively, to a slightly higher value of 1.1% for the TiN-Nit sample. At the saturation stage, the TiN-Nit sample shows the highest crack density with 120 cracks/mm, while the TiN-Ti sample exhibits the lowest density with ~95 cracks/mm. Figure 5.9 provides representative images showing the different stages of crack morphology and crack density level on TiN-Nit. Cracks can be observed with an average spacing of around 10 μm at the saturation point. Cracks are perpendicular to the tensile force direction, fulfilling the basic requirement of the periodic cracking method [274]. In addition, cross-linking cracks appear at 45° at a late stage of deformation as illustrated in Figure 5.9d. This corresponds to the maximum shear stress orientation.

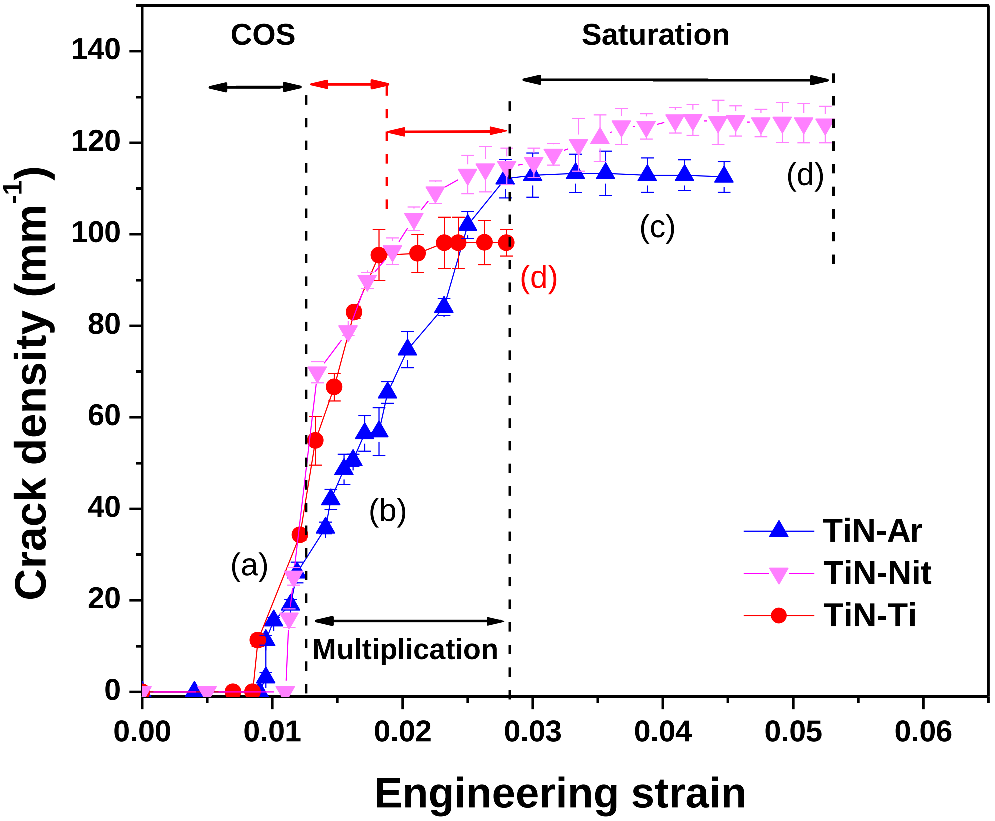

Figure 5.8- Average crack density as a function of the engineering strain of TiN coatings on Ti64 with different interfaces: (a) crack onset, (b) multiplication, (c) saturation, and (d) specimen fracture.

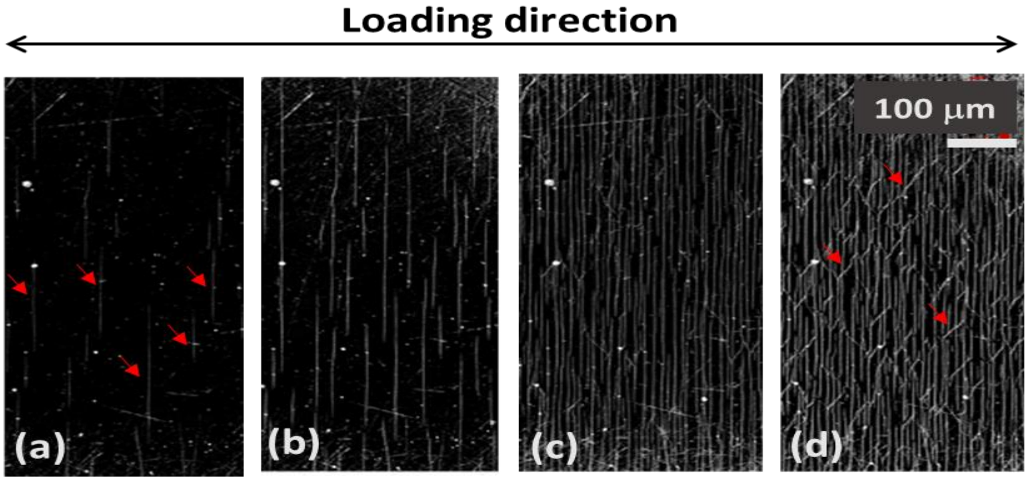

Figure 5.9 Representative confocal optical images of TiN-Nit surfaces as a function of the engineering strain: (a) crack onset, (b) multiplication, (c) saturation, and (d) secondary crack stages. The red arrows in images (a) identify initial cracks, and in (d) secondary cracks.

The surfaces of the Ti64 substrate and of the treated and coated specimens following the tensile test were further characterized by SEM (Figures 5.10, 5.11 and 5.12). Figure 5.10 shows SEM images taken on the surface of Ti64 before and after interface treatments at 1 and 5 mm distances from the fracture zone (top and bottom, respectively). These images reveal the deformation of the microstructure and the presence of cracks. The Ti64 substrate displays grain deformation at a 1 mm distance due to the localization of the deformation in the fracture zone, but at 5 mm the grain deformation is no longer visible. Similarly, Ti impl and Ar plasma samples show surface grain deformation at 1 mm, but it is significantly decreased at 5 mm. Ti impl presented small surface defects in the zone close to the fracture, and none at 5 mm. On the contrary, the Nit specimen presents little to no surface grain deformation, but a high amount of cracks at 1 mm, and to a lower extend at 5 mm. These observations correlate very well with the measured fracture strains (see Figure 5.7a), where Ti64 and Ar plasma, with no surface cracks, presented high strain to fracture values compared to the much lower strain to fracture for the Nit specimen.

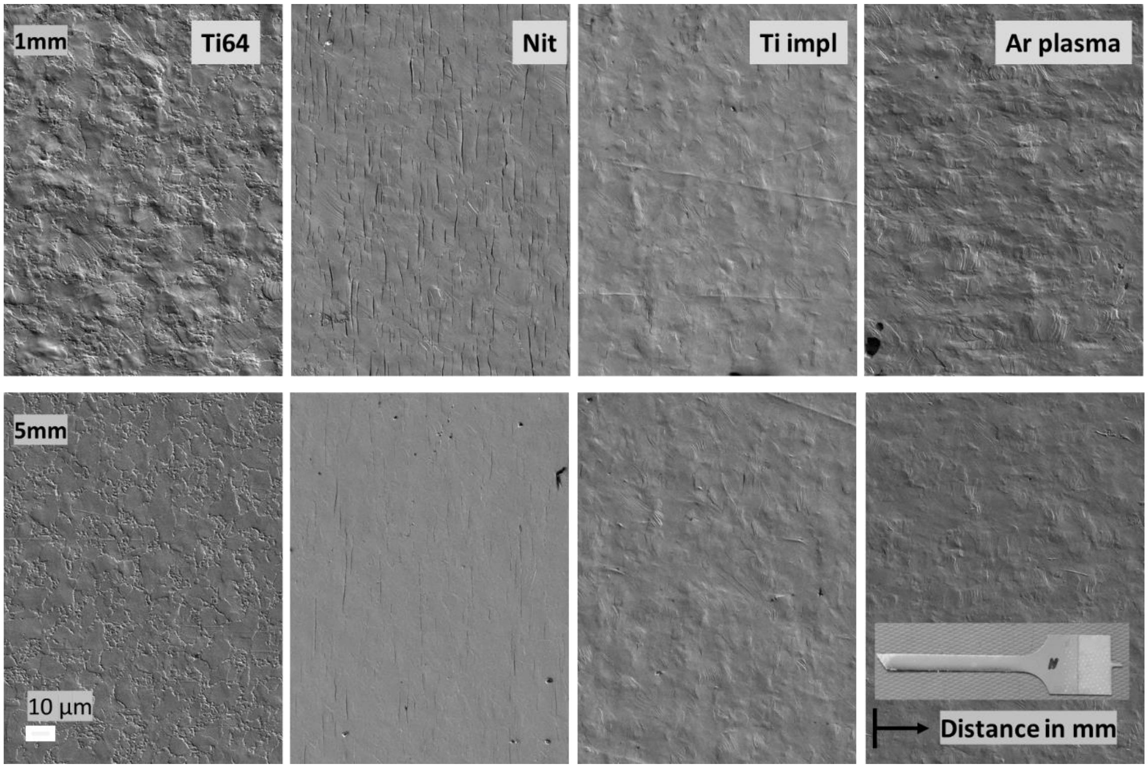

Figure 5.10 SEM images of treated surfaces of Ti64 at 1mm (top) and 5mm (bottom) distances from the fracture zone after the tensile test.

The analyses of optical and cross-sectional SEM images indicate that during tensile testing, the coating-substrate fracture process starts with cracks in the coating perpendicular to the loading direction (Figures 5.9, 5.11 and 5.12). Once the strain is increased, the substrate's deformation, as observed in Figure 10, causes grain deformation, which leads to crack nucleation in the coatings. These cracks propagate from the surface towards the interface layer as was observed in Figure 5.2 and as it is typical for cracking behaviour of brittle ceramic coatings [272], [282], [283].

Figures 5.11 a and b present a panorama of the fracture zone, and a cross-section of the TiN-Ti specimen after micro-tensile testing. In both images, cracks can be seen to penetrate through the coating and stop in the interface zone (top of the images and in Figure 5.2b). In all samples, the fracture morphology of the Ti64 substrate is consistent with the expected ductile fracture of this material [254]. Coated specimens with different plasma treatments show a similar fracture behaviour.

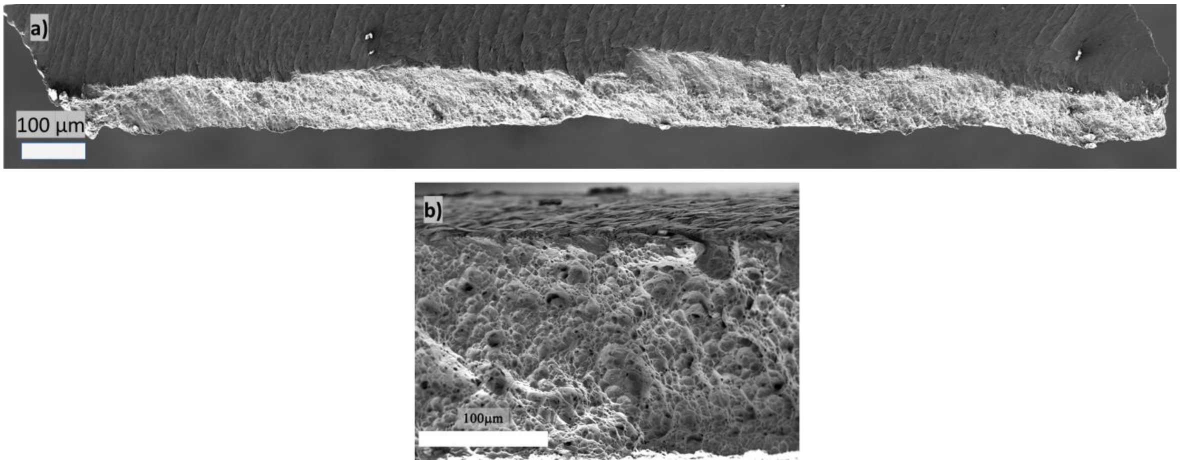

Figure 5.11 SEM images of the TiN-Ti specimen show a) panorama of the fracture zone, and b) a cross section view, after the tensile test.

Figure 5.12 presents the surfaces of coated specimens observed by SEM at distances of 0, 1, 3 and 5 millimeters from the fracture zone. It is worth to note that all samples have undergone similar amounts of deformation at rupture (about 8%). All coatings show delamination at the fracture surface and present a high number of cracks perpendicular and at 45° to the tensile force direction. The presence of secondary (or cross-linking) cracks at 45° can be attributed to the fact that the relatively thin coating (~400 times thinner than the substrate) is affected by the deformation of thin Ti64 substrate that in plain stress and the onset of sample necking (ductile failure) under the applied strain [272], [282]. However, in the images at 1 mm distance, the cracking pattern is minimum only for TiN-Ar, while for TiN-Nit and TiN-Ti, the density of cracks is still high. Images taken at distances of 3 and 5 mm show that TiN-Ar presents only small grain deformation with almost no visible cracks, in contrast to TiN-Nit and TiN-Ti, for which many perpendicular surface cracks are observed at 5 mm.

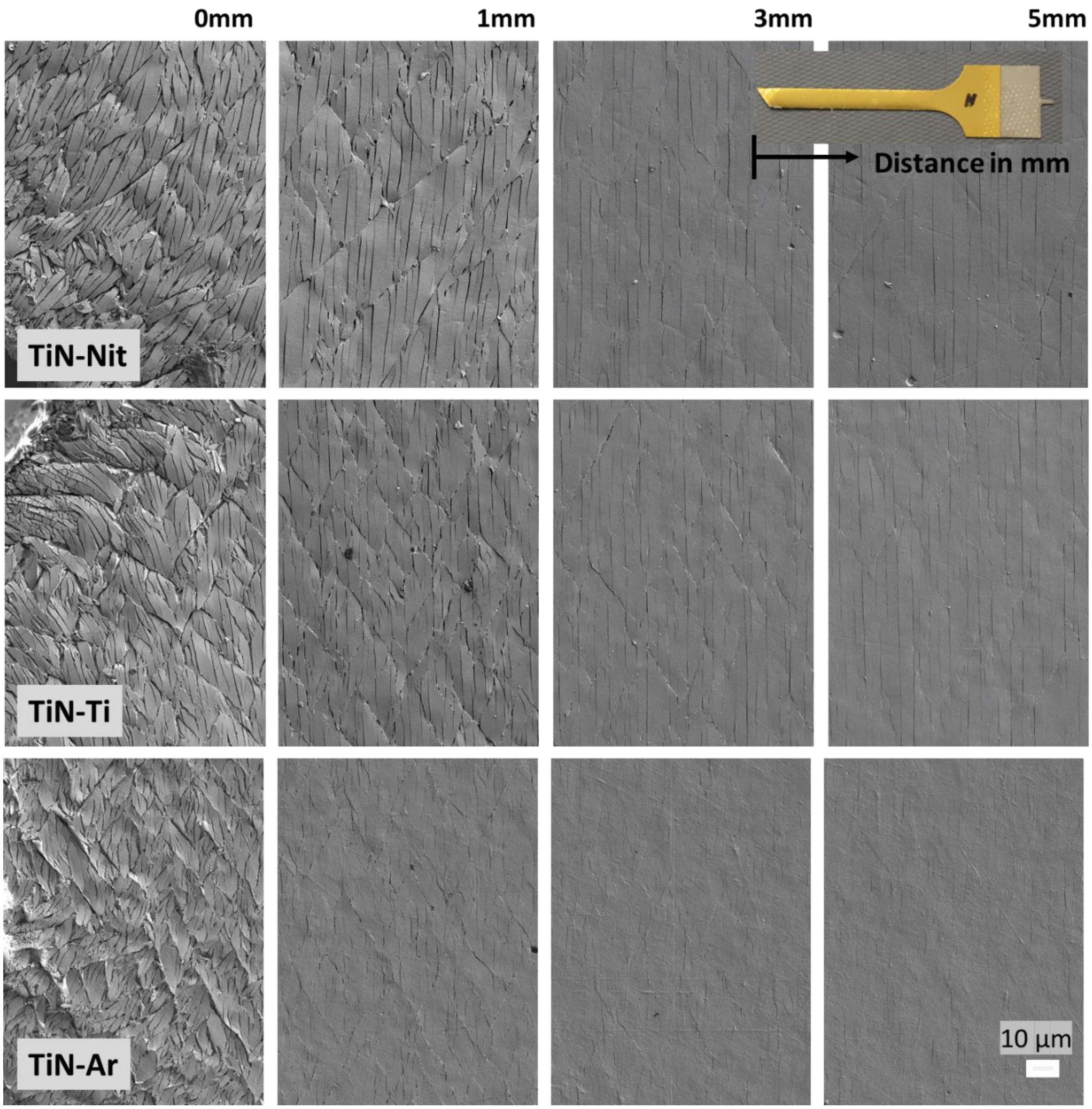

Figure 5.12 SEM images of coated specimens with different interface treatments. Images were taken at 0, 1, 3 and 5 mm distances from the fracture zone after the tensile test.

5.5 Discussion

The coating-substrate system presented in this work is composed of a brittle thin coating and a ductile substrate with an interface layer. As shown, such systems present a gradient of RS characterized by a high compressive stress level in coatings, and a lower compressive stress level at interface until it is close to zero in the substrate, as shown in Figure 5.5. In this context, the compressive RS improves the mechanical properties, fracture resistance, and adhesion of brittle materials such as ceramics as also reported by others [284], [285]. However, a high difference of RS between coating and substrate could lead to catastrophic failure. Therefore, the application and optimization of interface treatments is fundamental to control the RS gradient through the coating-interface-substrate system influencing the structural stability and durability.

In metallic substrates coated with ceramic films, as in our case, a competition of mechanisms can occur between the brittle coating with a high level of compressive RS and the ductile substrate with RS close to the tensile regime. This influences the crack nucleation and propagation during the micro tensile test, specifically when considering a shear lag model [157] by which the transfer of shear strain from ductile substrate to brittle coatings during the application of tensile strain to the substrate can relieve the compressive RS in the coating [261], [286], [287]. The interfacial shear stress creates tensile stress in the coating leading to the coating's fracture, forming cracks perpendicular to the tensile loading as it was observed on the SEM images in Figure 5.12 and on the saturation stage in the crack density curves in Figure 5.8, specially for TiN-Nit. For strains larger than the COS, cracks are produced and propagated with reduced crack spacing. Once the crack nucleation occurs, the load supported by the coating is maintained by the substrate underneath, generating additional stress in the substrate. Therefore, the RS gradient present through the coating-interface not only enhances the coating-substrate adhesion, but it also plays a significant role in delaying component failure.

The sample with a highest compressive RS gradient, TiN-Nit, shows a higher resistance to crack onset, and a higher crack density with a reduced crack spacing as observed in Figure 5.8, Indeed, since the interface with compressive RS represents an elastic coupling between coating and substrate, when the applied stress is increased, the coating fracture strength is exceeded, generating a new crack at the center of the width between two already existing cracks, leading to a saturation of crack density also observed by others [157], [288].

The XRD and nanoindentation analyses indicated that the TiN-Nit sample presents a (111) preferred orientation with a higher hardness value compared to TiN-Ar and TiN-Ti samples that favor (200) preferred orientation. Similar microstructural characteristics and their relation to the mechanical properties, specially hardness, were reported in our previous study [275]. This phenomenon can be explained by the relationship between the (111) preferred orientation and the resolved shear stress on the slip system of TiN with a NaCl-type structure, in which the active slip of this phase can occur within the {110}<110> boundary [274], [289]. Therefore, if the applied force is perpendicular to the (111) plane, the resolved shear stress on all the slip systems is zero, and plastic deformation cannot be induced, leading to a higher measured hardness.

Micro scratch testing is widely recognized as a qualitative technique to predict crack initiation resistance in fracture mechanics. Specifically, the L_{C1} and L_{C2} results indicate that interface treatments influence the TiN coating adhesion by inducing different RS levels in the coating; consequently, the onset of cracks is influenced when an external load is applied. In such case, the more difficult it is to create a crack, the higher the L_{C1}. In fact, the crack propagation resistance is proportional to L_{C1} and to the difference between L_{C1} and L_{C2} [290]. This assumption considers that the crack onset does not represent the coating's total failure; thus, it is fundamentally related to the amount of load a coating can resist before delamination.

The above phenomena agree with the coating effect on the COS (0.9% and 1.1%) determined by our micro tensile tests (Figure 5.8) where the presence of higher levels of compressive RS retards cracking onset results in higher L_{C1} values from 8 N up to 13 N on TiN-Ti and TiN-Nit with RS of -1.35 GPa and -2.1 GPa, respectively. Therefore, we can conclude that the cohesive and adhesive properties calculated from micro-scratch testing well predict the trend of COS observed in Figure 5.8, as well as the crack density at saturation observed experimentally by the fragmentation test.

In order to quantify the effect of RS on the fracture behavior of the TiN/Interface/Ti64 system, the critical energy release rate, G_C, and interfacial shear strength, τ, can be calculated from the experimental results obtained in the present work. Considering a brittle coating, the data from the tensile testing and the modulus results from nanoindentation are used to analyse the fracture resistance in terms of G_C given by [112]:

$$G_c = \frac{\sigma_C^2 t}{2*E}[\pi g(\alpha_D \beta_D)] \tag{1}$$

where σ_c is the stress when cracks first appear, known as critical stress $\sigma_c = E\varepsilon_{COS}$. Here, ε_{COS} is the tensile crack onset strain, t is the coating's thickness, and $g(\alpha_D \beta_D)$ is a dimensionless coefficient given by Dundurs' parameters [113], which characterizes the elastic mismatch of the coating and of the substrate in relation to E and the Poisson ratio of both materials; typical Poisson ratio is 0.25 and 0.30 for TiN and Ti64, respectively. Additionally, τ was calculated from

$$\tau = 2\rho t \sigma_{Sat} = \pi \hat{\sigma} t/\delta \tag{2}$$

where $\hat{\sigma} = E\varepsilon_{COS} + \sigma_{Res}$, σ_{Res} corresponds to the coating RS, ρ is the average crack distance at the saturation regime, and δ is the maximum inter-crack spacing when the crack density reaches saturation.

The relation between the COS values (obtained from the crack density curves in Figure 5.8), the τ and the RS values are shown plotted in Figure 5.13 as a function of energy release rate, G_C corresponding to the formation of the first cracks.

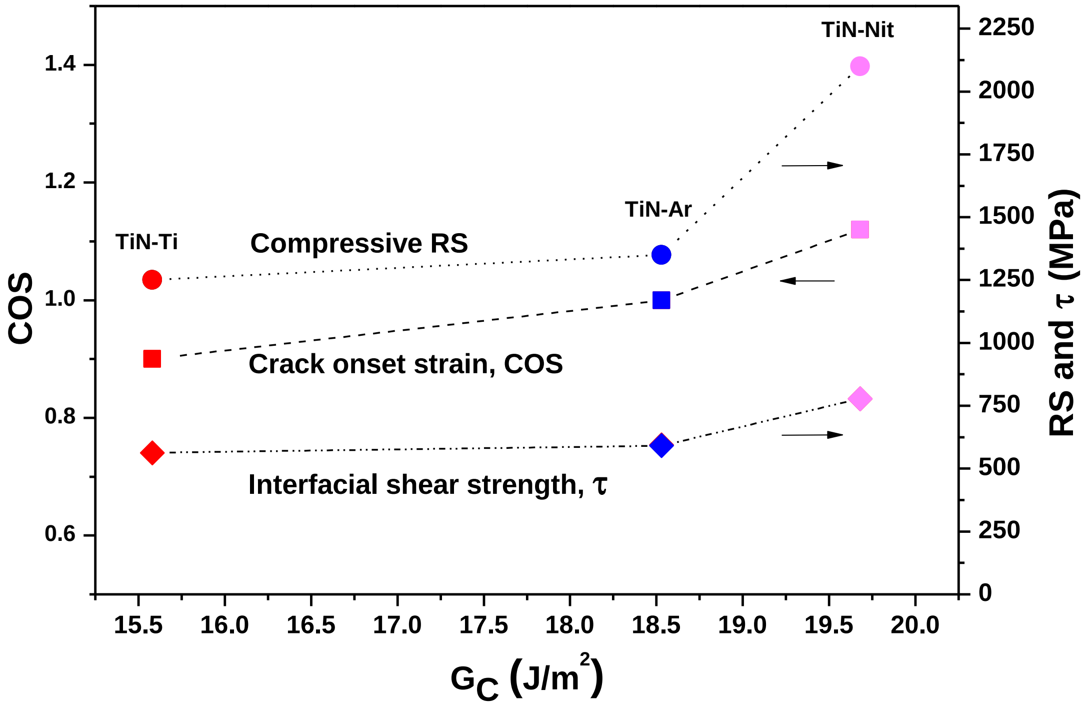

Figure 5.13 COS, coating residual stress (RS) and interfacial shear strength (τ) as a function of critical energy release rate (G_C) for TiN coatings with different interfaces.

The difference in COS between samples is relatively small; still, we conclude that higher COS is favored by compressive RS in the coating. The G_C reported in Figure 5.13 can be used to determine the fracture toughness, K_{1C} of the coating given by the linear elastic mechanics equation, $K_{1c} = \sqrt{G_c E}$. In our case, fracture toughness of the three systems is between 2.3 and 2.6 $\text{MPa}\cdot\text{m}^{0.5}$, indicating that TiN-Nit has the higher fracture toughness, followed by the TiN-Ar and TiN-Ti. The

G_C and K_{1C} values agree with the results in other works obtained for PVD TiN coatings by bending, indentation, tension and internal energy induced cracking [270], [271], [291]–[294].

The interfacial shear strength (τ) values shown in Figure 5.13 are 580, 610 and 795 MPa for TiN-Ti, TiN-Ar and TiN-Nit, respectively. It is interesting to point out that these values are comparable to that of the substrate (τ for Ti64 is ~760 MPa) as supported by the observations by optical and SEM imaging (Figures 5.8 and 5.12). In addition, we note that our results are also in agreement with those obtained in [273], [295] that reported τ = 650 MPa for 1.3 μm thick TiN coatings on stainless steel after applying a factor $\sqrt{3}$ corresponding to the von Mises' yield criterion [296].

It can be considered that in coatings with a similar thickness (~1 μm), the presence of smaller crack spacing represents a higher stress-transfer between the coating and the substrate, resulting from a higher interfacial adhesion [272]. The stress relief between coating cracks and the presence of RS into the substrate's surface (interface zone) reduced the elastic-plastic deformation on the substrate; however, surface cracks are formed at the nitrided interface. When the crack spacing becomes saturated, the interfacial shear stress approaches its critical value to delaminate from the interface. As a consequence, a higher compressive RS observed for TiN-Nit samples in comparison to TiN-Ar and TiN-Ti in Figure 5.5, gives rise to enhanced elastic coupling between the coating and the substrate that generate higher interfacial shear strength, higher energy release rate, and consequently higher COS as shown in Figure 5.13.

5.6 Conclusion

In this study, the mechanical properties, plastic deformation and coating-substrate fracture of TiN coatings on Ti64 substrate with different interfacial layers were evaluated and correlated with the residual stress in the system. The initial hardness of the Ti64 substrate (5 GPa) was substantially enhanced by plasma interface treatments that were performed to create interface layers and by subsequent TiN coating deposition up to ~15 GPa and ~29 GPa, respectively. In addition, plasma surface treatments gave rise to a significant increase of the near-surface compressive RS (-300 to -500 MPa), leading to a further enhanced RS in the TiN coatings due to a strong effect on the film growth (between -1.2 and -2.1 GPa depending on the interface). The RS was shown to have a considerable impact on the failure mechanism of the TiN/interface/Ti64 systems. Specifically, scratch tests showed that higher compressive RS results in higher L_{C1} and L_{C2} values: Nit surface yielded 13 N and 23 N, respectively, compared to Ar plasma treatment and Ti implantation with L_{C1} around 8 N and L_{C2} around 18 N.

The above described results are in agreement with the elasto-plastic properties determined by fracture analyses performed using micro-tensile tests. The COS varied between 0.9% to 1.1%, while critical energy release rate (15.0 J/m^2 and 19.7 J/m^2) and interfacial shear strength (550-760 MPa) are mainly influenced by compressive residual stress in the coating. The interface treatment appears to particularly affect the fracture mechanism of Ti64; however, this detrimental effect can be mitigated by a coating with a high compressive RS at the interface layer and within the coating itself. The results underlined the fact that the mechanical behavior in general, and adhesion in particular, of the coatings are significantly governed by the coating-substrate system's collective response to delay crack nucleation and propagation through the substrate, and therefore delay the component fracture. The global RS of the coating-interface-substrate system, represented by the RS depth profiles, impacts the fracture mechanism of coated specimens, whereas optimum compressive RS levels allow one to delay failure of the components to enhance their durability.

5.7 Acknowledgments

The authors wish to thank Dr. Walid Jomaa, Mr. Francis Turcot and Mr. Sébastien Chénard for expert technical assistance. This work has been supported by the Natural Sciences and Engineering Research Council of Canada (NSERC) and Pratt & Whitney Canada through the NSERC Multisectoral Industrial Research Chair in Coatings and Surface Engineering grant (IRCPJ 433808-11), and through the NSERC Discovery Grant of JEKS (RGPIN-2016-06409).

CHAPTER 6 ARTICLE 3: SOLID SOLUTION HARDENING IN NANOLAMINATE ZRN-TIN COATINGS WITH ENHANCED WEAR RESISTANCE

E.J. Herrera-Jimenez[1], A. Raveh[1,2], T. Schmitt [1], E. Bousser[1], J.E. Klemberg-Sapieha[1], L. Martinu[1]

[1]*Department of Engineering Physics, Ecole Polytechnique, Box 6079, Station A, Montreal H3C 3A7, Quebec, Canada*

[2]*Advanced Coatings Center, Rotem Industries Ltd., Mishor Yamin, D.N. Arava 86800, Israel*

The article was accepted in Thin Solid Films (July 2019)

6.1 Abstract

Coating architectures with a microstructure controlled on nanoscale enables the attainment of enhanced mechanical, tribological and other properties. In the present study, we fabricated nanolaminate ZrN/TiN systems with various modulation periods, *L*, ranging from 1 to 100 nm using pulsed DC magnetron sputtering. It was observed that a modulation period of *L*=10 nm is a threshold value for the transition from a periodic to a solid solution structure. We demonstrate that the coatings with *L*<10 nm displayed a single-phase solid solution with a Zr-rich composition of $Ti_{0.35}Zr_{0.65}N$. This indicates the effect of mixing and/or diffusion between the two phases that occurred during the film growth. The crystallite size was found to vary with the modulation periodicity: we obtained 11-12.5 nm for the $Ti_{0.35}Zr_{0.65}N$ solid solution, and 14.5-25 nm for the laminate structure. The solid solution and interface strengthening were found to be the main cause of the hardening of the nanolaminate structure presenting a hardness of 32-35 GPa, significantly higher than for the individual TiN (21 GPa) and ZrN (16 GPa) single-layer coatings. The hard, solid solution system was found to exhibit the highest wear resistance corresponding to the highest values of the H/E and H^3/E^2 ratios related to a high resistance to plastic deformation and a high toughness. Finally, a model for the $Ti_{0.35}Zr_{0.65}N$ solid solution phase formation related to internal residual stress is proposed.

6.2 Introduction

Physical and mechanical properties of single-layer and multilayer coatings can be tailored by their microstructure [297]; specifically, an architecture based on the nanolaminate design can significantly enhance the tribological performance, most notably in harsh environments [298]. Such microstructures and the resulting film properties can be adjusted by an appropriate choice of the fabrication conditions [114], [299]. These possibilities have also been well documented by the development of nanocomposite (nc) coatings [300], [301]. It has been shown that the nanostructured hard coatings provide an unusual combination of mechanical and chemical properties, such as high thermal stability [302], [303], oxidation resistance [304], [305], high hardness and toughness, and high wear and corrosion resistance [114], [300].

High-performance nanostructured protective coatings can possess 2D or 3D architectures, and they can be formed of nanometer thick bilayers, a columnar nanostructure, nanograins surrounded by a tissue phase (nanocomposites), and a mixture of nanograins with varied crystallographic orientations [114]. Veprek et al. [300], [306] and Mitterer et al. [307] pointed out that compounds exhibiting a certain affinity with one another generally provide high thermal stability and service durability, and they are frequently super-hard, and possess unusual mechanical and physical properties. The participating compounds possess high chemical activity, and the system exhibits a thermodynamic driving force for phase segregation [308]. Most often, the synthesis requires sufficiently high temperature during deposition to promote rapid diffusion necessary to complete segregation during the growth, and to fulfill conditions for spinodal decomposition. These conditions are satisfied when the second derivative of the Gibbs free energy of the nanocomposite is negative, and when the interface strain energy is small related to the de-mixing energy of mixed phases. Examples of such systems include TiN-Si_3N_4, TiN-AlN, CrN-AlN and other combinations of materials [309], [310].

The structure and the mechanical properties of hard TiN and ZrN have been investigated for coatings deposited by various techniques including chemical and physical vapor deposition [311]. Recently, ternary Ti-Zr-N has attracted special attention due to a possibility of forming a single-phase solid solution [312] that may increase the hardness, thermal stability and corrosion/oxidation resistance at temperatures higher than those of the individual binary compounds.

Multilayer systems composed of individual layers that are several nanometers thick with a specific periodicity (nanolaminates) have attracted much interest because of their wear resistance in cutting tools and other applications [313], [314]. Since hard nitrides are frequently deposited on softer substrates, the design of the coating-substrate interface must be tailored for adhesion enhancement. Good adhesion is required in order to enable a wide range of uses in harsh environments such as in aerospace applications. Common methods include fabricating a metallic intermediate layer (frequently Cr or Ti) or a duplex treatment which includes surface hardening (nitriding or carburizing) prior to deposition [315].

In the present study we explain the main source of the enhanced tribological properties of nanolaminate ZrN/TiN coatings in the case of a high periodicity structure, $L<10$ nm, by the formation of a single solid solution phase, and for $L=10$ nm by formation of intermixing region at the interfaces, in comparison with monolithic ZrN and TiN or multilayer coatings with a low periodicity structure ($L\geq100$ nm).

6.3 Experimental methods

Individual coatings with a total thickness of about 3.5 μm, including monolithic ZrN and TiN, and ZrN-TiN multilayers with different modulation periods, were deposited on Ti-6Al-4V (Ti64) alloy substrates and silicon (c-Si) wafers. The thickness of the monolithic coatings, of the dual-layers, and the thickness of each layer in the multilayer coatings was designed by the control of the deposition rate and of the substrate rotation speed (1-20 rpm); the specific sample architectures studied in this work are illustrated in Figure 6.1.

Prior to deposition, the substrates were sputter cleaned for 30 min in an Ar plasma at a negative bias of 900 V. The constant process parameters were: argon pressure 5 mTorr, flow rate 100 sccm, and substrate temperature, T_s, of 573-593K. The sputter-cleaning was used in order to remove the surface oxide layer, and for surface activation. Nitriding was then performed to increase surface hardness and to improve the coating-substrate adhesion. The nitriding duration was 60 min with a substrate temperature, T_s, of 723K, while using a N_2 flow rate of 120 sccm, a pressure of 390 mTorr (52 Pa), and a self-bias of -400 V (~300 W).

Following pre-treatment (sputter-cleaning and nitriding), the coatings were prepared at a total pressure of 5 mTorr ($N_2/(N_2+Ar)) = 0.06$ and 0.10), and in an asynchronous mode by reactive pulsed-DC dual-magnetron sputtering using 50 mm diameter Zr and Ti targets and T_s = 673±10K. Both targets were operated at 300 kHz with a reverse time of 1.1 µs (duty cycle ~70%) using a Pinnacle Plus (Advanced Energy) power supply. The target power was kept constant for both targets at 225 W (typically, for the Ti target: 1.05 A; -215 V, and for the Zr target: 0.93 A; -240 V).

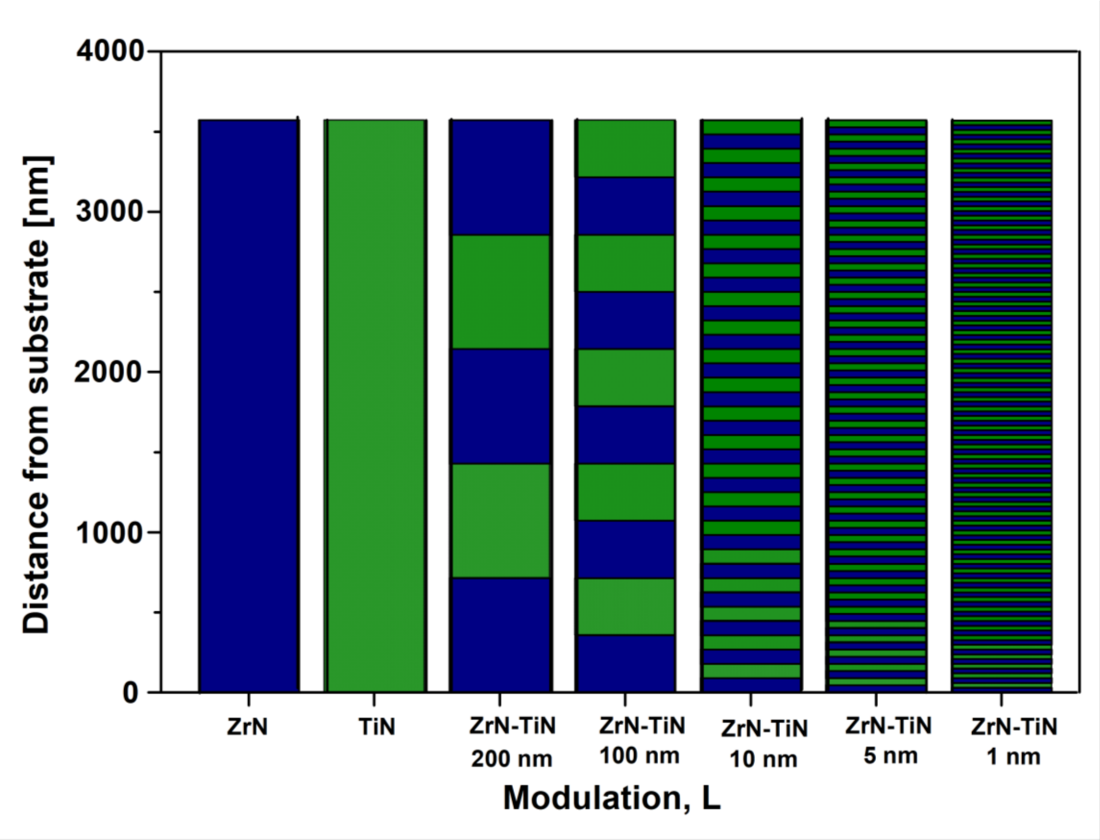

Figure 6.1 Schematic presentation of the thickness distribution when tailoring the single layer, multi-layer and nanolaminate systems studied in this work.

The silicon wafers were used mainly for stress analysis, and the Ti64 alloy substrates were applied for analyzing the hardness, Young's modulus, and wear resistance. The coating thickness and residual stress were determined by a Sloan Dektak III profilometer and by a Tencor Flexus Model 2900 instrument, respectively.

The crystallographic structure and the microstructural phase were assessed by X-ray diffraction (XRD) measurements using a Bragg-Brentano (BB) geometry on the Philips X'PERT X-ray Diffractometer with a Cu target (Kα line, $\lambda = 0.154$ nm). The average crystallite size (D) perpendicular to the (hkl) plane was estimated using Jade Software and the Debye-Scherrer formula calculated as an average of the 3 main peaks [316]: $D=0.9\ \lambda_{cu}/(\beta\cos\theta_{hkl})$, where β is the full width at half maximum of the diffraction lines, and θ_{hkl} is the angle of the most intense diffraction line. The lattice parameter, a, of the identified cubic phases was calculated using the equation $a=d_{hkl}/(h^2+k^2+l^2)^{1/2}$, where d is the spacing parameter calculated for (hkl) plane position.

The morphology of the microstructure was examined on the cross-sections of films prepared on the c-Si substrates using Field-Emission Scanning Electron Microscopy (FE-SEM, JEOL JSM 7600F) using an acceleration voltage of 15 kV. Before acquisition of the SEM micrographs, we performed microscope calibration to verify the 1 nm resolution limit of the system.

The hardness, H, and the reduced Young's modulus, E_r, were determined by depth-sensing indentation (TI950, Bruker) using a Berkovich pyramidal tip and the Oliver and Pharr method [216]. For each sample, H and E_r were obtained from a 5x5 matrix as 25 indentations were repeated 4 times with peak loads varying from 100 to 9500 μN. The indentation depth in all measurements was below 150 nm. This means that the measured hardness for $L\leq10$ nm represents the hardness value of the single layer of solid solution, while for the laminate structure the hardness is composed of ZrN and TiN layers.

The wear coefficient, K, was evaluated using a linear reciprocating ball-on-flat tribometer described in Ref. [226]. The tests were performed at a room temperature of 295K and 40% R.H. A normal load, F, of 3 N applied to an alumina ball (6.35 mm dia.) used as a counterpart material at a frequency of 2.5 Hz resulted in a linear speed of 5 cm/s for a total distance, s, of 200 m. A new ball was used for each test. The samples were examined by the Sloan Dektak III profilometer, and the worn volume, V, was calculated from the wear track profile. W was then obtained as $W = V/(F \times s)$.

6.4 Results and discussions

6.4.1 Effect of periodicity on the structure and mechanical properties

In the first set of experiments we evaluated the effect of periodicity L and of the individual film thickness on the overall microstructure. SEM examinations reveal that coatings with L <10 nm appear as a monolithic single layer, while for L=10 nm we can see a multilayer structure with an intermixing region (solid solution) at the interface as confirmed by the XRD observation below.

Coatings with *L* ≥100 nm show distinct alternating ZrN and TiN layers with thicknesses of 140 nm and 90 nm, respectively (see Figure 6.2).

Complementary XRD analyses presented in Figure 6.3 exhibit a clear microstructural transition when *L* is subsequently decreased. Initially, the monolithic ZrN and TiN single layers (~3.5 µm thick) show sharp peaks largely corresponding to the (111) orientation. For multilayer coatings with *L* ≥100 nm, two characteristic separate phases of ZrN and TiN can be distinguished: alternating ZrN and TiN phases show a broadening and a shift of the reflection peaks toward smaller 2θ values indicating a reduction of the crystallite size and/or a reduction of the lattice parameters. Finally, coatings with *L* <10 nm exhibit a single solid solution represented by a $Ti_{1-x}Zr_xN$ phase.

The transition from the ZrN and TiN multilayer films that preserve both phases to a single-phase solid solution coating is observed to occur at a modulation value of *L* < 10 nm. However, intermixing can already be present at the interfaces for *L*=10 nm as indicated in Figure 6.3b by a significant broadening of the (111) and (200) diffraction peaks of the ZrN, and by the formation of the $Ti_{1-x}Zr_xN$ phase; this reveals that the solid solution material is composed of a ZrN-enriched phase with mainly (111) and (200) orientations. In fact, the presence of the ZrN-rich phase correlates with the relatively low formation energy (0.06 eV/atom) compared with that of the $Ti_{1-x}Zr_xN$ phase (for example, for x=0.5, the formation energy is 0.75 eV/atom) in agreement with ref. [312]. The formation energy for the TiN and ZrN phases is very close to 0 eV/atom which implies that mixing of the $Ti_{1-x}Zr_xN$ phase is not necessarily stable. However, the intermixing region can be stabilized under certain conditions (such as temperature and composition) since the entropy is positive and promotes a decrease in the formation energy.

The mixing between phases can be supported by the analyses of the lattice parameters and of the crystallite sizes (see Figure 6.4). We found that the average lattice parameter of the ZrN phase, a_{avg}, decreases with decreasing *L* when the multilayer structure evolves toward solid-solution coatings. Similar *D* values were found for coatings with modulations of *L* = 1 nm and 5 nm. Here too, this finding can be explained by the formation of a solid solution ($Ti_{1-x}Zr_xN$ phase) when the diffusion of TiN into ZrN is completed during the growth. Calculations of the $Ti_{1-x}Zr_xN$ composition using the Vegard's law [317], while considering $a_{avg} = (1-x)\, a_{TiN} + x\, a_{ZrN}$, $a_{TiN} = 0.424$ nm and $a_{ZrN} = 0.458$ nm, show that the coating is a solid solution phase composed of $Ti_{0.35}Zr_{0.65}N$

when L = 1 nm and 5 nm. This indicates that the coating is Zr-rich and the Zr atoms substitute for Ti atoms, and that the ZrN content increases as the lattice parameter increases in agreement with ref. [312].

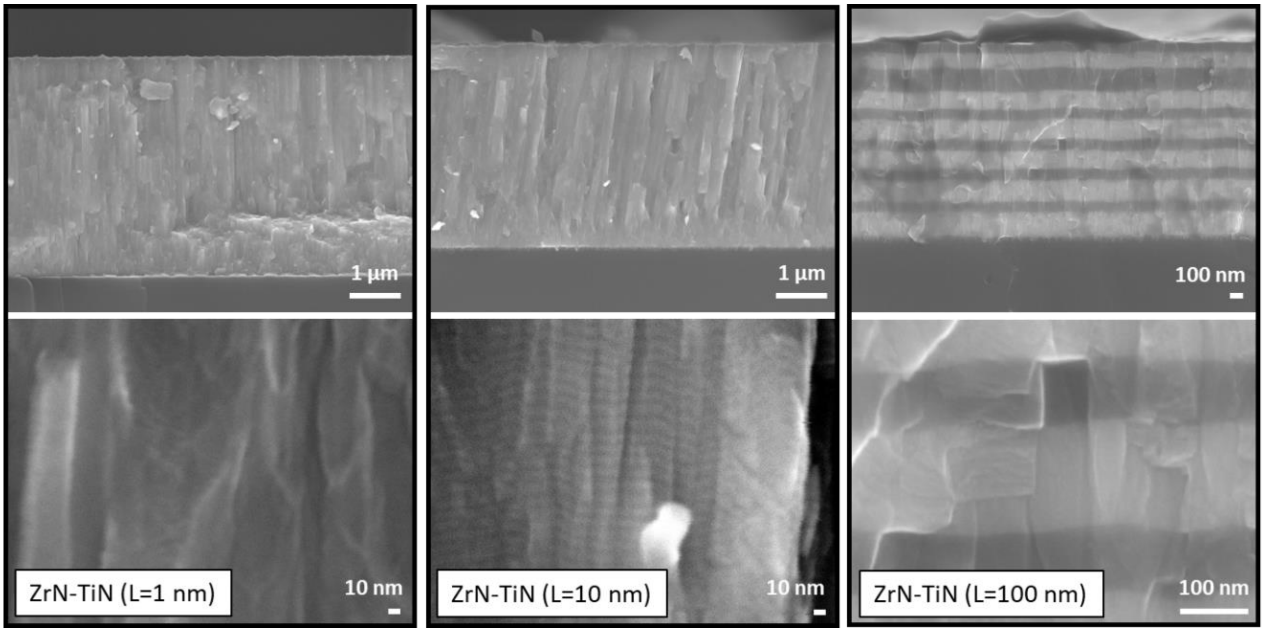

Figure 6.2 SEM cross section micrographs of the ZrN-TiN systems at low (Top) and high magnifications (Bottom) obtained using an electron beam acceleration voltage of 15 kV: (a) L = 1 nm, (b) L = 10 nm, and (c) L = 100 nm periods.

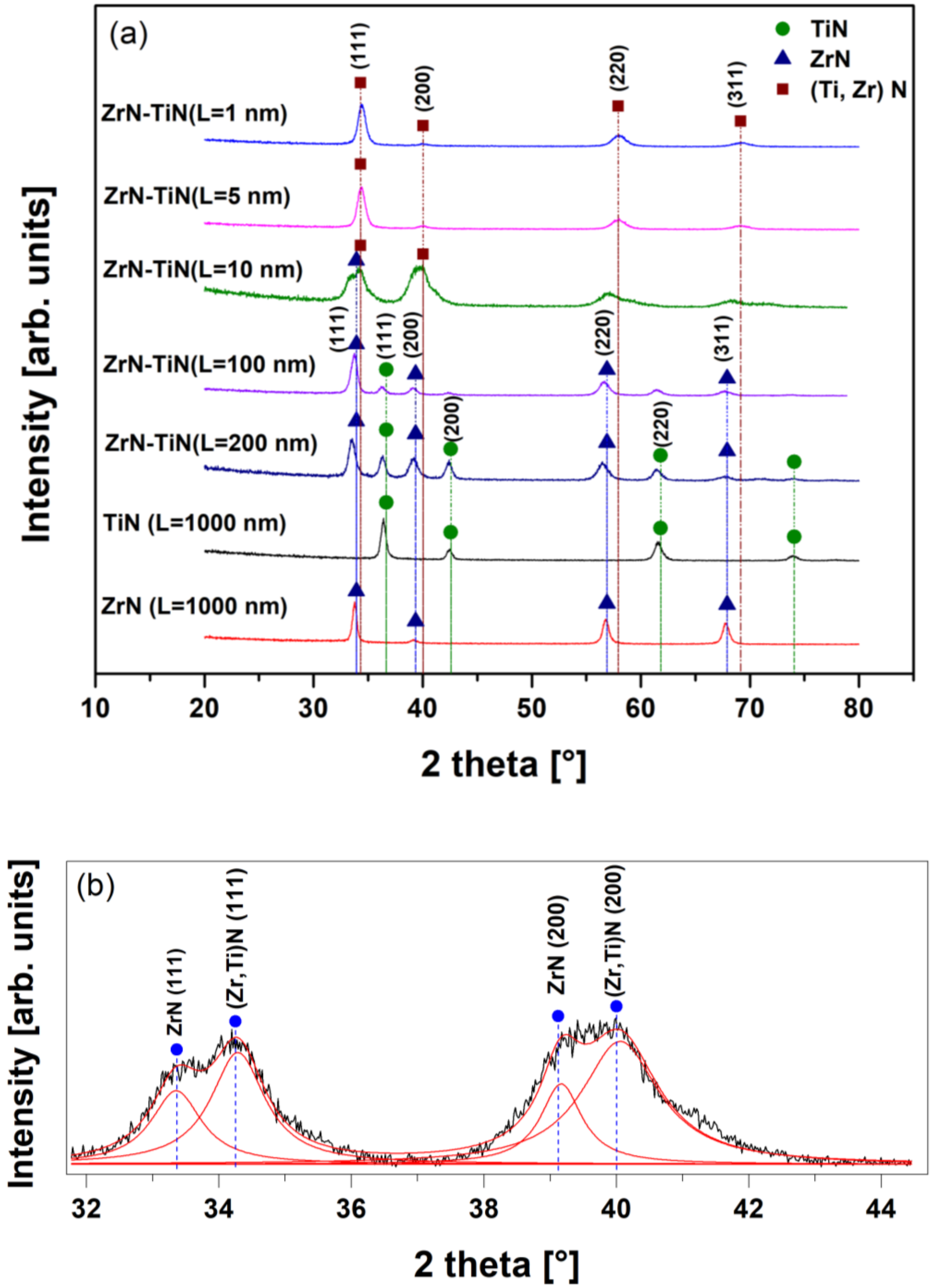

Figure 6.3 X-ray patterns of the ZrN-TiN systems: a) different modulations represented by the values of *L*, and b) a partial pattern of a coating with *L* = 10 nm.

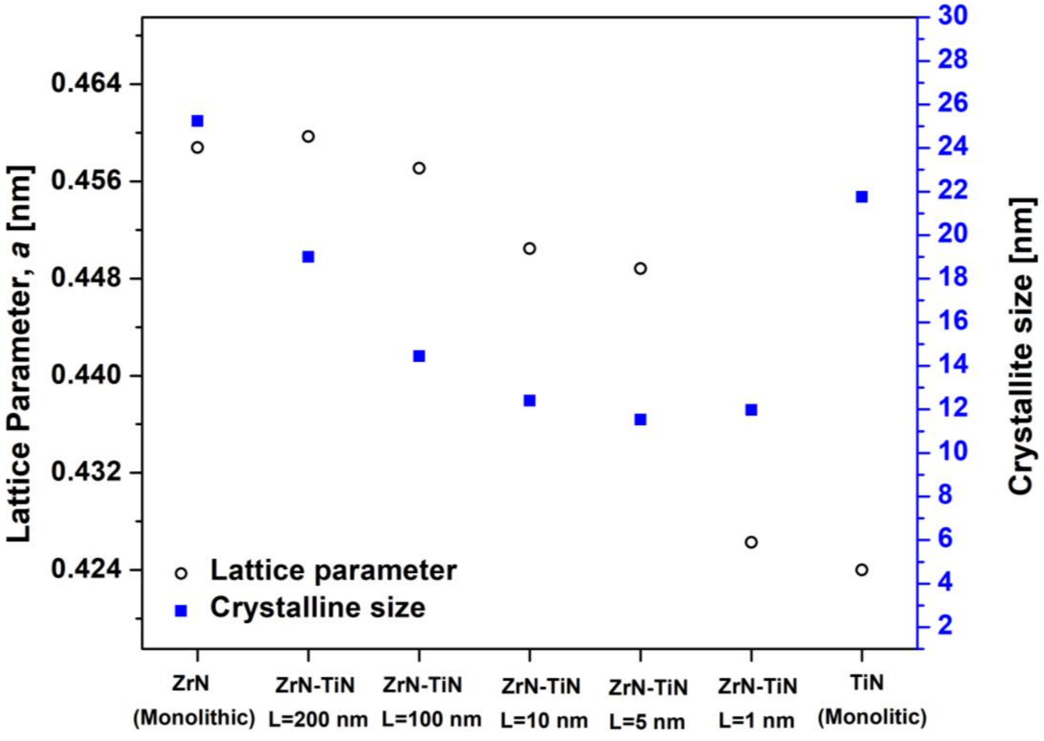

Figure 6.4 Lattice parameters *a* (a) and crystallite size *D* (b) of monolithic ZrN and TiN coatings and of various ZrN/TiN multilayer coatings as a function of the nanolaminate layer modulation, *L*.

In summary, we conclude that when the periodicity $L < 10$ nm, the system forms a single solid solution phase, whereas when the periodicity is higher ($L \geq 10$ nm), the structure remains a multilayer. Therefore, $L = 10$ nm appears to be the limiting periodicity modulation for the formation of the prevalent solid solution microstructure.

In the second set of experiments, we assessed the mechanical and tribological properties of the ZrN-TiN coatings for different *L*. The *H* and E_r values determined for monolithic ZrN and TiN films are 16±2 GPa and 160±10 GPa, and 21±2 GPa and 180±10 GPa, respectively, which is in agreement with other authors [318]. When employing these two materials in the multilayer and nanolaminate structures, *H* and E_r were found to increase, and the maximum values of *H* (~35 GPa) and E_r (~320 GPa) were obtained for $L = 10$ nm.

Besides the enhanced hardness, we also observed that the H/E_r and H^3/E_r^2 ratios increase with decreasing *L*, and their highest values correspond to the highest wear resistance (lowest *K*) as shown in Figure 6.5. This indicates that the hardness enhancement with decreasing *L* is due to the presence of strengthened interfaces (by a progressively increasing fraction of the solid solution-affected interfacial regions) till a complete solid solution structure ($Ti_{0.35}Zr_{0.65}N$ phase in our case) for L < 10 nm. Furthermore, the “dual phase” structure with a crystallite size of about 12.5 nm is presumably a critical value for the maximum H/E_r and H^3/E_r^2 ratios, as illustrated in Figure 6.6, in agreement with the Hall-Petch effect.

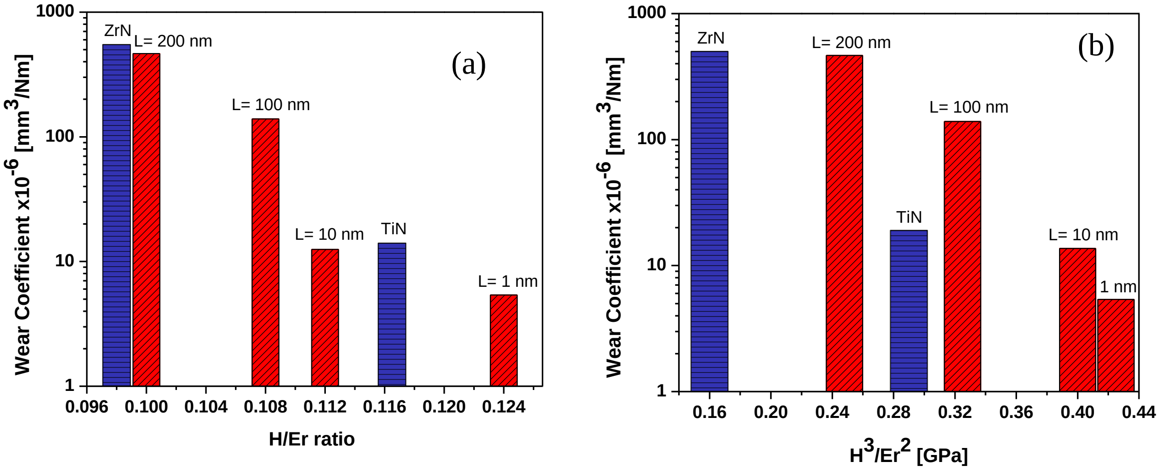

Figure 6.5 Wear coefficient *K* as a function of the H/E_r (a) and of H^3/E_r^2 (b) ratios for the ZrN-TiN nanolaminate structures.

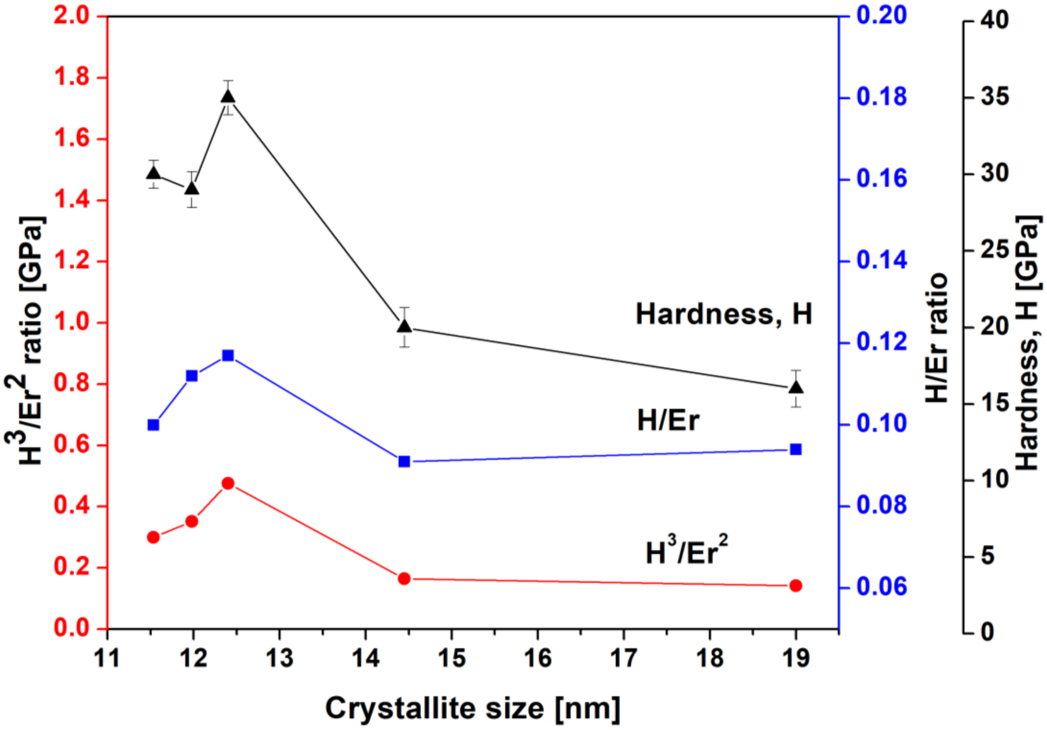

Figure 6.6 Mechanical properties (H, H/E_r and H^3/E_r^2 values) of the nanolaminate ZrN-TiN films as a function of the crystallite size.

6.4.2 Phenomenological model of solid solution phase formation

One or more of the following three conditions may affect two adjacent layers to produce a solid solution phase, namely: (i) a synergistic effect of mutual diffusion and solubility of Zr in the TiN layer; (ii) stored energy and stress relaxation as a driving force; and (iii) the combination of several driving forces, such as temperature, stored energy and stress. In all factors, a threshold value of modulation periodicity ($L \leq 10$ nm) is required during the simultaneous deposition of ZrN and TiN materials, while taking into account the experimental conditions, such as those in the present study, in terms of the substrate temperature ($T_s = 673$ K) and deposition rate ($r_D = 0.1$-0.2 nm/s).

In condition (i) we evaluated that the diffusion and/or solubility length of Zr atoms in TiN does not exceed the range of 10 nm. This value is deduced from the very low diffusivity of Zr into Ti (less than 10^{-16} m^2/s at ~1173 K), and from the much lower diffusivity of Zr into TiN (FCC structure) [319]. This diffusion length is relatively small with respect to a larger thickness of individual ZrN and TiN layers for the large values of L ($L \geq 100$ nm); in this case the effect of the solid solution and its impact on the mechanical properties is small. However, this effect is strongly accentuated when the diffusion length is comparable with L, such as for $L \leq 10$ nm. In such a case, the total volume occupied by the solid solution at the interlayer is comparable with the layer thickness, leading to the material's hardening and enhancement of the mechanical and tribological properties due to the suppression of dislocation movement.

Additionally, the intermixing region during deposition between two adjacent layers is smaller or equal to the diffusion and/or solubility lengths. In our model the substrate temperature is much lower than the temperature required for the formation of a Ti and a Zr compound. For example, the temperature required for the formation of 50%Ti + 50%Zr is ~873K [313], [320]. Also, as an empirical rule, a solid solution can only be formed if the difference in atomic size of the two elements is less than 15% [318]; in the case of Zr and Ti, the atomic radii are 0.155 nm and 0.140 nm, respectively, making a solid solution possible.

In condition (ii), the solid solution hardening can be supported by stress relaxation and annealing-stimulated phase separation as suggested by our experimental results. In this context, the formation energy, which is equivalent to the stored energy in the layers during the film growth, can be considered proportional to the residual stress. Specifically, stress analyses reveal that the monolithic ZrN layer has a low tensile stress (~400 MPa), while the monolithic TiN layer has a high compressive stress (~1620 MPa) (see Figure 6.7). The residual stress of the multilayer and the solid solution structures is given by the sum of the stresses of ZrN and TiN layers. Here, the reason for the tensile stress of the ZrN layer is due to the tensile thermal stress component that developed upon cooling down from T_s = 723 K and then from T_s = 673 K, after the nitriding and deposition steps, to room temperature (see Section 6.3). This is because of the larger thermal expansion coefficient of ZrN and TiN compounds (7-9x10^{-6}/K) in comparison to that of the Si substrate (3x10^{-6}/K). This tensile stress component can compensate for the compressive stress component due to point defect creation (atomic peening) [17, 28].

In our work, we consider that the relative stored energy and stress relaxation as a driving force for solid solution formation increase as the modulation L decreases. For comparison, Abadias et al. found that when the modulation L is close to 10 nm, the $Ti_{1-x}Zr_xN$ composition of the mixing region is x~0.5, and the corresponding $Ti_{1-x}Zr_xN$ energy formation is ~0.75 eV/atom [312]. Therefore, decreasing the modulation enables formation of a single solid solution with Zr-rich $Ti_{1-x}Zr_xN$ phase (where x>0.5) at a lower formation energy; specifically in our case, for $Ti_{0.35}Zr_{0.65}N$ formed at *L* <10 nm, about 0.06 eV/atom is required. This can be obtained because: a) the Ti-N bond in the mixing region is weaker compared to that in pure TiN, and b) while Zr atoms substitute Ti atoms (forming a Zr-rich compound), the stored energy increases. This then drives the formation of a single solid solution in which case all the Zr atoms have been consumed to form the Zr-rich phase.

Based on our observations and the assumptions above, condition (iii) further expands the model by combining conditions (i) and (ii) while considering two distinct pathways. In the first pathway, the Zr atoms can replace Ti atoms when the formation energy is sufficient at high temperature. Since T_s is constant (= 673K), we can consider that the stored energy is represented by the internal stress which develops during the growth (see Figure 6.7). When $L \geq 100$ nm, the internal stress is relatively low, as is the energy dissipated into the layers. Therefore, the intermixing region is relatively small with respect to a larger thickness of the individual ZrN and TiN layers. Only when the modulation periodicity is low (L=10 nm), and the activated Zr atoms substitute Ti atoms at the interface, the stored energy due to stress increases to a critical value and promotes diffusion of the Zr atoms into TiN. This critical energy is the driving force for the initiation of the solid solution formation. As discussed above, since the diffusion length of Zr atoms in TiN is lower than 10 nm, decreasing the modulation *L* requires less energy to complete the solid solution phase formation.

In the second pathway, we assume that the thickness of the intermixing region between two adjacent layers in the multilayer structure (for all modulations) is constant during deposition (since all the parameters are constant). This intermixing region decreases the amount of heat (stored energy) in the individual ZrN and TiN layers, and therefore, the internal stress is low when $L \geq 100$ nm and $L \geq 200$ nm (see Figure 6.7). Only when L=10 nm, the thickness of the intermixing region and the diffusion length are almost equal: therefore, the formation energy to initiate the reaction at the interface to produce a solid solution is achieved. However, only when L<10 nm the reaction can be completed to produce a single solid solution phase (see XRD patterns of samples L=1 and 5 nm) because all the Zr atoms have been consumed. This single-phase formation ($Ti_{0.35}Zr_{0.65}N$) is accompanied by heat release reaction during the growth, and therefore, the internal stress decreases (relaxes) as *L* decreases from L=10 nm toward L=1 nm. Thus, we can conclude that lowering *L* enhances the energy reduction required to complete the formation of a single solid solution phase, and it is accompanied by heat release reaction during growth.

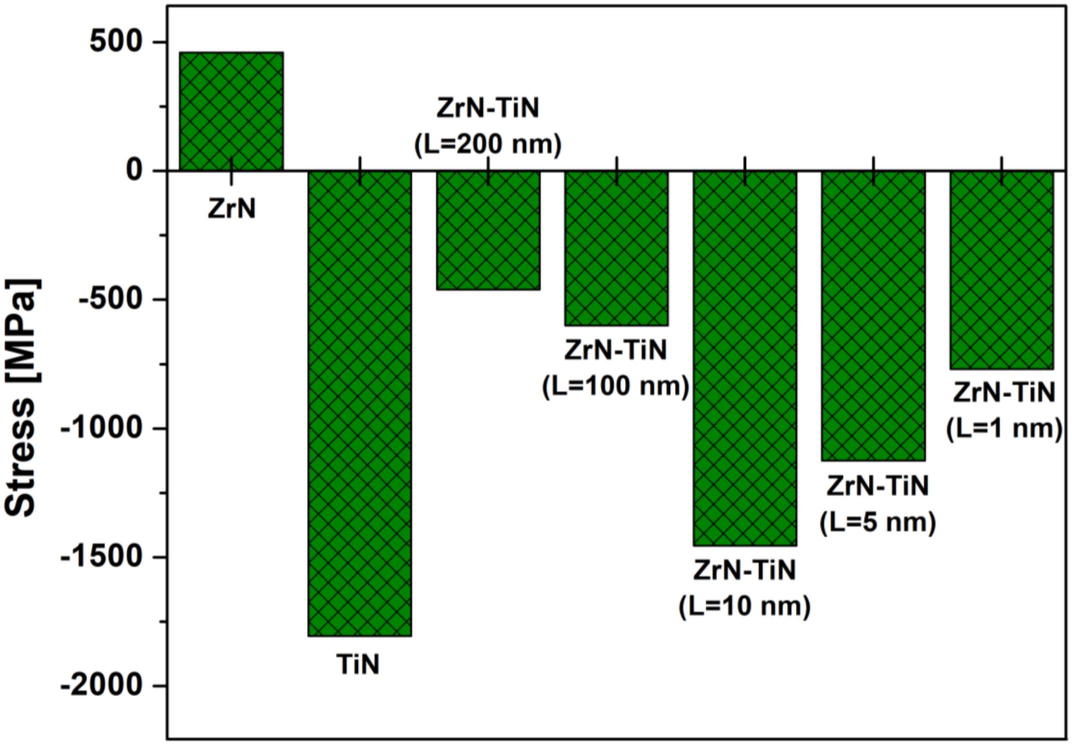

Figure 6.7 Effect of modulation on the total residual stress in the single layer, multilayer and nanolaminate coatings.

6.5 Summary and conclusions

Multilayer ZrN-TiN coatings with various modulation periods were prepared by pulsed DC reactive magnetron sputtering in asynchronous mode using Zr and Ti targets. The coatings were deposited on nitrided Ti-6Al-4V alloy and c-Si substrates, and they were characterized by different complementary techniques. Specifically, the results presented in this study show that decreasing the periodicity in the multilayer structure enhanced the hardness, Young's modulus as well as the wear resistance of the films, while formation of a solid solution structure and strengthening of the interfaces was found to be the main cause of the hardening. The highest H and E_r values were found for nanolaminates with a periodic structure of L = 10 nm, or with a solid solution structure with L < 10 nm. It was observed that the maximum hardness (~35 GPa), the maximum plastic index parameter (H/E_r ~0.12) and the highest film resistance to crack propagation (H^3/E_r^2 ~0.42 GPa) occur for coatings with a modulation periodicity of $L \leq 10$ nm. Furthermore, the coatings with $L \leq 10$

nm also display the highest wear resistance (lowest wear coefficient, K~ 2-8x10^{-6} mm^3/Nm). It is proposed that the critical value of L for optimized wear resistance coincides with the diffusion length of Zr in TiN, leading to localized solid solution. Finally, based on our experimental results and observations, we proposed a phenomenological model for the $Ti_{0.35}Zr_{0.65}N$ solid solution phase formation related to the dissipation of the stored energy in terms of residual stress.

6.6 Acknowledgments

The authors wish to thank Dr. Zbigniew Rożek (Technical University of Lodz, Poland) for fruitful discussions, and Mr. Francis Turcot and Mr. Sébastien Chénard for expert technical assistance. This project has been supported in part by the Natural Sciences and Engineering Research Council (NSERC) of Canada through the NSERC Discovery Grants of LM and JEKS.

CHAPTER 7 FRACTURABILITY STUDY ON MULTILAYER COATINGS

In the following section the effects of two architectures, the multilayer coating with improved tribo-mechanical performance chosen from Chapter 6 and TiN-Nit from Chapters 4 and 5 are compared and related to the fracturability behavior of Ti-6Al-4V. This section presents a study of the fracturability behaviour of the ZrN/TiN multilayer system with a periodicity of L= 10 nm in comparison with the fracturability results of TiN-Nit samples seen in Chapter 5.

7.1 Context

The study presented in Chapter 6 involves TiN and ZrN coatings as single-layer coatings, and ZrN/TiN multilayer systems with various modulation periods, L, ranging from 1 to 100 nm. The results showed that all coated systems presented a (111) preferable orientation determined by XRD analysis. In addition, it was observed that decreasing the periodicity in the multilayer structure enhanced the hardness and wear resistance due to the formation of solid solution structure and the strengthening of interfaces between each layer. Systems with L equal or below 10 nm are considered nanolaminate structures.

Finally, the following analyses presented in this section are a complementary study of the fracture mechanism and elasto-plastic properties evaluation between TiN single-layer coatings and ZrN/TiN multilayers with an L = 10 nm. They aim at complementing the advantages~~,~~ in terms of fracture resistance, of each architecture (TiN single-layer and ZrN/TiN multilayer) studied in this thesis.

Several reports in the literature indicate that multilayers can retard crack propagation due to a zig-zag, deflection and hardening effect between layers [201], [322]–[325], as is illustrated in Figure 7.1. However, there are also some other authors who have shown that the presence of nanocomposite structure led to a catastrophic failure dominated by lateral and radial cracks [326]–[328].

In the literature, the studies of crack onset and crack propagation in multilayer coatings have been mainly performed with a nanoindentation test; they have also shown that multilayer systems are effective to minimize shear sliding and crack propagation [327]. In the present section, the fracture mechanism is studied using tensile testing to evaluate the effect of uniaxial external load on the coated components which is more representative of the external load present during the final component application.

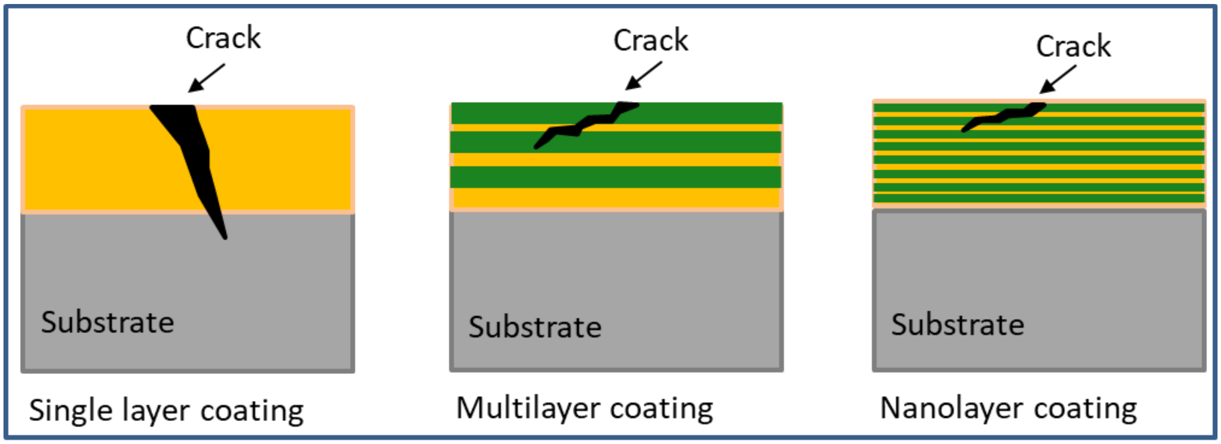

Figure 7.1 Schematic representation of toughening and strengthening mechanisms in ceramic multilayer coatings [201]

7.2 Experimental methodology

The experimental approach has been described in detail in Chapters 3 and 5, including the microstructural and nanoindentation results. In this section, we focused primarily on the analysis of fracture mechanism of the ZrN/TiN system. It is worth noting that while in Chapter 6 the RS measurement for all samples was performed on Si substrates, while in the present section, the RS evaluation was done on thin Ti-6Al-4V substrates. The overall RS in ZrN and TiN single-layers and multilayer coating with L=10 nm on thin Ti-6Al-4V substrate were measured by the curvature technique using a Tencor Flexus Model 2900 instrument.

7.3 Results and discussions

Figure 7.2 shows compressive RS for single-layer and multilayer coatings. Single-layer TiN-Nit and ZrN-Nit presented RS values of -1,300 MPa and -300 MPa, respectively, while the multilayer system exhibits an RS value of -750 MPa. These results agree with the values presented in the literature; some reports have shown that the ZrN layer can possess a low level of compressive RS or even tensile stress [312], [321]. In Chapter 6, the ZrN sample presented a RS around +480 MPa in the tensile regime. The main difference between both samples is the substrate; as mentioned above, the RS measurement in Chaper 6 was done on Si substrates, while the results presented in

Figure 6.7 were performed when using Ti-6Al-4V substrates. Therefore, tensile thermal stresses were developed upon cooling down from Ts = 400 °C to room temperature after the deposition process; this is due to the fact that the CTE of ZrN (7×10^{-6}/°C) is 1.3 times lower in comparison to that of the Ti-6Al-4V substrate (9.35×10^{-6}/°C), while it is 2.3 times higher compared to the Si substrate (3×10^{-6}/°C).

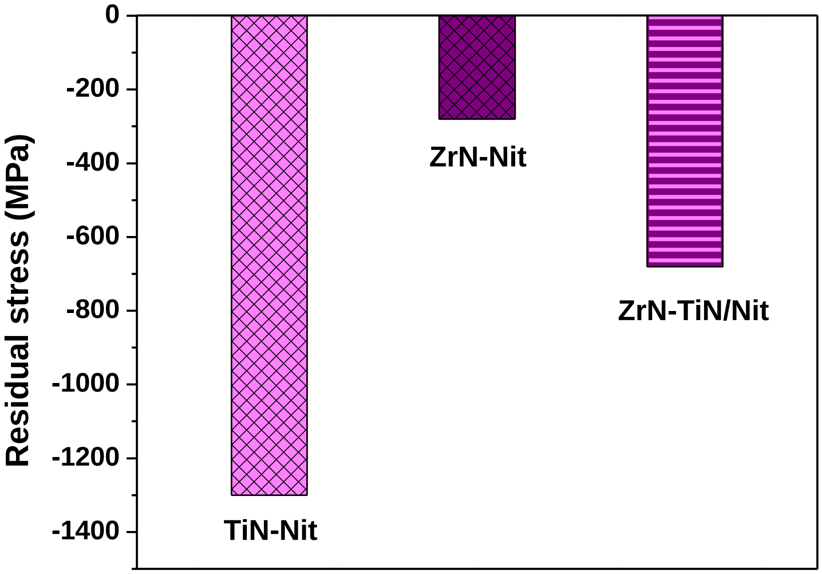

Figure 7.2 Residual stress of single layer and multilayer systems on nitrided Ti-6Al-4V obtained by Stoney equation.

The Ti-6Al-4V substrate, and the TiN-Nit and ZrN/TiN systems were evaluated by micro-tensile testing with the continuous and interrupted configurations. The stress-strain relations (*S-S* curves) of the three specimens under investigation are presented in Figure 7.3 and they were obtained by continuous measurements. The UTS and YS for both, single-layer TiN coating and ZrN/TiN multilayer are around 1,000 MPa and 960 MPa, respectively. The UTS and YS results of both systems are within the uncertainty of the micro-tensile testing, which is typically around 10 to 15% experimental error. The strain to fracture was considerably reduced on the coated specimens. The detrimental effect of the interface on the strain to fracture of Ti-6Al-4V, from 13.5% to 10% and 8% for TiN-Nit and ZrN/TiN samples can be attributed to deformation and surface cracking developed on the substrate surface due to the nitriding pre-treatment as it was observed in Chapter 5.

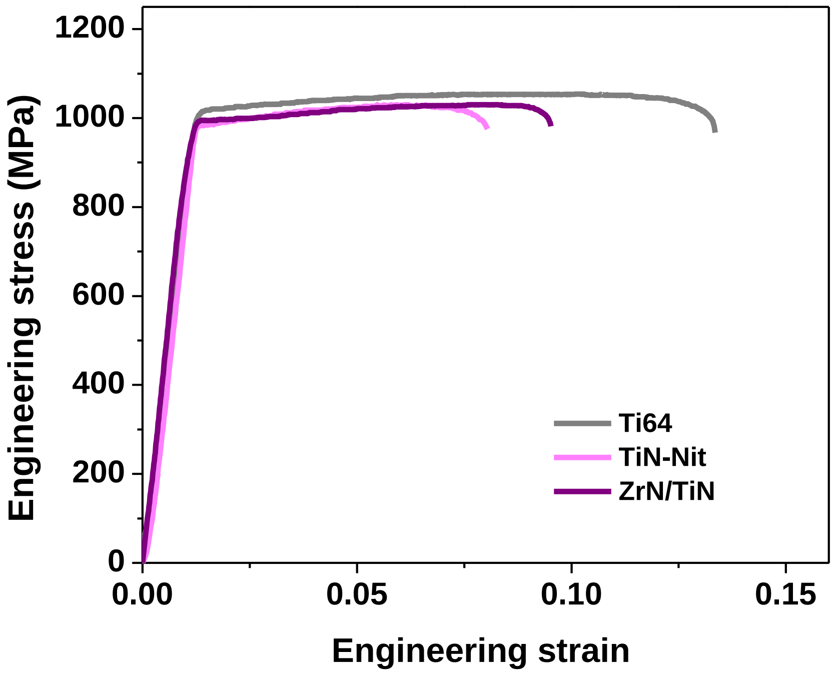

Figure 7.3 S-S curves of TiN-Nit and ZrN/TiN during continuous tensile tests.

The cracks evolution, including COS, multiplication, saturation, strain to fracture and average crack density of TiN-Nit and ZrN/TiN samples are shown in Figure 7.4. Crack evolution was evaluated by optical images acquired during each cycle of the interrupted test. Specimens with TiN and with ZrN/TiN multilayer presented different crack density. TiN-Nit shows the highest crack density with 120 cracks/mm, and ZrN/TiN exhibits the lowest density with ~80 cracks/mm. The COS values of the two coating systems, represented by the first point of each curve in Figure 7.4, are in the range of 1.1 and 1.3 % strain, documenting that the multilayer system delays crack onset.

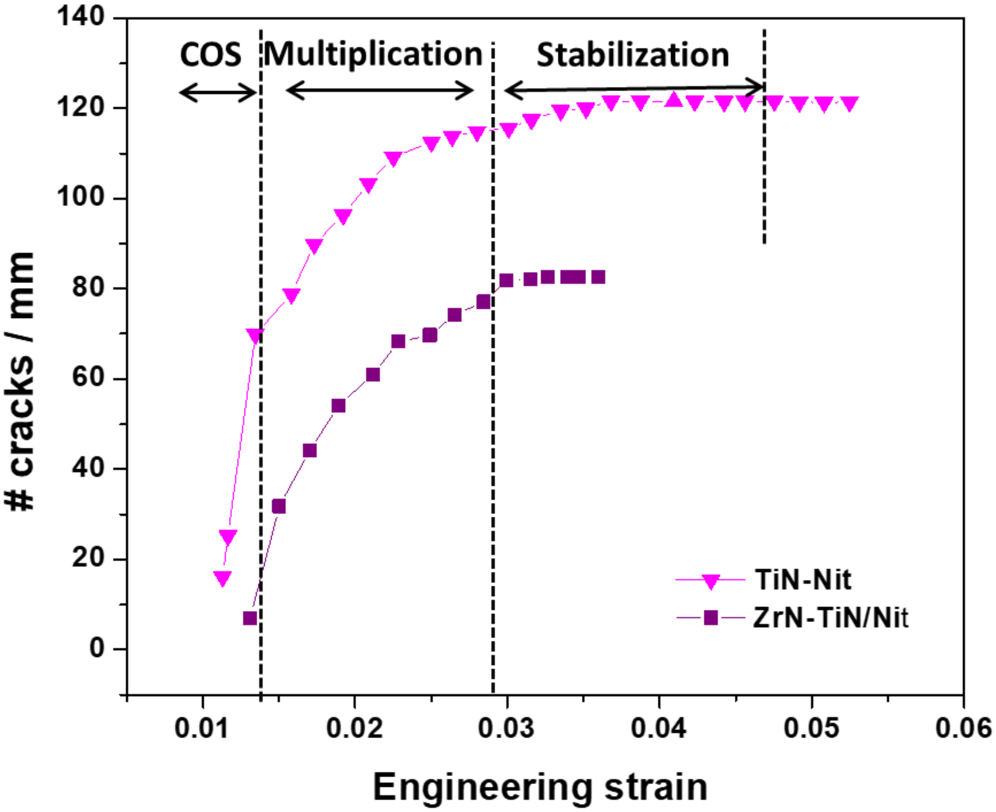

Figure 7.4 Crack density curves of TiN-Nit and ZrN/TiN systems.

The surface of both specimens after micro-tensile testing were evaluated by SEM at distances of 0, 1, 3, and 5 millimeters from the fracture zone, see Figure 7.5. At 0 mm, both coatings present a high number of cracks perpendicular and at 45° to the tensile force direction. The ZrN/TiN coating shows more delamination than TiN-Nit at 0 mm distance. which can be attributed to the specimen fracture. However, it is possible that for ZrN/TiN, shear stress between layers also contributes to the delamination mechanism. In the images at 1 mm distance, delamination is not visible, but both coatings show a presence of cracks perpendicular and at 45° to the tensile force direction, whereas in TiN-Nit cracks at 45° are more pronounced than in ZrN/TiN. At a distance of 5 mm, the cracking pattern is minimum for both coatings with a predominant presence of perpendicular surface cracks.

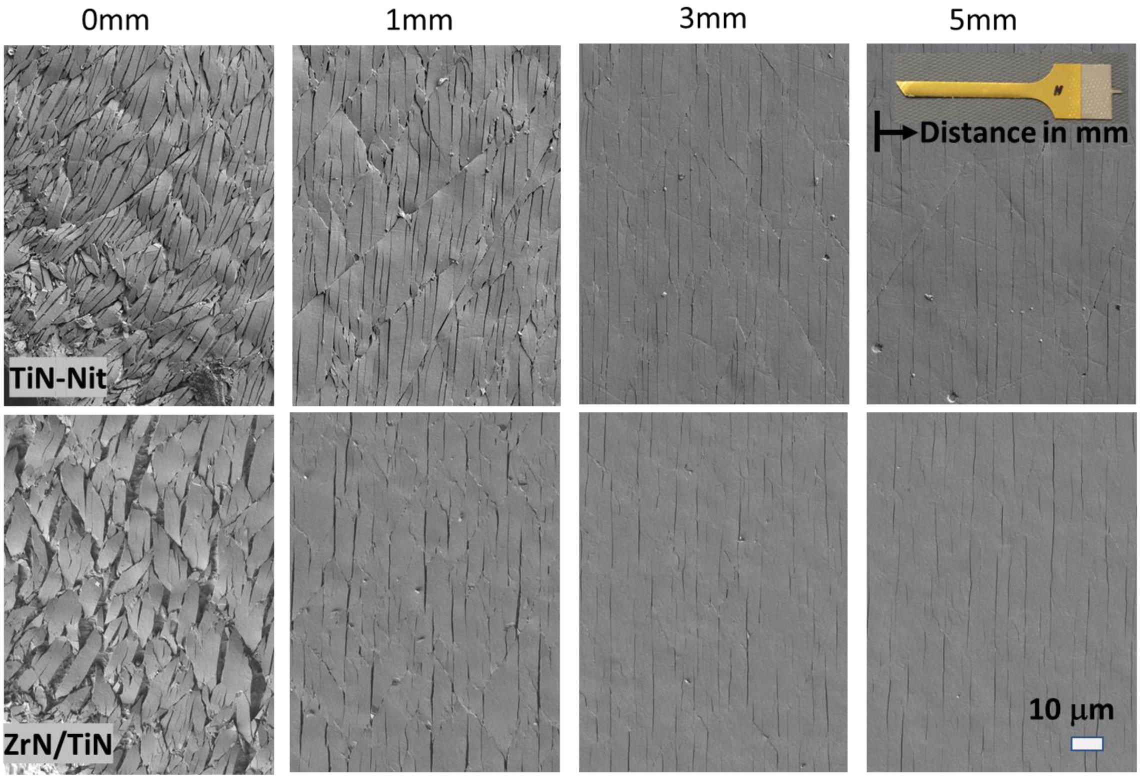

Figure 7.5 SEM images of parallel and secondary surface cracks on TiN-Nit and ZrN/TiN systems taken at 0, 1, 3, and 5 mm distance from the fracture zone after the tensile load was removed.

The cross-section of the fracture area on the multilayer system was evaluated by SEM after the tensile test. Figure 7.6a shows the presence of secondary surface crack which propagate through the coating and stops at a depth of around 100 μm inside the substrate. Secondary cracks result from shear bands during plastic deformation of Ti-6Al-4V subjected to high uniaxial load. Figure 7.6b shows the multilayer structure with a presence of two representative cracks within coating which are formed by multiple layers and/or with a nanolaminate region. In our case, from the study performed by XRD and in complement to the results shown in Chapter 6, we know that the structure of the ZrN/TiN multilayer with L = 10 nm consists of ZrN and TiN nanolaminates with a solid solution ($Ti_{1-x}Zr_xN$ phase) along the interfaces between the neighboring layers. Calculations of the $Ti_{1-x}Zr_xN$ composition using Vegard's law [317] indicated that the solid solution phase is composed of $Ti_{0.35}Zr_{0.65}N$.

The lateral crack between layers, similar to that reported in the literature for nanocomposite structures, is observed in the green area, while a semi zig-zag crack, normally reported for multilayer systems, is observed in the blue area. Lateral cracks are critical in coated structures because they can favor detachment of the coating from the substrate, however, they can also contribute to stopping the propagation of perpendicular cracks formed in the coating. Zig-zag cracks delay crack propagation in the coating, however the cracks are expected to grow through the coating.

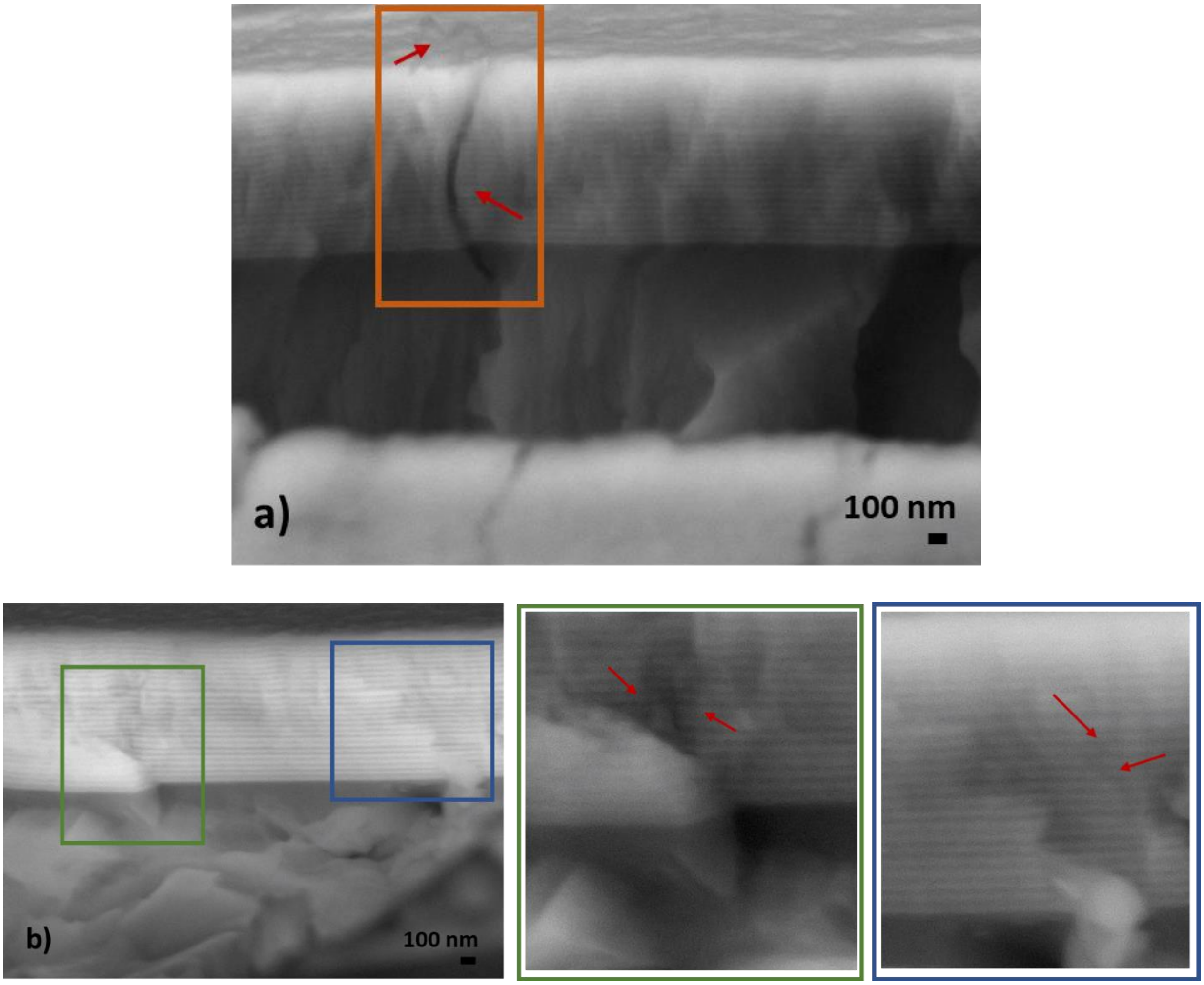

Figure 7.6 SEM images of the fracture in the multilayer system cross-section after tensile test: a) surface secondary crack propagation through coating, and b) two areas as close-up of a lateral crack between layers (green square) and a zig-zag crack though layers (blue square).

Finally, considering a brittle coating, the fracture resistance was analyzed in terms of the critical energy release rate, G_C [112], fracture toughness, K_{1c}, and interfacial shear strength, τ. The results presented in Table 7.1 were obtained using the Equations presented in Chapter 5 considering the data from the tensile testing, nanoindentation, and the Poisson ratios of each film (0.25, 0.26 and 0.3 for TiN, ZrN and Ti-6Al-4V, respectively).

Table 7.1 Fracture properties of the single layer and multilayer structures. Hardness and Young's modulus obtained by nanoindentation are given in the parenthesis.

	G_C (J/m^2)	K_{IC} (MPa·m$^{0.5}$)	τ (MPa)	COS (%)
TiN-Nit (H=29GPa, Er=350GPa)	19.7	2.5	790	1.1
ZrN/TiN (H=35GPa, Er=320GPa)	~30	~3.0	795	1.3

The higher fracture results obtained for the ZrN/TiN system can be favored by a hardening mechanism attributed to the difference between the size of the Ti and Zr atoms [329] which is absent in the single-layer TiN coatings. This is rather due to the presence of the $Ti_{1-x}Zr_xN$ phase, which is considered a solid solution hardening medium. However, in this study, the "dual-phase" structure with a crystallite size of about 12 nm is presumably a critical value for the maximum H/E_r and H^3/E_r^2 ratios, 0.11 and 0.4 GPa, compared to the H/E_r and H^3/E_r^2 ratios,0.08 and 0.2 GPa of the single-layer. This is in agreement with the Hall-Petch effect [330] and the reason for the enhanced energy release rate and fracture toughness.

The difference between the interfacial shear strengths (τ) in Table 7.1 is only 5 MPa for the two systems; this should not be surprising considering that yielding of a coated sample begins when the substrate reaches a critical value of the yield shear strength. Taking into account that the yield shear strength of Ti-6Al-4V is ~760 MPa, we conclude that the τ values calculated in this work are primarily influenced by surface pre-treatment; therefore, for the nitrided systems, the τ values are comparable independently of the coating.

7.4 Discussion

The mechanical properties suggest that the ZrN/TiN multilayer is a promising candidate for applications as a very effective protective coating. As well, we consider that fracture toughness is one of the critical mechanical properties needed for design purposes. In this context, based on the micro-tensile test results, we underline the following main arguments:

First, the stress-strain curves acquired by the micro-tensile test (see **Erreur ! Source du renvoi introuvable.** 7.3) show a negligible difference in YS or UTS between the multilayer structure and the single TiN layer being both around 1,000 MPa. On the other hand, the multilayer structure showed a higher strain to fracture than the TiN-Nit, and 1.5 times lower crack density.

Results indicate that micro-scratch values reported in Chapter 6 are consistent with the observations in Figure 7.4. The trend of COS presented in Table 7.1 agrees with L_{C1}, and the crack density follows the trend observed by the L_{C1} (L_{C2} - L_{C1}) rule, which indicates complete coating failure. Therefore, the cohesive and adhesive properties calculated from micro-scratch testing, L_{C1} =13 N and 15 N, L_{C2} = 23N and 30 N, for single-layer and multilayer systems, respectively; predict well the crack onset strain, namely 1.1% strain for the single layer and 1.3% for the multilayer, while the crack density at saturation observed experimentally by the fragmentation test varies from 80 to 120 cracks/mm for ZrN-TiN and TiN coatings, respectively. SEM image analyses performed on the fracture specimen after tensile test reveal lateral cracks between layers that can be associated with shear stress acting on the grain boundary. For the multilayer system, the formation of lateral and perpendicular cracks was suppressed as some of the energy was dissipated by deformation in the sublayers forming a zig-zag effect. A similar situation was observed for TiSiN coatings with TiN sublayers, tested by nanoindentation [328].

The energy release rate and fracture toughness reported in the literature for ZrN are 23.9 to 29.9 J/m^2, and ~1.9 $MPa \cdot m^{0.5}$, respectively [331]. We have observed that the ZrN/TiN multilayer with $Ti_{0.35}Zr_{0.65}N$ solid solution Zr-rich phase has an energy release rate and fracture toughness of ~32 J/m^2 and ~3.6 $MPa \cdot m^{0.5}$, respectively. These values agree with the ones reported in the literature [271] for ZrN/TiN multilayers and $Ti_{1-x}Zr_xN$ that range from 26 to 48 J/m^2 and 2.66 to 3.18 $MPa \cdot m^{0.5}$, for the energy release rate and fracture toughness, respectively. We believe that the difference in toughness is mainly given by the presence of the Zr-rich phase: a higher the Zr content gives rise to higher fracture toughness.

7.5 Conclusion

The application of surface nitriding of Ti-6Al-4V before coating deposition and the optimization of coating microstructure with a preferable orientation in (111) has a significant effect on the durability of the coated component. The use of nitrided interface with hard coatings enhances the mechanical properties and elasto-plastic deformation characteristic of the metallic component. Multilayer structure with L=10 nm presented surface cracks whose propagation can be delayed due to the zig-zag mechanism created by the layers, but they also show lateral cracks between interfaces which can cause delamination and consequently lead to catastrophic failure of the coating under further loading. The use of a nanolaminate structure with an appropriate modulation can develop a crystallite size and a solid solution Zr-rich phase, which by strengthening the material increases wear resistance and delays crack nucleation and propagation.

CHAPTER 8 GENERAL DISCUSSION

This chapter summarizes the main results and discusses the major achievements of this thesis and the contributions to the field of research and technology in response to the objectives proposed in Chapter 1.

In this work many state-of-the-art techniques were applied. Table 8.1 presents the list of activities and characterization techniques applied through the development of this thesis work. Therefore, a group collaboration was essential. Table 8.1 illustrates with different colors which activities were performed by myself (green), those ones in which I assisted (orange), and the specific ones that were performed by someone else (red).

Table 8.1 Activities and characterization techniques required for the realization of this thesis.

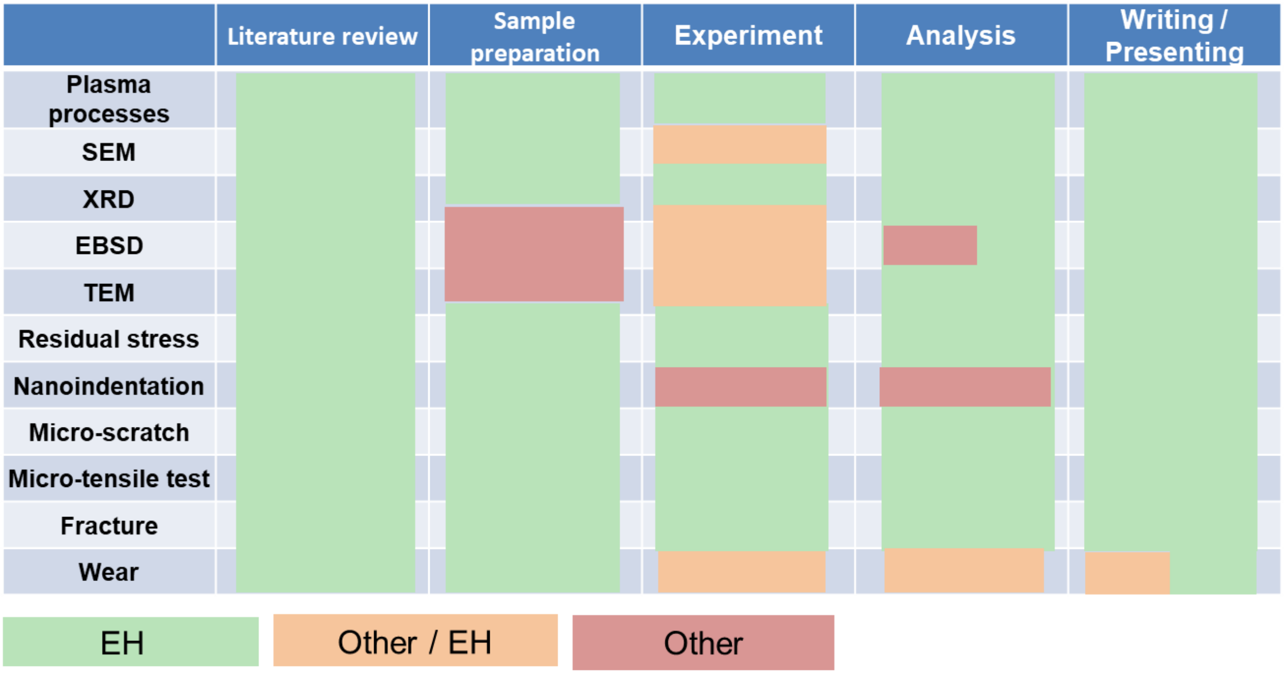

	Literature review	Sample preparation	Experiment	Analysis	Writing / Presenting
Plasma processes	🟩	🟩	🟩	🟩	🟩
SEM	🟩	🟩	🟧	🟩	🟩
XRD	🟩	🟩	🟩	🟩	🟩
EBSD	🟩	🟥	🟧	🟥🟩	🟩
TEM	🟩	🟥	🟧	🟩	🟩
Residual stress	🟩	🟩	🟩	🟩	🟩
Nanoindentation	🟩	🟩	🟥	🟥	🟩
Micro-scratch	🟩	🟩	🟩	🟩	🟩
Micro-tensile test	🟩	🟩	🟩	🟩	🟩
Fracture	🟩	🟩	🟩	🟩	🟩
Wear	🟩	🟩	🟧	🟧	🟧🟩

🟩 EH 🟧 Other / EH 🟥 Other

The work presented in this thesis is in response to the aeronautical industry, which involves diverse applications, for example, commercial, military and business aviation. All these applications require high-quality materials with no compromise on durability and performance. An aircraft is a highly complex assembly of specific components with their own technical requirements that are generally subjected to an array of conditions that demand ultimate performance of their coated components, especially in the jet engine. Their performance includes temperature variations from -60°C to 1300°C. In the present work, we are concerned with the compressor part where the temperature ranges from -60°C to about 400°C. Additional solicitation including particle erosion, flexing/deformation during rotation, ice accumulation, high pressures, corrosive gases, and fluctuation of mechanical loads can create degradation mechanisms such as corrosion, oxidation and/or fatigue in structures that are expected to be in use for a period of at least 20 years. Therefore, the selection of materials and coatings for aeronautical applications is critical. Ti-based alloys are used in components of the cold section, typically for both stator and rotor parts of the engine (see Figure 8.1), which are subjected to an operation at a constant speed and temperature levels for long periods of time corresponding to a low cycle fatigue regime (high-stress level), which shortens its lifespan [9].

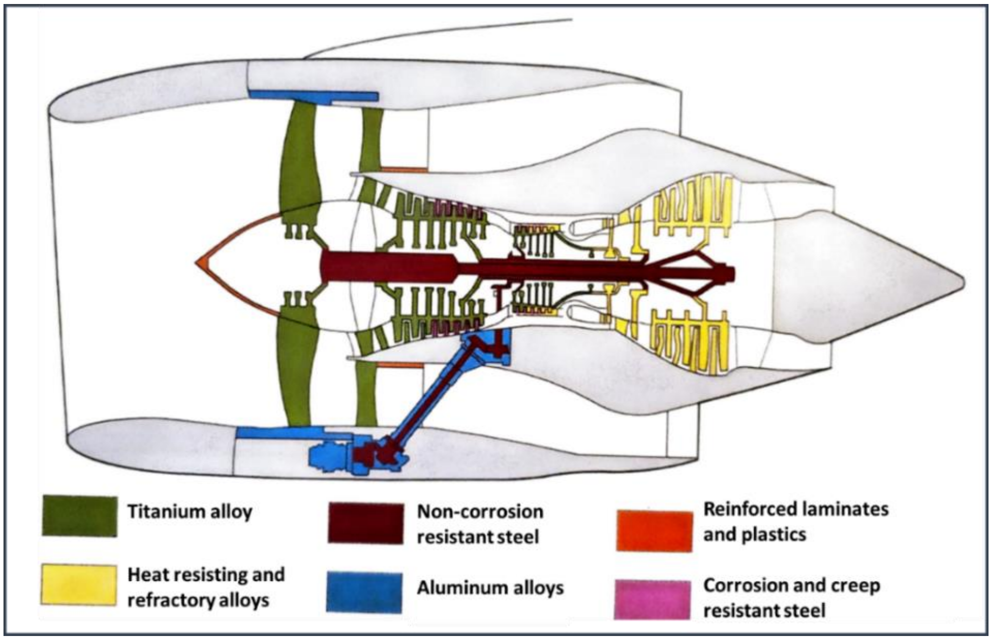

Figure 8.1 Different materials in a jet engine [332].

One of the most promising methods used for the protection of aircraft components from problems caused by aggressive environments and high operating temperatures is the application of protective coatings. Erosion resistant coating systems, such as the ones presented in this work, namely TiN, ZrN single-layer and ZrN/TiN multilayer coatings, have a substantial impact on engine parts [15] because they prevent compressor blades from premature loss of material; however, they also have an effect on the components fatigue resistance. The coatings must possess good mechanical and tribological properties, they also must be smooth, without vulnerable stress points. Therefore, their application should ensure improved coating-substrate properties to retard or stop failure mechanisms, in particular crack nucleation and crack propagation. This work investigates three surface treatments, coatings and Ti-6Al-4V substrates separately and as a coated system, to fill a knowledge gap in understanding the influence of local and overall stress on i) the durability of coated metallic components, and ii) the impact of erosion-resistant coatings with controlled stress, and their potential for retarding crack propagation, as a viable means of creating safer aircraft with longer life span.

RS values that can be found in the literature can be evaluated by various techniques including XRD, synchrotron diffraction, neutron diffraction, wafer curvature, ultrasonic method, micro-Raman spectroscopy, and focused ion beam methods [134], [333]. Among these techniques, the XRD and wafer curvature techniques have been widely employed for the determination of surface RS. However, a comparison of RS results of magnetron sputtered hard coatings normally show inconsistency in the stress reported from one study to another [121], [334]. It is worth noting that the wafer curvature method (Stoney's equation) measures the average stress, known as 'overall stress', in a surface layer or a coating. This method is based on assumptions that the system is homogeneous, isotropic and the coating and substrate exhibit a linear and elastic behaviors [335]. In contrast, the XRD measurements, based on the $\sin^2\psi$ technique, were established from the theories of crystallography and solid mechanics [128], [336]. It is capable of measuring the surface RS in a depth of up to a few micrometers, normally below 10 μm for grazing angle measurements, into the coated system [337]. The RS assessment by XRD evaluated at various fixed incident angles provides a 'local stress' at the desired depth penetration of the coated system. This method can thus take into account the anisotropy in coatings and substrates [153], [209].

Due to the importance of assessing an optimal RS level in the coated systems, we consider it critical to explore both the overall stress and the contribution of the local stress of each part of the coated system, and their effect on the resulting mechanical/tribological properties. Therefore, the local stress was evaluated by performing RS depth profiles and surface stress measurements in the surface of the coating and the interface independently. In this study, two main observations have been made:

i) Surface engineering by plasma-based processes using different interface approaches, namely Ar plasma, surface nitriding and Ti implantation, leads to variations in the microstructure and texture of the substrate's surface, and it consequently affects the protective coating growth. These modifications imposed different levels of sub-surface compressive RS spanning to a depth of several micrometers under the Ti-6Al-4V surface. RS depth profiles for 1 μm TiN coatings presented RS values between -1 GPa and -4 GPa. As a consequence, the RS gradient spans over a depth of about 5 μm across which it varies from several MPa within the substrate to several GPa at the coating surface. The TiN-Nit sample presented the highest compressive RS level, while TiN-Ti exhibited the lowest compressive RS through the coated system.

ii) A strong effect of the deposition methodology on RS, namely its anisotropy in relation to the configuration of the substrate holder and substrate mounting has been detected. Specifically, the relation between the associated geometry during stress assessment in dependence on the way how the substrate had been attached to the holder was quantified. In particular, we founded a significant difference (anisotropy) in the RS values (more than 100%) for different orientations of the coated samples during the XRD measurements for situations when the substrates were rigidly clamped to the substrate holder; These differences were much smaller (comparable to the experimental error) when the substrates were non-clamped. The assessment of RS on different sample orientations and their comparison with RS obtained by the curvature technique allows us to determine that overall stress corresponds only to specific characteristics of the material, limiting the correct interpretation of the RS effect on other properties of the coated material. This study can therefore explain some of the reasons for the inconsistent published values for different coatings. The deformation and stresses thus formed can, in general, be described by the deflection of plates explained by the plates' theory [338] that is, however, outside of the scope of the present work.

Identifying anisotropic behaviour on RS was vital in this work, allowing us to understand the nanoindentation results and use the correct RS values, especially in the case fracture mechanisms analyses. For example, the nanoindentation results (*H* and *E*) reported here are an average of 300 measurements performed at three different areas of the sample's surface, randomly selected. The overall stress of TiN coatings measured by the curvature method in Chapter 6 showed about -1.3 GPa; this coincides better with the values obtained by XRD at the 90° sample orientation (about – 1.4 GPa), however, it is still lower than the local stress. These observations suggest that considering the highest RS obtained by XRD at 0° sample orientation could lead to a misestimation of some of the critical results, especially in the analysis of interfacial shear strength. Therefore, the analyses of elasto-plastic and fracture characteristics were performed using the lowest local RS, taking into account that the allowed direction of the sample in the micro-tensile equipment corresponds to the one measured as 90° sample orientation by XRD and micro-scratch testing.

Besides controlling the RS in a judicial manner, plasma processes favored the film's mechanical performance. The enhancement of hardness and adhesion was observed according to the interface treatment applied before coating deposition. We observed a relation between hardness-adhesion-RS and the fracture mechanism of the TiN coatings. Surface nitriding was identified as the interface which provided the highest system support. Chapter 2 described that according to [193], the RS, fracture toughness, and cracking resistance of TiN coatings are influenced by the coating's elastic modulus, namely higher elastic modulus of the coating results in higher fracture toughness. The authors have shown that higher RS results in higher fracture toughness (calculated by scratch test), which for TiN with a compressive RS 3.5 GPa is reported to be around 8.7 $\mathrm{MPa{\cdot}m^{1/2}}$, showing a cracking resistance of 1.3% in a bending test [193].

The discrepancy in fracture toughness results reported in the literature can be explained, in part, by the difference in measurement techniques, which can be categorized into three main groups: (i) the stress approach, (ii) the energy approach, and (iii) the use of pre-cracks created in the material before testing. The stress approach is normally performed by bending test using pre-cracks, scratch and indentation techniques; this method evaluates the stress state near the tip of the crack. On the other hand, the energy approach performed by bending without pre-cracking, buckling, indentation with chipping and tensile test techniques evaluates the system's energy state before and after coating fracture. The resulting difference in energy is considered as the energy required to form new cracks in the coating [339].

With respect to the above, we must clarify that our fracture toughness is reported in terms of energy; therefore, critical energy release rate, G_C, was calculated for the different surface engineering approaches. The obtained results, between 15.0 and 19.7 $\mathrm{J/m^2}$ for single-layer coatings with different interfaces and ~30 $\mathrm{J/m^2}$ for the ZrN/TiN multilayer coating, both on nitrided Ti-6Al-4V, agree with the results in other works for PVD coatings [270], [271], [291]–[294]. The film thickness is of primary concern in the complex fracture toughness measurement. In our case, the system's micro-tensile test was dominated by substrate thickness due to the large difference compared to the coating thickness. The main advantage of using micro-tensile test methods is the larger area of study on the sample surface; therefore, the property evaluated is closer to the material's intrinsic property compared with other methods, such as indentation or bending. This allowed us to conclude that the crack onset strain was favored by high RS, i.e., a higher compressive

RS provides a higher crack resistance, in agreement with the literature review results reported in Chapter 2.

The design of coating architectures has also been found to favour the mechanical, fracture and tribological performance of coated Ti-6Al-4V. The evaluation of different architectures allowed us to show that the nanolaminates have the highest hardness (~35 GPa), the highest elastic strain to failure parameter (H/Er ~0.12) and the highest film resistance to crack propagation (H^3/Er^2 ~0.42 GPa) compared to single-layer coatings (H/Er ~0.08 and H^3/Er^2 ~0.2 GPa). It is worth noting that the H/Er value of the nanolaminate structure is larger than 0.1. This agrees with Chapter 2 that indicated that coatings with H/Er > 0.1 possess enhanced resistance to plastic deformation that allows one to distribute the load applied to the coating over a wider area than do other protective coatings, thus delaying the appearance of cracks. These coatings are considered to be hard and tough [114].

Furthermore, the phenomenological model proposed here indicates that the relative stored energy and stress relaxation are a driving force for solid solution formation that increases as the modulation *L* decreases, leading to strengthening of the interfaces. The formation of a solid solution resulted in the enhancement of wear resistance (lowest wear coefficient obtained for $L \leq 10$ was found as $K \sim 2\text{-}8 \times 10^{-6}$ mm^3/Nm).

CHAPTER 9 CONCLUSIONS AND RECOMMENDATIONS

9.1 Conclusions

The subject of this thesis was proposed as a response to the needs of the aeronautical industry. As the main objective, it was suggested to investigate the influence of model TiN and ZrN single-layer and ZrN/TiN multilayer coatings, and of their growth conditions and surface treatments, on the residual stress and the stress depth profile on the fracture performance of aerospace metallic substrates, namely Ti-6Al-4V. The transition metal nitride coatings were deposited by reactive magnetron sputtering. Before coating deposition, three different interface engineering approaches were explored, namely Ar plasma, surface nitriding, and Ti implantation, to form systems with large differences in the microstructural and mechanical characteristics.

This thesis work had *three specific objectives*; their description and the main conclusions from the fabrication processes, materials characterizations and the corresponding analyses can be summarized as follows:

A) First, different process conditions were evaluated in order to optimize the plasma parameters, plasma-surface interactions, and other process-related characteristics with respect to the growth mechanisms and properties of protective coatings and interface layers. This allowed us to establish a stress assessment methodology (including depth profile and anisotropy) and investigate how the stress depth profile depends on the film growth when considering different interfaces. As a result, thus pre-selected conditions such as pressure, gas composition, bias voltage, and substrate temperature were used to fabricate high-quality hard films with large differences in RS.

The effect of each interface engineering process on the microstructural characteristics of TiN coatings and Ti-6Al-4V substrate were evaluated by comparative analyses performed using XRD, TKD, and TEM. It was concluded that Ar plasma, nitriding, and Ti implantation influence the near-surface region of the Ti-6Al-4V substrate due to Ar^+, N_2^+ or Ti^+ ion bombardment that causes local changes in strain, giving rise to surface/interface hardening, while some of the ions (Ti^+, N_2^+) have a high bonding affinity and can be incorporated at the substrate's lattice sites. The created interface layers affected the texture coefficient of the near surface of Ti-6Al-4V treated with Ar plasma, nitriding and Ti implantation while developing $\bar{1}2\bar{1}0$, 0001, and $01\bar{1}0$ preferred orientations, respectively. The texture of TiN-coated systems resulted in a 001 preferred orientation for TiN-Ar and TiN-Ti, and a transition in the grain orientation within TiN-Nit consisting of a mix where 001 and 111 planes predominate.

Ti or Ar bombardment lead to similar microstructural and mechanical results, as well as a similarity in RS values mainly because both ions have about the same mass causing comparable effects close to the substrate surface. However, during sputtering the Ar and Ti atoms have a minimal depth (2-10 nm) interaction with the substrate material, while during nitriding treatment at 400°C, nitrogen diffuses in the substrate influencing the microstructure and mechanical properties leading to a thicker compressive layer in the Ti64.

The difference in microstructure, including the crystallite size variation between 11 and 16 nm, and the texture imposed by interface treatments gave rise to a significant increase of the Ti-6Al-4V near-surface compressive RS (-300 to -500 MPa), leading to an enhanced RS in the TiN coatings due to a strong effect on the film growth (between -1 and -4 GPa depending on the interface). The RS gradient was found to span over a depth of about 5 μm across the substrate to the coating surface. The TiN-Nit sample presented the highest compressive RS level, while TiN-Ti exhibited the lowest compressive RS through the coated system.

In addition, it was concluded that RS are strongly influenced by the deposition methodology, specially the way in which the substrate is attached to the sample holder can develop anisotropy into the coated material. In particular, we found a significant difference in the RS values with more than 100% on the coated samples for XRD measurements done at different orientations. Such differences were observed on substrates that were rigidly clamped to the substrate holder; however, these differences were much smaller (comparable to the experimental error) on non-clamped substrates.

B) As it was proposed in the *second* specific goal of this work, the micro-scratch and *in-situ* tensile test analyses were used to study crack initiation and propagation in the coating-substrate systems in order to assess the effect of pre-determined RS profiles on the fracture mechanism(s). From the micro-scratch analyses, we concluded that the compressive RS in the coating is the main parameter responsible for the cohesive failure behavior as it was documented by a higher value of the L_{C1} critical load parameter at high compressive RS. Similarly, surface/interface nitriding was found to enhance adhesion more than the Ar plasma exposure and Ti implantation as indicated by higher values of L_{C2}.

The cohesive and adhesive failure extracted from scratch results can be related to the elasto-plastic properties determined by fracture analyses performed using micro-tensile tests, especially the COS and crack density. The COS varied between 0.9% and 1.0% for Ti implantation and Ar plasma treatments with L_{C1} around 8 N and L_{C2} around 18 N, while for TiN and ZrN/TiN with a nitrided interface, it varied between 1.1% to 1.3% presenting L_{C1}~13 N and L_{C2}=23 N for TiN and 29 N for ZrN/TiN. In addition, the ZrN/TiN multilayer showed a lower density (80 cracks/mm) whereas the TiN single layer exhibited the highest one with 120 cracks/mm. These results indicate that the mechanical behavior of the coatings is significantly governed by the coating-substrate system's collective response to delay crack nucleation and propagation through the substrate, and therefore delay the component fracture.

C) Finally, with respect to the *third* specific objective devoted to the effects of different coatings architectures, the nanolaminate, multilayer and single-layer systems were optimized in order to benefit from the relationships between the microstructural features of the coatings and their mechanical, elasto-plastic, and tribological properties, including wear resistance.

In this part of the work, we have demonstrated a significant enhancement of the hardness of the Ti-6Al-4V substrate (5 GPa) by plasma interface treatments up to ~15 GPa, which in turn influenced the hardness of TiN single-layer, and ZrN/TiN multilayer coatings which presented H values up to ~29 GPa and ~35 GPa, respectively. Multilayer ZrN-TiN coatings with various modulation periods showed that decreasing the periodicity in the multilayer structure enhanced the hardness, Young's modulus as well as wear resistance of the films. Formation of a solid solution structure and strengthening of the interfaces was the main cause of the hardening, therefore the highest H and Er values were found for nanolaminates with a periodic structure of L=10 nm, or with a solid solution structure characterized by L<10 nm. We also concluded that the maximum hardness (~35 GPa), the maximum elastic strain to failure parameter (H/Er~0.12) and the highest film resistance to crack propagation ($H^3/E\text{r}^2$ ~0.42 GPa) occur, as it was observed for coatings with a modulation periodicity of L≤10 nm.

The elasto-plastic properties calculated based on the results and observations from nanoindentation and micro-tensile test analyses indicated that the critical energy release rate (15 J/m^2 and 19.7 J/m^2) and interfacial shear strength (550-760 MPa) are mainly controlled by the compressive RS in the coating. The interface treatment appears to particularly affect the fracture mechanism of Ti-6Al-

4V; however, this detrimental effect can be mitigated by a coating with a high compressive RS at the interface layer and within the coating itself. The global RS of the coated system impacts the fracture mechanism of coated specimens, whereas optimum compressive RS levels allow one to delay the failure of the components to enhance their durability.

In terms of wear resistance, the multilayer and nanolaminate coatings, especially those with $L \leq 10$ nm, display the lowest wear coefficient, $K \sim 2\text{-}8 \times 10^{-6}$ mm^3/Nm, compared to TiN single-layer coatings, $K \sim 6 \times 10^{-5}$ mm^3/Nm. For comparison, the wear coefficient of Ti-6Al-4V is about 5×10^{-5} mm^3/Nm. We conclude that nanolaminate coatings showed a higher wear resistance because the critical value of L for optimized wear resistance coincides with the diffusion length of Zr in TiN, leading to the localized solid solution. In this context, a phenomenological model for the $Ti_{0.35}Zr_{0.65}N$ solid solution phase formation related to the dissipation of the stored energy in terms of residual stress was proposed based on our experimental results and observations.

The use of several experimental techniques allowed us to identify the ideal surface engineering approach to maximize wear resistance, strength, and toughness of Ti-6Al-4V.

The application of surface nitriding of Ti-6Al-4V before coating deposition and the optimization of coating microstructure with a preferable (111) orientation has a significant effect on the durability of the coated component. The use of a nitrided interface with hard coatings enhances the tribo-mechanical properties and elasto-plastic deformation characteristics of the metallic component. Multilayer coatings present surface cracks whose propagation can be delayed due to the zig-zag mechanism created by the superimposed layers, but they also show lateral cracks between interfaces which can cause delamination and subsequently lead to catastrophic failure of the coating under further loading. The use of a nanolaminate structure with an appropriate modulation can develop a crystallite size and a Zr-rich solid solution phase, which, by strengthening the material, increases wear resistance and delays crack nucleation and propagation.

9.2 Recommendations

This thesis was focused on the study of surface engineering applied to the fabrication of model TiN-based coatings with three different interface approaches, namely Ar plasma, surface nitriding and Ti implantation. The evaluations of microstructural and mechanical characteristics, especially the residual stress depth profiles, have provided an insight for the understanding of the fracture mechanisms of coated Ti-6Al-4V components exposed to severe conditions. With this in mind, this thesis establishes the background for future orientation of research, especially in the context of the performance of real-life coated components; specifically, this includes:

i) **Coating residual stress.** The RS depth profiles by XRD on single-layer coatings were systematically studied in this work. However, the coating RS in more complex multilayer architectures represents additional challenges; further progress can be seen in the development of a methodology to identify possible phases formed during coating deposition due to periodicity modulation.

ii) **Improvement of interface performance.** The interface treatments proposed in this work demonstrated to be able to induce a high level of compressive stress in the coating and in the near-surface region within the substrate. Optimization of the treatment parameters must be considered in order to induce compressive stress deeper in the substrate to enhance the durability of materials by larger counteracting crack nucleation and crack propagation.

iii) **Fatigue test.** The durability of the coated structure is critical in aeronautic applications. Even though the micro-tensile tests gave us a great insight into the fracture mechanism of the coated system, ultimately, fatigue tests should be performed on the coated specimens. This would help to verify the validity and relevance of the results from other test methods in order to assure performance of the components in the high and low cycle regimes to which they are exposed the aircraft engine.

iv) Development of crack propagation models related to stress. The development of finite element models to study the RS as a critical factor to mitigate fracture mechanisms in order to propose RS depth profiles optimization strategies to delay crack nucleation and propagation.

REFERENCES

[1] T. Captain, “Deloitte 2016 Global aerospace and defense sector outlook - Poised for a rebound,” 2016.

[2] R. Lineberger, “Deloitte 2020 global aeropsace and defense industry outlook,” 2019.

[3] R. Rajendran, “Gas turbine coatings - An overview,” *Eng. Fail. Anal.*, vol. 26, pp. 355–369, 2012.

[4] E. Benini, *Progress in gas turbine performance*. BoD–Books on Demand, 2013.

[5] M. Hetmańczyk, “Advanced materials and protective coatings in aero-engines application,” vol. 24, no. 1, pp. 372–381, 2007.

[6] R. G. J. S. Millan, I. Armendariz, J. Garcia-Martinez, “Stratgies for static failure analysis on aerospace structures,” in *Handbook of materials failure analysis with case studies from the aerospace and automative industries,* Waltham, MA: Elsevier Ltd, 2016, pp. 1–498.

[7] A. Mouritz, *Introduction to Aerospace Materials*. 2012.

[8] S. Zhang and D. Zhao, *Aerospace materials handbook*. CrC Press, 2016.

[9] C. Bathias and A. Pineau, “Fatigue of Materials and Structures: Fundamentals, ISTE Ltd and John Wiley & Sons.” Inc, 2010.

[10] U. G. Goranson, “Fatigue issues in aircraft maintenance and repairs,” *Int. J. Fatigue*, vol. 19, no. 1, pp. 413–431, 1997.

[11] “The Jet engine,” in *Rolls-Royce plc*, Derby, England, 1996, pp. 1–292.

[12] E. Bousser, L. Martinu, and J. E. Klemberg-Sapieha, “Solid particle erosion mechanisms of protective coatings for aerospace applications,” *Surf. Coatings Technol.*, vol. 257, pp. 165–181, 2014.

[13] G. Cassar, S. Banfield, J. C. Avelar-Batista Wilson, J. Housden, A. Matthews, and A. Leyland, “Impact wear resistance of plasma diffusion treated and duplex treated/PVD-coated Ti-6Al-4V alloy,” *Surf. Coatings Technol.*, vol. 206, no. 10, pp. 2645–2654, 2012.

[14] B. Borawski, J. Singh, J. A. Todd, and D. E. Wolfe, “Multi-layer coating design architecture for optimum particulate erosion resistance,” *Wear*, vol. 271, no. 11–12, pp. 2782–2792, 2011.

[15] E. Bousser, L. Martinu, and J. E. Klemberg-Sapieha, “Solid particle erosion mechanisms of hard protective coatings,” *Surf. Coat. Technol.*, vol. 235, pp. 383–393, 2013.

[16] M. E. Gross and P. M. Martin, “Vacuum Polymer Deposition,” in *Handbook of Deposition Technologies for Films and Coatings,* Third Edit., Elsevier, 2010, pp. 532–553.

[17] A. Anders, “High power impulse magnetron sputtering and related discharges: Scalable plasma sources for plasma-based ion implantation and deposition,” *Surf. Coatings Technol.*, vol. 204, no. 18–19, pp. 2864–2868, Jun. 2010.

[18] D. Lundin, J. T. Gudmundsson, and T. Minea, “High power impulse magnetron sputtering: fundamentals, technologies, challenges and applications,” 2019.

[19] L. Ben Freund and S. Suresh, *Thin film materials: stress, defect formation and surface evolution*. Cambridge university press, 2004.

[20] J. A. Thornton, “Structure-zone models of thin films,” in *Modeling of Optical Thin Films*, 1988, vol. 821, pp. 95–105.

[21] S. Baragetti and F. Villa, “An Updated Review of the Fatigue Behavior of Components Coated with Thin Hard Corrosion-Resistant Coatings,” *Open Mater. Sci. J.*, vol. 8, no. 1, pp. 87–98, Nov. 2014.

[22] A. I. Journal, S. Baragetti, and F. Tordini, “Experimental and Numerical Study of Shot Peened Thin Hard-Coated Components,” vol. 7734, no. August, 2016.

[23] G. Cassar *et al.*, “Evaluating the effects of plasma diffusion processing and duplex diffusion/PVD-coating on the fatigue performance of Ti–6Al–4V alloy,” *Int. J. Fatigue*, vol. 33, no. 9, pp. 1313–1323, Sep. 2011.

[24] G. Lütjering and J. C. Williams, *Titanium*. Springer Science & Business Media, 2007.

[25] C. Veiga, A. J. R. Loureiro, and J. P. Davim, “Proprties and applications of titanium alloys,” *Rev. Adv. Mater. Sci.*, vol. 32, p. s. 133-148, 2012.

[26] Britannica Science, “Common metallic crystal structures,” *Encyclopedia Britannica*. Encyclopedia Britannica, Inc, 2012.

[27] C. Leyens and M. Peters, *Titanium and titanium alloys: fundamentals and applications*. John Wiley & Sons, 2003.

[28] M. J. Donachie, *Titanium: a technical guide*. ASM international, 2000.

[29] Y. Itoh, A. Itoh, H. Azuma, and T. Hioki, “Improving the tribological properties of Ti-6Al-4V alloy by nitrogen-ion implantation,” *Surf. Coatings Technol.*, vol. 111, no. 2–3, pp. 172–176, 1999.

[30] L. Martinu, O. Zabeida, and J. E. Klemberg-Sapieha, “Plasma-Enhanced Chemical Vapor Deposition of Functional Coatings,” in *Handbook of Deposition Technologies for Films and Coatings*, Elsevier, 2010, pp. 392–465.

[31] D. Framil Carpeño *et al.*, “Nanomechanical and in situ TEM characterization of boron carbide thin films on helium implanted substrates: Delamination, real-time cracking and substrate buckling,” *Mater. Sci. Eng. A*, vol. 639, pp. 54–64, 2015.

[32] M. Ikeyama *et al.*, “Increase of surface hardness induced by O, Ca or P ion implantation into titanium,” *Surf. Coatings Technol.*, vol. 128–129, pp. 400–403, 2000.

[33] R. . Rodríguez, A. Medrano, M. Rico, R. Sánchez, R. Martínez, and J. . García, “Niche sectors for economically competitive ion implantation treatments,” *Surf. Coatings Technol.*, vol. 158–159, pp. 48–53, Sep. 2002.

[34] S. Sobieszczyk, “Surface modifications of ti and its alloys,” *Adv. Mater. Sci.*, vol. 10, no. 1, pp. 29–42, Jan. 2010.

[35] P. Sioshansi, “Improving the properties of titanium alloys by ion implantation,” *Jom*, vol. 42, no. 3, pp. 30–31, 1990.

[36] S. Gokul Lakshmi, D. Arivuoli, and B. Ganguli, “Surface modification and characterisation of Ti-Al-V alloys,” *Mater. Chem. Phys.*, vol. 76, no. 2, pp. 187–190, 2002.

[37] T. Bell, H. W. Bergmann, J. Lanagan, P. H. Morton, and A. M. Staines, “Surface Engineering of Titanium with Nitrogen,” *Surf. Eng.*, vol. 2, no. 2, pp. 133–143, 1986.

[38] H. J. Spies, “Surface engineering of aluminium and titanium alloys: An overview,” *Surf. Eng.*, vol. 26, no. 1–2, pp. 126–134, 2010.

[39] H. J. Spies, B. Reinhold, and K. Wilsdorf, “Gas nitriding - Process control and nitriding non-ferrous alloys,” *Surf. Eng.*, vol. 17, no. 1, pp. 41–54, 2001.

[40] J. Lanagan, P. H. Morton, and T. Bell, “Surface engineering of titanium with glow discharge plasma,” *Des. with Titan.*, pp. 136–150, 1986.

[41] K. Farokhzadeh and A. Edrisy, “Fatigue improvement in low temperature plasma nitrided Ti-6Al-4V alloy,” *Mater. Sci. Eng. A*, vol. 620, pp. 435–444, 2015.

[42] H. Dong, T. Bell, and A. Mynott, “Surface engineering of titanium alloys for the motorsports industry,” *Sport. Eng.*, vol. 2, no. 4, pp. 213–220, 1999.

[43] C. Kwietniewski, H. Dong, T. Strohaecker, X. Y. Li, and T. Bell, “Duplex surface treatment of high strength Timetal 550 alloy towards high load-bearing capacity,” *Surf. Coatings Technol.*, vol. 139, no. 2–3, pp. 284–292, 2001.

[44] Y. Fu, J. Wei, B. Yan, and N. L. Loh, “Characterization and tribological evaluation of duplex treatment by depositing carbon nitride films on plasma nitrided Ti-6Al-4V,” *J. Mater. Sci.*, vol. 35, no. 9, pp. 2215–2227, 2000.

[45] B. S. Yilbas, M. S. J. Hashmi, and S. Z. Shuja, “Laser treatment and PVD TiN coating of Ti-6Al-4V alloy,” *Surf. Coatings Technol.*, vol. 140, no. 3, pp. 244–250, 2001.

[46] H. Dong, A. Bloyce, and T. Bell, “Oxygen thermochemical treatment combined with DLC coating for enhanced loadbearing capacity of Ti-6AI-4V,” *Surf. Eng.*, vol. 14, no. 6, pp. 505–512, 1998.

[47] H. Dong, “Current status and trends in duplex surface engineering of titanium alloys,” in *20 th ASM Heat Treating Society Conference*, 2000, pp. 170–176.

[48] V. Fouquet, L. Pichon, M. Drouet, and A. Straboni, “Plasma assisted nitridation of Ti-6Al-4V,” *Appl. Surf. Sci.*, vol. 221, no. 1–4, pp. 248–258, 2004.

[49] A. Zhecheva, W. Sha, S. Malinov, and A. Long, “Enhancing the microstructure and properties of titanium alloys through nitriding and other surface engineering methods,” *Surf. Coatings Technol.*, vol. 200, no. 7, pp. 2192–2207, 2005.

[50] F. Galliano, E. Galvanetto, S. Mischler, and D. Landolt, “Tribocorrosion behavior of plasma nitrided Ti-6Al-4V alloy in neutral NaCl solution,” *Surf. Coatings Technol.*, vol. 145, no. 1–3, pp. 121–131, 2001.

[51] E. Kusano, M. Kitagawa, Y. Kuroda, H. Nanto, and A. Kinbara, “Adhesion and hardness of compositionally gradient TiO2/Ti/TiN, ZrO2/Zr/ZrN, and TiO2/Ti/Zr/ZrN coatings,” *Thin Solid Films*, vol. 334, no. 1–2, pp. 151–155, 1998.

[52] M. Pizzorni, C. Gambaro, E. Lertora, and C. Mandolfino, “Effect of process gases in vacuum

plasma treatment on adhesion properties of titanium alloy substrates," *Int. J. Adhes. Adhes.*, vol. 86, no. July, pp. 113–122, 2018.

[53] A. Anders, "A review comparing cathodic arcs and high power impulse magnetron sputtering (HiPIMS)," *Surf. Coatings Technol.*, vol. 257, pp. 308–325, Oct. 2014.

[54] K. Sarakinos, J. Alami, and S. Konstantinidis, "High power pulsed magnetron sputtering: A review on scientific and engineering state of the art," *Surf. Coatings Technol.*, vol. 204, no. 11, pp. 1661–1684, 2010.

[55] J. Musil, "Hard nanocomposite coatings: Thermal stability, oxidation resistance and toughness," *Surf. Coatings Technol.*, vol. 207, pp. 50–65, 2012.

[56] A. P. Ehiasarian, P. E. Hovsepian, L. Hultman, and U. Helmersson, "Comparison of microstructure and mechanical properties of chromium nitride-based coatings deposited by high power impulse magnetron sputtering and by the combined steered cathodic arc/unbalanced magnetron technique," *Thin Solid Films*, vol. 457, no. 2, pp. 270–277, 2004.

[57] K. Yamamoto, S. Kujime, and K. Takahara, "Properties of nano-multilayered hard coatings deposited by a new hybrid coating process: Combined cathodic arc and unbalanced magnetron sputtering," *Surf. Coatings Technol.*, vol. 200, no. 1-4 SPEC. ISS., pp. 435–439, 2005.

[58] M. Ohring, *The Materials Science of Thin Films*. Academic Press, 1992.

[59] M. T. Mubarak, A., E. Hamzah, "Review of physical vapour deposition (PVD) techniques for hard coating," *J. Mek.*, vol. 20, pp. 42–51, 2005.

[60] J. Musil, P. Baroch, J. Vlček, K. H. Nam, and J. G. Han, "Reactive magnetron sputtering of thin films: Present status and trends," *Thin Solid Films*, vol. 475, no. 1-2 SPEC. ISS., pp. 208–218, 2005.

[61] G. Este and W. D. Westwood, "A quasi-direct-current sputtering technique for the deposition of dielectrics at enhanced rates," *J. Vac. Sci. Technol. A Vacuum, Surfaces, Film.*, vol. 6, no. 3, pp. 1845–1848, 1988.

[62] A. P. Ehiasarian, J. G. Wen, and I. Petrov, "Interface microstructure engineering by high power impulse magnetron sputtering for the enhancement of adhesion," *J. Appl. Phys.*, vol. 101, no. 5, 2007.

[63] J. T. Gudmundsson *et al.*, "A quasi-direct-current sputtering technique for the deposition of dielectrics at enhanced rates," *Thin Solid Films*, vol. 475, no. 3, p. 030801, 2005.

[64] W. D. Sproul, D. J. Christie, and D. C. Carter, "Control of reactive sputtering processes," *Thin Solid Films*, vol. 491, no. 1–2, pp. 1–17, 2005.

[65] V. Kouznetsov, K. Macak, J. M. Schneider, U. Helmersson, and I. Petrov, "A novel pulsed magnetron sputter technique utilizing very high target power densities," *Surf. Coatings Technol.*, vol. 122, no. 2–3, pp. 290–293, 1999.

[66] A. P. Ehiasarian, J. G. Wen, and I. Petrov, "Interface microstructure engineering by high power impulse magnetron sputtering for the enhancement of adhesion," *J. Appl. Phys.*, vol. 101, no. 5, 2007.

[67] J. T. Gudmundsson, N. Brenning, D. Lundin, and U. Helmersson, “High power impulse magnetron sputtering discharge,” *J. Vac. Sci. Technol. A Vacuum, Surfaces, Film.*, vol. 30, no. 3, p. 030801, 2012.

[68] J. T. Gudmundsson, “Physics and technology of magnetron sputtering discharges,” *Plasma Sources Sci. Technol.*, vol. 29, no. 11, 2020.

[69] B. A. Movchan and A. V Demchishin, “Structure and properties of thick condensates of Nickel, Titatinum, Tungsten, Aluminium Oxides, and Zirconium Dioxide in vacuum,” *Fiz. Met. Met. 28 653-60 (Oct 1969).*, 1969.

[70] J. V Sanders, “Structure of Evaporated Metal Films,” in *Chemisorption and Reaction on Metallic Films*, J. R. Anderson, Ed. Londond & New York: Academic Press, New York, 1971.

[71] J. A. Thornton, “Influence of Apparatus Geometry and Deposition Conditions on the Structure and Topography of Thick Sputtered Coatings.,” *J Vac Sci Technol*, vol. 11, no. 4, pp. 666–670, 1974.

[72] A. Anders, “A structure zone diagram including plasma-based deposition and ion etching,” *Thin Solid Films*, vol. 518, no. 15, pp. 4087–4090, May 2010.

[73] J. A. Thornton, “High Rate Thick Film Growth,” *Annu. Rev. Mater. Sci.*, vol. 7, no. 1, pp. 239–260, 1977.

[74] J. Chen and S. J. Bull, “Approaches to investigate delamination and interfacial toughness in coated systems: An overview,” *J. Phys. D. Appl. Phys.*, vol. 44, no. 3, 2011.

[75] M. F. Othman, A. R. Bushroa, and W. N. R. Abdullah, “Evaluation techniques and improvements of adhesion strength for TiN coating in tool applications: A review,” *J. Adhes. Sci. Technol.*, vol. 29, no. 7, pp. 569–591, 2015.

[76] A. Bloyce, “Surface engineering of titanium alloys for wear protection,” *Proc. Inst. Mech. Eng. Part J J. Eng. Tribol.*, vol. 212, no. 6, pp. 467–476, 1998.

[77] H.-J. Spies, “Surface engineering of aluminium and titanium alloys: an overview,” *Surf. Eng.*, vol. 26, no. 1–2, pp. 126–134, Feb. 2010.

[78] A. Amassian, M. Dudek, O. Zabeida, S. C. Gujrathi, J. E. Klemberg-Sapieha, and L. Martinu, “Oxygen incorporation and charge donor activation via subplantation during growth of indium tin oxide films,” *J. Vac. Sci. Technol. A Vacuum, Surfaces, Film.*, vol. 27, no. 2, pp. 362–366, 2009.

[79] G. Betz and G. . Wehner, “Sputtering of multicomponent materials,” 1983, pp. 11–90.

[80] D. M. Mattox, “Front-matter,” in *Handbook of Physical Vapor Deposition (PVD) Processing*, 2nd ed., Oxford: Elsevier, 2010.

[81] J. Heydenreich, “G. Dearnaley, JH Freeman, RS Nelson, J. Stephen. Ion implantation. North-Holland Publishing Company 1973 (Series: Defects in Crystalline Solids, Eds. S. Amelinckx et al., Vol. 8) 802 Seiten, 408 Abbildungen. Preis etwa US $79.00,” *Krist. und Tech.*, vol. 9, no. 6, pp. K41–K42, 1974.

[82] J. Jagielski, A. Piatkowska, P. Aubert, L. Thomé, A. Turos, and A. Abdul Kader, “Ion

implantation for surface modification of biomaterials," *Surf. Coatings Technol.*, vol. 200, no. 22-23 SPEC. ISS., pp. 6355–6361, 2006.

[83] D. Manova, J. W. Gerlach, F. Scholze, S. Mändl, and H. Neumann, "Nitriding of austenitic stainless steel by pulsed low energy ion implantation," *Surf. Coatings Technol.*, vol. 204, no. 18–19, pp. 2919–2922, 2010.

[84] R. Figueroa, C. M. Abreu, M. J. Cristóbal, and G. Pena, "Effect of nitrogen and molybdenum ion implantation in the tribological behavior of AA7075 aluminum alloy," *Wear*, vol. 276–277, pp. 53–60, 2012.

[85] P. Vlcak, F. Cerny, J. Drahokoupil, J. Sepitka, and Z. Tolde, "The microstructure and surface hardness of Ti6Al4V alloy implanted with nitrogen ions at an elevated temperature," *J. Alloys Compd.*, vol. 620, pp. 48–54, 2015.

[86] S. R. Hosseini and A. Ahmadi, "Evaluation of the effects of plasma nitriding temperature and time on the characterisation of Ti 6Al 4V alloy," *Vacuum*, vol. 87, pp. 30–39, 2013.

[87] A. Grill, A. Raveh, and R. Avni, "Layer structure and mechanical properties of low pressure r.f. plasma nitrided Ti-6Al-4V alloy," *Surf. Coatings Technol.*, vol. 43–44, no. PART 2, pp. 745–755, Dec. 1990.

[88] A. Raveh, P. L. Hansen, R. Avni, and A. Grill, "Microstructure and composition of plasma-nitrided Ti-6Al-4V layers," *Surf. Coatings Technol.*, vol. 38, no. 3, pp. 339–351, 1989.

[89] A. Raveh, A. Bussiba, A. Bettelheim, and Y. Katz, "Plasma-nitrided α-β Ti alloy: layer characterization and mechanical properties modification," *Surf. Coatings Technol.*, vol. 57, no. 1, pp. 19–29, 1993.

[90] A. Molinari, G. Straffelini, B. Tesi, T. Bacci, and G. Pradelli, "Effects of load and sliding speed on the tribological behaviour of Ti-6A1-4V plasma nitrided at different temperatures," *Wear*, vol. 203–204, no. 96, pp. 447–454, 1997.

[91] H. A. Wriedt and J. L. Murray, "The N-Ti (Nitrogen-Titanium) system," *Bull. Alloy Phase Diagrams*, vol. 8, no. 4, pp. 378–388, 1987.

[92] E. Rolinski, G. Sharp, D. F. Cowgill, and D. J. Peterman, "Ion nitriding of titanium alpha plus beta alloy for fusion reactor applications," *J. Nucl. Mater.*, vol. 252, no. 3, pp. 200–208, 1998.

[93] A. Nishimoto, T. E. Bell, and T. Bell, "Feasibility study of active screen plasma nitriding of titanium alloy," *Surf. Eng.*, vol. 26, no. 1–2, pp. 74–79, 2010.

[94] A. Edrisy and K. Farokhzadeh, "Plasma Nitriding of Titanium Alloys," in *Plasma Science and Technology - Progress in Physical States and Chemical Reactions*, T. Mieno, Ed. Rijeka, Croatia: InTech, 2016.

[95] T. Bacci, G. Pradelli, B. Tesi, C. Gianoglio, and C. Badini, "Surface engineering and chemical characterization in ion-nitrided titanium and titanium alloys," *J. Mater. Sci.*, vol. 25, no. 10, pp. 4309–4314, 1990.

[96] K. C. Chen and G. J. Jaung, "D.c. diode ion nitriding behavior of titanium and Ti-6Al-4V," *Thin Solid Films*, vol. 303, no. 1–2, pp. 226–231, 1997.

[97] R. J. Wasilewski and G. L. Kehl, “Diffusion of nitrogen and oxygen in titanium,” *J. Inst. Met.*, vol. 83, 1954.

[98] A. A. Il’in, S. V. Skvortsova, L. M. Petrov, E. A. Lukina, and A. A. Chernysheva, “Effect of the phase composition and structure of titanium alloys on their interaction with nitrogen during low-temperature ion nitriding,” *Russ. Metall.*, vol. 2006, no. 5, pp. 400–405, 2006.

[99] B. Edenhofer, “Physical and Metallurgical Aspects of Ionitriding. Pt. 1,” *Heat Treat. Met.*, no. 1, pp. 23–28, 1974.

[100] S. L. R. Da Silva, L. O. Kerber, L. Amaral, and C. A. Dos Santos, “X-ray diffraction measurements of plasma-nitrided Ti-6Al-4V,” *Surf. Coatings Technol.*, vol. 116–119, pp. 342–346, 1999.

[101] N. N. Koval *et al.*, “Influence of the composition of a plasma-forming gas on nitriding in a non-self-maintained glow discharge with a large hollow cathode,” *J. Surf. Investig.*, vol. 6, no. 1, pp. 154–158, 2012.

[102] M. Tamaki, Y. Tomii, and N. Yamamoto, “The role of hydrogen in plasma nitriding: Hydrogen behavior in the titanium nitride layer,” *Plasmas Ions*, vol. 3, no. 1–4, pp. 33–39, 2000.

[103] X. Li, D. Q. Sun, X. Y. Zheng, and Z. A. Ren, “Effect of N2/Ar gas flow ratios on the nitrided layers by direct current arc discharge,” *Mater. Lett.*, vol. 62, no. 2, pp. 226–229, 2008.

[104] H. Yilmazer, S. Yilmaz, and M. E. Acma, “Treatment of surface properties of titanium with plasma (ion) nitriding,” *Defect Diffus. Forum*, vol. 283–286, pp. 401–405, 2009.

[105] T. A. Panaioti and G. V. Solov’ev, “Ion nitriding of aging (α + β) titanium alloys,” *Met. Sci. Heat Treat.*, vol. 38, no. 5–6, pp. 216–219, 1996.

[106] D. Rodríguez, J. M. Manero, F. J. Gil, and J. A. Planell, “Low cycle fatigue behavior of Ti6AI4V thermochemically nitrided for its use in hip prostheses,” *J. Mater. Sci. Mater. Med.*, vol. 12, no. 10–12, pp. 935–937, 2001.

[107] J. Musil, F. Kunc, H. Zeman, and H. Poláková, “Relationships between hardness, Young’s modulus and elastic recovery in hard nanocomposite coatings,” *Surf. Coatings Technol.*, vol. 154, no. 2–3, pp. 304–313, 2002.

[108] J. Musil, “Hard and superhard nanocomposite coatings,” *Surf. Coatings Technol.*, vol. 125, no. 1–3, pp. 322–330, 2000.

[109] A. Leyland and A. Matthews, “On the significance of the H/E ratio in wear control: A nanocomposite coating approach to optimised tribological behaviour,” *Wear*, vol. 246, no. 1–2, pp. 1–11, 2000.

[110] D. L. Joslin and W. C. Oliver, “A new method for analyzing data from continuous depth-sensing microindentation tests,” *J. Mater. Res.*, vol. 5, no. 1, pp. 123–126, 1990.

[111] D. Broek, *Elementary engineering fracture mechanics*. Dordrecht: Springer Netherlands, 1982.

[112] B. Q. Yang, K. Zhang, G. N. Chen, G. X. Luo, and J. H. Xiao, “Measurement of fracture

toughness and interfacial shear strength of hard and brittle Cr coating on ductile steel substrate," *Surf. Eng.*, vol. 24, no. 5, pp. 332–336, 2008.

[113] J. L. Beuth and N. W. Klingbeil, "Cracking of thin films bonded to elastic plastic substrates," *J. Mech. Phys. Solids*, vol. 44, no. 9, pp. 1411–1428, 1996.

[114] J. Musil, "Hard nanocomposite coatings: Thermal stability, oxidation resistance and toughness," *Surf. Coatings Technol.*, vol. 207, pp. 50–65, 2012.

[115] P. H. Mayrhofer, C. Mitterer, L. Hultman, and H. Clemens, "Microstructural design of hard coatings," *Prog. Mater. Sci.*, vol. 51, no. 8, pp. 1032–1114, 2006.

[116] E. Klokholm and B. S. Berry, "Intrinsic Stress in Evaporated Metal Films," *J. Electrochem. Soc.*, vol. 115, no. 8, p. 823, 1968.

[117] Y. Pauleau, "Generation and evolution of residual stresses in physical vapour-deposited thin films," *Vacuum*, vol. 61, no. 2–4, pp. 175–181, 2001.

[118] M. F. Doerner *et al.*, "Strain, ion bombardment and energetic neutrals in magnetron sputtering," *Thin Solid Films*, vol. 1, no. 1, pp. 845–851, 1988.

[119] H. Windischmann, "Intrinsic stress in sputter-deposited thin films," *Crit. Rev. Solid State Mater. Sci.*, vol. 17, no. 6, pp. 547–596, 1992.

[120] G. Abadias, A. Michel, C. Tromas, C. Jaouen, and S. N. Dub, "Stress, interfacial effects and mechanical properties of nanoscale multilayered coatings," *Surf. Coatings Technol.*, vol. 202, no. 4–7, pp. 844–853, 2007.

[121] G. C. A. M. Janssen, "Stress and strain in polycrystalline thin films," *Thin Solid Films*, vol. 515, no. 17, pp. 6654–6664, 2007.

[122] R. C. Cammarata, T. M. Trimble, and D. J. Srolovitz, "Surface stress model for intrinsic stresses in thin films," *J. Mater. Res.*, vol. 15, no. 11, pp. 2468–2474, Nov. 2000.

[123] R. Koch, "The intrinsic stress of polycrystalline and epitaxial thin metal films," *J. Phys. Condens. Matter*, vol. 6, no. 45, pp. 9519–9550, 1994.

[124] R. Koch, "Stress in Evaporated and Sputtered Thin Films - A Comparison," *Surf. Coatings Technol.*, vol. 204, no. 12–13, pp. 1973–1982, 2010.

[125] R. Daniel, J. Keckes, I. Matko, M. Burghammer, and C. Mitterer, "Origins of microstructure and stress gradients in nanocrystalline thin films: The role of growth parameters and self-organization," *Acta Mater.*, vol. 61, no. 16, pp. 6255–6266, 2013.

[126] A. Moridi, H. Ruan, L. C. Zhang, and M. Liu, "Residual stresses in thin film systems: Effects of lattice mismatch, thermal mismatch and interface dislocations," *Int. J. Solids Struct.*, vol. 50, no. 22–23, pp. 3562–3569, 2013.

[127] M. D. Thouless, "Modeling the Development and Relaxation of Stresses in Films," *Annu. Rev. Mater. Sci.*, vol. 25, no. 1, pp. 69–96, Aug. 1995.

[128] I. C. Noyan and J. B. Cohen, *Residual Stress*. New York, NY: Springer New York, 1987.

[129] P. J. Withers and H. K. D. H. Bhadeshia, "Residual stress. Part 1 – Measurement techniques," *Mater. Sci. Technol.*, vol. 17, no. 4, pp. 355–365, Apr. 2001.

[130] E. Bemporad, M. Sebastiani, F. Casadei, and F. Carassiti, “Modelling, production and characterisation of duplex coatings (HVOF and PVD) on Ti-6Al-4V substrate for specific mechanical applications,” *Surf. Coatings Technol.*, vol. 201, no. 18, pp. 7652–7662, 2007.

[131] S. Schmidt *et al.*, “SiNx coatings deposited by reactive high power impulse magnetron sputtering: Process parameters influencing the residual coating stress,” *J. Appl. Phys.*, vol. 121, no. 17, 2017.

[132] A. Fluri *et al.*, “Enhanced Proton Conductivity in Y-Doped BaZrO3 via Strain Engineering,” *Adv. Sci.*, vol. 4, no. 12, 2017.

[133] D. Sander, Z. Tian, and J. Kirschner, “The role of surface stress in structural transitions, epitaxial growth and magnetism on the nanoscale,” *J. Phys. Condens. Matter*, vol. 21, no. 13, 2009.

[134] G. Abadias *et al.*, “Review Article: Stress in thin films and coatings: Current status, challenges, and prospects,” *J. Vac. Sci. Technol. A Vacuum, Surfaces, Film.*, vol. 36, no. 2, p. 020801, 2018.

[135] H. Oettel and R. Wiedemann, “Residual stresses in PVD hard coatings,” *Surf. Coatings Technol.*, vol. 76–77, pp. 265–273, Nov. 1995.

[136] C. R. M. Grovenor, H. T. G. Hentzell, and D. A. Smith, “The development of grain structure during growth of metallic films,” *Acta Metall.*, vol. 32, no. 5, pp. 773–781, May 1984.

[137] H. F. Winters, H. Coufal, C. T. Rettner, and D. S. Bethune, “Energy transfer from rare gases to surfaces: Collisions with gold and platinum in the range 1–4000 eV,” *Phys. Rev. B*, vol. 41, no. 10, pp. 6240–6256, Apr. 1990.

[138] T. C. Huang, G. Lim, F. Parmigiani, and E. Kay, “Effect of ion bombardment during deposition on the x-ray microstructure of thin silver films,” *J. Vac. Sci. Technol. A Vacuum, Surfaces, Film.*, vol. 3, no. 6, pp. 2161–2166, 1985.

[139] H. F. Winters and E. Kay, “Gas incorporation into sputtered films,” *J. Appl. Phys.*, vol. 38, no. 10, pp. 3928–3934, 1967.

[140] A. M. Engwall, Z. Rao, and E. Chason, “Origins of residual stress in thin films: Interaction between microstructure and growth kinetics,” *Mater. Des.*, vol. 110, pp. 616–623, 2016.

[141] A. Entenberg, V. Lindberg, K. Fletcher, A. Gatesman, and R. S. Horwath, “Stress measurement in sputtered copper films on flexible polyimide substrates,” *J. Vac. Sci. Technol. A Vacuum, Surfaces, Film.*, vol. 5, no. 6, pp. 3373–3377, 1987.

[142] A. M. Haghiri-Gosnet, F. R. Ladan, C. Mayeux, and H. Launois, “Stresses in sputtered tungsten thin films,” *Appl. Surf. Sci.*, vol. 38, no. 1–4, pp. 295–303, Sep. 1989.

[143] M. Konuma, *Film deposition by plasma techniques*, vol. 10. Springer Science & Business Media, 2012.

[144] S. . Rossnagel, J. . Cuomo, and W. . Westwood, *Handbook of plasma processing technology: fundamentals, etching, deposition, and surface interactions*. William Andrew, 1990.

[145] J. A. Thornton and G. E. McGuire, “Semiconductor Materials and Process Technology Handbook,” *Noyes, Park Ridge, NJ*, vol. 329, 1988.

[146] H. Leplan, J. Y. Robic, and Y. Pauleau, “Kinetics of residual stress evolution in evaporated silicon dioxide films exposed to room air,” *J. Appl. Phys.*, vol. 79, no. 9, pp. 6926–6931, 1996.

[147] K. Dahmen, S. Lehwald, and H. Ibach, “Bending of crystalline plates under the influence of surface stress - a finite element analysis,” *Surf. Sci.*, vol. 446, no. 1–2, pp. 161–173, 2000.

[148] W. Ratuszek, E. Kusior, S. J. Skrzypek, and A. Baczman, “research papers New approach to stress analysis based on grazing- incidence X-ray diffraction research papers,” *J. Appl. Cryst.*, vol. 34, pp. 427–435, 2001.

[149] M. Marciszko *et al.*, “Multireflection grazing incidence diffraction used for stress measurements in surface layers,” *Thin Solid Films*, vol. 530, pp. 81–84, Mar. 2013.

[150] M. Klaus and C. Genzel, “X-ray residual stress analysis on multilayer systems: An approach for depth-resolved data evaluation,” *J. Appl. Crystallogr.*, vol. 46, no. 5, pp. 1266–1276, 2013.

[151] M. Ferrari, L. Lutterotti, and L. Lutterotti, “Method for the simultaneous determination of anisotropic residual stresses and texture by x - ray diffraction Method for the simultaneous determination stresses and texture by x-ray diffraction of anisotropic residual,” vol. 7246, no. 1994, 2013.

[152] M. Marciszko *et al.*, “Application of multireflection grazing incidence method for stress measurements in polished Al–Mg alloy and CrN coating,” *Appl. Surf. Sci.*, vol. 266, pp. 256–267, Feb. 2013.

[153] A. J. Perry, “The state of residual stress in TiN films made by physical vapor deposition methods; the state of the art,” *J. Vac. Sci. Technol. A Vacuum, Surfaces, Film.*, vol. 8, no. 3, pp. 1351–1358, 2002.

[154] C.-H. Ma, J.-H. Huang, and H. Chen, “Chen_2017_R-loops,” *Thin Solid Films*, vol. 418, pp. 73–78, 2002.

[155] G. G. Stoney, “The Tension of Metallic Films Deposited by Electrolysis,” *Proc. R. Soc. A Math. Phys. Eng. Sci.*, vol. 82, no. 553, pp. 172–175, May 1909.

[156] M. Hÿtch, F. Houdellier, F. Hüe, and E. Snoeck, “Nanoscale holographic interferometry for strain measurements in electronic devices,” *Nature*, vol. 453, no. 7198, pp. 1086–1089, 2008.

[157] F. Ahmed, K. Bayerlein, S. M. Rosiwal, M. Göken, and K. Durst, “Stress evolution and cracking of crystalline diamond thin films on ductile titanium substrate: Analysis by micro-Raman spectroscopy and analytical modelling,” *Acta Mater.*, vol. 59, no. 14, pp. 5422–5433, 2011.

[158] A. J. Wilkinson, G. Meaden, and D. J. Dingley, “High-resolution elastic strain measurement from electron backscatter diffraction patterns: New levels of sensitivity,” *Ultramicroscopy*, vol. 106, no. 4–5, pp. 307–313, 2006.

[159] A. J. Wilkinson, E. Tarleton, A. Vilalta-Clemente, J. Jiang, T. B. Britton, and D. M. Collins, “Measurement of probability distributions for internal stresses in dislocated crystals,” *Appl. Phys. Lett.*, vol. 105, no. 18, 2014.

[160] K. J. Kang, N. Yao, M. Y. He, and A. G. Evans, “A method for in situ measurement of the residual stress in thin films by using the focused ion beam,” *Thin Solid Films*, vol. 443, no. 1–2, pp. 71–77, Oct. 2003.

[161] N. Sabaté *et al.*, “Digital image correlation of nanoscale deformation fields for local stress measurement in thin films,” *Nanotechnology*, vol. 17, no. 20, pp. 5264–5270, 2006.

[162] R. Schöngrundner *et al.*, “Critical assessment of the determination of residual stress profiles in thin films by means of the ion beam layer removal method,” *Thin Solid Films*, vol. 564, pp. 321–330, Aug. 2014.

[163] M. E. Fitzpatrick and A. Lodini, *Analysis of residual stress by diffraction using neutron and synchrotron radiation*. CRC Press, 2003.

[164] I. C. Noyan and J. B. Cohen, *Residual Stress*, vol. 24, no. 2. New York, NY: Springer New York, 1987.

[165] U. Welzel, J. Ligot, P. Lamparter, A. C. Vermeulen, and E. J. Mittemeijer, “Stress analysis of polycrystalline thin films and surface regions by X-ray diffraction,” *J. Appl. Crystallogr.*, vol. 38, no. 1, pp. 1–29, Feb. 2005.

[166] S. Zhang, H. Xie, X. Zeng, and P. Hing, “Residual stress characterization of diamond-like carbon coatings by an X-ray diffraction method,” *Surf. Coatings Technol.*, vol. 122, no. 2–3, pp. 219–224, Dec. 1999.

[167] A. J. Perry, V. Valvoda, and D. Rafaja, “X-ray residual stress measurement in TiN, ZrN and HfN films using the Seemann-Bohlin method,” *Thin Solid Films*, vol. 214, no. 2, pp. 169–174, 1992.

[168] K. Holmberg, H. Ronkainen, and A. Matthews, “Tribology of thin coatings,” *Ceram. Int.*, vol. 26, no. 7, pp. 787–795, 2000.

[169] K. Bobzin, “CIRP Journal of Manufacturing Science and Technology High-performance coatings for cutting tools,” *CIRP J. Manuf. Sci. Technol.*, vol. 18, no. 2016, pp. 1–9, 2018.

[170] F. Klocke and T. Krieg, “Coated tools for Metal Cutting - Features and Applications,” *Keynote Pap.*, vol. 48, no. Annals of the CIRP, pp. 515–525, 1999.

[171] A. P. Serro *et al.*, “A comparative study of titanium nitrides, TiN, TiNbN and TiCN, as coatings for biomedical applications,” *Surf. Coatings Technol.*, vol. 203, no. 24, pp. 3701–3707, Sep. 2009.

[172] B. Pécz, N. Frangis, S. Logothetidis, I. Alexandrou, P. B. Barna, and J. Stoemenos, “Electron microscopy characterization of TiN films on Si, grown by d.c. reactive magnetron sputtering,” *Thin Solid Films*, vol. 268, no. 1–2, pp. 57–63, Nov. 1995.

[173] R. W. Harrison and W. E. Lee, “Processing and properties of ZrC, ZrN and ZrCN ceramics: a review,” *Adv. Appl. Ceram.*, vol. 115, no. 5, pp. 294–307, 2016.

[174] J. P. Bars, E. Etchessahar, and J. Debuigne, “Étude cinétique, diffusionnelle et morphologique de la nitruration du titane par l’azote à haute température: Propriétés mécaniques et structurales des solutions solides Tiα-azote,” *J. Less-Common Met.*, vol. 52, no. 1, pp. 51–76, 1977.

[175] P. Patsalas, C. Gravalidis, and S. Logothetidis, “Surface kinetics and subplantation phenomena affecting the texture, morphology, stress, and growth evolution of titanium nitride films,” *J. Appl. Phys.*, vol. 96, no. 11, pp. 6234–6235, 2004.

[176] J. O. Kim, J. D. Achenbach, P. B. Mirkarimi, and S. A. Barnett, “Acoustic-microscopy measurements of the elastic properties of TiN/(VxNb1-x)N superlattices,” *Phys. Rev. B*, vol. 48, no. 3, pp. 1726–1737, 1993.

[177] J. E. Greene, J. -E. Sundgren, L. Hultman, I. Petrov, and D. B. Bergstrom, “Development of preferred orientation in polycrystalline TiN layers grown by ultrahigh vacuum reactive magnetron sputtering,” *Appl. Phys. Lett.*, vol. 67, no. 20, pp. 2928–2930, Nov. 1995.

[178] J. Pelleg, L. Z. Zevin, S. Lungo, and N. Croitoru, “Reactive-sputter-deposited TiN films on glass substrates,” *Thin Solid Films*, vol. 197, no. 1–2, pp. 117–128, Mar. 1991.

[179] Y. Kajikawa, S. Noda, and H. Komiyama, “Comprehensive perspective on the mechanism of preferred orientation in reactive-sputter-deposited nitrides,” *J. Vac. Sci. Technol. A Vacuum, Surfaces, Film.*, vol. 21, no. 6, pp. 1943–1954, 2003.

[180] L. Hultman, J. -E. Sundgren, J. E. Greene, D. B. Bergstrom, and I. Petrov, “High-flux low-energy (≈20 eV) N + 2 ion irradiation during TiN deposition by reactive magnetron sputtering: Effects on microstructure and preferred orientation,” *J. Appl. Phys.*, vol. 78, no. 9, pp. 5395–5403, Nov. 1995.

[181] J.-S. Chun, I. Petrov, and J. E. Greene, “Dense fully 111-textured TiN diffusion barriers: Enhanced lifetime through microstructure control during layer growth,” *J. Appl. Phys.*, vol. 86, no. 7, pp. 3633–3641, Oct. 1999.

[182] T.-Q. Li, S. Noda, Y. Tsuji, T. Ohsawa, and H. Komiyama, “Initial growth and texture formation during reactive magnetron sputtering of TiN on Si (111),” *J. Vac. Sci. Technol. A Vacuum, Surfaces, Film.*, vol. 20, no. 3, pp. 583–588, 2002.

[183] G. Beensh-Marchwicka, L. Kròl-Stępniewska, and W. Posadowski, “Structure of thin films prepared by the cosputtering of titanium and aluminium or titanium and silicon,” *Thin Solid Films*, vol. 82, no. 4, pp. 313–320, Aug. 1981.

[184] V. Valvoda, R. Kužel Jr, R. Černý, and J. Musil, “Structure of TiN coatings deposited at relatively high rates and low temperatures by magnetron sputtering,” *Thin Solid Films*, vol. 156, no. 1, pp. 53–64, 1988.

[185] J. I. Jeong, J. H. Hong, J. S. Kang, H. J. Shin, and Y. P. Lee, “Analysis of TiC and TiN films prepared by an arc-induced ion plating,” *J. Vac. Sci. Technol. A Vacuum, Surfaces, Film.*, vol. 9, no. 5, pp. 2618–2622, Sep. 1991.

[186] M.-K. Lee, H.-S. Kang, W.-W. Kim, J.-S. Kim, and W.-J. Lee, “Characteristics of TiN film deposited on stellite using reactive magnetron sputter ion plating,” *J. Mater. Res.*, vol. 12, no. 9, pp. 2393–2400, Sep. 1997.

[187] B. Pecz, N. Frangis, S. Logothetidis, I. Alexandrou, P. B. Barna, and J. Stoemenos, “Electron microscopy characterization of TiN films on Si, grown by dc reactive magnetron sputtering,” *Thin Solid Films*, vol. 268, no. 1–2, pp. 57–63, 1995.

[188] U. C. Oh and J. H. Je, “Effects of strain energy on the preferred orientation of TiN thin

films," *J. Appl. Phys.*, vol. 74, no. 3, pp. 1692–1696, 1993.

[189] J. H. Je, D. Y. Noh, H. K. Kim, and K. S. Liang, "Preferred orientation of TiN films studied by a real time synchrotron x-ray scattering," *J. Appl. Phys.*, vol. 81, no. 9, pp. 6126–6133, 1997.

[190] P. H. Mayrhofer *et al.*, "Evolution of nanoscale texture in ultrathin TiN films," *J. Appl. Phys.*, vol. 78, no. 4, pp. 1270–1274, 1996.

[191] D. R. McKenzie, Y. Yin, W. D. McFall, and N. H. Hoang, "The orientation dependence of elastic strain energy in cubic crystals and its application to the preferred orientation in titanium nitride thin films," *J. Phys. Condens. Matter*, vol. 8, no. 32, pp. 5883–5890, 1996.

[192] Y. M. Chen, G. P. Yu, and J. H. Huang, "Characterizing the effects of multiprocess parameters on the preferred orientation of TiN coating using a combined index," *Vacuum*, vol. 66, no. 1, pp. 19–25, Jun. 2002.

[193] K. Holmberg *et al.*, "Residual stresses in TiN, DLC and MoS2 coated surfaces with regard to their tribological fracture behaviour," *Wear*, vol. 267, no. 12, pp. 2142–2156, 2009.

[194] S. P. Oettel, H., R. Wiedmann, "Residual stresses in nitride hard coatings prepared by magnetron sputtering and arc evaporation," *Surf. Coatings Technol.*, vol. 74–75, no. PART 1, pp. 273–278, 1995.

[195] M. F. Othman, A. R. Bushroa, and W. Abdullah, "Evaluation techniques and improvements of adhesion strength for TiN coating in tool applications: a review," *J. Adhes. Sci. Technol.*, vol. 29, no. 7, pp. 569–591, Apr. 2015.

[196] A. Liu, J. Deng, H. Cui, Y. Chen, and J. Zhao, "Friction and wear properties of TiN, TiAlN, AlTiN and CrAlN PVD nitride coatings," *Int. J. Refract. Met. Hard Mater.*, vol. 31, pp. 82–88, 2012.

[197] P. C. Jindal, A. T. Santhanam, U. Schleinkofer, and A. F. Shuster, "Performance of PVD TiN, TiCN, and TiAlN coated cemented carbide tools in turning," *Int. J. Refract. Met. Hard Mater.*, vol. 17, no. 1, pp. 163–170, 1999.

[198] M. Khadem, O. V. Penkov, H. K. Yang, and D. E. Kim, "Tribology of multilayer coatings for wear reduction: A review," *Friction*, vol. 5, no. 3, pp. 248–262, 2017.

[199] O. V. Penkov, A. Y. Devizenko, M. Khadem, E. N. Zubarev, V. V. Kondratenko, and D. E. Kim, "Toward Zero Micro/Macro-Scale Wear Using Periodic Nano-Layered Coatings," *ACS Appl. Mater. Interfaces*, vol. 7, no. 32, pp. 18136–18144, 2015.

[200] Y. Chang and C. Wu, "Surface & Coatings Technology Mechanical properties and impact resistance of multilayered TiAlN / ZrN coatings," *Surf. Coat. Technol.*, vol. 231, pp. 62–66, 2013.

[201] H. Holleck and V. Schier, "Multilayer PVD coatings for wear protection," *Surf. Coatings Technol.*, vol. 76–77, no. 1995, pp. 328–336, 1995.

[202] M. Azadi, A. S. Rouhaghdam, S. Ahangarani, and H. H. Mofidi, "Mechanical behavior of TiN/TiC multilayer coatings fabricated by plasma assisted chemical vapor deposition on AISI H13 hot work tool steel," *Surf. Coatings Technol.*, vol. 245, pp. 156–166, 2014.

[203] Beck and A. I. R. and J., “Grinding and polishing machine,” *J. Sci. Instrum.*, vol. 34, no. 11, pp. 468–469, 1957.

[204] R. R. Keller and R. H. Geiss, “Transmission EBSD from 10 nm domains in a scanning electron microscope,” *J. Microsc.*, vol. 245, no. 3, pp. 245–251, 2012.

[205] G. B. Harris, “Quantitative measurement of preferred orientation in rolled uranium bars,” *Philos. Mag. J. Sci.*, vol. 43, no. 336, pp. 113–123, 1952.

[206] O. V Maksakova *et al.*, “Multilayered ZrN / CrN coatings with enhanced thermal and mechanical properties,” vol. 776, 2019.

[207] H. Yoshimura, S. Yamada, A. Yoshimura, I. Hirosawa, K. Kojima, and M. Tachibana, “Grazing incidence X-ray diffraction study on carbon nanowalls,” *Chem. Phys. Lett.*, vol. 482, pp. 125–128, 2009.

[208] M. Marciszko, A. Baczmański, C. Braham, M. Wróbel, S. Wroński, and G. Cios, “Stress measurements by multi-reflection grazing-incidence X-ray diffraction method (MGIXD) using different radiation wavelengths and different incident angles,” *Acta Mater.*, vol. 123, pp. 157–166, Jan. 2017.

[209] C. Sarioglu, “The effect of anisotropy on residual stress values and modification of Serruys approach to residual stress calculations for coatings such as TiN, ZrN and HfN,” *Surf. Coatings Technol.*, vol. 201, no. 3–4, pp. 707–717, 2006.

[210] M. Marciszko *et al.*, “Multireflection grazing incidence diffraction used for stress measurements in surface layers,” *Thin Solid Films*, vol. 530, pp. 81–84, 2013.

[211] A. Kumar, U. Welzel, and E. J. Mittemeijer, “A method for the non-destructive analysis of gradients of mechanical stresses by X-ray diffraction measurements at fixed penetration/information depths,” *J. Appl. Crystallogr.*, vol. 39, no. 5, pp. 633–646, Oct. 2006.

[212] A. Baczmanski, C. Braham, W. Seiler, and N. Shiraki, “Multi-reflection method and grazing incidence geometry used for stress measurement by X-ray diffraction,” *Surf. Coatings Technol.*, vol. 182, no. 1, pp. 43–54, Apr. 2004.

[213] M. Marciszko, “l ’ École Nationale Supérieure d ’ Arts et Métiers,” L’École Nationale Supérieure d ’ Arts et Métiers, 2013.

[214] V. Hauk, *Structural and residual stress analysis by nondestructive methods: Evaluation-Application-Assessment*. Elsevier, 1997.

[215] M. R. Ardigo, M. Ahmed, and A. Besnard, “Stoney formula: Investigation of curvature measurements by optical profilometer,” *Adv. Mater. Res.*, vol. 996, pp. 361–366, 2014.

[216] W. C. Oliver and G. M. Pharr, “An improved technique for determining hardness and elastic modulus using load and displacement sensing indentation experiments,” *J. Mater. Res.*, vol. 7, no. 06, pp. 1564–1583, Jun. 1992.

[217] *International Organization for Standardization. Metallic materials – instrumented indentation test for hardness and materials parameters – Part 4: test method for metallic and non-metallic coatings.* Geneva, Switzerland: ISO 14577-4, 2007.

[218] N. Saba, M. Jawaid, and M. T. H. Sultan, *An overview of mechanical and physical testing of composite materials*. Elsevier Ltd, 2019.

[219] "ASTM C28 Advanced Ceramic Standards," vol. 15, p. 2012, 2012.

[220] S. T. Gonczy and N. Randall, "An ASTM standard for quantitative scratch adhesion testing of thin, hard ceramic coatings," *Int. J. Appl. Ceram. Technol.*, vol. 2, no. 5, pp. 422–428, 2005.

[221] T. Arai, H. Fujita, and M. Watanabe, "Evaluation of adhesion strength of thin hard coatings," *Thin Solid Films*, vol. 154, no. 1–2, pp. 387–401, 1987.

[222] P. J. Blau, "Chapter 7, scratch adhesion testing," *Lab Handb. Scratch Testing,, Blue Rock Tech. Publ., Oak Ridge, TN*, p. 7, 2002.

[223] C. Ingelbrecht, N. Jennett, R. Jacobs, and J. Meneve, *Report EUR 20986. The certification of critical coating failure loads: a reference material for scratch testing according to ENV 1071-3: 1994*. 2004.

[224] M. H. Blees, G. B. Winkelman, A. R. Balkenende, and J. M. J. den Toonder, "Effect of friction on scratch adhesion testing: Application to a sol-gel coating on polypropylene," *Thin Solid Films*, vol. 359, no. 1, pp. 1–13, 2000.

[225] ASTM International, "G133-05 Linearly Reciprocating Ball-on-Flat Sliding Wear," *ASTM Int.*, vol. i, no. Reapproved 2016, pp. 1–9, 2016.

[226] M. Azzi and J. E. Klemberg-Sapieha, "Tribocorrosion test protocols for sliding contacts," *Tribocorrosion Passiv. Met. Coatings*, pp. 222–238, 2011.

[227] H. J. Brading, P. H. Morton, T. Bell, and L. G. Earwaker, "Plasma Nitriding with Nitrogen, Hydrogen, and Argon Gas Mixtures: Structure and Composition of Coatings on Titanium," *Surf. Eng.*, vol. 8, no. 3, pp. 206–212, 1992.

[228] T. M. Muraleedharan and E. I. Meletis, "Surface modification of pure titanium and Ti-6Al-4V by intensified plasma ion nitriding," *Thin Solid Films*, vol. 221, no. 1–2, pp. 104–113, Dec. 1992.

[229] E. J. Herrera-Jimenez, A. Raveh, T. Schmitt, E. Bousser, J. E. Klemberg-Sapieha, and L. Martinu, "Solid solution hardening in nanolaminate ZrN-TiN coatings with enhanced wear resistance," *Thin Solid Films*, vol. 688, no. April, p. 137431, 2019.

[230] T. Sprute, W. Tillmann, D. Grisales, U. Selvadurai, and G. Fischer, "Influence of substrate pre-treatments on residual stresses and tribo-mechanical properties of TiAlN-based PVD coatings," *Surf. Coatings Technol.*, vol. 260, pp. 369–379, 2014.

[231] B. J. Jones, L. Anguilano, and J. J. Ojeda, "Argon plasma treatment techniques on steel and effects on diamond-like carbon structure and delamination," *Diam. Relat. Mater.*, vol. 20, no. 7, pp. 1030–1035, 2011.

[232] Y. Z. Xing, G. Wang, Y. Zhang, Y. N. Chen, and M. Dargusch, "Development in plasma surface diffusion techniques of Ti-6Al-4V alloy: a review," *Int. J. Adv. Manuf. Technol.*, vol. 92, no. 5–8, pp. 1901–1912, 2017.

[233] M. Raaif, F. M. El-Hossary, N. Z. Negm, S. M. Khalil, and P. Schaaf, "Surface treatment of

Ti–6Al–4V alloy by rf plasma nitriding,” *J. Phys. Condens. Matter*, vol. 19, no. 39, p. 396003, 2007.

[234] M. M. Verdian, “Finishing and Post-Treatment of Thermal Spray Coatings,” *Compr. Mater. Finish.*, vol. 3–3, pp. 191–206, 2016.

[235] G. Abadias, Y. Y. Tse, P. Guérin, and V. Pelosin, “Interdependence between stress, preferred orientation, and surface morphology of nanocrystalline TiN thin films deposited by dual ion beam sputtering,” *J. Appl. Phys.*, vol. 99, no. 11, 2006.

[236] P. H. Mayrhofer, F. Kunc, J. Musil, and C. Mitterer, “A comparative study on reactive and non-reactive unbalanced magnetron sputter deposition of TiN coatings,” *Thin Solid Films*, vol. 415, no. 1–2, pp. 151–159, 2002.

[237] E. Atar, C. Sarioglu, H. Cimenoglu, and E. S. Kayali, “Residual stresses in (Zr,Hf)N films (up to 11.9 at.% Hf) measured by X-ray diffraction using experimentally calculated XECs,” *Surf. Coatings Technol.*, vol. 191, no. 2–3, pp. 188–194, 2005.

[238] U. C. Oh and J. H. Je, “Effects of strain energy on the preferred orientation of TiN thin films,” *J. Appl. Phys.*, vol. 74, no. 3, pp. 1692–1696, Aug. 1993.

[239] G. Williamson and W. Hall, “X-ray line broadening from filed aluminium and wolfram,” *Acta Metall.*, vol. 1, no. 1, pp. 22–31, Jan. 1953.

[240] P. W. Trimby, “Orientation mapping of nanostructured materials using transmission Kikuchi diffraction in the scanning electron microscope,” *Ultramicroscopy*, vol. 120, pp. 16–24, Sep. 2012.

[241] V. Birman, *Plate Structures*, vol. 178. Dordrecht: Springer Netherlands, 2011.

[242] F. M. D’Heurle, “Aluminum films deposited by rf sputtering,” *Metall. Mater. Trans. B*, vol. 1, no. 3, pp. 725–732, Mar. 1970.

[243] G. Abadias, “Stress and preferred orientation in nitride-based PVD coatings,” *Surf. Coatings Technol.*, vol. 202, no. 11, pp. 2223–2235, 2008.

[244] L. Zhang, H. Yang, X. Pang, K. Gao, and A. A. Volinsky, “Microstructure, residual stress, and fracture of sputtered TiN films,” *Surf. Coatings Technol.*, vol. 224, pp. 120–125, 2013.

[245] A. Kilicaslan, O. Zabeida, E. Bousser, T. Schmitt, J. E. Klemberg-Sapieha, and L. Martinu, “Hard titanium nitride coating deposition inside narrow tubes using pulsed DC PECVD processes,” *Surf. Coatings Technol.*, vol. 377, no. August, p. 124894, Nov. 2019.

[246] A. Raveh, “Mechanisms of r.f. plasma nitriding of Ti-6Al-4V alloy,” *Mater. Sci. Eng. A*, vol. 167, no. 1–2, pp. 155–164, Aug. 1993.

[247] S. Banerjee and P. Mukhopadhyay, “‘Phase transformations: examples from titanium and zirconium alloys,’” Oxford: Elsevier, 2007, p. 557.

[248] S. Guo, Q. Meng, X. Zhao, Q. Wei, and H. Xu, “Design and fabrication of a metastable β-type titanium alloy with ultralow elastic modulus and high strength,” *Sci. Rep.*, vol. 5, no. September, pp. 1–8, 2015.

[249] M. I. Jones, I. R. McColl, and D. M. Grant, “Effect of substrate preparation and deposition conditions on the preferred orientation of TiN coatings deposited by RF reactive sputtering,”

Surf. Coatings Technol., vol. 132, no. 2–3, pp. 143–151, 2000.

[250] S. J. Chipera and D. L. Bish, "Fitting Full X-Ray Diffraction Patterns for Quantitative Analysis: A Method for Readily Quantifying Crystalline and Disordered Phases," *Adv. Mater. Phys. Chem.*, vol. 03, no. 01, pp. 47–53, 2013.

[251] B. Rajasekaran and S. Ganesh Sundara Raman, "Plain fatigue and fretting fatigue behaviour of plasma nitrided Ti-6Al-4V," *Mater. Lett.*, vol. 62, no. 16, pp. 2473–2475, 2008.

[252] X. Song *et al.*, "Microstructures and residual strain/stresses of YSZ coatings prepared by plasma spraying," *Mater. Lett.*, vol. 240, pp. 217–220, 2019.

[253] E. M. Lehockey, Y.-P. Lin, and O. E. Lepik, "Mapping Residual Plastic Strain in Materials Using Electron Backscatter Diffraction," in *Electron Backscatter Diffraction in Materials Science*, Boston, MA: Springer US, 2000, pp. 247–264.

[254] B. E. Carroll, T. A. Palmer, and A. M. Beese, "Anisotropic tensile behavior of Ti-6Al-4V components fabricated with directed energy deposition additive manufacturing," *Acta Mater.*, vol. 87, pp. 309–320, 2015.

[255] D. G. Bansal, O. L. Eryilmaz, and P. J. Blau, "Surface engineering to improve the durability and lubricity of Ti-6Al-4V alloy," *Wear*, vol. 271, no. 9–10, pp. 2006–2015, 2011.

[256] S. Kim and J. Nairn, "Fracture mechanics analysis of coating/substrate systems: Part I: Analysis of tensile and bending experiments," *Eng. Fract. Mech.*, vol. 65, pp. 595–607, 2000.

[257] M. Dong, Y. Zhu, C. Wang, L. Shan, and J. Li, "Structure and tribocorrosion properties of duplex treatment coatings of TiSiCN/nitride on Ti6Al4V alloy," *Ceram. Int.*, vol. 45, no. 9, pp. 12461–12468, 2019.

[258] V. Totolin, V. Pejaković, T. Csanyi, O. Hekele, M. Huber, and M. Rodríguez Ripoll, "Surface engineering of Ti6Al4V surfaces for enhanced tribocorrosion performance in artificial seawater," *Mater. Des.*, vol. 104, pp. 10–18, 2016.

[259] A. P. Gopkalo and A. V. Rutkovskyy, "The effect of PVD coatings on the tensile strength and low-cycle fatigue resistance of stainless steel and titanium alloys," *Fatigue Fract. Eng. Mater. Struct.*, vol. 34, no. 12, pp. 1012–1020, 2011.

[260] C. Martini and L. Ceschini, "A comparative study of the tribological behaviour of PVD coatings on the Ti-6Al-4V alloy," *Tribol. Int.*, vol. 44, no. 3, pp. 297–308, 2011.

[261] F. Ahmed, K. Durst, S. Rosiwal, J. Fandrey, J. Schaufler, and M. Göken, "In-situ tensile testing of crystalline diamond coatings using Raman spectroscopy," *Surf. Coatings Technol.*, vol. 204, no. 6–7, pp. 1022–1025, 2009.

[262] Y. Sun and T. Bell, "The role of oxidation in the wear of plasma nitrided and PVD TiN coated steel," *Wear*, vol. 166, no. 1, pp. 119–125, 1993.

[263] D. Nolan, S. W. Huang, V. Leskovsek, and S. Braun, "Sliding wear of titanium nitride thin films deposited on Ti-6Al-4V alloy by PVD and plasma nitriding processes," *Surf. Coatings Technol.*, vol. 200, no. 20–21, pp. 5698–5705, 2006.

[264] A. D. Wilson, A. Leyland, and A. Matthews, "A comparative study of the influence of

plasma treatments, PVD coatings and ion implantation on the tribological performance of Ti-6Al-4V," *Surf. Coatings Technol.*, vol. 114, no. 1, pp. 70–80, 1999.

[265] A. F. Yetim, A. Alsaran, I. Efeoglu, and A. Çelik, "A comparative study: The effect of surface treatments on the tribological properties of Ti-6Al-4V alloy," *Surf. Coatings Technol.*, vol. 202, no. 11, pp. 2428–2432, 2008.

[266] S. Djaziri *et al.*, "Comparative study of the mechanical properties of nanostructured thin films on stretchable substrates," *J. Appl. Phys.*, vol. 116, no. 9, p. 093504, Sep. 2014.

[267] S. Bull, "Techniques for improving thin film adhesion," *Vacuum*, vol. 43, no. 5–7, pp. 517–520, May 1992.

[268] A. V Byeli, S. K. Shikh, and V. V Khatko, "Friction and wear of high speed steel doped with low energy nitrogen ions," *Wear*, vol. 159, pp. 185–190, 1992.

[269] H. Kovac, A. F. Yetim, Ö. Baran, and A. Çelik, "Materials Science & Engineering A Fatigue crack growth analysis of plasma nitrided AISI 4140 low-alloy steel : Part 1-constant amplitude loading," vol. 672, pp. 257–264, 2016.

[270] A. N. Wang, G. P. Yu, and J. H. Huang, "Fracture toughness measurement on TiN hard coatings using internal energy induced cracking," *Surf. Coatings Technol.*, vol. 239, pp. 20–27, 2014.

[271] J. H. Huang, Y. F. Chen, and G. P. Yu, "Evaluation of the fracture toughness of Ti1-xZrxN hard coatings: Effect of compositions," *Surf. Coatings Technol.*, vol. 358, no. July 2018, pp. 487–496, 2019.

[272] B. A. Latella, B. K. Gan, K. E. Davies, D. R. McKenzie, and D. G. McCulloch, "Titanium nitride/vanadium nitride alloy coatings: Mechanical properties and adhesion characteristics," *Surf. Coatings Technol.*, vol. 200, no. 11, pp. 3605–3611, 2006.

[273] B. F. Chen, J. Hwang, G. P. Yu, and J. H. Huang, "In situ observation of the cracking behavior of TiN coating on 304 stainless steel subjected to tensile strain," *Thin Solid Films*, vol. 352, no. 1–2, pp. 173–178, 1999.

[274] W. J. Chou, G. P. Yu, and J. H. Huang, "Mechanical properties of TiN thin film coatings on 304 stainless steel substrates," *Surf. Coatings Technol.*, vol. 149, no. 1, pp. 7–13, 2002.

[275] E. J. Herrera-Jimenez, T. Schmitt, E. Bousser, J. E. Klemberg-Sapieha, and L. Martinu, "Effect of plasma interface treatment on the microstructure, residual stress profile, and mechanical properties of PVD TiN coatings on Ti-6Al-4V substrates," *submited to Surf. Coat. Technol.*, 2021.

[276] M. Marciszko *et al.*, "Application of multireflection grazing incidence method for stress measurements in polished Al–Mg alloy and CrN coating," *Appl. Surf. Sci.*, vol. 266, pp. 256–267, Feb. 2013.

[277] D. Nečas and P. Klapetek, "Gwyddion: An open-source software for SPM data analysis," *Cent. Eur. J. Phys.*, vol. 10, no. 1, pp. 181–188, 2012.

[278] E. Török, A. J. Perry, L. Chollet, and W. D. Sproul, "Young's modulus of TiN, TiC, ZrN and HfN," *Thin Solid Films*, vol. 153, no. 1–3, pp. 37–43, Oct. 1987.

[279] M. Wojtaszek, T. Sleboda, A. Czulak, G. Weber, and W. A. Hufenbach, “Quasi-Static and Dynamic Tensile Properties of Ti-6Al-4V AlloyWojtaszek, M., Sleboda, T., Czulak, A., Weber, G., & Hufenbach, W. A. (2013). Quasi-Static and Dynamic Tensile Properties of Ti-6Al-4V Alloy. Archives of Metallurgy and Materials, 58(4), 1261–1,” *Arch. Metall. Mater.*, vol. 58, no. 4, pp. 1261–1265, Dec. 2013.

[280] G. Jaeger, I. Endler, M. Heilmaier, K. Bartsch, and A. Leonhardt, “New method of determining strength and fracture toughness of thin hard coatings,” *Thin Solid Films*, vol. 377–378, pp. 382–388, 2000.

[281] M. Qin, D. Y. Ju, Y. N. Wu, C. Sun, and J. B. Li, “Determination of the fracture strength for ceramic film on substrate by X-ray stress analysis method,” *Mater. Charact.*, vol. 56, no. 3, pp. 208–213, 2006.

[282] M. Ignat, T. Marieb, H. Fujimoto, and P. A. Flinn, “Mechanical behaviour of submicron multilayers submitted to microtensile experiments,” *Thin Solid Films*, vol. 353, no. 1, pp. 201–207, 1999.

[283] M. S. Hu and A. G. Evans, “The cracking and decohesion of thin films on ductile substrates,” *Acta Metall.*, vol. 37, no. 3, pp. 917–925, Mar. 1989.

[284] B. Taskonak, J. J. Mecholsky, and K. J. Anusavice, “Residual stresses in bilayer dental ceramics,” *Biomaterials*, vol. 26, no. 16, pp. 3235–3241, 2005.

[285] G. Skordaris *et al.*, “Effect of PVD film’s residual stresses on their mechanical properties, brittleness, adhesion and cutting performance of coated tools,” *CIRP J. Manuf. Sci. Technol.*, vol. 18, pp. 145–151, 2017.

[286] J. Jeong and D. Kwon, “Evaluation of the adhesion strength in DLC film- coated systems using the film-cracking technique,” vol. 4243, 2012.

[287] D. C. Agrawal and R. Raj, “Measurement of the ultimate shear strength of a metal-ceramic interface,” *Acta Metall.*, vol. 37, no. 4, pp. 1265–1270, Apr. 1989.

[288] M. Yanaka, Y. Tsukahara, N. Nakaso, and N. Takeda, “Cracking phenomena of brittle films in nanostructure composites analysed by a modified shear lag model with residual strain,” *J. Mater. Sci.*, vol. 33, no. 8, pp. 2111–2119, 1998.

[289] L. Hultman, M. Shinn, P. B. Mirkarimi, and S. A. Barnett, “Characterization of misfit dislocations in epitaxial (001)-oriented TiN, NbN, VN, and (Ti,Nb) N film heterostructures by transmission electron microscopy,” *J. Cryst. Growth*, vol. 135, no. 1–2, pp. 309–317, Jan. 1994.

[290] S. Zhang and X. Zhang, “Toughness evaluation of hard coatings and thin films,” *Thin Solid Films*, vol. 520, no. 7, pp. 2375–2389, 2012.

[291] S. Kataria *et al.*, “Nanocrystalline TiN coatings with improved toughness deposited by pulsing the nitrogen flow rate,” *Surf. Coatings Technol.*, vol. 206, no. 19–20, pp. 4279–4286, 2012.

[292] S. Zhang, D. Sun, Y. Fu, and H. Du, “Toughness measurement of ceramic thin films by two-step uniaxial tensile method,” *Thin Solid Films*, vol. 469–470, no. SPEC. ISS., pp. 233–238, 2004.

[293] G. Wei, B. Bhushan, and S. J. Jacobs, “Nanoscale fatigue and fracture toughness measurements of multilayered thin film structures for digital micromirror devices,” *J. Vac. Sci. Technol. A Vacuum, Surfaces, Film.*, vol. 22, no. 4, pp. 1397–1405, 2004.

[294] S. Massl, W. Thomma, J. Keckes, and R. Pippan, “Investigation of fracture properties of magnetron-sputtered TiN films by means of a FIB-based cantilever bending technique,” *Acta Mater.*, vol. 57, no. 6, pp. 1768–1776, 2009.

[295] B. F. Chen, J. Hwang, I. F. Chen, G. P. Yu, and J. H. Huang, “A tensile-film-cracking model for evaluating interfacial shear strength of elastic film on ductile substrate,” *Surf. Coatings Technol.*, vol. 126, no. 2–3, pp. 91–95, 2000.

[296] R. V. Mises, “Mechanik der festen Körper im plastisch-deformablen Zustand,” *Nachrichten von der Gesellschaft der Wissenschaften zu Göttingen, Math. Klasse*, vol. 1913, pp. 582–592, 1913.

[297] P. H. Mayrhofer, C. Mitterer, L. Hultman, and H. Clemens, “Microstructural design of hard coatings,” *Prog. Mater. Sci.*, vol. 51, no. 8, pp. 1032–1114, 2006.

[298] E. Kelesoglu, C. Mitterer, and M. Ürgen, “Corrosion characteristics of plain carbon steel coated with TiN and ZrN under high-flux ion bombardment,” *Surf. Coatings Technol.*, vol. 160, no. 1, pp. 82–86, 2002.

[299] A. Rizzo, M. A. Signore, M. Penza, M. A. Tagliente, F. De Riccardis, and E. Serra, “RF sputtering deposition of alternate TiN/ZrN multilayer hard coatings,” *Thin Solid Films*, vol. 515, no. 2 SPEC. ISS., pp. 500–504, 2006.

[300] S. Veprek, M. G. J. Veprek-Heijman, P. Karvankova, and J. Prochazka, “Different approaches to superhard coatings and nanocomposites,” *Thin Solid Films*, vol. 476, no. 1, pp. 1–29, 2005.

[301] C. S. Sandu, R. Sanjinés, M. Benkahoul, F. Medjani, and F. Lévy, “Formation of composite ternary nitride thin films by magnetron sputtering co-deposition,” *Surf. Coatings Technol.*, vol. 201, no. 7 SPEC. ISS., pp. 4083–4089, 2006.

[302] A. Raveh, I. Zukerman, R. Shneck, R. Avni, and I. Fried, “Thermal stability of nanostructured superhard coatings: A review,” *Surf. Coatings Technol.*, vol. 201, no. 13, pp. 6136–6142, 2007.

[303] T. Schmitt *et al.*, “Cathodic arc deposited (Cr,Six)N coatings: From solid solution to nanocomposite structure,” *Surf. Coatings Technol.*, vol. 213, pp. 117–125, Dec. 2012.

[304] Z. Lei, Y. Liu, F. Ma, Z. Song, and Y. Li, “Oxidation resistance of TiAlN/ZrN multilayer coatings,” *Vacuum*, vol. 127, pp. 22–29, 2016.

[305] A. Mège-Revil *et al.*, “Correlation between thermal fatigue and thermomechanical properties during the oxidation of multilayered TiSiN nanocomposite coatings synthesized by a hybrid physical/chemical vapour deposition process,” *Thin Solid Films*, vol. 518, no. 21, pp. 5932–5937, 2010.

[306] S. Veprek and S. Reiprich, “A concept for the design of novel superhard coatings,” *Thin Solid Films*, vol. 268, pp. 64–71, 1995.

[307] C. Mitterer *et al.*, “Microstructure and properties of nanocomposite Ti–B–N and Ti–B–C

coatings," *Surf. Coatings Technol.*, vol. 120–121, pp. 405–411, Nov. 1999.

[308] S. Vepřek, S. Reiprich, and Li Shizhi, "Superhard nanocrystalline composite materials: The TiN/Si3N4 system," *Appl. Phys. Lett.*, vol. 66, no. 20, pp. 2640–2642, 1995.

[309] R. F. Zhang and S. Veprek, "Phase stabilities of self-organized nc-TiN/a-Si3N4 nanocomposites and of Ti1−xSixNy solid solutions studied by ab initio calculation and thermodynamic modeling," *Thin Solid Films*, vol. 516, no. 8, pp. 2264–2275, 2008.

[310] J. Lin *et al.*, "Thick CrN/AlN superlattice coatings deposited by the hybrid modulated pulsed power and pulsed dc magnetron sputtering," *Surf. Coatings Technol.*, vol. 228, no. SUPPL.1, pp. 601–606, 2013.

[311] K. Lukaszkowicz, "Review of Nanocomposite Thin Films and Coatings Deposited by PVD and CVD Technology," *Intechopen*, pp. 145–162, 2011.

[312] G. Abadias, V. I. Ivashchenko, L. Belliard, and P. Djemia, "Structure, phase stability and elastic properties in the Ti 1-xZr xN thin-film system: Experimental and computational studies," *Acta Mater.*, vol. 60, no. 15, pp. 5601–5614, 2012.

[313] O. Knotek, M. Böhmer, T. Leyendecker, and F. Jungblut, "The structure and composition of Ti-Zr-N, Ti-Al-Zr-N and Ti-Al-V-N coatings," *Mater. Sci. Eng. A*, vol. 105–106, pp. 481–488, Dec. 1988.

[314] B. Wendler, W. Pawlak, M. Makówka, K. Włodarczyk, P. Nolbrzak, and A. Rylski, "Hard and superhard nanolaminate and nanocomposite coatings for machine elements based on Ti6Al4V alloy," *Vacuum*, vol. 43, no. 1, pp. 455–462, 2010.

[315] L. Cunha, M. Andritschky, L. Rebouta, and R. Silva, "Corrosion of TiN, (TiAl)N and CrN hard coatings produced by magnetron sputtering," *Thin Solid Films*, vol. 317, no. 1–2, pp. 351–355, 1998.

[316] L. V. Azaroff, *Elements of X-ray Crystallography*. New York, 1968.

[317] L. Vegard, "Die Konstitution der Mischkristalle und die Raumfullung der Atome," *Zeitschrift fur Phys.*, vol. 5, no. 1, pp. 17–26, Jan. 1921.

[318] D. Oh, H. Kim, and C. Chung, "A study on mechanical properties of TiN , ZrN AND WC coated film on the titanium alloy surface," *J. Korean Acad Prosthodont*, vol. 44, no. 6, pp. 740–750, 2006.

[319] H. Nakajima and M. Koiwa, "Diffusion in α-Titanium," *Defect Diffus. Forum*, vol. 95–98, no. 8, pp. 775–782, Jan. 1993.

[320] B. P. Panda, "Electronic structure and equilibrium properties of hcp titanium and zirconium," *Pramana - J. Phys.*, vol. 79, no. 2, pp. 327–335, 2012.

[321] G. Abadias and P. Guerin, "In situ stress evolution during magnetron sputtering of transition metal nitride thin films," *Appl. Phys. Lett.*, vol. 93, no. 11, pp. 36–39, 2008.

[322] R. Daniel *et al.*, "Grain boundary design of thin films: Using tilted brittle interfaces for multiple crack deflection toughening," *Acta Mater.*, vol. 122, pp. 130–137, 2017.

[323] M. J. Cordill, T. Jörg, O. Glushko, R. Franz, and C. Mitterer, "Crack deflecting microstructure for improved electro-mechanical lifetimes of flexible systems," *Mater. Lett.*,

vol. 244, pp. 47–49, 2019.

[324] M. Gsellmann *et al.*, "Near-interface cracking in a TiN coated high speed steel due to combined shear and compression under cyclic impact loading," *Surf. Coatings Technol.*, vol. 394, no. March, p. 125854, 2020.

[325] R. Daniel *et al.*, "Fracture toughness enhancement of brittle nanostructured materials by spatial heterogeneity: A micromechanical proof for CrN/Cr and TiN/SiOx multilayers," *Mater. Des.*, vol. 104, pp. 227–234, 2016.

[326] X. Zhao, Z. Xie, and P. Munroe, "Nanoindentation of hard multilayer coatings: Finite element modelling," *Mater. Sci. Eng. A*, vol. 528, no. 3, pp. 1111–1116, 2011.

[327] J. M. Cairney, M. J. Hoffman, P. R. Munroe, P. J. Martin, and A. Bendavid, "Deformation and fracture of Ti-Si-N nanocomposite films," *Thin Solid Films*, vol. 479, no. 1–2, pp. 193–200, 2005.

[328] P. C. Wo, P. R. Munroe, Z. F. Zhou, K. Y. Li, and Z. H. Xie, "Effects of TiN sublayers on the response of TiSiN nanocomposite coatings to nanoidentation and scratching contacts," *Mater. Sci. Eng. A*, vol. 527, no. 16–17, pp. 4447–4457, 2010.

[329] V. V. Uglov *et al.*, "Structural characterization and mechanical properties of Ti–Zr–N coatings, deposited by vacuum arc," *Surf. Coatings Technol.*, vol. 180–181, pp. 519–525, Mar. 2004.

[330] S. Veprek, "Recent search for new superhard materials: Go nano!," *J. Vac. Sci. Technol. A Vacuum, Surfaces, Film.*, vol. 31, no. 5, p. 050822, Sep. 2013.

[331] M. Bielawski and K. Chen, "Computational evaluation of interfacial fracture toughness of thin coatings," *WIT Trans. Eng. Sci.*, vol. 62, pp. 85–94, 2009.

[332] Rolls-Royce, *The Jet Egine*. London, England: John Wiley & Sons, 2015.

[333] E. Salvati, L. Romano-Brandt, M. Z. Mughal, M. Sebastiani, and A. M. Korsunsky, "Generalised residual stress depth profiling at the nanoscale using focused ion beam milling," *J. Mech. Phys. Solids*, vol. 125, pp. 488–501, 2019.

[334] R. Machunze and G. C. A. M. Janssen, "Stress and strain in titanium nitride thin films," *Thin Solid Films*, vol. 517, no. 20, pp. 5888–5893, 2009.

[335] A. Mézin, "Coating internal stress measurement through the curvature method: A geometry-based criterion delimiting the relevance of Stoney's formula," *Surf. Coatings Technol.*, vol. 200, no. 18–19, pp. 5259–5267, 2006.

[336] S. R. Cullity, B. D., & Stock, *Elements of X-ray diffraction*, 6th ed. Upper Saddle River, NJ: Prentice Hall, 2001.

[337] Q. Luo and A. H. Jones, "High-precision determination of residual stress of polycrystalline coatings using optimised XRD-sin2ψ technique," *Surf. Coatings Technol.*, vol. 205, no. 5, pp. 1403–1408, 2010.

[338] P. . Kelly, "Mechanics Lecture Notes: An introduction to Solid Mechanics," 2013, pp. 120–187.

[339] S. Zhang, D. Sun, Y. Fu, and H. Du, "Toughness measurement of thin films: A critical

review," *Surf. Coatings Technol.*, vol. 198, no. 1-3 SPEC. ISS., pp. 74–84, 2005.